

**Impedance Spectroscopy Study of Water Uptake and Long-Term Degradation of Immersed Polyimide Coatings**

by  
Krassimir P. Nenov

Dipl.-Ing., Metallurgy, Bergakademie-Freiberg, Germany (1988)  
M.S., Ocean Engineering, Florida Atlantic University, Boca Raton (1991)

Submitted to the Department of  
Materials Science and Engineering  
in partial fulfillment of the requirements  
for the Degree of

**Doctor of Philosophy in Materials Engineering**  
at the  
**Massachusetts Institute of Technology**

May (1994)

© Massachusetts Institute of Technology, 1994

Signature of Author \_\_\_\_\_  
Department of Materials Science and Engineering  
April, 1994

Certified by \_\_\_\_\_  
Ronald M. Latanision  
Professor of Materials Science and Engineering  
Thesis Supervisor

Accepted by \_\_\_\_\_  
Carl V. Thompson II  
Professor of Electronic Materials  
Chair, Departmental Committee on Graduate Students

Science  
MASSACHUSETTS INSTITUTE  
OF TECHNOLOGY

AUG 18 1994

LIBRARIES



# Impedance Spectroscopy Study of Water Uptake and Long-Term Degradation of Immersed Polyimide Coatings

by  
Krassimir P. Nenov

Submitted to the Department of Materials Science and Engineering  
in partial fulfillment of the requirements for the Degree of  
Doctor of Philosophy in Materials Engineering  
May, 1994

## Abstract

This thesis reports on a feasibility study of lifetime prediction for polyimide/metal structures immersed in 0.5 M NaCl, by means of short-term, non-destructive, *in-situ* measurements. Polyimide coatings for use in electronic packaging: PMDA-ODA, BPDA-PDA, BTDA-ODA/MPDA, and HFDA-APBP spin-cast on Cr, Al, or Cu-metallized Si substrates were investigated. The coating thicknesses ranged between 0.5  $\mu\text{m}$  and 8  $\mu\text{m}$ . Permittivity transient measurements were employed to obtain the diffusion coefficient and the solubility of water in the coatings. The diffusion coefficients of chlorides in the water-saturated coatings were measured via membrane permeation. Impedance spectroscopy (IS) was used to monitor the irreversible long-term degradation and to detect failure of the coated structures. X-ray photoelectron spectroscopy (XPS) was employed for failure analyses and polymer chemistry investigations. The various polyimide/metal combinations were compared in terms of their long-term reliability. The effects of non-standard processing: lower cure temperature, electron-beam irradiation, or repeated cure on the coating properties were investigated. Failure of the coated substrates, manifested in the abrupt increase in the amount of exposed interfacial area measured by IS was attributed to cohesive or adhesive osmotic delamination in coatings on Cr or Al, respectively. HFDA-APBP coatings on Cr yielded the longest lifetimes. Non-standard processing produced coatings whose reliability was inferior to that of standard-processed ones. In the case of a cohesive failure mode, the time-to-failure of the coated substrates was a function of the long-term degradation rate of the polymer. IS could be used to measure the amount of exposed interfacial area through defects in the coating, however it could not detect delaminated regions at the interface in the absence of a low-resistance connection between the interface and the electrolyte. Permittivity transients yielded reliable water diffusion and uptake data and could also detect defects in the coatings. In all investigated polyimides, water diffusion was Fickian with concentration-independent diffusion coefficients. The dielectric permittivity of the coatings continued to increase after saturation with water. This was attributed to hydrogen-bonding interactions among the absorbed water molecules, or between the absorbed water and the polymer.

Lifetime prediction from short-term measurements was not possible, because none of the parameters measurable within the first 10000 s since immersion: water diffusion coefficient, water solubility, and the parameter representative of hydrogen bonding exhibited a correlation with the time-to-failure.

**Thesis Supervisor:** Dr. Ronald M. Latanision  
Professor of Materials Science and Engineering



## Table of Contents

Abstract .....	3
Table of Contents .....	5
List of Figures .....	7
List of Tables .....	15
Acknowledgments .....	17
1. Introduction .....	19
1.1. Polyimides in Electronic Packaging .....	19
1.2. Corrosion in Electronic Packaging .....	23
1.3. Research Objectives and Significance .....	24
1.4. Outline of Thesis .....	26
2. Materials, Sample Preparation, and Experimental Methods .....	29
2.1. Materials and Sample Preparation .....	29
2.2. Experimental Methods .....	32
2.2.1. Impedance Spectroscopy .....	32
2.2.2. X-ray Photoelectron Spectroscopy .....	41
2.3.3. Other Experimental Methods .....	45
3. Solute Uptake and Diffusion in Polyimide Coatings.....	47
3.1. Methods of Measurement of Water Uptake and Diffusion in Polymers ....	47
3.2. Water Uptake and Diffusion from Relative Permittivity Measurements ....	49
3.2.1. Measurement Procedure .....	50
3.2.2. Effect of Absorbed Water on the Dielectric Properties of Polyimides .....	52
3.2.3. Modeling of Permittivity Transient Data .....	57
3.2.4. Application of the Water Diffusion Model to Experimental Data ...	62
3.3. Water Uptake and Diffusion Results .....	66
3.3.1. Water Diffusion. Results and Discussion .....	68
3.3.2. Water Uptake. Results and Discussion .....	73
3.4. Results from Measurements of Diffusion of Organic Solutes .....	77
3.5. Origins of the Logarithmic Trend in Dielectric Permittivity .....	79
3.6. Utility of Permittivity Transient Measurements for Defect Detection in Coatings .....	85
3.7. Measurements of Chloride Ion Diffusion via Membrane Permeation .....	87
4. Degradation and Lifetime of Coated Substrates .....	97

4.1.	Interpretation of Impedance Spectroscopy Data from Coated Substrates ..	97
4.2.	Results of Long-Term Exposure to 0.5 M NaCl .....	115
4.3.	Comparison among Short and Long-Term Results. Feasibility of Lifetime Prediction .....	123
5.	Investigation of Effects of Processing on Polyimide Coatings .....	125
5.1.	Specimen Preparation and Processing .....	125
5.2.	Chemical Analyses via XPS .....	126
5.3.	Density, Water Uptake and Diffusion, and Long-Term Degradation .....	131
5.4.	Summary of Processing Effects .....	138
6.	Conclusions and Future Work .....	141
6.1.	Conclusions .....	141
6.2.	Future Work .....	145
Appendix A.	Setup parameters for XPS Data Acquisition .....	147
Appendix B.	Equilibrium vs. Transient Water Uptake .....	149
Appendix C.	XPS Analyses of Failed and Processed Samples .....	151
Bibliography	.....	167
Biographical Note	.....	171

## List of Figures

Figure 1.1.1.	Schematic of a multichip module .....	19
Figure 1.1.2.	Major technologies in circuit base manufacturing .....	20
Figure 1.1.3.	Synthesis of polyimides .....	22
Figure 2.1.1.	Chemical structure of PMDA-4,4'-ODA .....	29
Figure 2.1.2.	Chemical structure of BPDA-PDA .....	29
Figure 2.1.3.	Chemical structure of HFDA-APBP .....	30
Figure 2.1.4.	Chemical structure of BTDA-ODA/MPDA .....	30
Figure 2.1.5.	Test cell assembly for impedance spectroscopy and long-term exposure experiments .....	32
Figure 2.2.1.	Schematic of a frequency response analyzer .....	33
Figure 2.2.2.	Schematic of the impedance spectroscopy setup .....	34
Figure 2.2.3.	Test circuit used for optimization of the data acquisition and comparison of impedance data acquired from it with data from a 3 $\mu\text{m}$ PMDA-ODA/Cr coating .....	35
Figure 2.2.4.	Comparison among the impedance spectra of four RC-circuits with different resistances .....	36
Figure 2.2.5.	Debye equivalent circuit model of an ideal insulator with a single relaxation time .....	37
Figure 2.2.6.	Dielectric loss spectrum of a 1.8 $\mu\text{m}$ BPDA-PDA/Cr coating 2 days after immersion in 0.5 M NaCl at 23 $^{\circ}\text{C}$ with evidence of dc conductivity .....	38
Figure 2.2.7.	Equivalent circuit model of a metal/electrolyte interface with faradaic charge transport and diffusion .....	39
Figure 2.2.8.	a) Structure, binding energy table, and XPS survey scan of PMDA-ODA. b) C1s, O1s, and N1s spectra of PMDA-ODA .....	43
Figure 2.2.9.	Calibration curve of the density gradient column at 23 $^{\circ}\text{C}$ .....	46
Figure 3.2.1.	Test cell drying and filling arrangement for permittivity transients .....	50
Figure 3.2.2.	Relative permittivity and ac conductivity transients at 1000 Hz in a 5.33 $\mu\text{m}$ PMDA-ODA/Cr coating upon immersion in 0.5 M NaCl at 23 $^{\circ}\text{C}$ .....	52

Figure 3.2.3.	Linear relationships between the relative humidity of the environment, the dielectric permittivity, and the equilibrium water uptake in 5-10 $\mu\text{m}$ polyimide capacitors .....	56
Figure 3.2.4.	Schematic representation of a coating with a gradient of water concentration as a series of capacitors with different capacitances .....	58
Figure 3.2.5.	Comparison of capacitance data simulated numerically by means of (3.2.20), (3.2.21), and (3.2.24) for a typical set of parameter values .....	61
Figure 3.2.6.	Non-linear regression fit of equation (3.2.24) to the data simulated via (3.2.21) .....	61
Figure 3.2.7.	Illustration of the logarithmic increase in the relative permittivity of various coatings as a function of time .....	63
Figure 3.2.8.	Capacitance transient in a 1.95 $\mu\text{m}$ BPDA-PDA/Cr coating in 0.5 M NaCl at 23 $^{\circ}\text{C}$ . Subtraction of the logarithmic trend from the data revealed the underlying water diffusion process .....	64
Figure 3.2.9.	Regression analysis of permittivity transients from PMDA-ODA, BPDA-PDA, HFDA-APBP, and BTDA-ODA/MPDA coatings, by means of a Fickian model with concentration-independent diffusion coefficients .....	65
Figure 3.2.10.	Experimental separation in time of the Fickian water uptake and the logarithmic trend in the permittivity transient .....	65
Figure 3.3.1.	Correlation among the free volume fractions and water diffusion coefficients in the four polyimides, indicative of the dominant role of morphology in determining the transport kinetics .....	69
Figure 3.3.2.	Water diffusion coefficients at 23 $^{\circ}\text{C}$ in PMDA-ODA, HFDA-APBP, and BPDA-PDA coatings on Cr and Al as a function of the coating's thickness .....	70
Figure 3.3.3.	Measured water diffusion coefficients and densities of standard-cure coatings ( $T_{\text{cure}} = 400$ $^{\circ}\text{C}$ ) vs. coatings cured at 250 $^{\circ}\text{C}$ .....	72
Figure 3.3.4.	Activation energies for water diffusion in PMDA-ODA, BPDA-PDA, and HFDA-APBP coatings on Cr .....	72
Figure 3.3.5.	Polarity of the dry polyimides, expressed as the difference between the low-frequency transverse dielectric permittivity and the square of the transverse refractive index (HeNe laser, 0.63 $\mu\text{m}$ ) .....	74
Figure 3.3.6.	a) Calculated dielectric permittivities of the absorbed water in PMDA-ODA, BPDA-PDA, HFDA-APBP, and BTDA-ODA/MPDA at 23 $^{\circ}\text{C}$ . b) Permittivity of absorbed water as a function of the free-volume fraction .....	75
Figure 3.3.7.	Equilibrium water uptake in PMDA-ODA, BPDA-PDA, and BTDA-ODA/MPDA coatings on Cr as a function of the cure temperature .....	77



Figure 3.4.1.	a) Permittivity transients in a HFDA-APBP/Cr coating immersed in acetone and ethanol at 23 °C. b) Regression to the permittivity transient in ethanol .....	78
Figure 3.4.2.	Diffusion coefficients of several organic solutes in PMDA-ODA and HFDA-APBP as a function of the solutes' molecular weights and van der Waals volumes .....	79
Figure 3.5.1.	Permittivity transients in a BPDA-PDA/Al coating in 0.5 M NaCl and 0.05 M La(NO <sub>3</sub> ) <sub>3</sub> .....	80
Figure 3.5.2.	Permittivity transients following concentration steps in a BPDA-PDA coating on Cu .....	81
Figure 3.5.3.	a) Negative logarithmic trend due to water desorption from the coating. b) Regression fit of the Fickian diffusion model to the permittivity transient yields the diffusion coefficient of water desorption and, using the b-value from Table 3.3.1, the amount of water desorbed from the coating .....	81
Figure 3.5.4.	Permittivity transients in BPDA-PDA/Al and PMDA-ODA/Al in response to concentration and dilution steps in the electrolyte .....	83
Figure 3.5.5.	Permittivity values, $\epsilon_{\text{equil}}$ , corresponding to the Fickian equilibrium water uptake of the coatings from Figure 3.5.4, as a function of water molarity in the electrolyte .....	83
Figure 3.5.6.	Enthalpy plots of the logarithmic process in HFDA-APBP and PMDA-ODA coatings immersed in 0.5 M NaCl .....	84
Figure 3.6.1.	An abnormal permittivity transient in a BPDA-PDA/Cr coating indicated a defective coating .....	86
Figure 3.6.2.	Capacitance transients of two PMDA-ODA/Cr coatings of similar thickness cured under different nitrogen gas-flow conditions. Too low N <sub>2</sub> flow rate probably resulted in internal oxidation and porosity .....	87
Figure 3.7.1.	Two-compartment cell used for membrane permeation measurements ...	88
Figure 3.7.2.	a) Chloride concentration in the acceptor compartment as a function of time during a BPDA-PDA membrane permeation experiment at 60 and 90 °C. b) Activation energy plots for chloride diffusion through spin-cast PMDA-ODA and BPDA-PDA membranes .....	93
Figure 3.7.3.	Permeation experiments with 7.5 $\mu\text{m}$ Kapton® HN 30 (PMDA-ODA) membranes revealed no chloride permeation even after 8 days at 90 °C .....	94
Figure 4.1.1.	The generally-accepted equivalent circuit for a polymer-coated metal ...	97
Figure 4.1.2.	Characteristic features in the Bode plots of impedance data simulated by means of the coating equivalent circuit of Figure 4.1.1 .....	98

Figure 4.1.3.	a) Impedance spectrum and CNLS parameter estimates for a 7.5 $\mu\text{m}$ PMDA-ODA <u>free film</u> suspended in 0.5 M NaCl at 23 $^{\circ}\text{C}$ . b) Impedance spectrum and CNLS parameter estimates for a 7.09 $\mu\text{m}$ PMDA-ODA/Al (PI2545) <u>coating</u> in 0.5 M NaCl at 23 $^{\circ}\text{C}$ .....	100
Figure 4.1.4.	Comparison between a permittivity transient acquired upon initial immersion in 0.5 M NaCl and a second transient acquired on the same coating after 16 days of exposure to 0.5 M NaCl at 60 $^{\circ}\text{C}$ followed by 10 days drying in a dessicator .....	101
Figure 4.1.5.	a) Increasing dielectric permittivity of free Kapton <sup>®</sup> film during exposure to 0.5 M NaCl or DI water at 23 $^{\circ}\text{C}$ . b) Isochronal resistivity (5400 s) of the same film as a function of exposure time .....	102
Figure 4.1.6.	Impedance spectrum, CNLS fit, and estimated metal film/electrolyte interface parameters of a Cr-coated Si wafer without a polymer coating .....	103
Figure 4.1.7.	Impedance spectrum, CNLS fit, and estimated metal film/electrolyte interface parameters of a Pt-coated Si wafer without a polymer coating .....	103
Figure 4.1.8.	Equivalent circuit model of a protective coating exhibiting delamination and porosity over a non-blocking electrode .....	105
Figure 4.1.9.	Simulated impedance spectra for a 3 $\mu\text{m}$ pore-free coating with three different degrees of delamination .....	106
Figure 4.1.10.	a) IS spectra of a 1.35 $\mu\text{m}$ HFDA-APBP/Al coating several hours and 100 days after immersion in 0.5 M NaCl at 23 $^{\circ}\text{C}$ . b) Photograph (x100) of a region of the coating after the 100-day exposure .....	107
Figure 4.1.11.	IS spectrum of the 100-days exposed 1.35 $\mu\text{m}$ HFDA-APBP/Al coating of Figure 4.1.10 1/2 hour after a small pore had been introduced in the coating above a delaminated region .....	108
Figure 4.1.12.	Simplified equivalent circuit model of the coated sample used for IS data analysis .....	109
Figure 4.1.13.	CNLS regression to impedance data from a 4.76 $\mu\text{m}$ BTDA-ODA/MPDA coating on Cr after 7 days of exposure to 0.5 M NaCl at 60 $^{\circ}\text{C}$ .....	110
Figure 4.1.14.	a) Bode-Angle plot of IS data from a 1.95 $\mu\text{m}$ BPDA-PDA/Cr coating exposed to 0.5 M NaCl at 23 $^{\circ}\text{C}$ , before and after the introduction of an artificial defect. b) Evolution of the CNLS parameter estimates at 0.5 h and 14 h after defect introduction .....	111

Figure 4.1.15. CNLS estimates of $C_{dl}$ and $R_f$ (Figure 4.1.12) as a function of exposed (scratched) area .....	112
Figure 4.1.16. a) Exposed area in PMDA-ODA/Cr prior to anodic bias (x32). b) Same region after 100 s of anodic bias at +1 V vs. OCP (x32). c) Change in the CNLS estimates of $C_{dl}$ and $R_f$ as a result of anodic bias .....	113
Figure 4.1.17. Impedance spectrum and CNLS parameter estimates of a BTDA-ODA/MPDA coating on Cr after 25 days in 0.5 M NaCl at 60 °C .....	114
Figure 4.2.1. Long-term degradation of a 0.50 $\mu\text{m}$ BPDA-PDA/Cr sample during exposure to 0.5 M NaCl at 23 °C .....	115
Figure 4.2.2. CNLS estimates of $C_{dl}$ , $R_f$ , and $\epsilon'$ , along with the open-circuit potentials for the BPDA-PDA coating of Figure 4.2.1. The sharp increase in exposed area indicated by $C_{dl}$ and $R_f$ was defined as coating failure .....	115
Figure 4.2.3. Illustration of the steady-state long-term rate of increase in dielectric permittivity, $d(\epsilon')/d(\sqrt{t})$ , and its average values for PMDA-ODA, BPDA-PDA, and HFDA-APBP during exposure to 0.5 M NaCl at 23 °C .....	116
Figure 4.2.4. Comparison among standard-cure and secondary-cure PMDA-ODA degradation rates in 0.5 M NaCl at 23 °C .....	117
Figure 4.2.5. Increase in $C_{dl}$ (proportional to the amount of exposed interfacial area) in PMDA-ODA, BPDA-PDA, and HFDA-APBP coatings (< 1 $\mu\text{m}$ ) during exposure to 0.5 M NaCl at 23 °C .....	118
Figure 4.2.6. Photograph and schematics of delamination-type failure (BPDA-PDA/Al) .....	119
Figure 4.2.7. Photograph and schematics of blistering-type failure (HFDA-APBP/Al) .....	119
Figure 4.2.8. Times-to-failure of PMDA-ODA, BPDA-PDA, and HFDA-APBP coatings on Cr as a function of the steady-state rate of permittivity increase, $d(\epsilon')/d(\sqrt{t})$ .....	121
Figure 4.2.9. Times-to-failure of PMDA-ODA, BPDA-PDA, and HFDA-APBP coatings on Cr as a function of the coatings thickness .....	122
Figure 4.3.1. Comparisons between the steady-state water diffusion flux and the time-to-failure in PMDA-ODA, BPDA-PDA, and HFDA-APBP coatings exposed to 0.5 M NaCl at 23 °C .....	123
Figure 4.3.2. Times-to-failure of PMDA-ODA, BPDA-PDA, and HFDA-APBP coatings on Cr as a function of the magnitude of the logarithmic trend..	124

Figure 4.3.3.	Long-term degradation rates of PMDA-ODA, BPDA-PDA, and HFDA-APBP coatings on Cr as a function of the magnitude of the logarithmic trend .....	124
Figure 5.2.1.	Chemical structure of BPDA-PDA with identified XPS contributions ..	127
Figure 5.2.2.	Chemical structure of BTDA-ODA/MPDA with identified XPS contributions .....	127
Figure 5.2.3.	Chemical structure of PMDA-ODA with identified XPS contributions .	128
Figure 5.3.1.	a) Normalized diffusion coefficients of water in BPDA-PDA, BTDA-ODA/MPDA, and PMDA-ODA/Cr coatings as a function of processing. b) Normalized diffusion coefficients of water as a function of processing averaged over all 3 polyimide types .....	132
Figure 5.3.2.	a) Normalized water uptake by BPDA-PDA, BTDA-ODA/MPDA, and PMDA-ODA/Cr coatings as a function of processing. b) Normalized water uptake as a function of processing averaged over all 3 polyimide types .....	133
Figure 5.3.3.	Positive correlation between the water diffusion coefficient and the water uptake in BPDA-PDA, BTDA-MPDA/ODA, and PMDA-ODA coatings on Cr .....	134
Figure 5.3.4.	a) Density of BPDA-PDA (PI2611) and PMDA-ODA (OCG627) coatings on Cr as a function of processing. b) Negative correlation between density and water diffusion coefficients in PMDA-ODA. A similar correlation was observed for water uptake .....	134
Figure 5.3.5.	Densities and water diffusion coefficients in BPDA-PDA .....	135
Figure 5.3.6.	PI-type-specific (a), and average (b) magnitudes of the logarithmic trends in the permittivity transients upon initial immersion in 0.5 M NaCl at 23 °C, as a function of the processing conditions .....	135
Figure 5.3.7.	a) Long-term increase in the relative permittivity of processed BTDA-ODA/MPDA (PI2525) coatings on Cr in 0.5 M NaCl at 60 °C. b) Long-term degradation of the interface (increase in exposed area) in processed BTDA-ODA/MPDA coatings on Cr in 0.5 M NaCl at 60 °C .....	136
Figure 5.3.8.	a) Long-term increase in the relative permittivity of processed PMDA-ODA (OCG627) coatings on Cr in 0.5 M NaCl at 60 °C. b) Long-term degradation of the interface (increase in exposed area) in processed PMDA-ODA coatings on Cr in 0.5 M NaCl at 60 °C .....	136
Figure 5.3.9.	Internal blistering in BTDA-ODA/MPDA coatings cured at 250 °C and treated with 3000 $\mu\text{C}/\text{cm}^2$ e-beam radiation .....	137
Figure B.1.	A comparison between two coatings with the same average water concentration. The capacitance values of the coatings are different due to the presence of a water concentration gradient in one of them .....	150

Figure C.1.1.	Survey, C1s, O1s, and N1s spectra of film side of failed BPDA-PDA/Cr sample at location of failure. Survey scan shows absence of Cr, indicative of cohesive delamination .....	151
Figure C.1.2.	Survey, Al1s, C1s, O1s, and N1s spectra of film side of failed BPDA-PDA/Al sample at location of failure. Survey scan shows presence of Al, indicative of adhesive delamination. Al1s spectrum shows presence of Al(OH <sub>3</sub> ) .....	152
Figure C.1.3.	Survey, Al1s, C1s, O1s, and N1s spectra of substrate side of failed BPDA-PDA/Al sample at location of failure. Survey scan shows presence of polyimide, indicative of adhesive delamination. Al1s spectrum shows presence of Al(OH <sub>3</sub> ) .....	153
Figure C.2.1.	Graphical representation of processed XPS data from six BPDA-PDA samples (peak assignments according to Figure 5.2.1): a) Deviation from the stoichiometric chemical composition, b) Deviation from the theoretical peak fractions in C1s, c) Deviation from the theoretical peak fractions in O1s, d) Relative shifts in peak BEs with respect to STC, e) Relative peak broadening with respect to STC .....	155
Figure C.2.2.	C1s spectral evolution of 6 BPDA-PDA samples .....	156
Figure C.2.3.	O1s spectral evolution of 6 BPDA-PDA samples .....	156
Figure C.2.4.	N1s spectral evolution of 6 BPDA-PDA samples .....	157
Figure C.2.5.	Graphical representation of processed XPS data from six BTDA-ODA/MPDA samples (peak assignments according to Figure 5.2.2): a) Deviation from the stoichiometric chemical composition, b) Deviation from the theoretical peak fractions in C1s, c) Deviation from the theoretical peak fractions in O1s, d) Relative shifts in peak BEs with respect to STC, e) Relative peak broadening with respect to STC .....	159
Figure C.2.6.	C1s spectral evolution of 6 BTDA-ODA/MPDA samples .....	160
Figure C.2.7.	O1s spectral evolution of 6 BTDA-ODA/MPDA samples .....	160
Figure C.2.8.	N1s spectral evolution of 6 BTDA-ODA/MPDA samples .....	161
Figure C.2.9.	Graphical representation of processed XPS data from six PMDA-ODA samples (peak assignments according to Figure 5.2.3): a) Deviation from the stoichiometric chemical composition, b) Deviation from the theoretical peak fractions in C1s, c) Deviation from the theoretical peak fractions in O1s, d) Relative shifts in peak BEs with respect to STC, e) Relative peak broadening with respect to STC .....	163
Figure C.2.10.	C1s spectral evolution of 6 PMDA-ODA samples .....	164
Figure C.2.11.	O1s spectral evolution of 6 PMDA-ODA samples .....	164
Figure C.2.12.	N1s spectral evolution of 6 PMDA-ODA samples .....	165

Figure C.3.1. Micrograph of laser-ablated polyimide .....	166
Figure C.3.2. XPS spectra of C1s, O1s, and N1s in pristine and treated Kapton® (heat treatment and laser ablation). The peak contributions (%) are indicated inside the peaks .....	167

## List of Tables

Table 1.1.1.	Advantages of polyimides in electronic packaging .....	22
Table 2.1.1.	Cure schedules for the polyimide coatings prepared at MIT .....	31
Table 3.3.1.	Water uptake and diffusion results for PMDA-ODA, BPDA-PDA, HFDA-APBP, and BTDA-ODA/MPDA coatings on various substrates (23 °C, immersion in 0.5 M NaCl) .....	67
Table 3.3.2.	Comparison among the present results and published data on water diffusion (T=22-25 °C) .....	68
Table 3.3.3.	Transverse refractive indices, $n_{TM}$ of dry and water-saturated coatings ...	74
Table 4.1.1.	Estimated parameters of the equivalent circuit model of the bare Cr/electrolyte interface as a function of test conditions (quiescent electrolyte) .....	104
Table 4.2.1.	Average days to failure $\pm$ standard error of PMDA-ODA, BPDA-PDA, and HFDA-APBP coatings on Cr, Al, and Cu substrates in 0.5 M NaCl at 23 °C .....	120
Table 5.2.1.	Stoichiometric composition and theoretical bond fractions in BPDA-PDA, BTDA-ODA/MPDA, and PMDA-ODA for XPS analysis .....	128
Table 5.3.1.	Results from density, water uptake, and water diffusion measurements of 24 BPDA-PDA, BTDA-ODA/MPDA, and PMDA-ODA-coated wafers supplied by FCPT (0.5 M NaCl, 23 °C) .....	131
Table C.2.1.	XPS data from analysis of six BPDA-PDA samples .....	154
Table C.2.2.	XPS data from analysis of six BTDA-ODA/MPDA samples .....	158
Table C.2.3.	XPS data from analysis of six PMDA-ODA samples .....	162





## Acknowledgments

First of all, I would like to thank my advisor, Prof. Ronald M. Latanision, for his guidance, financial and administrative support, and encouragement during the years at MIT.

The member companies of the Electronic Packaging Program (EPP) at MIT contributed financial support and pressure to this work. I am also grateful for the financial support from IBM which provided an year-long graduate fellowship.

Dr. Pradnya Nagarkar, then a research associate at the H. H. Uhlig Corrosion Laboratory spent many dark winter hours in a basement to make the XPS part of this work possible. Fred Trusell, then at the Microsystems Technology Laboratories at MIT prepared almost all specimens used in this work. Dave Volfson was ever helpful in addressing various EPP-related issues. Prof. Stephen D. Senturia, the EPP chairman, contributed with interest, tolerance, advice, and his astonishing memory and breadth of knowledge. Dr. Solomon Beilin of Fujitsu Computer Packaging Technologies supplied specimens and financial support for the processing-properties study, and answered many related questions. Dr. Andrew Dineen of Draper Lab and Dr. Herbert Neuhaus of Amoco Chemical provided help with specimen preparation.

I am grateful to Professors Donald Sadoway and Harry Tuller who served on my thesis committee. In two classes, Prof. Sadoway provided inspiration to me and others with his wonderful sense of humor, intellect, and skeptical enthusiasm.

I am grateful to Prof. Andreas Mortensen, the Department of Materials Science and Engineering, and MIT in general who gave me the opportunity to partake in the MIT experience.

I thank Dr. Bryce Mitton at the Corrosion Laboratory for his friendly help and discussion. Connie Beal, assisted by Ilda Moura and Kelly Fischer guided me through the administrative maze of mostly unadvertised deadlines, overdrawn accounts, and

outstanding fees. They also took care of my physical fitness by constant rearrangements of offices and laboratories under various pretexts.

My wife, Kay, deserves my loving thanks for putting up with years of quasi-married life and abuse of our family savings. To her I promise that this will be my last dissertation. My brother, Anastas, and sister-in-law, Nevyana participated in hours of mutual long-distance telephone counseling and provided occasional retreat from the cruel Boston weather. My parents, Yordanka and Peter, and my grandmothers, Ivanka and Kina suffered and continue to suffer from our absence from home, yet they helped, loved, and encouraged us in all of our endeavors.

Although unworthy of them, I dedicate this work to my parents, my grandmothers, Kay, Nevyana, and Anastas with love.

P.S. Because this is meant to be a recap of all the years spent at MIT, I would like to take this opportunity and disacknowledge the three Cambridge and Somerville drivers who on different occasions attempted, and nearly succeeded in taking my life while exposed on my commuter bicycle.

I thank and admire the surgeons at the Massachusetts Eye and Ear Infirmary, and particularly Drs. Bilyk and Vavares who successfully maintained my outward appearance.

# 1. Introduction

## 1.1. Polyimides in Electronic Packaging

Multichip modules (MCMs) are used increasingly in computer manufacturing. A multichip module is defined as a "structure consisting of two or more integrated circuit chips electrically connected to a common circuit base and interconnected by conductors in that base" [1]. The schematic of a MCM is illustrated in Figure 1.1.1.

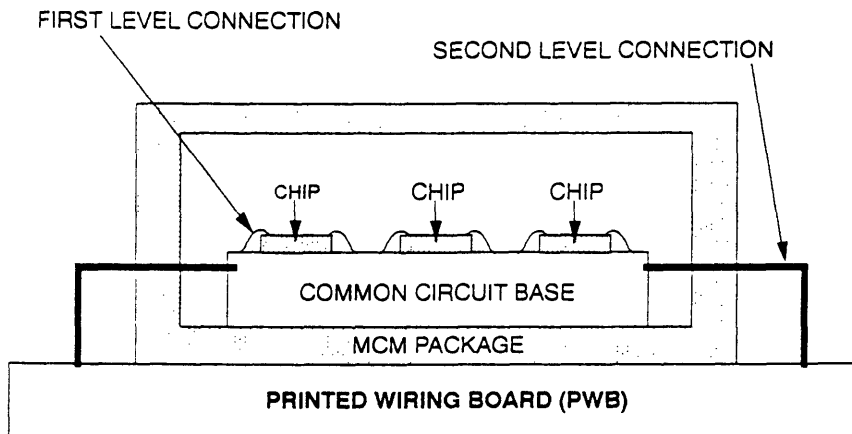


Figure 1.1.1. Schematic of a multichip module [1].

The advantages provided by MCMs include higher system speeds, reduced overall size, ability to handle chips with large numbers of inputs and outputs (I/Os), greater density of interconnects, and reduced number of external connections [1,2].

The common circuit base is a critical part of the MCM package because it defines numerous aspects of MCM performance. At present, there are three standard technologies for circuit base manufacturing: MCM-L, MCM-C, and MCM-D. These are defined and schematically illustrated in Figure 1.1.2, along with the less frequently employed MCM-D/C and MCM-Si technologies.

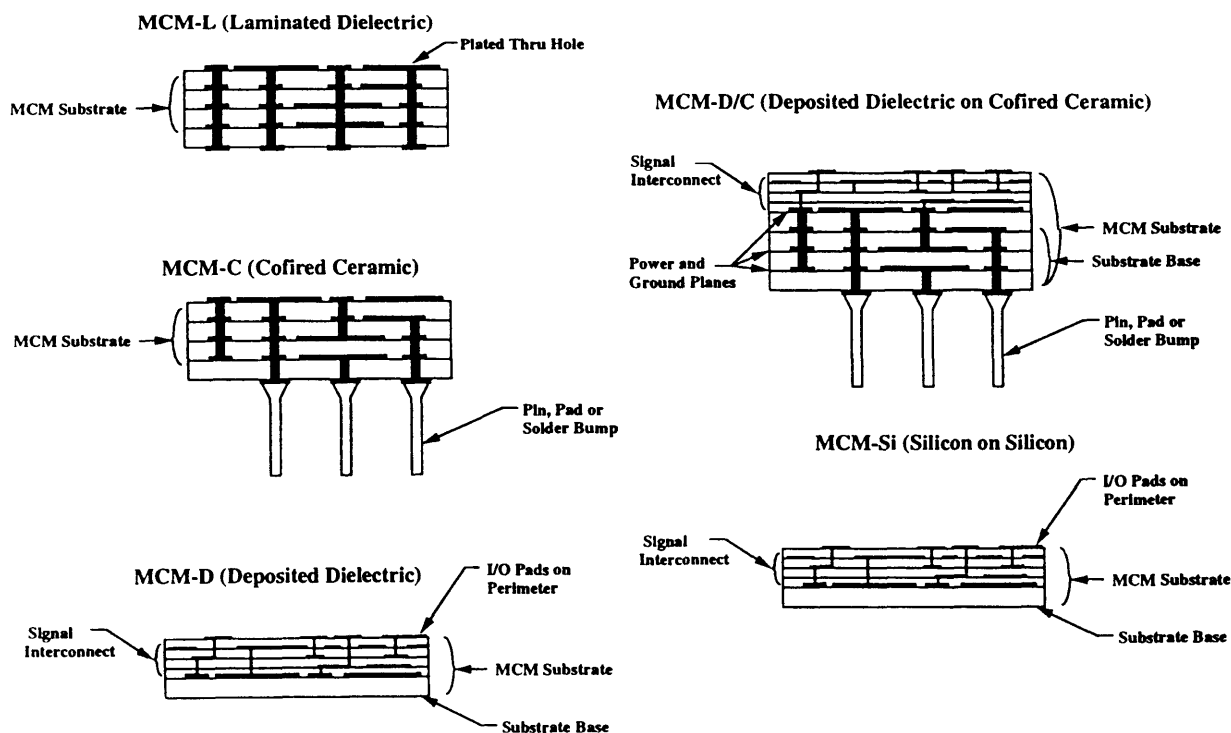


Figure 1.1.2. Major technologies in circuit base manufacturing [1].

MCM-L employs copper interconnection lines and epoxy/glass laminates as dielectrics. The cofired ceramic process uses alumina in combination with tungsten or molybdenum lines. Both MCM-L and MCM-C represent laminated technologies characterized by wide lines ( $\approx 100 \mu\text{m}$ ) and line pitch ( $150\text{-}625 \mu\text{m}$ ), and large layer thicknesses ( $100\text{-}750 \mu\text{m}$ ) [1]. Although these two technologies are less expensive per interconnection layer than MCM-D, a large number of stacked layers is needed in order to achieve a high interconnection density. In addition, the minimum bond pad pitch which MCM-L and MCM-C can accommodate is ca.  $200 \mu\text{m}$ , hence a fanout<sup>1</sup> is usually required.

The newer MCM-D technology is derived from chip manufacturing, and can therefore achieve very high interconnection density per layer. Typically, the dielectric material employed in MCM-D is polyimide, which has a low dielectric constant ( $\approx 3.0\text{-}3.5$ ) and thus

<sup>1</sup> Fanout interconnection is used to match the pitch of the chip pads with that of the circuit base pads.

provides shorter propagation delays<sup>2</sup> and signal rise times than either alumina ( $\epsilon \approx 9.5$ ) or epoxy/glass ( $\epsilon \approx 4.8$ ). Polyimide MCM circuit bases also exhibit low crosstalk<sup>3</sup> and low power dissipation. The low-temperature processing involved in MCM-D technology allows the use of high conductivity metallization: Cu, Al, and Au. All of the above advantages result in superior electrical performance. MCM-D circuit bases have been manufactured which can handle speeds in excess of 1 GHz [1]. Moreover, photosensitive polyimides have been developed which serve both to reduce the number of processing steps involved, as well as to improve MCM performance when used as optical interconnects.

Polyimides, the dielectrics in MCM-D, are a class of polymers with high glass-transition temperature ( $T_g$ ), high chemical resistance, and low dielectric constant. Polyimides for electronic packaging are typically synthesized in a two-step polycondensation and imidization process from solutions of two monomeric components: a dianhydride and a diamine. Initially, the monomers are condensation-polymerized to form polyamic acid with relatively high viscosity and a molecular weight similar to that of the final polyimide [3]. In microfabrication, the polyamic acid (precursor) is typically applied to the substrate through spin-coating, spray-coating, or extrusion, and subsequently dehydrated (imidized) to produce the polyimide coating. Final coating thicknesses depend on the particular application but most often are less than 5  $\mu\text{m}$  [1,2]. Imidization can be thermal or chemical. All coatings studied in the present work were formed from polyamic acid by thermal imidization (cure).

The polymerization and imidization reactions are shown in Figure 1.1.3.

---

<sup>2</sup> The propagation delay is the inverse of the phase velocity of electromagnetic waves in the dielectric, i.e. it is linearly proportional to  $\sqrt{\epsilon}$ .

<sup>3</sup> Crosstalk is the unintended coupling of energy between active and inactive sections of a circuit.

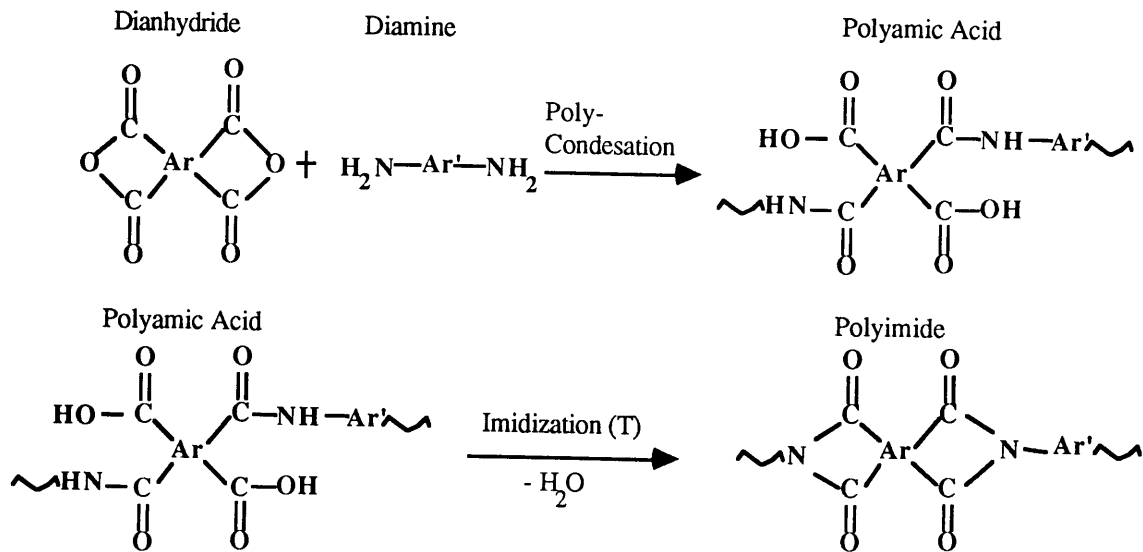


Figure 1.1.3. Synthesis of polyimides [3].

Table 1.1.1 contains a summary of some of the main advantages of polyimides for electronics packaging:

	<b>Advantages</b>
<b>General</b>	Purification via zone refining
	High thermal stability (loss <0.1 wt%/h at 400 °C)
	High chemical resistance
	Low dielectric permittivity (2.6-3.5)
	Alpha-ray absorption
<b>Technological</b>	Good planarization/step coverage
	Adequate mechanical properties
	Microfabrication
<b>Economical</b>	Low-temperature process
	In-line process, high throughput

Table 1.1.1. Some advantages of polyimides in electronic packaging [1,3].

The polyimide-based MCM-D technology, while providing better performance than laminated MCM technologies is considerably more expensive. Presently, one of the main cost factors is the inability to test the unfinished circuit base for reliability [1].

## 1.2. Corrosion in Electronic Packaging

One of the major disadvantages of organic dielectrics is their permeability to moisture and contaminants, which cause degradation of the electrical performance of the MCMs and in some cases may limit their lifetime. The most important factors which contribute to corrosion failure in electronics are relative humidity or moisture entrapment, temperature, contamination, intrinsic impurities, bias potential, galvanic couples, and low molecular weight organics in the packaging [4,5]. Surface contamination has been shown to affect strongly the water adsorption, and water condensation on contaminated surfaces has been reported even at 20% relative humidity (RH) [6]. Common corrosion-related failures in semiconductor products include loss of insulation resistance by metal migration, localized line corrosion, and bridging between adjacent conductive corrosion deposits [7]. The electronic industry has adopted various tests for estimating the susceptibility to environmental degradation and corrosion. However, most of them are qualitative, based on pass/fail criteria and destructive. Almost all of them test the end product - a package or a printed circuit board (PCB). Although tests vary among manufacturers, the autoclave test (100% RH at 121 °C, 1 atm pressure), the Highly Accelerated Stress Test (HAST) (100 % RH, 159 °C, 4 atm pressure, 10 V bias) and the THB (Temperature, Humidity, Bias) test (85 °C, 85% RH, bias) are among the most frequently used [8-10]. It has been pointed that data obtained through such highly accelerated tests cannot always be translated to the field, due to different failure mechanisms at the extreme test conditions [10]. Moreover, a number of factors can combine to cause failure of the package, and in many cases the specific causes may not be identifiable.

### 1.3. Research Objectives and Significance

The main goal of this work was to investigate the feasibility of a non-destructive, quantitative procedure for quality control and prediction of the lifetime, in terms of environmental degradation, of thin-film polyimide/metal structures from short-term measurements. The procedure was to be employed in the development and manufacturing of electronic packaging materials and electronic packages. Furthermore, it was desired to compare the corrosion-protective properties of several polyimides used or considered for use as dielectrics in MCM-D.

Organic coatings such as the polyimides used in electronic packaging are generally thought to protect against corrosion by restricting the access of reactants to the corroding interface, or by limiting the electrochemically active area. Hence, it was considered likely that water and chloride transport through the coatings, or the rate of delamination at the interface might represent the limiting steps in the failure of the coated substrates. Thus, knowledge of the above parameters would enable the prediction of the lifetime of the coatings. In the event these parameters were reliably measurable by means of non-destructive, fast, *in-situ* methods, the on-line evaluation of every substrate during manufacturing would become possible.

The main tools of the study were electrical and electrochemical measurements, with emphasis given to impedance spectroscopy (IS). All tests were performed under immersion in 0.5 M NaCl. The investigated materials included PMDA-ODA, BPDA-PDA, HFDA-APBP, and BTDA-ODA/MPDA (Section 2.1) on Cr, Al, and Cu-metallized substrates. Polyimide/Cr interfaces were emphasized because of their common occurrence in MCM manufacturing: in MCM-D, Cr is usually used as an interlayer between Cu and the polyimide, in order to prevent the diffusion of Cu into the polyimide and to improve adhesion [11].



The following subset of specific objectives was derived from the ultimate goal of the work:

- 1) Investigation and application of dielectric permittivity transients for measurement of the water and ion-uptake kinetics in thin polyimide films.
- 2) Investigation and application of impedance spectroscopy for monitoring and quantification of the long-term degradation of the coated system.
- 3) Study of the factors governing the lifetime of the coated system, and of the correlation between parameters characteristic of its short-term and long-term performance.
- 4) Investigation of the effects of non-standard processing on the corrosion-related properties of the coatings.

The potential significance of the research for the electronic packaging industry is apparent from the stated objectives. Furthermore, this work supplements the existing database on properties of polyimides and the effect of processing upon them. Some of the conclusions reached with regard to the utilization of impedance spectroscopy for the evaluation of polyimide/metal systems are also applicable to the evaluation of organic coatings for corrosion protection in general, and may serve to resolve ongoing controversial issues in the corrosion literature.

The work was conducted within the framework and under the sponsorship of MIT's Electronic Packaging Program (EPP), a multi-sponsor, multi-investigator research program aimed at addressing various materials-related issues in electronic packaging. The investigated materials and processing reflected current trends in MCM-D technology.

## 1.4. Outline of Thesis

Chapter 2 begins with a description of the investigated polyimides and the specimen preparation. In Section 2.2, the impedance spectroscopy and x-ray photoelectron spectroscopy (XPS) techniques are introduced briefly. The limits of the IS setup are established. The chapter concludes with a brief discussion of the other experimental methods used in this work.

Chapter 3 is devoted to the measurement of water uptake and diffusion via the permittivity transient method. The method is presented in detail, and a model for the data is developed on the basis of the theory of diffusion and basic dielectric theory. The application of the model to actual experimental data is illustrated. Both water absorption and desorption measurements on free and supported films are possible. Subsequently, the water uptake and diffusion results from the investigated materials are presented and discussed. In all specimens, water diffusion is determined to be Fickian, with concentration-independent diffusion coefficients. Diffusion coefficient values at room temperature range from  $1 \times 10^{-10}$   $\text{cm}^2/\text{s}$  for BPDA-PDA to  $3 \times 10^{-8}$   $\text{cm}^2/\text{s}$  for HFDA-APBP. The diffusion coefficient,  $D_w$ , and the permittivity,  $\epsilon'$ , of the absorbed water are functions of the free molar volume in the various polyimides. In Section 3.4, the permittivity transient method is applied towards the measurement of the diffusion of organic solutes in polyimides. The observed post-saturation increase in the relative permittivity of the coatings during immersion in water or organic solutes is investigated in Section 3.5. It is concluded that such behavior is most likely due to polymer-solute or solute-solute interactions, of the type of hydrogen bonding. In Section 3.6, the utility of permittivity transients for defect detection is demonstrated. The chapter concludes with an investigation of chloride permeation through polyimide membranes. The membrane permeation method is described in detail. An upper limit of ca.  $1 \times 10^{-15}$   $\text{cm}^2/\text{s}$  is obtained for the value of the chloride diffusion coefficient at room temperature in PMDA-ODA and BPDA-PDA.

The long-term degradation and failure of the coated substrates during exposure to 0.5 M NaCl is investigated in Chapter 4. The chapter begins with a detailed discussion of the interpretation and modeling of impedance spectroscopy data for coating evaluation. The impedance data are evaluated numerically, by means of nonlinear regression fitting to equivalent circuits. Contrary to claims in the corrosion literature, it is concluded that delaminated regions under the coating are not detectable via IS until low-resistance connections (pores or blisters) between the electrolyte and the metal film have formed. Furthermore, the double-layer capacitance is the only useful parameter for quantitative measurements of the exposed interfacial area under controlled conditions. Graphical analysis in terms of characteristic parameters in the impedance plots is found unreliable. The results from IS measurements during the long-term exposure of the coated substrates to 0.5 M NaCl are presented and discussed in Section 4.2. The long-term degradation of the bulk polymer is manifested in the irreversible increase in the coating's relative permittivity. Failure, defined as the sharp rise in the amount of exposed interfacial area determined from the impedance data, is the result of osmotic delamination or blistering. The lifetime of the coated substrates is longest on Cr, where coating delamination is cohesive and the time-to-failure is related to the long-term polymer degradation rate. By contrast, failure on Al is caused by adhesive delamination at the metal/polyimide interface. HFDA-APBP coatings are found superior to the other investigated coating types. With regard to the main objective, it is concluded in Section 4.3 that the mass-transport of water and chlorides through the coatings does not represent a limiting factor in failure, and therefore long-term performance cannot be predicted from short-term measurements. The effects of non-standard processing: low-temperature cure, electron-beam treatment, and secondary cure are discussed in Chapter 5. Electron-beam treatment causes severe chemical degradation of the irradiated coating surface, while the bulk of the coating remains relatively unaffected. Low-temperature cure results in coatings of decreased density, faster

degradation, and shorter lifetime. Secondary cure leads to increased water diffusional flux in the coatings, but better long-term performance than low-temperature cure.

Finally, Chapter 6 presents a summary of the conclusions and of the proposed future work.

## 2. Materials, Sample Preparation, and Experimental Methods

### 2.1. Materials and Sample Preparation

Four polyimides were investigated in the present work: PMDA-ODA, BPDA-PDA, HFDA-APBP, and BTDA-ODA/MPDA. Of the four, PMDA-ODA (Figure 2.1.1) was at the most advanced stage of the product cycle, available from many sources and also as fiber and free film (Kapton®). The PMDA-ODA precursor material used predominantly in this work was PI2545 (Du Pont Electronics). In addition, Kapton® 30 HN free films (Du Pont Electronics) with nominal thickness of 7.5 μm were employed in several experiments. PMDA-ODA specimens for the processing study (Chapter 5) were prepared from OCG627 precursor (Ciba-Geigy).

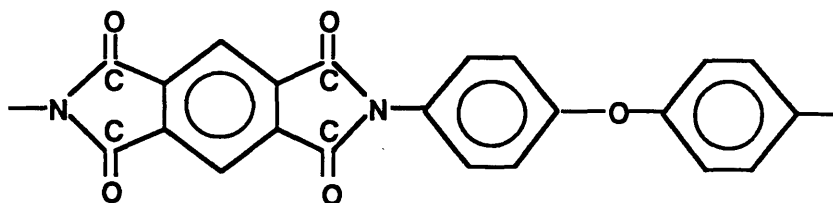


Figure 2.1.1. Chemical structure of PMDA-4,4'-ODA.

BPDA-PDA coatings were prepared from PI2611 (Du Pont). BPDA-PDA's chemical structure is illustrated in Figure 2.1.2. The material was identical with Upilex-S® (Ube Industries, Ltd., Japan).

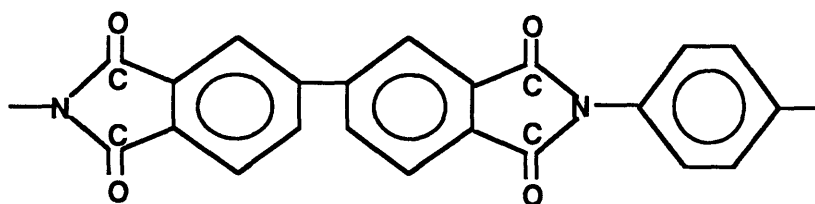


Figure 2.1.2. Chemical structure of BPDA-PDA.

HFDA-APBP (or 6FDA-APBP) coatings (Figure 2.1.3) were prepared from UD4212 (Ultradel<sup>®</sup> 4212, Amoco Chemical Co., Chicago, IL).

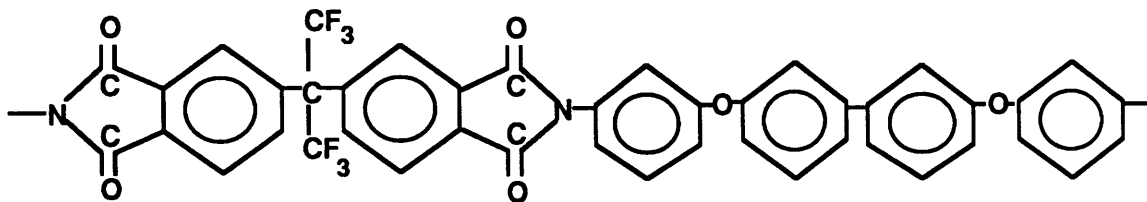


Figure 2.1.3. Chemical structure of HFDA-APBP.

BTDA-ODA/MPDA coatings were prepared from PI2525 precursor material (Du Pont) (Figure 2.1.4). PI2525 was a blend of ca. 58% BTDA-ODA and 42% BTDA-MPDA [11].

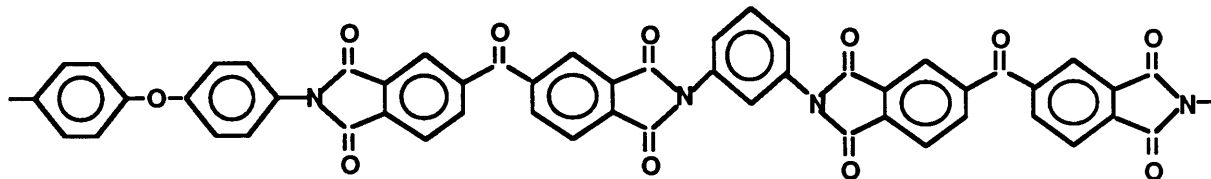


Figure 2.1.4. Chemical structure of BTDA-ODA/MPDA.

The majority of PMDA-ODA (PI2545), BPDA-PDA (PI2611), HFDA-APBP (UD4212) coatings used in the present work were produced at MIT's Microsystems Technology Laboratories. Metal films of 500-3000 Å thickness were deposited onto four inch RCA-cleaned silicon wafers with native oxide in an electron-beam evaporator. The polyimide coatings were prepared in a two-stage process. The (diluted) polyamic acid precursor was dispensed onto the slowly spinning substrate and spread uniformly by spinning at 500 rpm for 5 seconds. The final coating thickness was a function of the rotational speed (500-10000 rpm) during the following 60 s spin, and of the initial dilution of the precursor solution. The coated substrates were soft-baked in air at the manufacturer-suggested temperature in an exhausted oven. The final cure was conducted under 2.0 l/min N<sub>2</sub>-flow in a programmable tube furnace following the manufacturer-recommended cycles (Table 2.1.1).

Polymer	Soft Bake (t, min/T, °C)	Cure (t, min/T, °C)
PI2545	30'/140 °C	30'/RAMP: 200—>350 °C
		30'/RAMP: 350—>400 °C
		90'/SOAK: 400 °C
PI2611	30'/160 °C	30'/RAMP: 200—>350 °C
		30'/RAMP: 350—>400 °C
		90'/SOAK: 400 °C
UD4212	30'/140 °C	30'/RAMP: 100—>200 °C
		30'/SOAK: 200 °C
		10'/RAMP: 200—>400 °C
		60'/SOAK: 400 °C

Table 2.1.1. Cure schedules for the polyimide coatings prepared at MIT [12].

Some of the PMDA-ODA (OCG627), BPDA-PDA (PI2611), and all of the BTDA-ODA/MPDA (PI2525) samples were kindly provided by Dr. Solomon Beilin of Fujitsu Computer Packaging Technologies, Inc. (FCPT), San Jose, CA. Those samples were used almost exclusively in the processing-properties study (Chapter 5).

Thickness measurements were performed on a Dektak 8000 Profilometer by measuring the step height between the metal film and the coating surfaces. Steps were produced by means of a scalpel blade. Three measurements at locations corresponding to the radial position of the test area were made per wafer, and the results were averaged. The samples exhibited a small radial gradient of coating thickness within the test area, with an estimated variation of ca.  $\pm 0.5\%$ .

The coated wafers to be used in the IS and permittivity transient experiments were cut in quarters. After the samples had been visually inspected for flaws, 4 cm tall Plexiglas™ cylinders of 1.25" inner diameter were mounted onto them by means of Epoxi-Patch® (Hysol Aerospace and Industrial Products, Pittsburg, CA). Due to some epoxy overflow, the cell area could not be precisely defined and varied between a minimum of 7.1 cm<sup>2</sup> and a maximum of ca. 7.9 cm<sup>2</sup>. Alternatively, a clamped glass cell design with a Viton® O-ring

contact to the coated surface and well defined test area was considered, however it was found that the clamping introduced unwanted additional tensile stress in the coating that lead to deviations from normal behavior.

In order to provide an electrical contact for the working electrode, the coating was removed from a small area at the edge of the specimen to expose the metal film. A copper wire was attached to the exposed area by means of silver-filled epoxy. The assembled cells were dessicated for at least 5 days prior to initial exposure to 0.5 M NaCl. The complete test cell assembly for impedance spectroscopy measurements is shown in Figure 2.1.5.

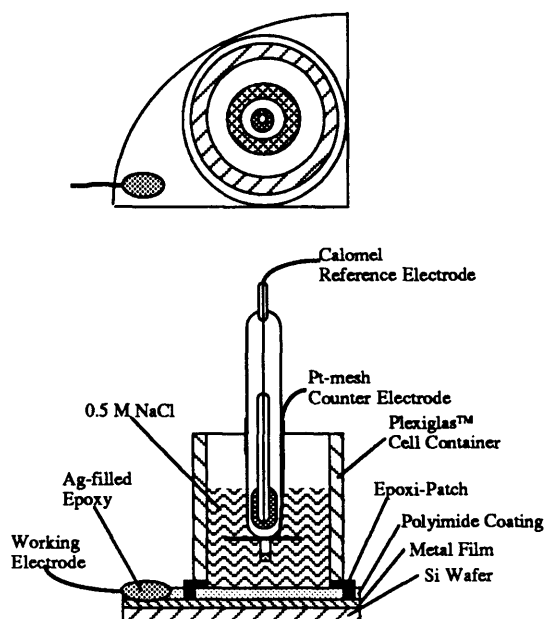


Figure 2.1.5. Test cell assembly for impedance spectroscopy and long-term exposure experiments.

## 2.2. Experimental Methods

### 2.2.1. Impedance Spectroscopy

Impedance spectroscopy (IS) can provide information about electrochemical reactions at interfaces, transport processes in electrolytes, and electrical properties of materials. A comprehensive analysis and discussion of the method is given by Macdonald [13]. The



most common among the various approaches to IS experiments is the application of a single-frequency sinusoidal voltage perturbation to the system under test. Measurements of the resultant current at each frequency allow the compilation of the impedance spectrum of the system. Although most real systems are inherently nonlinear, it has been shown that when the perturbation amplitude is smaller than the thermal voltage,  $V_T = RT/F$ , a linear response represents a very good approximation [13]. The perturbation and response signals can be defined and measured in either the frequency or time domains. The equipment used in this work was a frequency response analyzer (FRA) operating in the frequency domain. The impedance was calculated as:

$$Z^*(\omega) = \frac{E^*(\omega)}{I^*(\omega)}, \tag{2.2.1}$$

where  $\omega = 2\pi f$  was the angular frequency, and  $Z^*(\omega)$ ,  $E^*(\omega)$ , and  $I^*(\omega)$  were the complex impedance, voltage, and current as a function of frequency, respectively, e.g.:

$$Z^* = |Z| \exp(j \cdot \vartheta) = |Z|[\cos(\vartheta) + j \cdot \sin(\vartheta)] = Z' + j \cdot Z'' \tag{2.2.2}$$

In (2.2.2),  $\vartheta$  was the phase angle with respect to the real axis.

The core of the IS setup was the FRA, the basic schematics of which is illustrated in Figure 2.2.1.

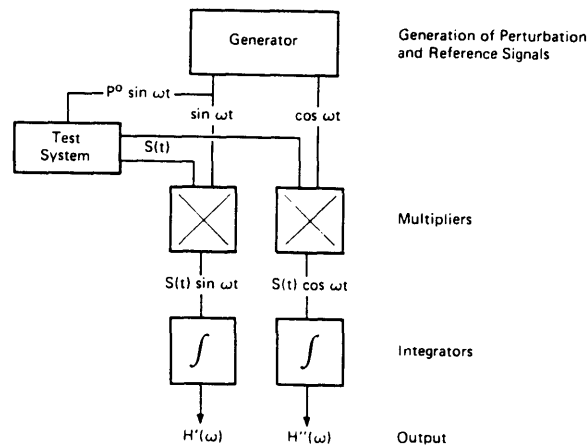


Figure 2.2.1. Schematic of a frequency response analyzer [13].

McKubre et al. have described the mathematical basis of frequency response analysis for impedance spectroscopy [13]. Most important from the experimenter's point of view is that the directly measured parameters are the real and imaginary impedance components, that non-fundamental harmonics can be excluded by performing the measurement over an integer number of cycles, and that random noise is reduced when the measurements are performed over longer time periods.

Figure 2.2.2 represents a schematic of the IS setup used in the present work. It consisted of a programmable EG&G PAR 273 potentiostat in combination with a Solartron 1260 FRA.

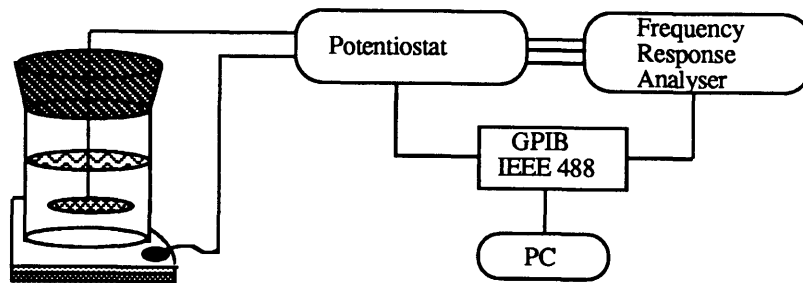


Figure 2.2.2. Schematic of the impedance spectroscopy setup.

The need to use a potentiostat arose from the linearity condition mentioned previously, which restricted the perturbation amplitude to 20 mV rms at room temperature. Thus, the response current was smaller than 1  $\mu$ A at low frequencies, below the limit of the built-in current analyzer of the FRA. The use of the potentiostat limited the maximum frequency of the setup to approximately 100 kHz. In addition, for most samples, the low frequency limit for data acquisition was approximately 20 mHz due to the insufficiently high input impedance ( $\approx 40$  G $\Omega$ ) of the potentiostat. Both instruments were controlled over the IEEE488 GPIB bus by data acquisition software written specifically for this work. The program represented an improvement over available commercial software, in terms of better utilization of hardware features for enhanced data quality as well as with regard to some of the control algorithms used.

The quality of the acquired data depended strongly on the instrumentation and software setup parameters. An electrical circuit was built in order to select the optimum set of setup parameters appropriate for the impedance range of the coated samples under investigation (Figure 2.2.3). The circuit components were chosen to model an intact coating with no dielectric relaxation processes within the frequency range of interest, and with finite dc conductivity. The modeling of such a coating is described in detail later in this work. The component values were selected to be representative of the impedance load in the case of data acquisition from a typical coated sample.

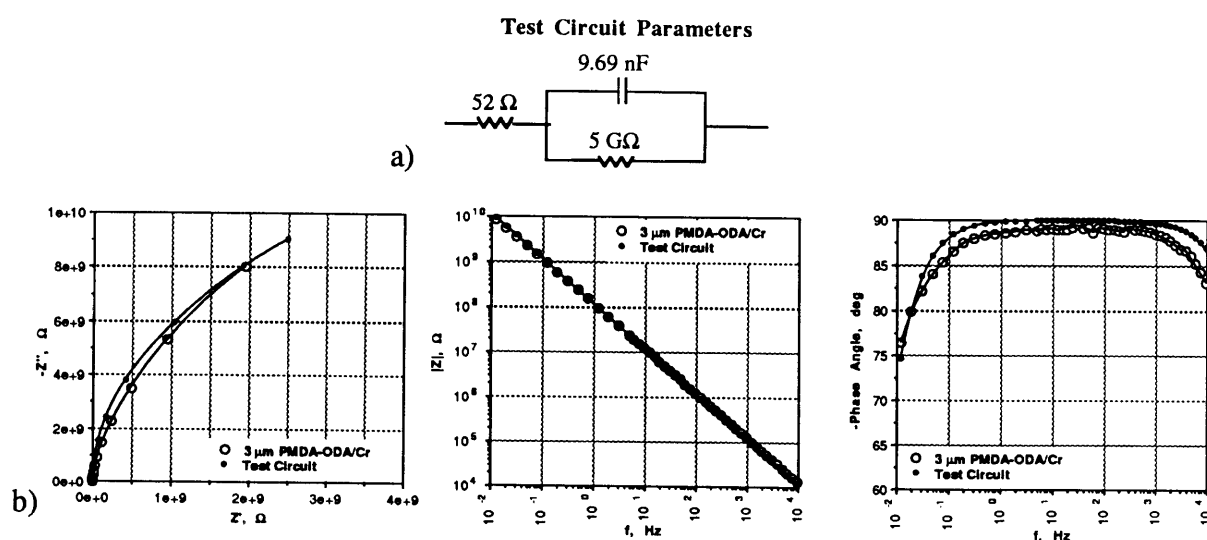


Figure 2.2.3. Test circuit used for optimization of the data acquisition (a) and comparison of impedance data acquired from it with data from a 3  $\mu\text{m}$  PMDA-ODA/Cr coating (b).

As all real electrical components exhibit some frequency dependence, a HP4275A multi-frequency meter was used to measure their values as a function of frequency. It was found that these were identical to the ones obtained by means of the stand-alone FRA using a 3 V rms amplitude. Thus, impedance spectra acquired with the standalone FRA were assumed to represent the true impedance spectra of the test circuit. Subsequently, repeated impedance scans of the circuit were conducted using the FRA/potentiostat combination with the actual experimental amplitude of 20 mV rms, and the setup parameters were varied until the minimum of:

$$S = \sum_{i=1}^N \frac{|Z_{\omega_i}^{\text{measured}} - Z_{\omega_i}^{\text{correct}}|}{Z_{\omega_i}^{\text{measured}}} \quad (2.2.3)$$

had been obtained. Equation (2.2.3) represented the sum of the normalized differences between the correct (standalone FRA, 3 V rms) and measured (FRA/potentiostat, 20 mV rms) impedance values at each angular frequency,  $\omega_i$ . The setup parameters optimized in this way were employed in all IS experiments.

Data was acquired from several RC-circuits in order to determine the highest measurable resistive load. Figure 2.2.4. illustrates that the validity limit was approximately 15 G $\Omega$ . Therefore, with regard to the test cell area of 7.9 cm<sup>2</sup>, numerical estimates of the resistive parameters of the coating equivalent circuit were considered of reduced significance if greater than 100 G $\Omega$ cm<sup>2</sup>. In addition, the maximum measurable resistance was inversely proportional to the amplitude of the voltage perturbation.

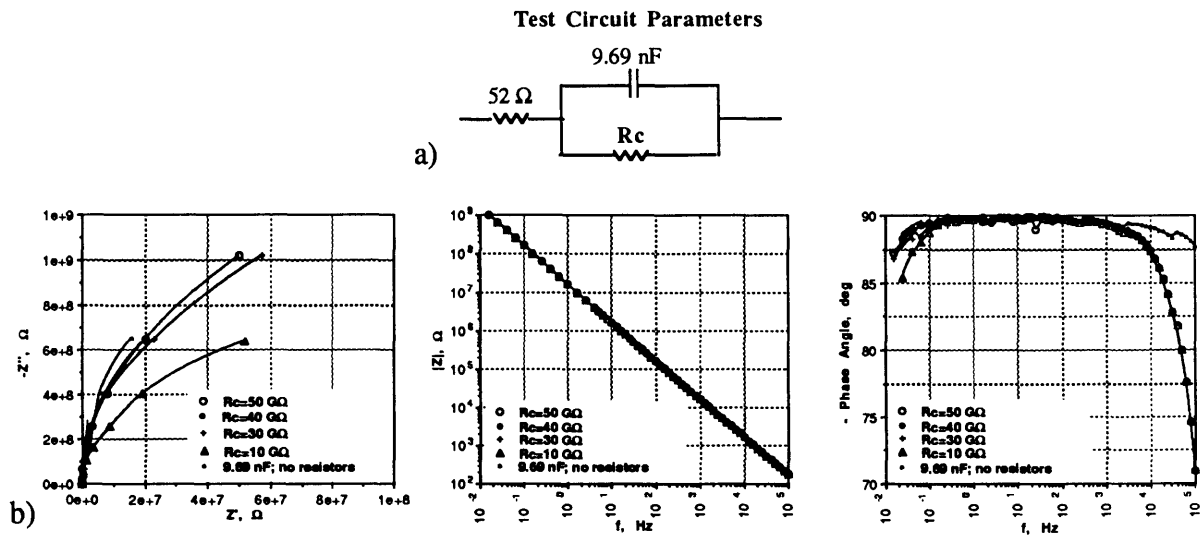


Figure 2.2.4. Comparison among the impedance spectra of four RC-circuits (a) with different resistances. Invariably, numerical analyses yielded estimates of  $R_c \approx 20$  G $\Omega$ , regardless of whether the actual value was 30, 40, 50 G $\Omega$ , or no resistor was used ( $R_c \rightarrow \infty$ ).

Usually, the graphical representation of impedance spectroscopy data includes three types plots: the complex plane ( $-Z''$  vs.  $Z'$ ), the Bode-magnitude ( $\log|Z|$  vs.  $\log(f)$ ), and the Bode-angle ( $-\vartheta$  vs.  $\log(f)$ ) plots (see Figures 2.2.3 and 2.2.4). While this format may

permit quick estimates of some characteristic cell parameters, the preferred data analysis method is to model the cell impedance analytically on the basis of electrochemical models or by means of electrical analogs, and to estimate the values of the model parameters via numerical procedures [13]. Electrical analogs have been developed and relationships between the equivalent circuit parameters and electrochemical parameters have been established for many common electrochemical systems [13,14]. The simple electrical analogs of polymer coatings and metal electrodes will be described briefly next.

The electrical analog of an ideal insulator with a single dielectric relaxation is represented by the Debye equivalent circuit of Figure 2.2.5, where  $\epsilon_0$  is the dielectric permittivity of vacuum,  $\epsilon_\infty$  is the high frequency dielectric constant,  $\epsilon_s$  the static dielectric constant, and  $\tau$  is the relaxation time [13,15]:

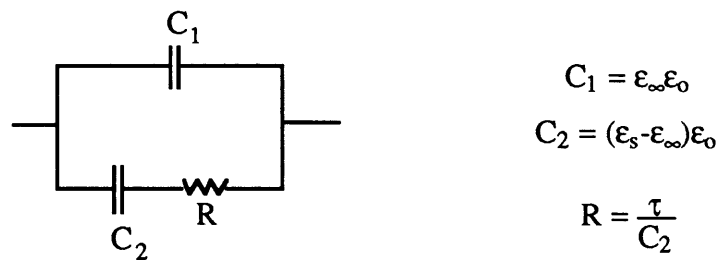


Figure 2.2.5. Debye equivalent circuit model of an ideal insulator with a single relaxation time [13].

Normally, impedance data from a Debye model are converted to the complex dielectric plane ( $\epsilon^* = \epsilon' + j\epsilon''$ ) by multiplying the impedance by  $j\omega\epsilon_0$ . In the dielectric plane, the characteristic parameters of the insulator are the dielectric permittivity,  $\epsilon'$ , the dissipation factor,  $\epsilon''$ , and the loss tangent,  $\tan(\delta) = \frac{\epsilon''}{\epsilon'}$  [15]. Real insulators typically exhibit a distribution of relaxation times which can be modeled by a Cole-Cole equivalent circuit in which the Debye resistor is replaced by a constant phase element (CPE). The impedance of a CPE is given by [13]:

$$Z_{\text{CPE}}^*(\omega) = \frac{1}{C} (j\omega)^\alpha = \frac{1}{C} (\omega)^\alpha [\cos(\alpha \frac{\pi}{2}) - j \cdot \sin(\alpha \frac{\pi}{2})], \quad (2.2.4)$$

where  $C$  is a constant, and  $\alpha$  is representative of the distribution width. For  $\alpha=0$ , the CPE represents a perfect resistor with  $R=1/C$ . For  $0<\alpha<1$ , the CPE's response is equivalent to that of a frequency-dependent capacitance (pseudocapacitance) and a frequency-dependent resistance (pseudoresistance) in series. Finally, for  $\alpha=1$  the CPE represents a perfect capacitor with a capacitance  $C$ .

All insulators also possess finite conductivity as shown in Figure 2.2.6, where the presence of dc conductivity in the polyimide coating is indicated by the continuous increase of the loss tangent at low frequencies.

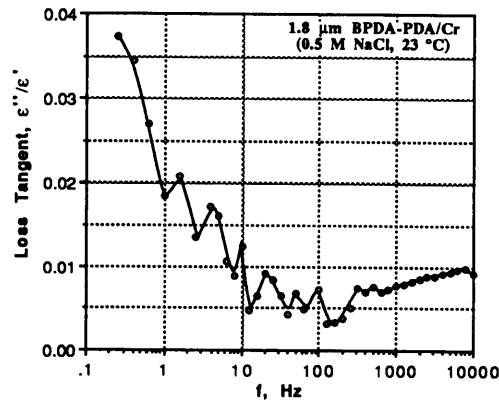


Figure 2.2.6. Dielectric loss spectrum of a 1.8  $\mu\text{m}$  BPDA-PDA/Cr coating 2 days after immersion in 0.5 M NaCl at 23  $^{\circ}\text{C}$  with evidence of dc conductivity.

The dc conductivity can be modeled by including a resistor in parallel with the insulator circuit from Figure 2.2.5, and the ionic conductivity of the film can be estimated from [15]:

$$\sigma = e \cdot \sum_{i=1}^N z_i \cdot n_i \cdot \mu_i, \quad (2.2.5)$$

where  $n_i$  is the concentration of mobile ions of type  $i$  and with charge  $z_i$ , and  $\mu_i$  is the drift mobility of the charge carriers. The drift mobility is related to the diffusion coefficient via the Nernst-Einstein relation,  $D_i = \mu_i RT$ . The ionic conductive process in polymers is thought to be a hopping process, in which ions hop over energy barriers between potential wells, and for which the ionic diffusion coefficient for dissociated ions in the absence of an applied electric field is given by [15, 16]:

$$D_{\text{ion}} = D_0 \exp\left(-\frac{\gamma V_i^*}{V_f} - \frac{\Delta U^*}{kT}\right), \quad (2.2.6)$$

where  $D_0$  is proportional to  $\nu$  (the vibrational frequency),  $\Delta U^*$  is the average height of the energy barrier between wells,  $V_i^*$  is the critical free volume required for an ion jump,  $V_f$  is the average free volume per molecular segment, and  $\gamma$  is a numerical factor.

A metal/electrolyte interface with faradaic charge transport and diffusion can be modeled by the circuit of Figure 2.2.7, where  $C_{dl}$  is the double-layer capacitance,  $R_f$  represents the faradaic charge transfer resistance, and  $Z_w$  is the Warburg (diffusional) impedance [13,14].

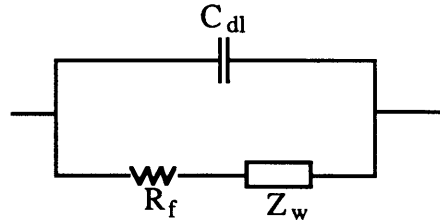


Figure 2.2.7. Equivalent circuit model of a metal/electrolyte interface with faradaic charge transport and diffusion [2.1, 2.2].

According to the Gouy-Chapman theory, the double layer capacitance,  $C_{dl}$ , is inversely proportional to the Debye length,  $L_{dl}$ , of the double layer. In addition,  $C_{dl}$  is a function of the potential of the electrode and of the concentration of mobile charges in the electrolyte [14]. For an 1:1 electrolyte, the double layer capacitance is approximately given by:

$$C_{dl} = \sqrt{\frac{2e^2 \epsilon \epsilon_0 n^0}{kT}} \cosh\left(\frac{e\Phi_0}{2kT}\right) = \frac{\epsilon \epsilon_0}{L_{dl}} \cosh\left(\frac{e\Phi_0}{2kT}\right), \quad (2.2.7)$$

where  $\epsilon$  is the permittivity of the electrolyte in the double layer (itself a function of electrolyte concentration),  $n^0$  is the concentration of mobile charges in the electrolyte (ions/cm<sup>3</sup>), and  $\Phi_0$  is the potential of the electrode with respect to the bulk electrolyte. From the above equation, it is calculated that the maximum potential dependence of the capacitance arising from the applied 20 mV sinusoidal perturbation is ca. 10%.

Furthermore, in highly concentrated electrolytes the capacitance of the diffuse layer is large,  $C_{dl}$  is dominated by the potential-independent Stern layer capacitance, and therefore can be assumed to be completely independent of potential and concentration [14].

The significance of the parameters involved in the  $R_f$ - $Z_w$  branch of the interface circuit model is shown below on the example of the reaction  $Me \leftrightarrow Me^{n+} + ne^-$  at the parent metal electrode. In a supported electrolyte, the charge transfer resistance,  $R_f$ , of the reaction is given by [13]:

$$R_f = \frac{RT}{n^2 F^2} \frac{1}{k^0 c_{M^{n+}}^0}, \quad (2.2.8)$$

where  $n$  is the number of electrons transferred,  $k^0$  is the reaction rate constant, and  $c_{M^{n+}}^0$  is the metal ion concentration in the bulk of the electrolyte.

The diffusional mass transfer of metal ions between the electrode and the bulk electrolyte may be given by the finite-length Warburg impedance [13,14]:

$$Z_w = \frac{RT}{z^2 F^2} \frac{1}{D_M c_{M^{n+}}^0} \frac{\tanh \sqrt{j\omega \frac{l^2}{D_M}}}{\sqrt{j\omega \frac{l^2}{D_M}}}, \quad (2.2.9)$$

where  $D_M$  is the diffusion coefficient of the metal ion,  $z$  its charge, and  $l$  is the effective diffusion length. For  $l^2/D_M \gg 4.66$ ,  $\tanh \approx 1$ , and  $Z_w$  can be replaced by an infinite-length Warburg impedance,  $Z_w^\infty$ , which can be modeled by means of a CPE with  $\alpha=0.5$  and the following identities:

$$Z_w^\infty = R_w T_w^\alpha (j\omega^{-\alpha}) \quad \text{where} \quad T_w = \frac{l^2}{D_M} \quad \text{and} \quad R_w = \frac{RT}{z^2 F^2} \frac{1}{D_M c_{M^{n+}}^0} \quad (2.2.10)$$

For  $\alpha \neq 0.5$ , the above element is termed the generalized Warburg element [13].



All IS data in the present work were analyzed numerically, by means of a complex nonlinear least squares procedure (CNLS) [13,17]. The CNLS procedure seeks to minimize the function:

$$S = \sum_{i=1}^n \left\{ w_i^{Z'} [Z'_{\text{meas}} - Z'_{\text{calc}}(\omega_i, \mathbf{A})]^2 + w_i^{Z''} [Z''_{\text{meas}} - Z''_{\text{calc}}(\omega_i, \mathbf{A})]^2 \right\}, \quad (2.2.11)$$

where  $n$  is number of discrete frequencies in the impedance spectrum,  $w_i^{Z'}$ ,  $w_i^{Z''}$  are the weights applied to the  $i$ -th data point,  $\omega_i$  is the angular frequency of the  $i$ -th data point, and  $\mathbf{A}$  is the vector of parameter estimates. The verification tests performed on the IS setup used in this work established the higher accuracy of the high-frequency (low impedance magnitude) data. Therefore, proportional weighting [17]:

$$w_i^{Z'} = \frac{1}{(Z'_{\text{meas}})^2} \quad \text{and} \quad w_i^{Z''} = \frac{1}{(Z''_{\text{meas}})^2} \quad (2.2.12)$$

was used in the CNLS minimization function (2.2.11) throughout the IS data analysis. Like the data acquisition, the numerical procedure was verified on the impedance data from test circuits similar to the one in Figure 2.2.3.

### 2.2.2. X-ray Photoelectron Spectroscopy

In the present work, analyses of the effects of processing on polymer chemistry (Chapter 5) as well as chemical investigations of failed polymer/metal interfaces (Chapter 4) were performed by means of X-ray photoelectron spectroscopy. XPS is a surface-analytical technique applicable to both metals and insulators. Along with infrared spectroscopy (IR) and nuclear magnetic resonance spectroscopy (NMR), XPS is being used extensively in the characterization of solid state polymers [18]. In XPS, the sample is irradiated by monochromatic X-rays produced by electron beam bombardment of a rotating target anode. Mg ( $\text{Mg}_{K\alpha}$ ,  $E=1254$  eV) and Al ( $\text{Al}_{K\alpha}$ ,  $E=1487$  eV) are the two target metals commonly

employed for X-ray generation in XPS. Upon striking the sample under investigation, the incident monochromatic X-rays eject electrons from the core electron levels of the atoms of the sample. The emitted photoelectron and the remaining photoion represent the reaction products of photoionization. Since momentum transfer is inversely proportional to the masses of the products, X-ray photon energy in excess of the ionization potential is transferred almost entirely to the ejected photoelectron as kinetic energy. When the remaining photoion is left in its ground energy state, the photoionization process is elastic and the binding energy (BE) or the ionization potential of the photoelectron can be calculated from:

$$E_{\text{kin}} = h\nu - \text{BE} - K, \quad (2.2.13)$$

where  $h\nu$  is the incident X-ray energy, and  $K$  is a correction term dependent on the sample and on the spectrometer.  $E_{\text{kin}}$  is determined by means of an electrostatic concentric hemispherical energy analyzer (CHA) in which only photoelectrons of a certain kinetic energy interval around a selected mean (pass energy) are focused to pass between two concentric hemispheres and through a slit into an electron detector. The mean energy is scanned by varying the electrostatic potential of the concentric hemispheres of the CHA until the entire spectrum of interest has been acquired. Scans are repeated until the desired signal-to-noise ratio has been achieved. Thus, XPS spectra consist of a sequence of peaks at discrete energy values, representative of the binding energies of the core level electrons of the present atoms. The relative peak intensities are a function of the atomic fraction of the respective element in the sample, as well as of the atomic photoemission cross-section,  $\alpha$  of the particular element-electron combination. In general, photoemission cross-sections depend on the atomic number,  $Z$ , increasing with increasing  $Z$  [18]. After correcting for the photoemission cross-section, the XPS spectra can be used for quantitative determination of the sample's composition. Moreover, non-equivalent atoms of the same element exhibit differences in the binding energies of the core electrons due to variations in

the atomic environment. In molecular solids, the core level binding energies of a particular atom are affected only by the atoms bonded to it, or in the atom's immediate vicinity [18]. The resulting "chemical shifts" in the electrons binding energies are characteristic of the particular molecule. The directions and amounts of the chemical shifts for various molecules have been tabulated [18-20]. In addition to its binding energy, an XPS peak is characterized quantitatively by its full width at half maximum (FWHM), with large FWHMs corresponding to large fluctuations in the atomic environment from molecule to molecule.

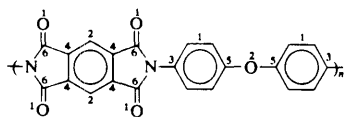
The utility of XPS for polymer identification and quantitative characterization is illustrated in Figure 2.2.8.

**Poly(ether imide) (Kapton HN)<sup>TM</sup> (KAP)**

	C 1s						O 1s		N 1s
	1	2	3	4	5	6	1	2	
BE (eV)	284.70	285.55	285.68	285.76	286.29	288.61	532.03	533.26	400.60
FWHM (eV)	0.92	0.95	0.90	0.95	0.95	0.90	1.13	1.13	1.10
Area (%)	36	10	10	19	10	17	77	23	
A	0.15	0.09	0.17	0.16	0.12	0.16	0.16	0.12	0.15
m	0.86	0.80	0.87	0.83	0.83	0.84	0.73	1.00	0.78

**Binding Energy Table**

**Structure with Identified XPS Contributions**



Source: E.I. du Pont de Nemours & Co., Inc.  
 Casting solution: (film, scraped)  
 Degradation index: 10, O/C  
 VB acquisition: 1  
 Charging reference: aromatic CH = 284.70 eV  
 Shake-up intensity: 24% (C 1s), 44% (O 1s)

Comments: O 1s components 3-5 due to shake-up. C 1s components 7-9 due to shake-up

**XPS Survey Scan**

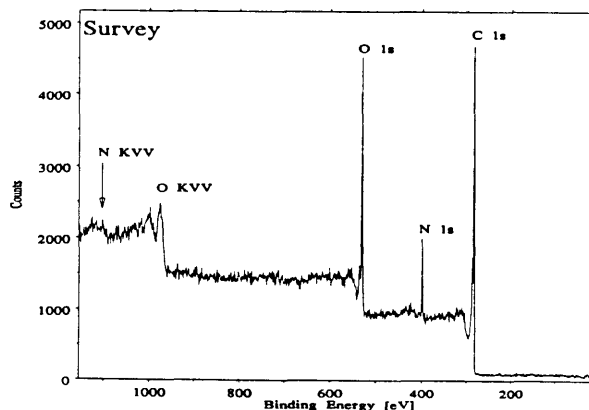


Figure 2.2.8. a) Structure, binding energy table, and XPS survey scan of PMDA-ODA. Equivalent atoms carry same numbers [19].

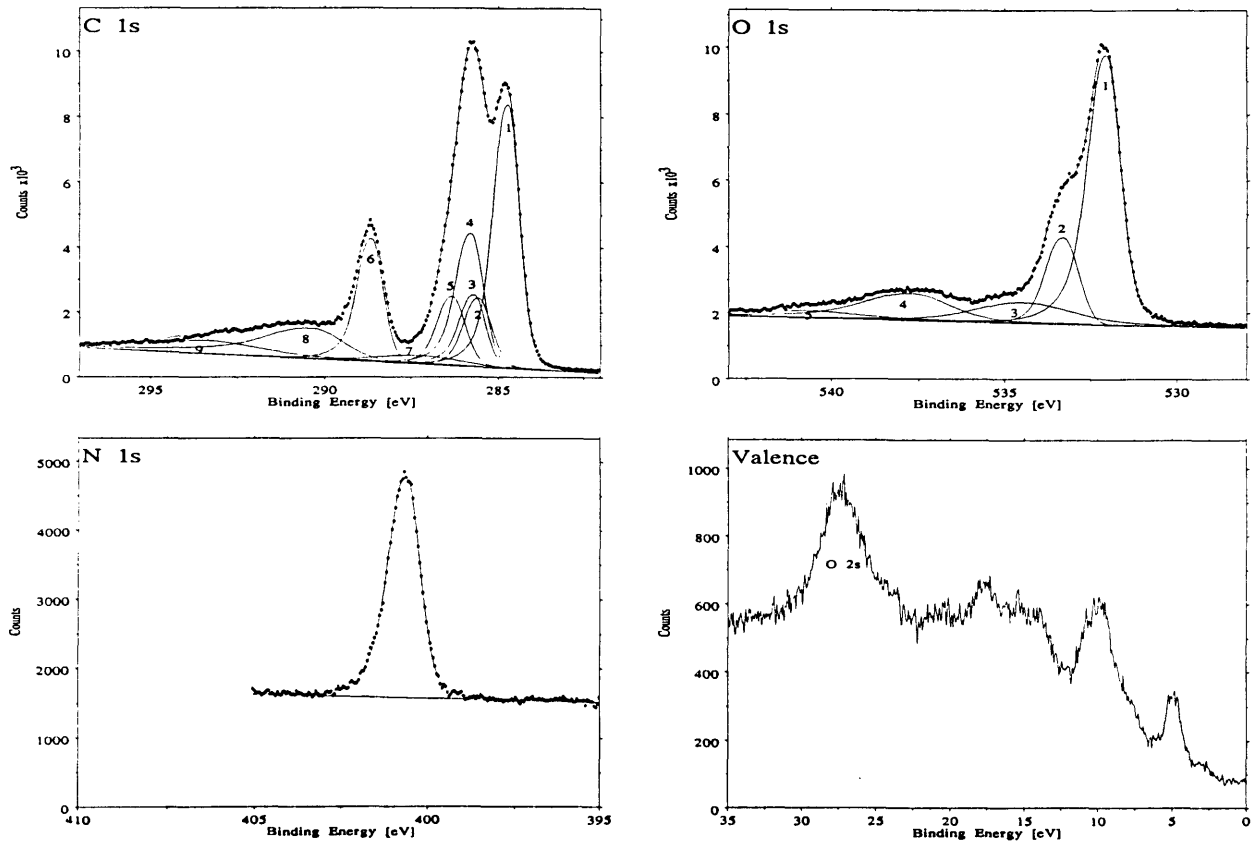


Figure 2.2.8. b) C1s, O1s, and N1s spectra of PMDA-ODA [19]. Equivalent atoms carry same numbers. Peaks are identified by their corresponding numbers (a).

As evident from the C1s spectrum in Figure 2.2.8 b), appropriate deconvolution of overlapping peaks is vital for the correct interpretation of the spectra. The peaks are fitted by iterative nonlinear least squares as summed Gaussian-Lorentzian functions, with the parameters  $A$  and  $m$  representing an asymmetry and a mixity parameter, respectively. More details on envelope deconvolution are given in [18,19]. Appendix A contains the specific XPS instrument settings and additional relevant information regarding the XPS work in the present thesis.

### 2.2.3. Other Experimental Methods

The permittivity transient method was used throughout the present work for measuring the kinetics of solute uptake by the coatings. The method consisted simply of impedance measurements at a fixed frequency over a period of time and was therefore closely related to IS. The same instrument setup was used. Detailed discussion of the method, the data analysis procedure, and interpretation of the results are given in Chapter 3.

Membrane permeation experiments were employed to measure the diffusion coefficients of  $\text{Cl}^-$  ions in the water-saturated polyimides. The method, along with data analysis and results is presented in Chapter 3 as well.

Refractive index measurements were used in Chapter 3. The equipment (Metricon Prism Coupler PC 2000) and the method have been described by Noe [21].

Density measurements were employed in Chapter 5 to supplement the processing-properties investigation. The density-gradient method consisted of measuring the depth to which polyimide film samples sank after immersion in a column with a vertical gradient of density [22,23]. A graduated glass tube (1 m total length, 80 cm graduated length, 1 mm graduations, 48 mm inner diameter) was immersed to  $\approx 2$  cm below the open end in a large temperature-controlled bath ( $T=23\pm 0.5$  °C). A 1.3500-1.5000  $\text{g/cm}^3$  density gradient was established over 80 cm of column by careful incremental addition [22, Method A] of 72 19.3 ml  $\text{Ca}(\text{NO}_3)_2$  solutions of different densities ( $\approx 0.0021$   $\text{g/cm}^3$  increments). The 72 solutions were prepared by mixing proportionately a 1.5000  $\text{g/cm}^3$  and a 1.3500  $\text{g/cm}^3$  solutions. Subsequently, glass density floats (American Density Materials, Inc, Belvidere, NJ) were used to calibrate the column in increments of 0.0020  $\text{g/cm}^3$ . The column was found to be linear in the range of 1.4000-1.5000  $\text{g/cm}^3$  (Figure 2.2.9).

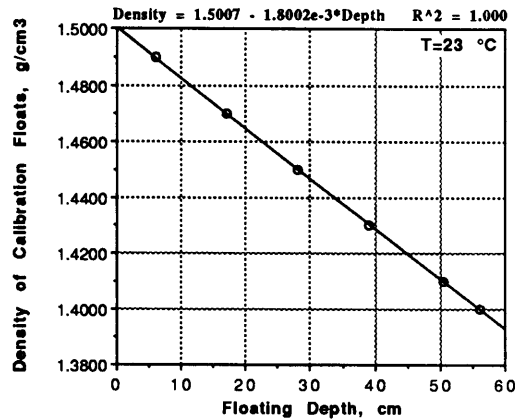


Figure 2.2.9. Calibration curve of the density gradient column at 23 °C.

The resultant sensitivity of the column was approximately 0.0002 g/cm<sup>3</sup> per mm [22]. Due to turbulence created during the filling, the upper 15 cm of the column were not linear and could not be used.

Polyimide film samples of 2-4 μm thickness and ca. 5 mm diameter were prepared by breaking the coated substrate to lift the coating, and slowly peeling off the lifted film. The samples were cut in various shapes for easy distinction. The underlying chromium metal layer lifted together with the polyimide, and an electronics grade Cr-etchant was used to remove it in an ultrasonic cleaner. The absence of surface tension effects was verified by immersing control samples from the same coating with very different surface areas. The many details of the column preparation and density measurement procedure have been described adequately in [22] and [23]. The density gradient column remained stable for approximately 70 days.

Finally, it was attempted to use secondary ion mass spectroscopy (SIMS) for chloride depth-profiling in the coating. Unfortunately, excessive charging resulted in irreproducible data.

### 3. Solute Uptake and Diffusion in Polyimide Coatings

#### 3.1. Methods of Measurement of Water Uptake and Diffusion in Polymers

Numerous publications deal with the measurement of the uptake and diffusion of water and other solutes and electrolytes in polymers. Several books have been devoted entirely to the subject [24-27].

By far, the great majority of studies of water uptake in polymers have been gravimetric, i.e. involving measurements of the weight gained by polymer films in controlled relative humidity (RH) environments. To achieve sufficient sensitivity, gravimetric measurements of thin films may require relatively large free-film samples. Moreover, the gravimetric method is destructive by nature because samples generally need to be cut. Most importantly, gravimetric experiments have suffered from relative humidity control problems, as well as from problems caused by surface moisture condensation and evaporation [26,28]. *In-situ* gravimetric measurements are impossible.

However, the method's significant advantage is that water uptake is measured directly, i.e. that in almost all cases any measured weight gain or loss represent directly absorption or desorption of water. A number of investigators of moisture uptake by polyimides and related polymers have employed the gravimetric method [28-38].

Another method for investigation of the kinetics of water uptake is based on the changes in the state of stress associated with moisture absorption [39]. In bending-beam experiments, the curvature of a polymer-coated (quartz) beam is recorded as a function of time since the introduction of a particular controlled environment [40]. Experiments are limited to supported films only, involve sample preparation and cannot be performed *in-situ*. Unlike gravimetric measurements, bending-beam measurements can also be conducted under

immersion thus avoiding all problems associated with RH control. Although determination of the amount of water taken up is theoretically possible, it requires precise knowledge of the hygroscopic stress coefficient which is a function of many processing variables and may vary significantly among samples [41]. Several studies have utilized the bending-beam method for water diffusion measurements in polyimides [40-43].

From a survey of the literature, it appears that relative permittivity measurements have not been seriously utilized in the study of water transport. Denton [28,44] has been successful in a feasibility study of capacitance transient measurements for determination of the diffusion coefficient of moisture in PMDA-ODA. However, she has employed a controlled relative humidity environment and has faced problems related to surface evaporation and condensation [28]. In addition, the patterned Al/PI/Al capacitors used in her study may have deviated from the one-dimensional diffusion model.

Other researchers may have misinterpreted the capacitance transient measurements, due in part to faulty samples [45].

The present work is apparently the first to employ routinely dielectric permittivity measurements in the study of water uptake and diffusion in a large number of samples. The advantages of the capacitance or relative permittivity transient method lie in its ability to measure the water uptake and diffusion non-destructively, *in-situ*, in thin coatings or free films, with very little sample preparation, and under immersion. Measurements of both water absorption and desorption kinetics are possible. The method is non-destructive because the short-term effects of water uptake are reversible, and *in-situ* because it can be applied to coatings which have undergone the same processing, are on the same substrate, and under the same state of stress as coatings in the field.

The main disadvantage of the permittivity transient method is the need to account for water's multilateral effect on the polymer: in addition to contributing its own polarizability to that of the dry material, water promotes processes like swelling and stress relaxation,



water-polymer interactions, and polymer hydrolysis which also affect the polymer's permittivity. These processes may have different but comparable characteristic time constants and thus may necessitate the separation of their individual contributions.

The permittivity transient method and the data analysis model are described in the next.

### **3.2. Water Uptake and Diffusion from Relative Permittivity Measurements**

Water is a polar liquid and its absorption causes the relative dielectric permittivity of the polymer to increase. The transient in relative permittivity associated with the dynamic water uptake by the coating can be used to measure the diffusion coefficient of water in it. The equilibrium value of the permittivity is related to the amount of absorbed water. The experiments presented here were performed on coatings under immersion. In this way, two major problems faced by Denton [28] were avoided: 1) the need for depositing a patterned counter-electrode on the polyimide which might disturb the one-dimensional diffusion process, and 2) surface condensation and evaporation effects resulting in more complicated and unstable surface boundary conditions. In addition, the whole issue of RH establishment and control was sidestepped. One tradeoff associated with immersion was the inability to investigate directly the concentration dependence of the water diffusion coefficient in the coating. It has been reported by some researchers that the diffusion coefficient of water was a function of the relative humidity in the environment [36,46]. However, it will be shown here that a concentration-independent diffusion treatment provides a completely adequate model of the experimental data. Since the same researchers were also among the few who observed non-Fickian behavior in Kapton<sup>®</sup>, the above reports may be attributed at least in part to experimental problems. Likewise, according to Crank [26] it appears that differences reported by researchers between liquid and vapor permeabilities are largely due to experimental difficulties in maintaining the vapor phase.

### 3.2.1. Measurement Procedure

Permittivity transient measurements were performed by means of the impedance spectroscopy setup described in Section 2.2. The procedure consisted of continuous impedance measurements at a single frequency, typically 1 kHz, starting at the moment of immersion of the coating. The arrangement of Figure 3.2.1 was used to provide a completely dry coating at the start of the measurement, and instantaneous filling of the cell with electrolyte.

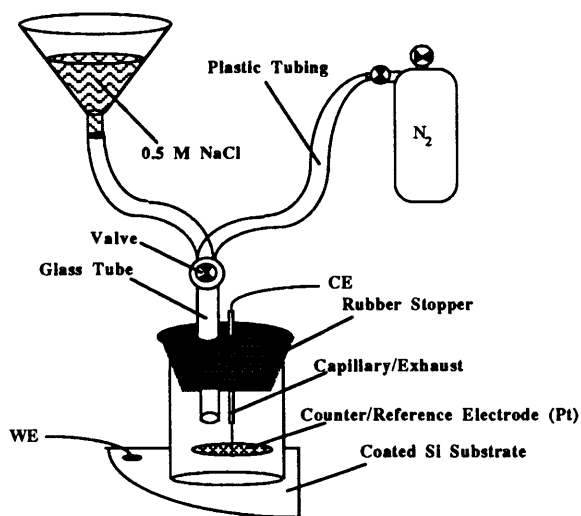


Figure 3.2.1. Test cell drying and filling arrangement for permittivity transients.

All test samples had been stored in the dessicator for several days prior to the measurement. Before filling with electrolyte, a positive dry N<sub>2</sub> pressure was maintained in the cell for 0.5 h or more, depending on the coating type and thickness. Cell filling occurred by switching the two-way valve to a funnel containing the electrolyte. The filling was complete within 1.5 s. Data acquisition was started immediately after. The time elapsed between the initial introduction of electrolyte into the cell and the start of data acquisition was recorded and subsequently added to the experimental time. During the first 100 s after immersion, the impedance was recorded continuously. The interval between consecutive data points was typically 1.4-2.5 s, depending on the frequency and the associated current

measurement resistor, and on the dielectric thickness of the coating. In all experiments, the integration error condition on the current channel of the FRA was set to  $\leq 1\%$  for maximum data quality. As a result of the initial very rapid transient in the cell capacitance, the acquisition of the first valid data point was not completed until at least 7 s after the moment of immersion. The above circumstance limited the upper value of the measurable diffusion coefficient to ca.  $2 \times 10^{-8} \text{ cm}^2/\text{s}$  in  $3 \text{ }\mu\text{m}$  thick coatings.

The calculation of the complex dielectric constant from the impedance data was based on an equivalent circuit comprised of parallel coating resistance and capacitance,  $-R_c=C_c-$ , in series with a solution resistance,  $R_s$  [47]:

$$\epsilon^* = \epsilon' - j\epsilon'' = \frac{\epsilon_0 d}{\omega} \left[ \frac{-Z''}{(Z'')^2 + (Z' - R_s)^2} - j \frac{Z' - R_s}{(Z'')^2 + (Z' - R_s)^2} \right]. \quad (3.2.1)$$

In the above equation,  $Z'$  and  $Z''$  were the isochronal, area-specific real and imaginary components of the complex impedance, respectively,  $\omega$  the constant angular frequency at which the measurements were performed,  $\epsilon_0$  the permittivity of vacuum,  $d$  the coating's thickness,  $\epsilon'$  the relative permittivity of the coating, and  $\epsilon''$  the dielectric loss factor. The value of the solution resistance,  $R_s$ , was determined as the high-frequency limit of  $Z'$  [13] from the IS scan immediately following the permittivity transient measurement. Complex dielectric constant data derived from the impedance measurements in accordance with (3.2.1) showed excellent agreement with data measured by means of a HP4275A multi-frequency meter.

In a previous study, Denton [28] had concluded that the "ac conductivity" could be used as an additional indicator of water absorption. This conductivity, dominated by the energy dissipated in the dielectric polarization process was calculated from the dielectric loss factor as:

$$\sigma = \omega \epsilon_0 \epsilon''. \quad (3.2.2)$$

Figure 3.2.2 shows relative permittivity and ac conductivity transient data acquired from a 5.33  $\mu\text{m}$  PMDA-ODA coating on Cr.

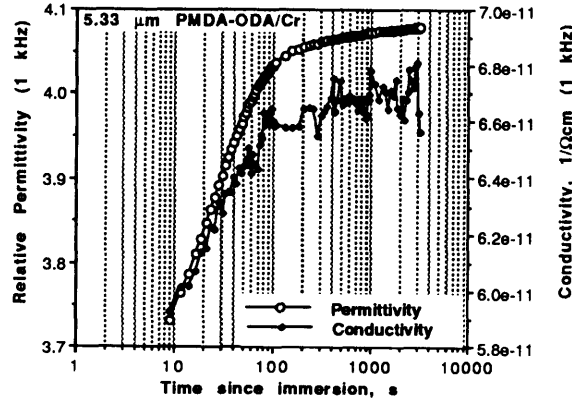


Figure 3.2.2. Relative permittivity and ac conductivity transients at 1000 Hz in a 5.33  $\mu\text{m}$  PMDA-ODA/Cr coating upon immersion in 0.5 M NaCl at 23 °C.

As an alternative to using (3.2.1), the coating capacitance and permittivity could be calculated approximately from the area-specific imaginary impedance component:

$$C(t) = -\frac{1}{\omega \cdot Z''(t)} \quad \text{and} \quad \epsilon'(t) = C(t) \frac{d}{\epsilon_0}, \quad (3.2.3)$$

where  $C(t)$  and  $Z''(t)$  were the coating capacitance and the imaginary impedance component as a function of time, respectively. The validity of the above approximation was verified on electrical test circuits similar to the ones discussed in Section 2.2. Comparisons between  $\epsilon'(t)$  determined via (3.2.1) and (3.2.3) produced an agreement to within 0.1%.

### 3.2.2. Effect of Absorbed Water on the Dielectric Properties of Polyimides

The dimensions of the coated samples used in this study were such that an one-dimensional treatment of their dielectric properties, based on the parallel-plate capacitor was appropriate. The following brief review is based on the discussions in [15,47-49].

The introduction of a homogeneous dielectric material between the plates of an evacuated parallel plate capacitor causes a reduction in the strength of the applied electrical field. Alternatively, when the field strength is maintained constant, the charge stored in the capacitor increases by the amount  $|\mathbf{P}|$ , where  $\mathbf{P}$  is the vector of the dielectric polarization in the material defined as:

$$\mathbf{P} = (\epsilon - 1)\epsilon_0\mathbf{E}. \quad (3.2.4)$$

In (3.2.4),  $\mathbf{E}$  is the electrical field strength,  $\epsilon_0$  the absolute permittivity of vacuum, and  $\epsilon$  the dielectric constant or relative permittivity of the material. The bulk effect of polarization originates in the induction of an electrical dipole moment,  $\mathbf{m}$ , on each molecule of the dielectric material:

$$\mathbf{m} = \alpha\mathbf{E}_L, \quad (3.2.5)$$

where  $\alpha$  is the molecular polarizability and  $\mathbf{E}_L$  is the local field strength. The polarization vector represents the total induced electrical moment per unit volume and can be expressed as:

$$\mathbf{P} = N\alpha\mathbf{E}_L = \frac{N_A}{V_M}\alpha\mathbf{E}_L = \frac{N_A\rho}{MW}\alpha\mathbf{E}_L, \quad (3.2.6)$$

with  $N$  being the number of molecules per unit volume,  $N_A$  the Avogadro number,  $V_M$  the molar volume,  $MW$  the molecular weight, and  $\rho$  the density of the dielectric material. For simple cubic lattices and completely random molecular arrays, the equation of the local electrical field strength has been derived by Lorenz:

$$\mathbf{E}_L = \mathbf{E} + \frac{\mathbf{P}}{3\epsilon_0} = \frac{\epsilon + 2}{3}\mathbf{E}. \quad (3.2.7)$$

By combining equations (3.2.7), (3.2.6), and (3.2.4), the Clausius-Mosotti polarization equation is derived:

$$\frac{\epsilon-1}{\epsilon+2} = \frac{4\pi N\alpha}{3\epsilon_0}, \quad (3.2.8)$$

from which the molar polarization can be obtained by multiplying by the molar volume,

$V_M$ :

$$P_M = \frac{4\pi N_A \alpha}{3\epsilon_0} = \frac{\epsilon-1}{\epsilon+2} \frac{MW}{\rho} \quad (3.2.9)$$

In the above equations, the molecular polarizability,  $\alpha$  represents the sum of the contributions of the electronic, atomic, and orientational polarizabilities:

$$\alpha = \alpha_e + \alpha_a + \alpha_o. \quad (3.2.10)$$

The electronic polarizability is related to the refractive index,  $n$ , of the dielectric:  $\alpha_e = n^2$ . Its characteristic frequency is  $\approx 10^{16}$  Hz. It is largely insensitive to temperature and pressure changes. The atomic polarizability manifests itself at infrared frequencies ( $\approx 10^{13}$  Hz), and in molecular solids is much smaller than  $\alpha_e$ .

Only molecular substances with permanent dipole moments exhibit orientational polarizability. In general,  $\alpha_o$  is a strong function of frequency, temperature, and pressure.

Its dependence on temperature is expressed by the relation:

$$\alpha_o = \frac{\mu^2}{3kT}, \quad (3.2.11)$$

where  $\mu$  is the permanent molecular dipole moment. The decrease in  $\alpha_o$  with increasing temperature is due to the interference of thermal motion with the orientation of the permanent dipoles in the electrical field.

Hence, for polar substances the molar polarization can be expressed more generally as:

$$P_M = \frac{\epsilon-1}{\epsilon+2} \frac{MW}{\rho} = \frac{4\pi N_A}{3\epsilon_0} \left( \alpha' + \frac{\mu^2}{3kT} \frac{1}{1+j\omega\tau} \right) \quad (3.2.12)$$

In the above equation,  $\alpha'$  is the temperature-independent deformational polarizability (sum of  $\alpha_e$  and  $\alpha_a$ ), and the complex multiplier accounts for the frequency dependence of the orientational polarizability [48]. The above relation permits the calculation of molecular dipole moments from molar polarization as a function of temperature data. Although (3.2.12) does not account for intermolecular interactions and therefore applies strictly only to gases, it has been utilized extensively for determination of the permanent dipole moments of polar molecules, by measuring the polarization of dilute solutions of such molecules in nonpolar solvents and extrapolating to zero concentration. If the polarization of the solvent is known, the polarization of the solute can be derived from that of the solution by means of:

$$P_M^{\text{solvent}} \cdot x^{\text{solvent}} + P_M^{\text{solute}} \cdot x^{\text{solute}} = \frac{\epsilon - 1}{\epsilon + 2} \frac{MW^{\text{solvent}} \cdot x^{\text{solvent}} + MW^{\text{solute}} \cdot x^{\text{solute}}}{\rho}, \quad (3.2.13)$$

where  $\rho$  is the density of the solution, and  $x^i$  the mol-fraction of solute or solvent, respectively. Denton has used (3.2.13) to determine the permanent dipole moment of water absorbed in PMDA-ODA [28]. She obtained a value of  $5.6 \times 10^{-30}$  C·m (=1.68 D), very similar to the dipole moment of unassociated water molecules in the gaseous state ( $\approx 6.2 \times 10^{-30}$  C·m or 1.85 D). This finding implies that water in the polyimide resides in the form of free molecules, i.e. not in the form of molecular clusters or liquid water.

By means of parallel gravimetric and capacitance measurements, Denton has demonstrated that a linear relationship exists between the capacitance or the relative permittivity, and the equilibrium water uptake in PMDA-ODA capacitors [28].

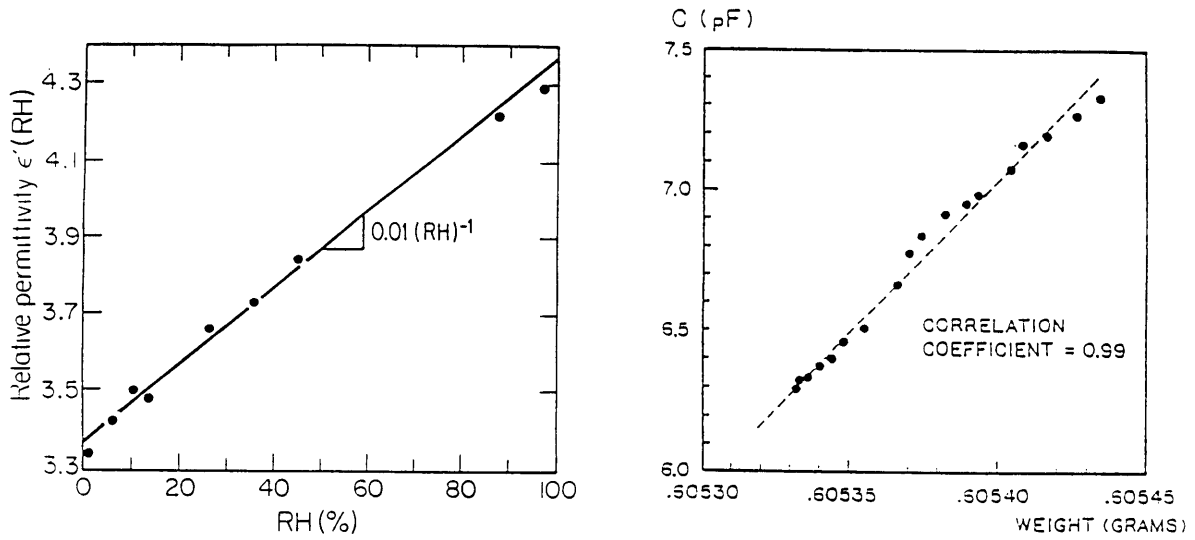


Figure 3.2.3. Linear relationships between the relative humidity of the environment, the dielectric permittivity, and the equilibrium water uptake in 5-10  $\mu\text{m}$  polyimide capacitors [28].

The relationship between the capacitance and water uptake by the coating can be expressed in the form:

$$C_{\text{equil}} = C_{\text{dry}} + a \cdot C_{\text{equil}}^{\text{w}} \quad (3.2.14 \text{ a})$$

or, alternatively

$$\epsilon'_{\text{equil}} = \epsilon'_{\text{dry}} + b \cdot C_{\text{equil}}^{\text{w}} \quad b = \frac{d}{\epsilon_0} \quad (3.2.14 \text{ b})$$

with  $C$  being the coating capacitance,  $\epsilon'$  the relative permittivity,  $C_{\text{equil}}^{\text{w}}$  the concentration of water in the coating in equilibrium with the environment,  $a$  is a constant, and  $d$  the coating thickness. The linear relationships of Figure 3.2.3 have also been confirmed experimentally by Lim and others [29,33,50].

By contrast, an exponential relationship between the coating's capacitance and its water uptake has been universally adopted in the corrosion literature [45,51-56]:

$$C_{\text{equil}} = C_{\text{dry}} (80)^{(x_v/100)}, \quad (3.2.15)$$



where  $C_{\text{equil}}$  is the capacitance of the coating in equilibrium with the environment,  $C_{\text{dry}}$  is the capacitance of the dry coating, and  $x_v$  is the equilibrium water uptake in v-%. The original source of (3.2.2) is a paper published in 1937 by Hartshorn et al [57]. Not only does (3.2.15) contradict the more recent findings presented above, but it also assumes without a proof that the absorbed water in the coating has the same dielectric properties as bulk (liquid) water ( $\epsilon' = 80$ ). Yet, some researchers continue using (3.2.15) even in conjunction with PMDA-ODA coatings [51,58].

### 3.2.3. Modeling of Permittivity Transient Data

At equilibrium, i.e. in the absence of a water concentration gradient in the coating, the coating's capacitance  $C_{\text{equil}}$  is linearly proportional to the relative humidity in the environment and to the corresponding equilibrium water uptake in the coating,  $C_{\text{equil}}^w$  (Figure 3.2.3). However, as illustrated in Appendix B, in the presence of a water concentration gradient it does not follow from (3.2.14) that the capacitance is linearly proportional to the average water concentration in the coating as a function of time, i.e. that  $C(t) = C_{\text{dry}} + a \cdot \overline{C^w}(t)$ . Instead, (3.2.14) implies that the instantaneous local relative permittivity in the coating,  $\epsilon'(x,t)$  is linearly proportional to the instantaneous local water concentration  $C^w(x,t)$ , i.e.:

$$\epsilon'(x,t) = \epsilon'_{\text{dry}} + b \cdot C^w(x,t), \quad (3.2.16)$$

where  $\epsilon'_{\text{dry}}$  is the dielectric constant of the dry polymer. A coating with a gradient of water concentration can be represented by a nonuniform transmission line. Alternatively, because there is almost no current flow through the resistor branch of the line at 1000 Hz, the coating can be approximated by a series of parallel-plate capacitors with different permittivities, proportional to the corresponding water concentrations (Figure 3.2.4). In

the limit of infinitely small distances between the capacitor plates, the coating capacitance as a function of time can be expressed as:

$$\frac{1}{C(t)} = \frac{1}{\epsilon_0} \int_{x=0}^{x=d} \frac{dx}{\epsilon'(x,t)} \quad (3.2.17)$$

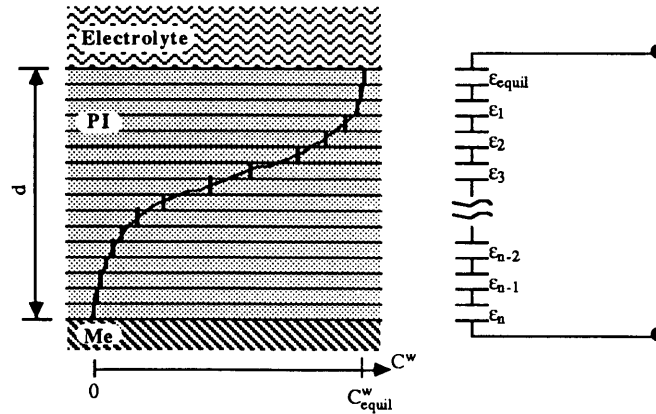


Figure 3.2.4. Schematic representation of a coating with a gradient of water concentration as a series of capacitors with different capacitances.

The one-dimensional water diffusion process in the coating is represented by the second Fickian equation of diffusion with constant boundary conditions:

$$\frac{\partial C^w(x,t)}{\partial t} = D \frac{\partial^2 C^w(x,t)}{\partial x^2} \quad \text{B.C.} \quad \begin{aligned} C^w(x,t=0) &= C_0^w \\ C^w(x,t=\infty) &= C_{equil}^w \end{aligned} \quad (3.2.18)$$

Assuming that the diffusion coefficient is not a function of the water concentration and that swelling is negligible, the local water concentration in the coating as a function of time is given by [59]:

$$\frac{C_{equil}^w - C^w(x,t)}{C_{equil}^w - C_0^w} = 2 \left\{ \sum_{n=0}^{\infty} \frac{(-1)^n}{(n+\frac{1}{2})\pi} \exp\left[-(n+\frac{1}{2})^2 \pi^2 \frac{D \cdot t}{d^2}\right] \cos\left[\left(n+\frac{1}{2}\right) \frac{\pi x}{d}\right] \right\}, \quad (3.2.19)$$

where  $D$  is the diffusion coefficient of water in the coating, and  $C_0^w$  is the initial water content. The swelling of PMDA-ODA, BPDA-PDA and BTDA-ODA/MPDA coatings in water has been investigated by several researchers [29,39,60]. All investigators report

equilibrium swelling strain values of less than 0.4 % at 100% RH, therefore swelling effects can be neglected.

The following equation of the coating capacitance as a function of time is obtained by combining (3.2.16), (3.2.17), and (3.2.19):

$$\frac{1}{C(t)} = \frac{1}{\epsilon_0} \int_{x=0}^{x=d} \frac{dx}{\epsilon'_{dry} + bC_{equil}^w - 2b(C_{equil}^w - C_o^w) \left( \sum_{n=0}^{\infty} \frac{(-1)^n}{(n+\frac{1}{2})\pi} \exp\left[-(n+\frac{1}{2})^2 \pi^2 \frac{D \cdot t}{d^2}\right] \cos\left[\left(n+\frac{1}{2}\right) \frac{\pi x}{d}\right] \right)},$$

which is also equivalent to:

(3.2.20)

$$\frac{1}{C(t)} = \frac{1}{\epsilon_0} \int_{x=0}^{x=d} \frac{dx}{\epsilon'_{equil} - 2 \left(1 - \frac{C_o^w}{C_{equil}^w}\right) (\epsilon'_{equil} - \epsilon'_{dry}) \left( \sum_{n=0}^{\infty} \frac{(-1)^n}{(n+\frac{1}{2})\pi} \exp\left[-(n+\frac{1}{2})^2 \pi^2 \frac{D \cdot t}{d^2}\right] \cos\left[\left(n+\frac{1}{2}\right) \frac{\pi x}{d}\right] \right)},$$

For  $t \geq 0.044 \frac{d^2}{D}$ , equation (3.2.20) can be approximated by the first term of the infinite series:

$$\frac{1}{C(t)} = \frac{1}{\epsilon_0} \int_{x=0}^{x=d} \frac{dx}{\epsilon'_{equil} - \frac{4}{\pi} \left(1 - \frac{C_o^w}{C_{equil}^w}\right) (\epsilon'_{equil} - \epsilon'_{dry}) \exp\left(-\frac{\pi^2 D \cdot t}{4d^2}\right) \cos\left(\frac{\pi x}{2d}\right)}. \quad (3.2.21)$$

Although equations (3.2.20) and (3.2.21) can be solved numerically, they cannot be fitted rigorously to experimental data. The analytical solution of equation (3.2.21) [61,p.A-139]:

$$C(t) = \frac{\epsilon_0 \sqrt{A^2 - B^2}}{2 \arctan\left(\frac{\sqrt{A^2 - B^2}}{A - B}\right)} \quad A = \frac{\pi \epsilon'}{2d} \epsilon'_{\text{equil}}, \quad B = \frac{2}{d} \left(1 - \frac{C_o^w}{C_{\text{equil}}^w}\right) (\epsilon'_{\text{equil}} - \epsilon'_{\text{dry}}) \exp\left(-\frac{\pi^2 D \cdot t}{4d^2}\right),$$

is also inconvenient for use as a regression model.

By contrast, although not strictly correct the use of equations (3.2.22) instead of (3.2.16) results in a much more convenient model.

$$C(t) = C_{\text{dry}} + a \cdot \overline{C^w}(t) \quad \text{or} \quad \epsilon'(t) = \epsilon'_{\text{dry}} + b \cdot \overline{C^w}(t), \quad (3.2.22)$$

The average water concentration in the coating as a function of time can be determined by integrating (3.2.19):

$$\overline{C^w}(t) = \frac{1}{d} \int_{x=0}^{x=d} C^w(x,t) \cdot dx = C_{\text{equil}}^w - \frac{2}{\pi^2} (C_{\text{equil}}^w - C_o^w) \sum_{n=0}^{\infty} \frac{(-1)^n}{\left(n + \frac{1}{2}\right)^2} \exp\left[-\left(n + \frac{1}{2}\right)^2 \pi^2 \frac{D \cdot t}{d^2}\right]. \quad (3.2.23)$$

For  $t \geq 0.044 \frac{d^2}{D}$ , a combination of the one-term approximation to (3.2.23) with (3.2.22)

leads to the following simple equation of the coating capacitance as a function of time:

$$C(t) = \frac{\epsilon_0}{d} \left[ \epsilon'_{\text{equil}} - \frac{8}{\pi^2} \left(1 - \frac{C_o^w}{C_{\text{equil}}^w}\right) (\epsilon'_{\text{equil}} - \epsilon'_{\text{dry}}) \exp\left(-\frac{\pi^2 D \cdot t}{4d^2}\right) \right]. \quad (3.2.24)$$

Figure 3.2.5 shows a comparison among data simulated by means of the exact  $C(t)$  function (3.2.20), its long-term approximation (3.2.21), and the above alternative model (3.2.24). In the numerical simulation, the cut-off error due to the finite number of terms in the series in (3.2.20) was 0.01%, and the round-off error estimate for the numerical integration in (3.2.20) and (3.2.21) was 0.001%.

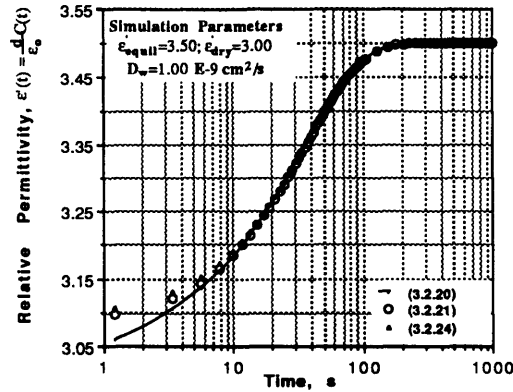


Figure 3.2.5. Comparison of capacitance data simulated numerically by means of (3.2.20), (3.2.21), and (3.2.24) for a typical set of parameter values.

Figure 3.2.6 illustrates that equations (3.2.21) and (3.2.24) yielded very similar data within the parameter range of interest.

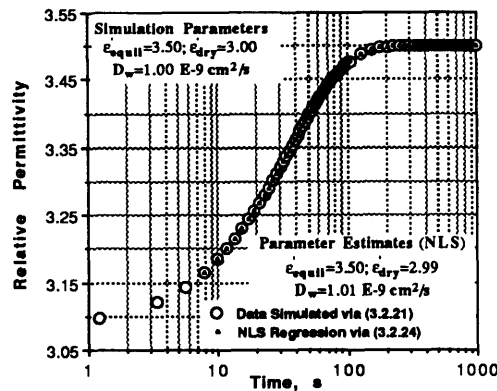


Figure 3.2.6. Non-linear regression fit of equation (3.2.24) to the data simulated via (3.2.21) (Figure 3.2.5). Data below 5 s were not used in the regression.

As expected, the difference between (3.2.21) and (3.2.24) was most significant at short times when the concentration gradient in the coating was largest. However, the dominant error at short times was the error involved in using (3.2.21) instead of (3.2.20). At  $t \approx 1$  s, this error was  $\approx 1.2\%$ , while that involved in the approximation of (3.2.21) by (3.2.24) was only ca.  $0.5\%$ . Similar results were obtained for other appropriate sets of simulation parameters. Therefore, it was concluded that although not strictly correct equation (3.2.24) represented a valid approximation of (3.2.21), and could be used instead of it as a model in the non-linear least squares (NLS) regression analysis of the experimental data.

Finally, it is obvious that a linear least-squares analysis procedure would have been equally appropriate if the capacitance or dielectric permittivity data were linearized by means of:

$$\ln [C_{\text{equil}} - C(t)] = \ln(a_1) - \frac{\pi^2 D}{4d^2} t. \quad (3.2.25)$$

However, although the use of (3.2.25) was quite legitimate for simulated data, its use in conjunction with the actual experimental data lead to large errors. This was a result of the inability to estimate  $C_{\text{equil}}$  accurately from the experimental data, which unlike the simulation in Figure 3.2.6 did not exhibit a saturation plateau.

The next section discusses the use of the model developed above in the analysis of the experimental data obtained from the polyimide coatings of interest.

#### **3.2.4. Application of the Water Diffusion Model to Experimental Data**

There was a significant qualitative discrepancy among the experimental data in Figure 3.2.2 and the data in Figure 3.2.5 which were simulated by means of the diffusion model. Experimental data appeared to suggest that the water uptake did not reach an equilibrium within the duration of the experiment, even after 10000 s. Recently, a similar continuous increase in the capacitance has been reported sketchily by Bellucci and Nicodemo [45] who attributed it to "corrosion of the metallic substrate or coating delamination". As demonstrated later in this chapter and subsequently in the discussion in Chapter 4, such interpretation is incorrect. Popov et al published capacitance data from epoxy coatings on steel also exhibiting a continuously increasing trend, but did not comment on its origins [55]. In the present work, the increase was initially attributed to the absorption of  $\text{Cl}^-$  and  $\text{Na}^+$  from the electrolyte, a process expected to be much slower than water uptake.

The continuous slow rise in the relative permittivity after the fast initial transient was common to all four investigated polymers. Moreover, so was its approximately logarithmic nature as a function of time (Figure 3.2.7).

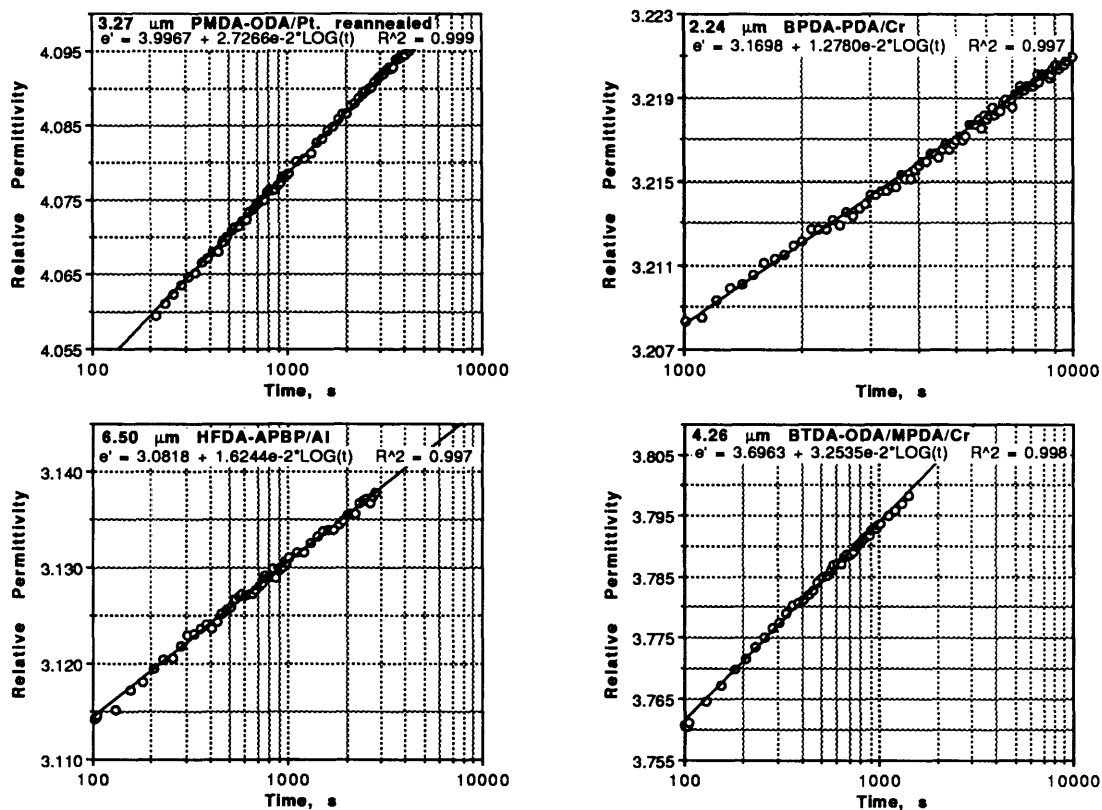


Figure 3.2.7. Illustration of the logarithmic increase in the relative permittivity of various coatings as a function of time.

In accordance with the above figure, after the initial transient the permittivity could be modeled by a relationship of the form (3.2.26) where L and M were constants.

$$\epsilon'(t) = L + M \cdot \log(t) \quad \text{or} \quad C(t) = L' + M' \cdot \log(t) \quad (3.2.26)$$

Based on the assumption that the logarithmic trend was due to ionic uptake, it was possible that the permittivity transients might represent a linear superposition of the fast water uptake and the slower ionic uptake processes. Indeed, as illustrated in Figure 3.2.8 on data from a BPDA-PDA coating, subtraction of the logarithmic trend from the total permittivity transient exposed the underlying Fickian water diffusion process.

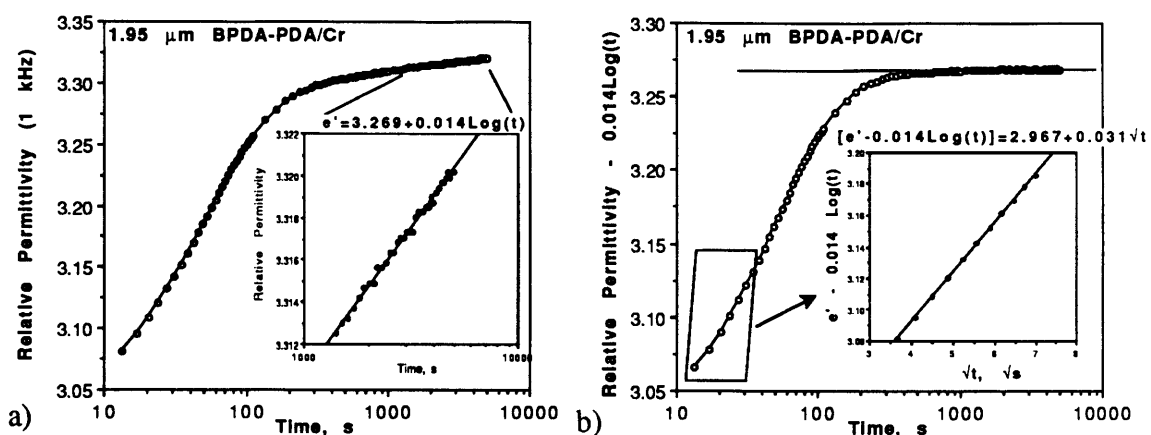


Figure 3.2.8. Capacitance transient in a 1.95  $\mu\text{m}$  BPDA-PDA/Cr coating in 0.5 M NaCl at 23  $^{\circ}\text{C}$ . Subtraction of the logarithmic trend from the data (a) revealed the underlying water diffusion process. The  $\sqrt{t}$ -behavior characteristic of Fickian diffusion at short times is indicated in the inset (b).

NLS regression analysis was conducted on subtracted capacitance or permittivity data using (3.2.24) as a model. The quality of the fit is demonstrated in Figure 3.2.9 for all four polyimide types. In each case, the simple Fickian diffusion process with constant boundary conditions and a concentration-independent diffusion coefficient yielded an adequate model of the experimental data. The data in Figure 3.2.9 constitute an indirect proof of the appropriateness of the assumptions involved in the derivation of (3.2.20) and in the data reduction process (logarithmic trend subtraction).

The nature of the logarithmic trend was explored further, and is discussed later in this chapter. It was understood that the trend was not caused by ionic uptake and that it might be possible to separate the Fickian and logarithmic processes experimentally in time. Figure 3.2.10 shows one successful experiment, in which a 1.83  $\mu\text{m}$  BPDA-PDA/Al sample had been desiccated for 24 hours following 24 days of exposure to 0.5 M NaCl. Upon reimmersion, the transient showed a delay in the onset of the logarithmic trend, evidence of the distinct nature of the two processes. Such data represent a direct proof of the correctness of the linear superposition approach.



$$\epsilon'(t) - M \cdot \log(t) = \epsilon'_{\text{equil}} + \frac{8}{\pi^2} b' \cdot \exp\left(-\frac{\pi^2 D}{4d} t\right)$$

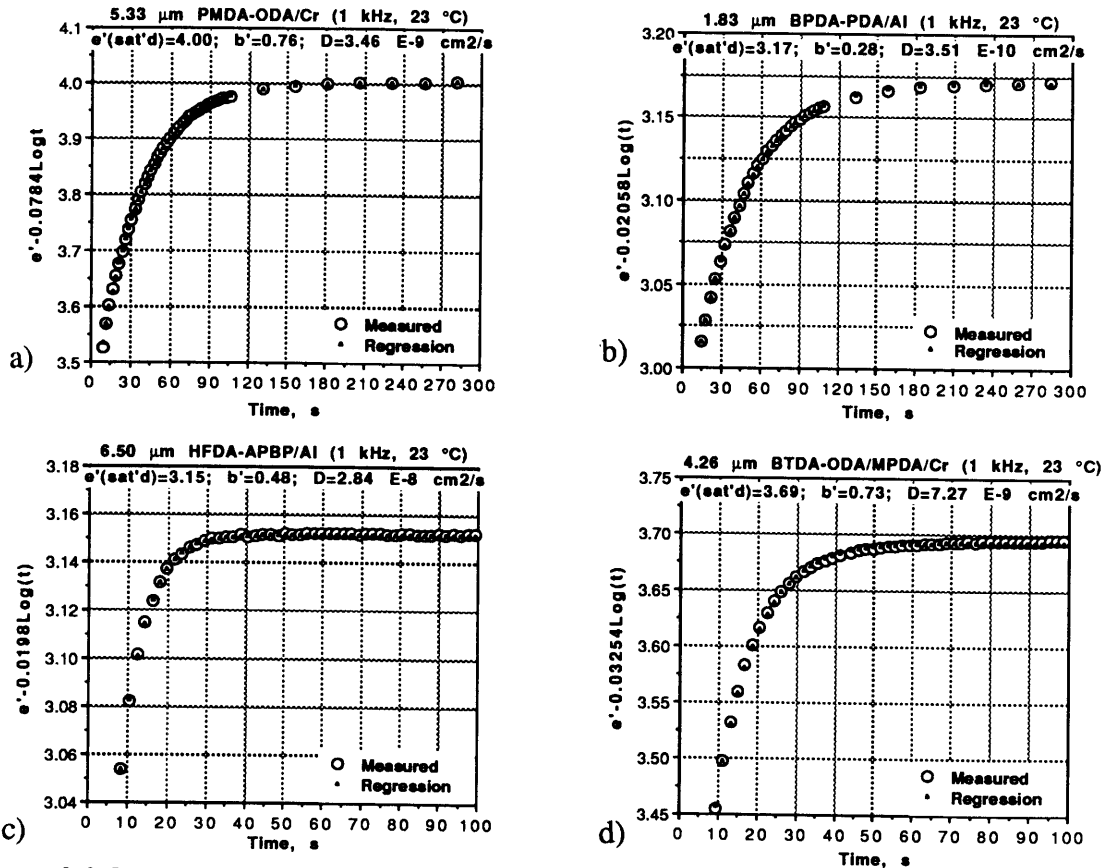


Figure 3.2.9. Regression analysis of permittivity transients from PMDA-ODA (a), BPDA-PDA (b), HFDA-APBP (c), and BTDA-ODA/MPDA (d) coatings, by means of a Fickian model with concentration-independent diffusion coefficients.

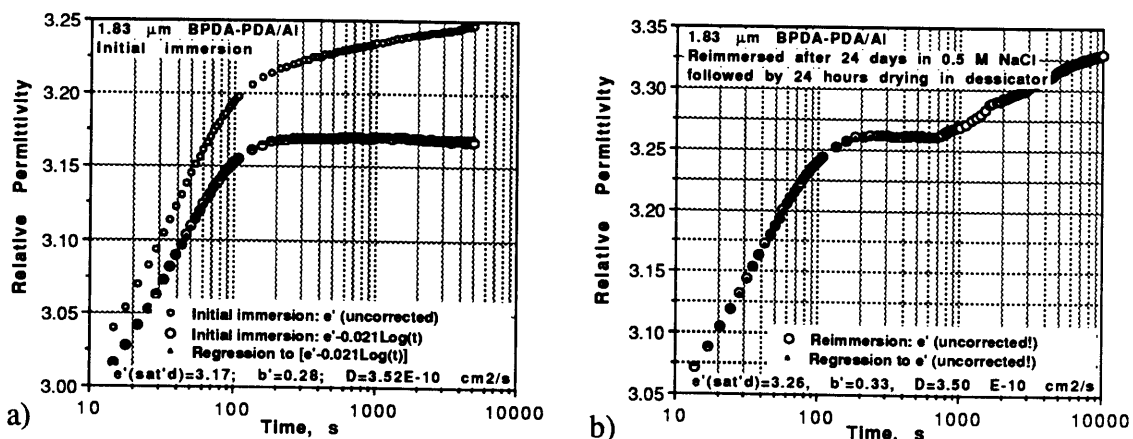


Figure 3.2.10. Experimental separation in time of the Fickian water uptake and the logarithmic trend in the permittivity transient.  
 a) Permittivity transient and NLS fit upon initial immersion.  
 b) Permittivity transient and NLS fit upon reimmersion after drying.

The procedure outlined in this section was used in the analysis of all permittivity transient data. The next section presents the experimental results and discussion of the water uptake and diffusion in polyimide coatings.

### 3.3. Water Uptake and Diffusion Results

Table 3.3.1 contains a summary of all results from the measurements of water uptake and diffusion in PMDA-ODA, BPDA-PDA, HFDA-APBP, and BTDA-ODA/MPDA polyimide coatings on Cr, Al, Cu, and Pt-metallized silicon substrates. Parameters measured in this work were indicated in bold. Several other parameters used in the following discussion were taken from the literature or calculated and also have been included in the table.

A number of repeat experiments were performed in order to assess the experimental errors associated with the above parameter estimates. The estimates of  $\epsilon'_{dry}$  and  $\epsilon'_{equil}$  included an experimental error of  $\approx \pm 5.5\%$  between samples (standard error). The reason was the imprecise knowledge of the exposed sample area as a consequence of epoxy overflow at the rim of the Plexiglas cylinder during cell assembly (Chapter 2). Both  $b$  and  $D_w$  showed error tolerances better than  $\pm 3\%$ . The maximum variation of parameter estimates among different samples from the same wafer was  $\pm 6\%$ . This was approximately equal to the variation among identical wafers from the same processing batch.

Coating Type	PMDA-ODA (PI2545)	PMDA-ODA (PI2545)	PMDA-ODA (PI2545)	PMDA-ODA (PI2545)
Substrate (#samples)	Cr (8)	Al (8)	Cu (2)	Pt (2)
Thickness range, $\mu\text{m}$	<u>3.1-8.2</u>	<u>3.6-7.9</u>	<u>2.3-2.5</u>	<u>3.2-3.3</u>
$q'$ dry	<u>3.25</u>	<u>3.20</u>	<u>3.18</u>	<u>3.20</u>
$q'$ equil	<u>3.98</u>	<u>3.95</u>	<u>3.83</u>	<u>3.91</u>
$\Delta q'$	<u>0.73</u>	<u>0.75</u>	<u>0.65</u>	<u>0.71</u>
$C_w$ (wt% 0)	<u>3.31</u>	<u>3.40</u>	<u>2.95</u>	<u>3.22</u>
$b=\Delta q'/C_w$ (1/wt%)		<u>0.22</u>		
$D_w$ , $\text{cm}^2/\text{s}$	<u>3.49E-9</u>	<u>3.64E-9</u>	<u>2.64E-9</u>	<u>3.91E-9</u>
$E_a$ , $\text{kJ/mol}$	<u>32.8</u>			
density, $\text{g/cm}^3$ 1)	1.42	1.42	1.42	1.42
MW (g/mol) 2)	372.3	372.3	372.3	372.3
$X_w$ (mol/mol PI) 3)	0.41	0.42	0.36	0.39
$V_w$ , $\text{cm}^3/\text{mol}$ 4)	194.3	194.3	194.3	194.3
$V_f=(V_m-1.3V_w)/V_m$ 5)	0.0366	0.0366	0.0366	0.0366
Coating Type	BPDA-PDA (PI2611)	BPDA-PDA (PI2611)	BPDA-PDA (PI2611)	
Substrate (#samples)	Cr (8)	Al (8)	Cu (2)	
Thickness range, $\mu\text{m}$	<u>1.5-6.2</u>	<u>1.8-8.1</u>	<u>3.0-3.1</u>	
$q'$ dry	<u>2.88</u>	<u>3.00</u>	<u>3.01</u>	
$q'$ equil	<u>3.19</u>	<u>3.24</u>	<u>3.30</u>	
$\Delta q'$	<u>0.31</u>	<u>0.24</u>	<u>0.29</u>	
$C_w$ (wt% 0)	<u>1.82</u>	<u>1.40</u>	<u>1.71</u>	
$b=\Delta q'/C_w$ (1/wt%)		<u>0.17</u>		
$D_w$ , $\text{cm}^2/\text{s}$	<u>2.22E-10</u>	<u>3.20E-10</u>	<u>1.02E-10</u>	
$E_a$ , $\text{kJ/mol}$	<u>41.0</u>			
density, $\text{g/cm}^3$ 1)	1.47	1.47	1.47	
MW (g/mol) 2)	356.3	356.3	356.3	
$X_w$ (mol/mol PI) 3)	0.29	0.22	0.27	
$V_w$ , $\text{cm}^3/\text{mol}$ 4)	184.4	184.4	184.4	
$V_f=(V_m-1.3V_w)/V_m$ 5)	0.0111	0.0111	0.0111	
Coating Type	HFDA-APBP (UD4208)	HFDA-APBP (UD4208)		BTDA-ODA/MPDA (PI2525)
Substrate (#samples)	Cr (6)	Al (6)		Cr (2)
Thickness range, $\mu\text{m}$	<u>4.0-7.5</u>	<u>4.5-6.6</u>		<u>3.8-4.3</u>
$q'$ dry	<u>2.55</u>	<u>2.60</u>		<u>3.05</u>
$q'$ equil	<u>3.09</u>	<u>3.18</u>		<u>3.98</u>
$\Delta q'$	<u>0.54</u>	<u>0.58</u>		<u>0.93</u>
$C_w$ (wt% 0)	<u>0.84</u>	<u>0.90</u>		<u>3.40</u>
$b=\Delta q'/C_w$ (1/wt%)		<u>0.64</u>		<u>0.27</u>
$D_w$ , $\text{cm}^2/\text{s}$	<u>2.32E-8</u>	<u>2.75E-8</u>		<u>7.83E-9</u>
$E_a$ , $\text{kJ/mol}$	<u>27.6</u>			
density, $\text{g/cm}^3$ 1)	1.10	1.10		1.39
MW (g/mol) 2)	742.5	742.5		435.3
$X_w$ (mol/mol PI) 3)	0.26	0.27		0.46
$V_w$ , $\text{cm}^3/\text{mol}$ 4)	374.7	374.7		228.1
$V_f=(V_m-1.3V_w)/V_m$ 5)	0.2784	0.2784		0.0532

- 0) The  $C_w$ -values given in *italics* were adopted from the literature (see Section 3.3.2). The other values were calculated from  $\Delta q'/b$ .
- 1) Approximate published values.
  - 2) MW = molecular weight per repeat unit of the polymer, g/mol.
  - 3)  $X_w$  = molar fraction of absorbed water, mol water per mol of polymer repeat unit.
  - 4)  $V_w$ , the van der Waals volume (volume enclosed by the electron clouds of the molecules) was calculated in accordance with Bondi [62] and van Krevelen [63].
  - 5)  $V_f$ , the free volume in film was calculated in accordance with Zaikov [24] as the difference between the molar volume,  $V_m=MW/\rho$  at 296 °K, and the molar volume at 0 °K ( $\approx 1.3V_w$  [63]).

Table 3.3.1. Water uptake and diffusion results for PMDA-ODA, BPDA-PDA, HFDA-APBP, and BTDA-ODA/MPDA coatings on various substrates (23 °C, immersion in 0.5 M NaCl). All samples had undergone the standard (manufacturer-recommended) cure cycle. Parameters measured in this work are underlined.

### 3.3.1. Water Diffusion. Results and Discussion

All samples in Table 3.3.1 were produced at the MIT MTL laboratory within a two-month period from the same precursor materials and by the same technician. Estimated diffusion coefficients were in relatively good agreement with published data despite the wide range of reported values in the literature, which could be attributed to differences in the processing conditions, film thickness, and to substrate effects. Table 3.3.2 shows a comparison between the present data and published diffusion data.

PMDA-ODA	BPDA-PDA	HFDA-APBP	BTDA-ODA/MPDA
1) 2.6-3.9 E-9	1) 1.0-3.2 E-10	1) 2.3-2.8 E-8	1) 7.8 E-9
2) 1.0-2.4 E-9	3) 1.1 E-10		
3) 5.6 E-9	8) 2.7 E-10		
4) 4.5 E-9	11) 0.6-2.7 E-10		
5) 4.6 E-9			
6) 4.5 E-9			
7) 1.0-2.0 E-9			
8) 5.2 E-9			
9) 1.1 E-9			
10) 7.5 E-9			
11) 1.1-2.5 E-9			

- 1) This study
- 2) [34] Gravimetric/Kapton-free/RH/12.5-125  $\mu\text{m}$
- 3) [38] Gravimetric/PMDA-ODA-supported/immersion/2  $\mu\text{m}$  & /BPDA-PDA-supported/immersion/2  $\mu\text{m}$
- 4) [30] Gravimetric/PMDA-ODA-supported/50% RH/50-100  $\mu\text{m}$
- 5) [42] Bending beam/PMDA-ODA-supported/55% RH/20-30  $\mu\text{m}$
- 6) [44] Capacitance/PMDA-ODA-supported/RH/2.6  $\mu\text{m}$
- 7) [31] Gravimetric/PMDA-ODA/Si/RH/4  $\mu\text{m}$
- 8) [41] Bending beam/PMDA-ODA/Si/immersion/6.7-27  $\mu\text{m}$  & /BPDA-PDA/Si/immersion/5-21  $\mu\text{m}$
- 9) [32] Gravimetric/Kapton-free/RH/12.5-125  $\mu\text{m}$
- 10) [28] Capacitance/PMDA-ODA/RH/6.5  $\mu\text{m}$
- 11) [29] Gravimetric/PMDA-ODA/RH/12.5-125  $\mu\text{m}$  & /BPDA-PDA/RH/12.5-125  $\mu\text{m}$

Table 3.3.2. Comparison between the present results and published data on water diffusion ( $T=22-25\text{ }^{\circ}\text{C}$ ),  $D_w$  in  $\text{cm}^2/\text{s}$ .

For standard-cure samples, the water diffusion coefficients were a function of the polyimide type, coating thickness, and the underlying metal film type.

The dependence of the diffusion coefficients on the polyimide type had been investigated by several researchers [30,38,41]. According to Moylan et al [38], water diffusion was affected most significantly by the chemical affinity of the polyimide for water. Because of

the greater affinity of the diphenyl moiety for water, the diffusion in -ODA polyimides was much faster than that in -PDA ones. However, Okamoto et al [30] concluded that the morphology of the films was more important than their chemistry. As illustrated in Figure 3.3.1, the present results support such a conclusion.

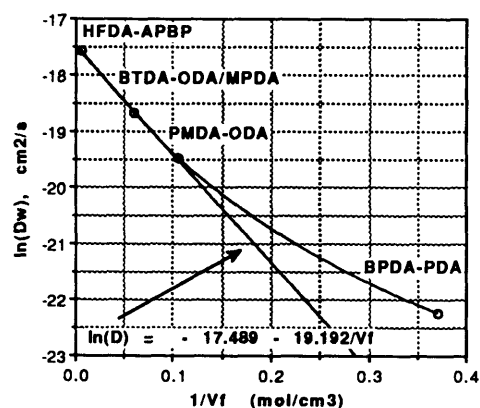


Figure 3.3.1. Correlation among the free volume fractions and water diffusion coefficients in the four polyimides, indicative of the dominant role of morphology in determining the transport kinetics.

The exponential nature of the above relationship was chosen by analogy with the critical free volume term in the equation of the ionic diffusion coefficient (2.2.6).

In addition to the free volume, crystallinity or amorphousness are generally regarded as important factors affecting  $D_w$  [30,42]. BPDA-PDA, the only one of the four polyimides with a significant degree of crystallinity [38,41] also exhibited the smallest diffusion coefficient. By contrast, amorphous films like BTDA-ODA/MPDA had high diffusion coefficients. However, the influence of order on diffusion may be due primarily to its effect on the free volume fraction. In fact, free volume in polymers in general is inversely proportional to the degree of crystallinity. Simultaneous studies of ordering, density, and diffusion are necessary in order to isolate their individual contributions.

Higher concentration of polar groups (e.g. C=O) has been reported to lead to a smaller diffusion coefficient while increasing the solubility [30]. However, this effect appears much smaller than that of morphology. Thus, although PMDA-ODA, BPDA-PDA, and BTDA-ODA/MPDA all had similar C=O concentrations ( $\approx 0.016N_A$  per cm<sup>3</sup>), their

diffusion coefficients were very different. Likewise, while the concentration of C=O groups in HFDA-APBP was much smaller ( $\approx 0.006N_A/\text{cm}^3$ ), its water uptake was similar to that of BPDA-PDA.

To investigate the effect of coating thickness on the diffusion coefficients, batches of coated samples of different thicknesses were manufactured at the same time and from the same precursor. The diffusion coefficients were a function of thickness as illustrated in Figure 3.3.2 for PMDA-ODA, BPDA-PDA, and HFDA-APBP on Cr and Al substrates.

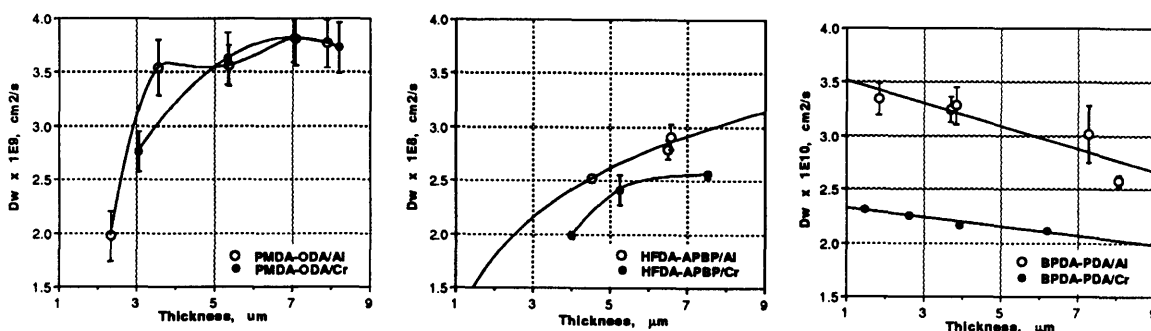


Figure 3.3.2. Water diffusion coefficients at 23 °C in PMDA-ODA (a), HFDA-APBP (b), and BPDA-PDA (c) coatings on Cr and Al as a function of the coating's thickness. The bars represent 95% confidence intervals (3 samples/wafer).

There is little agreement in the literature on the nature of the relationship between the film or coating thickness and the diffusion coefficients of solutes. As Figure 3.3.2 illustrates, the reason may be that different materials behave differently. Increasing diffusion coefficients with coating thickness have been reported for Kapton® or PMDA-ODA [34,43], and for PMMA [40]. Li et al [34] have attributed this increase to the lesser degree of in-plane ordering in thicker films, a relationship confirmed by Noe [21] via birefringence measurements. By contrast, other researchers have speculated that the diffusion coefficient of solvents decreases with increasing thickness for exactly the same reason [38]. Denton has also reported a decreasing  $D_w$  with increasing thickness, however she has attributed this to Al/polyimide interface effects in her samples [28]. Still others have reported that  $D_w$

in BPDA-PDA or PMDA-ODA are independent of the film thickness [33,41]. In general, it is probable that the variations in the ordering, morphology and residual stress in the coatings would cause the diffusion coefficients to vary as a function of coating thickness. Sikorski [64] has reported an increase in the residual stress in BPDA-PDA coatings with thickness, and Noe has observed a similar relationship in PMDA-ODA coatings [21]. Increasing (tensile) residual stress would lead to an increase in the water uptake but its impact on the diffusion coefficient is unclear. More importantly, it has been reported that the degree of crystallinity may increase (and thus  $V_f$  may decrease) with thickness due to slower cooling and better opportunity for equilibrium chain orientation [34,65] which may explain for the observed decrease in  $D_w$  in BPDA-PDA coatings.

The water diffusion coefficients in the coatings were also a function of the underlying metal film (Table 3.3.1). This was illustrated for Al and Cr in Figure 3.3.2. The effect of the substrate on water diffusion in the film has not been explored in the literature, although the residual stress in the film has been found to vary as a function of the substrate metal [12].

The relationship between the water diffusion coefficient and the cure temperature of the coatings was explored as part of the study of the effects of processing on their properties (Chapter 5). Figure 3.3.3 shows a comparison among the normalized diffusion coefficients in PMDA-ODA, BPDA-PDA, and BTDA-ODA/MPDA at cure temperatures of 400 °C (standard cure) and 250 °C. The results for the first two materials agree with the findings of Denton and Pranjoto [28,31] for PMDA-ODA, Lim [29,33] for PMDA-ODA and BPDA-PDA, and Jou [43] for NMP-solvent in PMDA-ODA and PMDA-PDA. Interestingly, the reverse relationship was observed in BTDA-ODA/MPDA. Once again,  $D_w$  is affected primarily through the free-volume, as indicated by the corresponding densities. Unfortunately, the densities of BTDA-ODA/MPDA films fell outside the range of the density gradient column and were not measured.

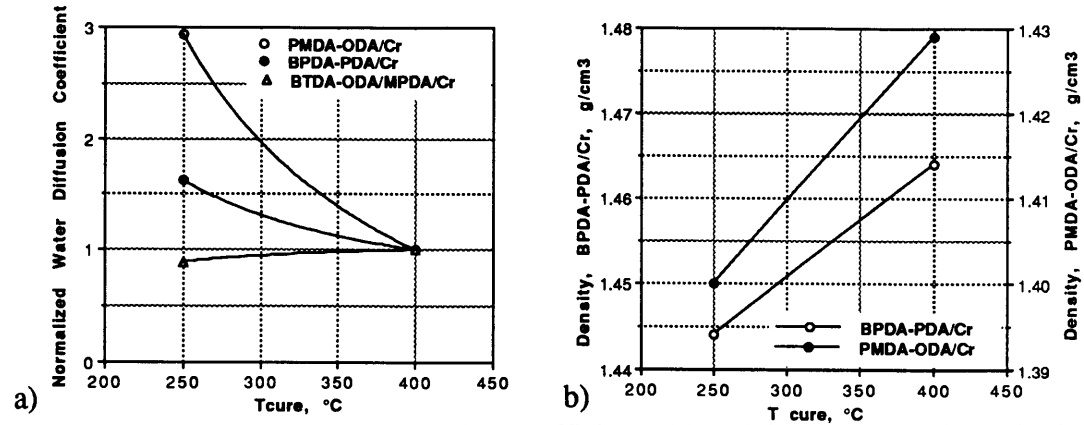


Figure 3.3.3. Measured water diffusion coefficients (a) and densities (b) of standard-cure coatings ( $T_{cure} = 400\text{ °C}$ ) vs. coatings cured at  $250\text{ °C}$  ( $23\text{ °C}$ ,  $0.5\text{ M NaCl}$ ).

The activation energies for water diffusion were determined by reimmersion experiments on the same sample at different temperatures. The results are presented in Figure 3.3.4. Water diffusion in all coatings was activated, meaning that it did not take place through pores or other defects. The activation energy was smallest in HFDA-APBP ( $27.6\text{ kJ/mol}$ ), followed by PMDA-ODA ( $32.8\text{ kJ/mol}$ ) and BPDA-PDA ( $41.0\text{ kJ/mol}$ ). The activation energies increased with increasing coating density or decreasing free volume (Table 3.3.1) but the increase was disproportionate.

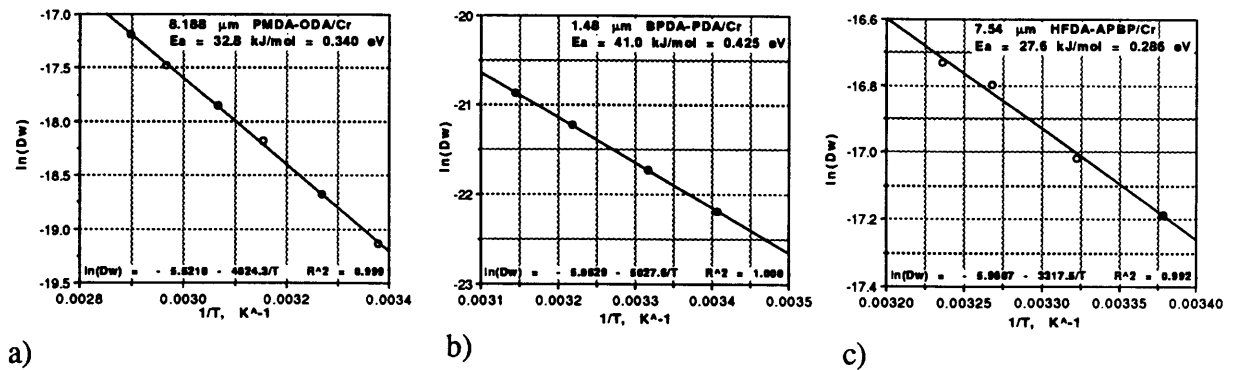


Figure 3.3.4. Activation energies for water diffusion in PMDA-ODA (a), BPDA-PDA (b), and HFDA-APBP (c) coatings on Cr.

For PMDA-ODA, the measured activation energy was very close to the values of  $0.32$  and  $0.31\text{ eV}$  reported by Denton and Lim [28,33,44], respectively. Values reported by others:



22.3 kJ/mol ( $\approx 0.23$  eV) [36] and 42-46 kJ/mol ( $\approx 0.44$ - $0.48$  eV) [66] for Kapton appear in error.

### 3.3.2. Water Uptake. Results and Discussion

Gravimetric experiments represent the only direct method for water uptake measurements. Published gravimetric data were used to calibrate the permittivity transient method for determination of water uptake. Most of the gravimetric data in the literature center on PMDA-ODA in its various forms, for which a range of 2.1-3.4 wt-% water uptake is reported [21,28-33,38]. The number reported for PMDA-ODA sample configuration and processing similar to the ones used in this work was 3.4 w-% [21]. The same PI2545 precursor was used in the present work as well, and the coatings were manufactured in the same laboratory under a similar cure cycle. Therefore, 3.4 wt-% was adopted as the average water uptake in the investigated standard-cure PI2545/Al coatings. For BPDA-PDA or PI2611, the numbers reported in the literature were 1.3-1.4 wt-% [28,29,38] and 1.4 wt-% was assumed in this case. Only one study of the water uptake in Ultradel (HFDA-APBP or UD4212) was found, reporting 0.9 w-% [67]. For BTDA-ODA/MPDA in its PI2525 form, 3.4 wt-% was quoted by Noe [21].

From permittivity transient measurements, the amount of absorbed water in the coatings could be determined by means of equation (3.2.14). The parameters  $\epsilon'_{\text{equil}}$  and  $\epsilon'_{\text{dry}} = \epsilon'_{\text{equil}} - \Delta\epsilon'$  were estimated from the experimental data in accordance with (3.2.24) and were given in Table 3.3.1. The parameter  $b$  in Table 3.3.1 was calculated as  $\Delta\epsilon'/C_w$  using the water uptake values adopted from the literature.

Table 3.3.3 shows the average values of the transverse refractive indices,  $n_{TM}$ , of dry and water-saturated polyimide coatings on Si. The refractive index data reported by Noe [21] were supplemented by additional measurements via a Metricon PC 2000 laser refractometer.

	PMDA-ODA	BPDA-PDA	HFDA-APBP	BTDA-ODA/MPDA
n <sub>TM</sub> , dry	1.631	1.622	1.603	1.670
n <sub>TM</sub> , equil	1.647	1.628	1.606	1.686

Table 3.3.3. Transverse refractive indices, n<sub>TM</sub> of dry and water-saturated coatings [21].

As illustrated in Figure 3.3.5, there was a considerable difference between ε'<sub>dry</sub> and the square of the transverse refractive index, (n<sub>TM</sub>)<sup>2</sup> in three of the four polyimides, indicating that the dry polyimides represented polar solvents.

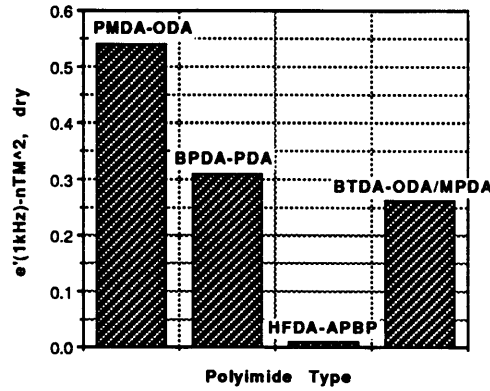


Figure 3.3.5. Polarity of the dry polyimides, expressed as the difference between the low-frequency transverse dielectric permittivity and the square of the transverse refractive index (HeNe laser, 0.63 μm).

Due to the polarity of the polyimides, a relationship for the molar polarization applicable to binary solutions of polar liquids was more appropriate than the equation for non-polar materials (3.2.12). The orientational polarization of a solution of a polar liquid in a polar solvent was given by the difference between the total polarization and the molar refraction [49]:

$$P_o = \frac{4}{3}\pi N_A \frac{x_{PI}\mu_{PI}^2 + x_w\mu_w^2}{3kT} = \left( \frac{MW_{PI} \cdot x_{PI} + MW_w \cdot x_w}{\rho} \right) \left[ \frac{(\epsilon' - 1)(\epsilon' + 2)}{8\epsilon'} - \frac{(n^2 - 1)(n^2 + 2)}{8n^2} \right], \quad (3.3.1)$$

where the subscripts PI and w applied to polyimide and water, respectively. Hence, the orientational polarization of the absorbed water, P<sub>o, w in PI</sub> could be calculated from:

$$P_{o, w \text{ in PI}} = \frac{P_o - P_{o, \text{dry PI}}}{x_w} + P_{o, \text{dry PI}} \quad (3.3.2)$$

In (3.3.2), the orientational polarizability of the dry polyimide was:

$$P_{o, \text{ dry PI}} = \left[ \frac{(\epsilon'_{\text{dry PI}} - 1)(\epsilon'_{\text{dry PI}} + 2)}{8\epsilon'_{\text{dry PI}}} - \frac{(n_{\text{dry PI}}^2 - 1)(n_{\text{dry PI}}^2 + 2)}{8n_{\text{dry PI}}^2} \right] \frac{MW_{\text{PI}}}{\rho_{\text{dry PI}}} \quad (3.3.3)$$

Equation (3.3.3) was used in conjunction with equations (3.3.1-2) and Table 3.3.3 to calculate the dielectric permittivity of the absorbed water in the PI,  $\epsilon'_{w \text{ in PI}}$ . The refractive index (1.333) and molar volume of water in the polymer were assumed equal to those of free water. Figure 3.3.6 a) shows the calculated values of  $\epsilon'_{w \text{ in PI}}$  at 23 °C in the four polyimides, along with the relative permittivity of bulk water. Figure 3.3.6 b) illustrates the linear correlation between the permittivity of the absorbed water and the free-volume fraction in the polymers.

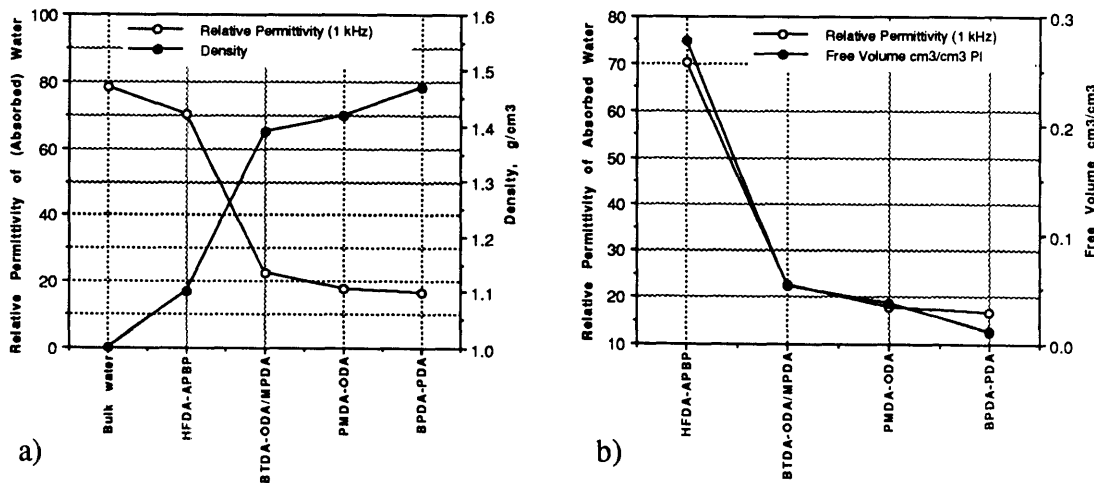


Figure 3.3.6. a) Calculated dielectric permittivities of the absorbed water in PMDA-ODA, BPDA-PDA, HFDA-APBP, and BTDA-ODA/MPDA at 23 °C. b) Permittivity of absorbed water as a function of the free-volume fraction.

The above data implies that water exists in hydrogen-bonded clusters in the polymer and the size of these clusters is inversely proportional to the free-volume fraction. The state of the absorbed water was not equivalent to that of bulk (liquid) water ( $\epsilon' \approx 79$  at 23 °C). Khare et al have addressed the estimation of the size of hydrogen-bonded clusters from dielectric measurements [68] but such calculations were not undertaken here. McCafferty

[69] has reported that the (transverse) relative permittivity of an absorbed monolayer of water was  $\epsilon' \approx 2$ , while that of two monolayers was ca. 28. By analogy, the average (transverse) size of the water clusters in the BPDA-PDA, PMDA-ODA, and BTDA-MPDA/ODA can be estimated from the corresponding absorbed water permittivities to vary between 1.5 and 1.8 molecules, respectively. The absorbed water permittivities of the latter three materials were similar to the ones reported by Matsuguchi et al for certain polyimide resins, although their estimates were made using a simpler approximation [50].

Figure 3.3.6 illustrates once again the error involved in assuming absorbed water permittivity of 80 in equation (3.2.15) for estimation of the water contents of coatings. However, the application of equation (3.2.14) is also not without its problems. In order to use (3.2.14) to estimate the water uptake in a polyimide film as a function of processing, the moisture-sensitivity coefficient  $b$  has to be assumed constant under all conditions. In fact, from the discussion above it can be expected that  $b$  will vary somewhat depending on the size of the clusters of water molecules in the polymer, and will thus be a function of the processing, substrate, thickness and other parameters affecting the free-volume fraction in the coating. Fortunately, as discussed in Chapter 5, the extent of the density and free-volume variations as a function of processing was found to be less than 2% within a given polyimide type. In accordance with the linear relationship from Figure 3.3.6 b), this implies a very small change in the permittivity of absorbed water. Therefore, for the purpose of this study  $b$  was assumed constant within a polyimide type.

Simultaneous gravimetric and dielectric measurements would be necessary in order to verify the above assumption directly.

Similar to the diffusion coefficient (Figure 3.3.3), the solubility had been reported to increase with decreasing cure temperature [28,31,33,50]. As shown in Figure 3.3.7, this

was confirmed by the present study for coatings cured at 250 °C. Like before, BTDA-ODA/MPDA was the only exception.

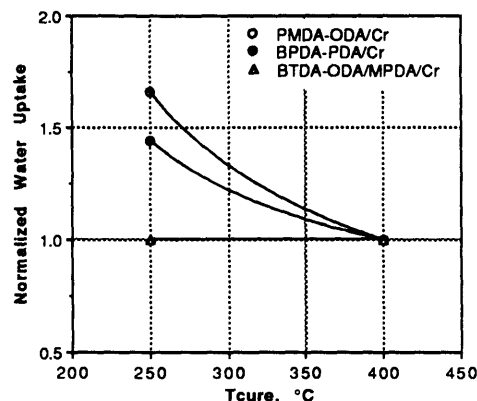


Figure 3.3.7. Equilibrium water uptake in PMDA-ODA, BPDA-PDA, and BTDA-ODA/MPDA coatings on Cr as a function of the cure temperature.

The water uptake was found to be independent of the coating thickness, confirming Denton's results [28].

### 3.4. Results from Measurements of Diffusion of Organic Solutes

In addition to water, the permittivity transient method can be used with other solutes as well. Such measurements might be of interest in characterizing the diffusion and uptake by electronic packaging materials of various chemicals used at different stages of MCM manufacture. In this work, the method was applied to methanol, ethanol, acetone, and acetic acid in order to illustrate its feasibility. Figure 3.4.1 shows the permittivity transients in a HFDA-APBP/Cr coating upon immersion in acetone and ethanol, and the NLS regression to the transient in ethanol.

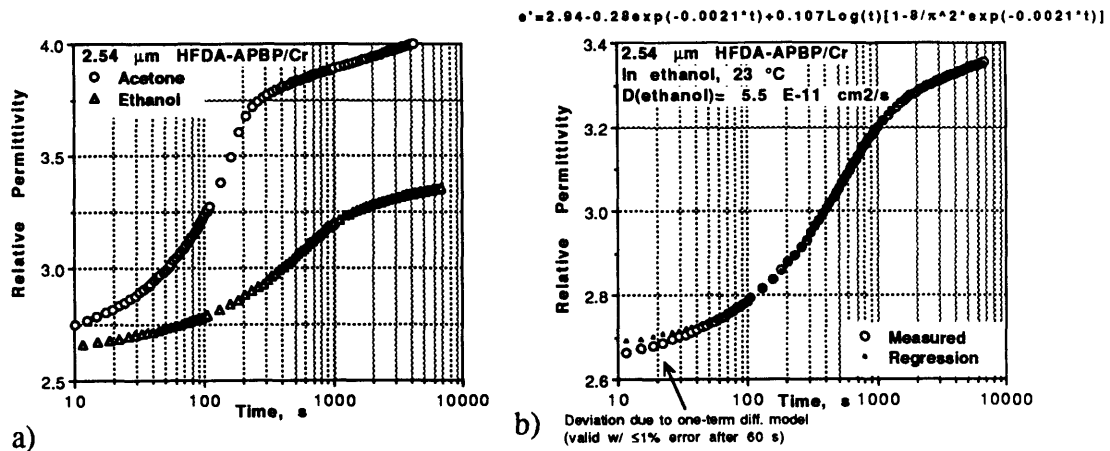


Figure 3.4.1. a) Permittivity transients in a HFDA-APBP/Cr coating immersed in acetone and ethanol at 23 °C.  
b) Regression to the permittivity transient in ethanol.

The transients appeared qualitatively similar to those in water, except that the logarithmic slope was much steeper. The same diffusion model (3.2.24) could be applied toward their analysis, however it was found that a modified equation expressing the logarithmic trend as a linear function of the normalized degree of saturation yielded slightly better fit:

$$\varepsilon' = \varepsilon'_{\text{equil}} - b \frac{8}{\pi^2} \exp\left(-\frac{\pi^2 D t}{4d}\right) + \frac{\overline{C^w(t)}}{C_{\text{equil}}^w} M \cdot \text{Log}(t). \quad (3.4.1)$$

In (3.4.1),  $M$  was the magnitude of the logarithmic slope (see (3.2.26)), and the normalized degree of saturation could be expressed as:

$$\frac{\overline{C^w(t)}}{C_{\text{equil}}^w} = 1 - \frac{8}{\pi^2} \exp\left(-\frac{\pi^2 D t}{4d}\right) \quad 0 \leq \frac{\overline{C^w(t)}}{C_{\text{equil}}^w} \leq 1. \quad (3.4.2)$$

The individual parameter estimates did not change significantly as a result of the modification. The measured diffusion coefficients of the different solutes are plotted as a function of the solutes' molecular weights and van der Waals volumes in Figure 3.4.2. The van der Waals volumes were calculated by the method of Bondi [62].

Solute	D, HFDA-APBP, cm <sup>2</sup> /s	D, PMDA-ODA, cm <sup>2</sup> /s
H <sub>2</sub> O	2.0E-08	3.5E-09
CH <sub>3</sub> OH	8.1E-10	2.6E-10
C <sub>2</sub> H <sub>5</sub> OH	5.5E-11	8.4E-12
CH <sub>3</sub> COCH <sub>3</sub>	1.5E-10	
CH <sub>3</sub> COOH	1.4E-11	

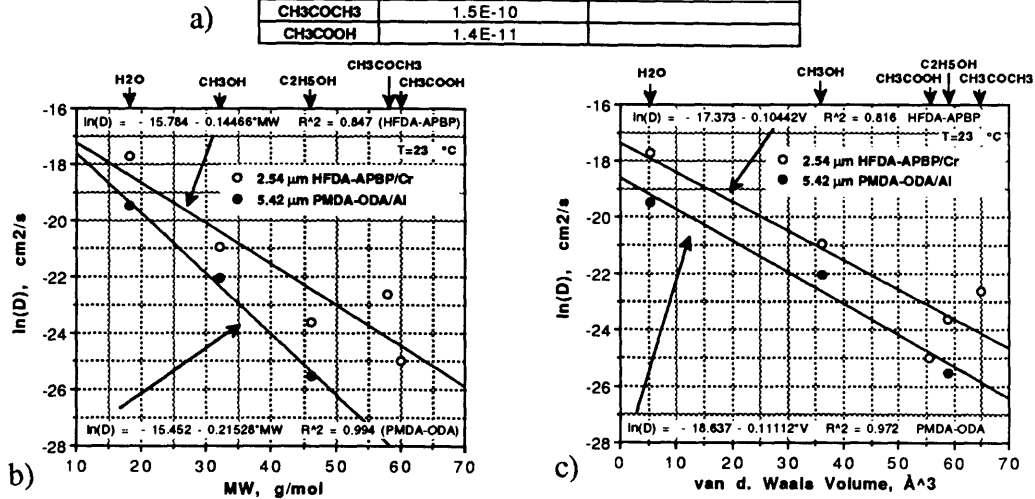


Figure 3.4.2. Diffusion coefficients of several organic solutes in PMDA-ODA and HFDA-APBP (a) as a function of the solutes' molecular weights (b) and van der Waals volumes (c).

### 3.5. Origins of the Logarithmic Trend in Dielectric Permittivity

The nature of the logarithmic trend observed in capacitance transient experiments and described in Section 3.2 was a major issue of interest. Initially, it was assumed to be the result of ionic uptake which would have enabled measurements of the Cl<sup>-</sup> and Na<sup>+</sup> diffusion coefficients in the coating. However, the results of several experiments presented in this section lead to the conclusion that the post-Fickian logarithmic increase in the relative permittivity was instead either due to water-polymer interactions of the type of hydrogen bonding, or to long-term stress relaxation processes promoted by the absorbed water.

The first experiment was already described in Section 3.2. As illustrated in Figure 3.2.10, under particular circumstances it was possible to separate the Fickian water uptake process from the logarithmic process. This could not be explained if it were assumed that ionic uptake were the reason for the logarithmic process.

Furthermore, based on the assumption of ionic uptake it follows that the absorption of ions with different radii should result in different magnitudes,  $M$  of the logarithmic slope (3.2.26). To verify this, permittivity transients were acquired on a BPDA-PDA specimen upon immersions in 0.5 M NaCl and in 0.05 M  $\text{La}(\text{NO}_3)_3$ . After the immersion in NaCl, the sample was dried for 72 hours in a dessicator and then reimmersed in the  $\text{La}(\text{NO}_3)_3$ -solution. Figure 3.5.1 shows the recorded permittivity transients.

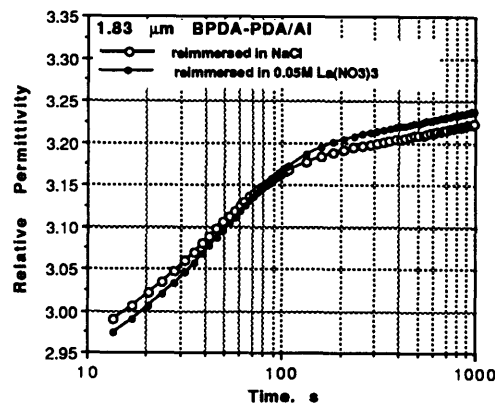


Figure 3.5.1. Permittivity transients in a BPDA-PDA/Al coating in 0.5 M NaCl and 0.05 M  $\text{La}(\text{NO}_3)_3$ .

Both the estimated diffusion coefficients as well as the magnitude of the logarithmic trends were approximately equal irrespective of the electrolyte type, suggesting that the logarithmic process was unrelated to the ionic uptake by the coating. The difference  $\Delta\epsilon = \epsilon_{\text{equil}} - \epsilon_{\text{dry}}$  was the only parameter which increased slightly following immersion in  $\text{La}(\text{NO}_3)_3$ . As illustrated by the experiments below, this increase in  $\Delta\epsilon$  was a consequence of the higher activity of water in the less concentrated  $\text{La}(\text{NO}_3)_3$  solution, resulting in a greater equilibrium water uptake by the polyimide.

The dependence of the equilibrium water uptake by the coating on the water activity in the electrolyte was investigated in a series of concentration step experiments. Figure 3.5.2 shows the response of a BPDA-PDA/Cu coating to a stepwise increase in the electrolyte concentration.



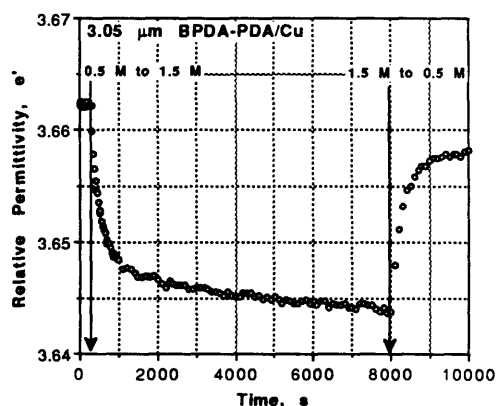


Figure 3.5.2. Permittivity transients following concentration steps in a BPDA-PDA coating on Cu.

Due to desorption of water, the permittivity of the coating decreased in response to an increase in electrolyte concentration. More importantly, as illustrated by Figure 3.5.3 a) the logarithmic slope became negative. This was a conclusive proof that the logarithmic trend did not originate in the ionic uptake by the coating, but was instead related to water.

In addition, as demonstrated in Figure 3.5.3 b), concentration step experiments could be used to determine the diffusion coefficient of water desorption from the coating.

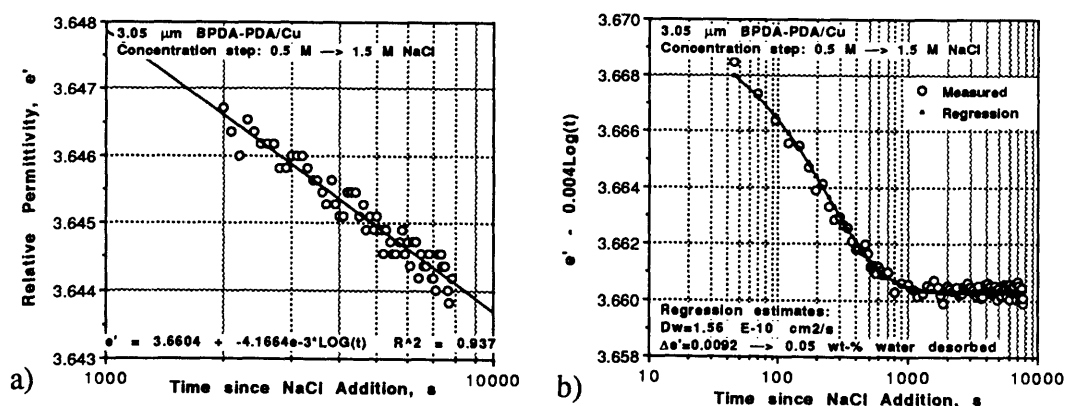


Figure 3.5.3. a) Negative logarithmic trend due to water desorption from the coating. b) Regression fit of the Fickian diffusion model to the permittivity transient yields the diffusion coefficient of water desorption and, using the b-value from Table 3.3.1, the amount of water desorbed from the coating.

The desorption of water from the coating following an increase in NaCl-concentration in the electrolyte is explained by considering that at equilibrium, the chemical potential of water in the electrolyte should be equal to that in the coating:

$$\begin{aligned} \mu_w^{el} &= \mu_w^{PI}, \quad \text{or} \\ \mu_w^{el,o} + RT \ln a_w^{el} + P \bar{V}_w^{el} &= \mu_w^{PI,o} + RT \ln a_w^{PI} + P \bar{V}_w^{PI}. \end{aligned} \quad (3.5.1)$$

If the pressure terms on both sides of equation (3.5.1) were assumed equal, concentration step experiments like the one in Figure 5.3.2 would allow the calculation of the water activity coefficient in the coating. If the activity coefficients of water are assumed constant for small changes in water concentration, it follows from (3.5.1) that the molarity of water in the electrolyte should be linearly proportional to that in the polyimide. The latter assumption was used in two multiple-concentration-step experiments to determine whether the logarithmic process was due to an additional, "post-Fickian" water uptake, or to interactions between the already absorbed water and the polymer. Figure 3.5.4 shows the permittivity transients in a BPDA-PDA/Al and a PMDA-ODA/Al coating in response to multiple concentration or dilution steps, respectively. It can be seen from the figure that the logarithmic slope was additive, i.e. its magnitude increased with each successive step away from the initial electrolyte concentration in which the coating had been equilibrated. The Fickian equilibrium values of the coating permittivity,  $\epsilon_{equil}$ , were calculated at each concentration by subtracting the compound slopes in a process similar to Boltzman superposition in viscoelasticity.

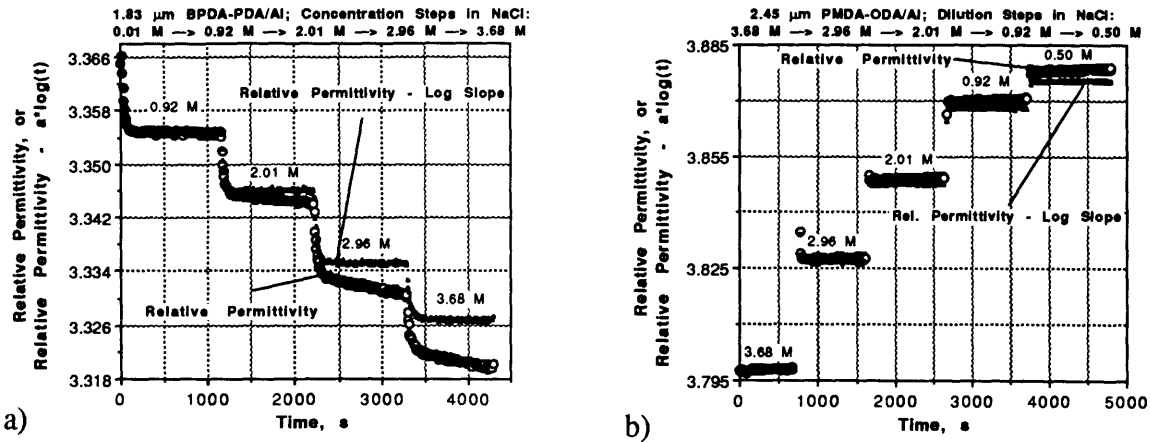


Figure 3.5.4. Permittivity transients in BPDA-PDA/Al (a) and PMDA-ODA/Al (b) in response to concentration and dilution steps in the electrolyte. The coatings had been equilibrated at the initial concentrations for more than 24 hours before the start of the experiment.

In Figure 3.5.5, the estimated equilibrium permittivity values from Figure 3.5.4 are plotted as a function of water molarity in the electrolyte.

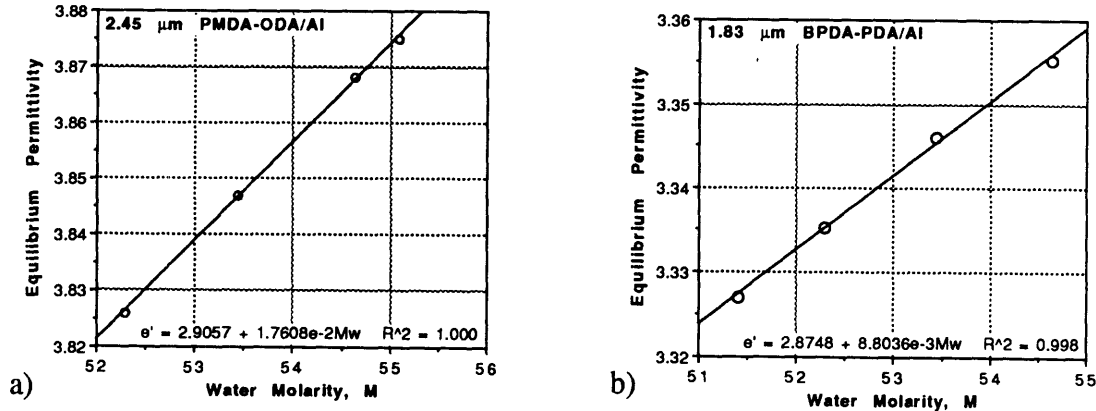


Figure 3.5.5. Permittivity values,  $\epsilon_{\text{equil}}$ , corresponding to the Fickian equilibrium water uptake of the coatings from Figure 3.5.4, as a function of water molarity in the electrolyte.

The linear relationship between the water molarity in the electrolyte and the permittivity upon achievement of the Fickian equilibrium,  $\epsilon_{\text{equil}}$ , implies that the thermodynamic equilibrium between the water concentration in the coating and in the electrolyte is completely attained through the Fickian absorption or desorption process alone. Hence, the logarithmic process did not represent an additional water uptake. Instead, possible

explanations were slow stress relaxation effects, or rearrangements and/or interactions of the already absorbed water in or with the polymer. One possible explanation for the increase in the relative permittivity was the formation of hydrogen bonds between water and polymer molecules. This hypothesis was explored further by measurements of the magnitude of the logarithmic slope as a function of temperature (Figure 3.5.6).

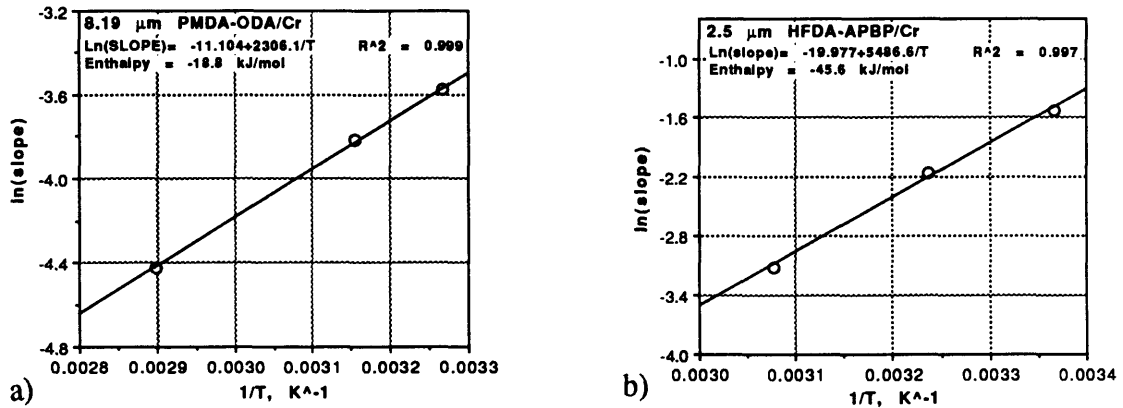


Figure 3.5.6. Enthalpy plots of the logarithmic process in HFDA-APBP (a) and PMDA-ODA (b) coatings immersed in 0.5 M NaCl.

As expected for hydrogen bonding, the process was exothermic. Moreover, the enthalpies of the logarithmic process were within the 10-50 kJ/mol range reported for hydrogen bonding in polymers [70,71]. The magnitudes of the logarithmic trends were also solute-specific, which represents further evidence of solute-polymer interactions. Typical values for  $M$  (3.2.26) in PMDA-ODA at 23 °C were 0.03, 0.17, and 0.10 for water, methanol, and ethanol, respectively, while the corresponding values in HFDA-APBP were 0.01, 0.25, and 0.11.

However, toward the end of this work it was discovered that  $M$  was also a function of the state of stress in the sample. For instance, use of clamped instead of glued cells lead to a large increase (doubling) of the logarithmic slope. Similarly, the logarithmic slope was greater in very thick coatings ( $>8 \mu\text{m}$ ). Also, the solute-specific magnitudes of the logarithmic trend reported above were in a similar relation as the amount of swelling of the coatings in the respective solute [29], a possible indication of a swelling process with first-order kinetics. Furthermore, Pan [39] has reported equilibration times for the biaxial

modulus in suspended PI2555 (BTDA-ODA/MPDA) membranes ( $\approx 7 \mu\text{m}$ ) of ca. 8 hours after a change in the relative humidity of the environment. Unfortunately, he did not document the quantitative nature of the process.

Although the above might be interpreted as evidence of long-term coating swelling and stress relaxation processes, it is contradicted by results from bending-beam studies of water diffusion which have not reported such effects [40-43]. In addition, transients acquired on free films suspended in the membrane permeation setup (Section 3.7) also exhibited logarithmic rise in permittivity, despite that the absence of residual stress and constraints on swelling in such films.

Alternatively, the post-saturation increase in the permittivity might be due to the formation of clusters by diffusion of unassociated water molecules within the polymer. Such an explanation might be able to reconcile the above experimental observations, as the bonds between associated water molecules are of hydrogen-bonding type, while the diffusion coefficient and solubility of water which affect the rate of association are likely to depend on the state of stress in the coating.

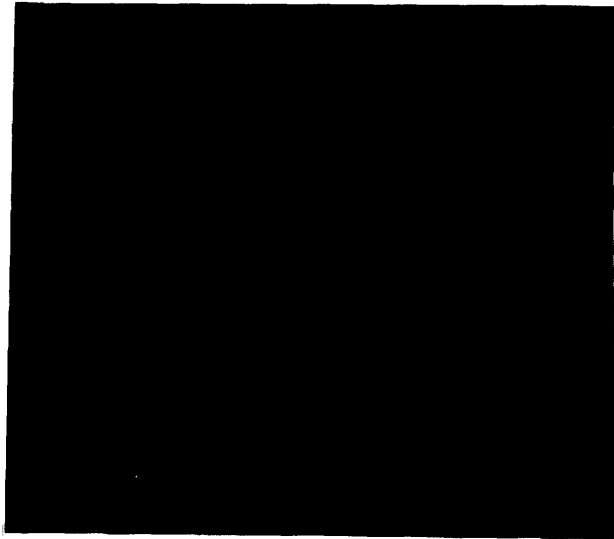
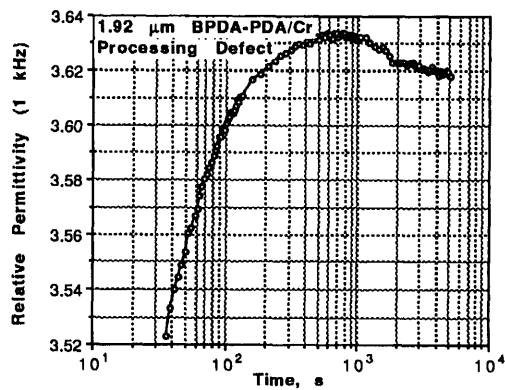
Solid state NMR and IR studies should be undertaken in order to confirm or reject the solute-polymer or solute-solute interactions hypotheses. Such analyses were not attempted in the present work.

Finally, irrespective of its exact nature, the existence of a logarithmic trend in the permittivity cast doubts about the feasibility of capacitive polyimide humidity sensors proposed by some researchers [28,50].

### **3.6. Utility of the Permittivity Transient Measurements for Defect-Detection in Coatings**

Anomalous behavior during IS or fast transient measurements was a clear indicator of a defective coating. Figure 3.6.1 b) shows a flaw found in a BPDA-PDA/Cr coating after both the permittivity transient and the subsequent impedance scan had signaled a problem

(Figure 3.6.1 a). Microscopic investigation of the sample revealed several processing defects whose relative area represented ca. 0.01 % of the sample area. The gradually downward-sloping permittivity resulted from the enlargement of the delaminated area around the manufacturing flow due to the bias during the permittivity transient measurement .



a)

b)

Figure 3.6.1. An abnormal permittivity transient in a BPDA-PDA/Cr coating indicated a defective coating (a). Microscopic examination (b) revealed several processing defects (x400) of total relative area  $\approx 0.01\%$  of the sample area.

In addition to through-the-coating defects like the one above, permittivity transients could be used to detect processing errors undetectable by other means. Figure 3.6.2 shows a comparison between a capacitance transient in a normal coating, versus one in a coating which was accidentally cured in the presence of excessive amounts of oxygen (insufficient  $N_2$  flow rate). Presumably, oxidation of the coating during cure resulted in internal porosity although there were no through-thickness pores. Comparison IR spectroscopy performed on both samples had failed to indicate a problem.

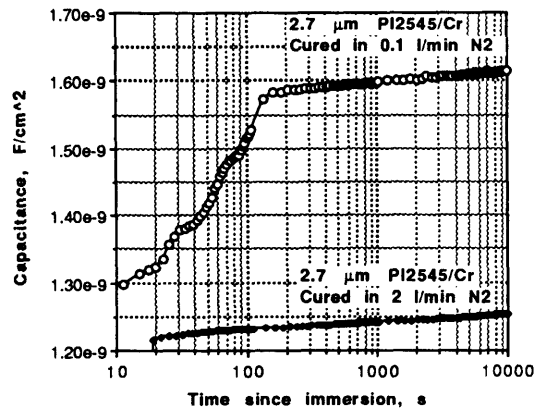


Figure 3.6.2. Capacitance transients of two PMDA-ODA/Cr coatings of similar thickness cured under different nitrogen gas-flow conditions. Too low  $N_2$  flow rate probably resulted in internal oxidation and porosity.

### 3.7. Measurements of Chloride Ion Diffusion via Membrane Permeation

Despite the recent claims of some researchers to the contrary [55], it was shown in Section 3.5 that the uptake of  $Na^+$  and  $Cl^-$  ions by the coatings was not reflected in the permittivity transients. Therefore, membrane permeation experiments were employed instead to measure the diffusion of chloride ions through the coating.

The two-compartment permeation cell is shown in Figure 3.7.1. It was similar to the one used by Doane et al. [72] in investigations of the diffusion of HF through PMDA-ODA (PI2540) membranes. The two cylindrical compartments of the cell were made of Pyrex<sup>®</sup>. Wrap-around heating mats were used in conjunction with switching thermometers. Due to the high-power heaters, the small volume of the compartments and the stirring, the temperature was easily maintained within  $\pm 0.5$  °C of the required.

The initial objective was to monitor simultaneously the concentrations of both of  $Cl^-$  and  $Na^+$  in the acceptor compartment. An Orion 94-17 solid state ion-selective electrode was employed for  $Cl^-$  detection, in combination with an Orion 90-02 double-junction reference electrode. A Fisher 13-620-501 glass-membrane  $Na^+$ -selective electrode was used for sodium detection, in conjunction with the same reference.

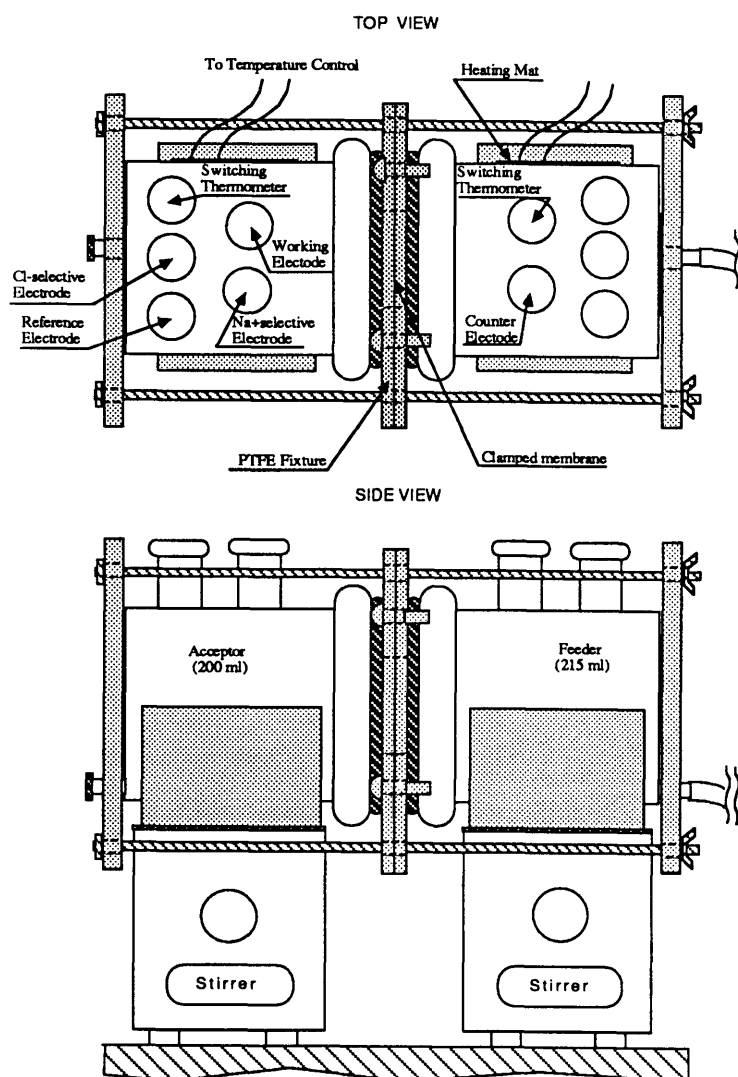


Figure 3.7.1. Two-compartment cell used for membrane permeation measurements.

The double-junction reference electrode consisted of an inner Ag/AgCl element, and an outer chamber isolating the electrolyte in the acceptor compartment from the reference element and from the AgCl-saturated KCl reference filling solution. The outer chamber of the reference electrode was filled with 0.05 M  $\text{La}(\text{NO}_3)_3$  which was equitransferent, did not interfere with neither the chloride nor the sodium ions, and had a high ionic strength,  $I_m=0.3$ . The transference numbers of the 0.05 M  $\text{La}(\text{NO}_3)_3$  were calculated from the ionic conductances at 25 °C and infinite dilution with a correction for the ionic strength [73,74] to



equal 0.487 and 0.513 for the  $\text{La}^{3+}$  and  $\text{NO}_3^-$  ions, respectively. The calculated conductivity of this electrolyte was  $0.031\Omega^{-1}\text{cm}^{-1}$  at 25 °C.

Many of the requirements toward the outer chamber filling electrolyte applied toward the cell electrolyte as well. Therefore, 0.05 M  $\text{La}(\text{NO}_3)_3$  was also used as the supporting electrolyte in the feeder and acceptor compartments.

Circular membranes ( $r=1$  cm) were prepared by etching the back of a polyimide-coated Si wafers in a PTFE jig. An etchant prepared of 6 parts hydrofluoric acid, 1 part nitric acid, and 1 part glacial acetic acid was used to etch the silicon. In the case of metallized wafers, the metal film was etched by means of an electronics grade etchant. Two circular membranes were prepared per wafer. After processing, the specimens were cleaned in DI water and stored in 0.05 M  $\text{La}(\text{NO}_3)_3$  for several days to remove eventual contamination. The wafers were cut in half and one half was clamped in the PTFE fixture between the two permeation cell compartments. The cell was filled with the supporting electrolyte and an impedance scan was performed in order to check for leaking membranes. Perfect membranes behaved capacitively (see Chapter 4). However, many of the tested membranes contained microscopic defects as a result of the manufacturing process, which appeared to have been aggravated by the membrane preparation process. In general, the preparation of defect-free samples was the main difficulty encountered in the permeation experiments. Although more than 20 wafers were prepared and etched, not a single completely defect-free membrane could be produced. Several of the samples behaved capacitively over a limited frequency range (10 Hz - 100 kHz) but even then the measured relative permittivity was 3 to 4 times greater than the nominal permittivity. According to Beilin [75], the increase in relative permittivity might be attributed to the irreversible uptake of undissociated HF during the etching process. After additional attempts with metallized wafers failed to resolve the problem, it was decided to use the pseudocapacitive samples for the measurements. Following the leak test, the good samples were left for more than 24 hours in the supporting electrolyte to equilibrate at the experimental

temperature. In a control experiment, test membranes were cut from 7.5  $\mu\text{m}$  Kapton<sup>®</sup> 30 HN (PMDA-ODA) free films supplied by DuPont Electronics. Unlike the spin-cast samples, these films behaved perfectly capacitively and exhibited dielectric properties in line with expectations.

The ion-selective electrodes were calibrated outside the permeation cell in the supporting electrolyte (0.05 M  $\text{La}(\text{NO}_3)_3$ ), at the experimental temperature and under a similar stirring rate as used in the actual experiments. A 0.05-100 ppm ionic concentration range was used in the calibrations. A programmable Keithley 617 electrometer was employed to measure the electrode potential. At 30 °C, the linear portion of the calibration curve of the chloride electrode extended down to approximately 5 ppm and that of the sodium electrode curve to only 30 ppm. The non-linear low-concentration portions of the curves were approximated by fifth-order polynomials.

Under the specific experimental conditions, the lowest measurable chloride concentration was on the order of 0.05 ppm. Unfortunately, it was discovered that the pH of the electrolyte ( $\approx 3.5$ ) was too low and interfered with the sodium ion measurements. Although it was possible to raise the pH to approximately 6.0 by addition of  $\text{La}(\text{OH})_3$ , this reduced the sensitivity of the chloride electrode. Therefore, simultaneous measurements of chloride and sodium had to be abandoned.

The magnitude of the electrode slope increased with increasing temperature. However, at higher temperatures the sensitivity of the electrodes diminished due to the increasing ionization product of water. Hence, ion concentration measurements were performed only in solutions at  $T \leq 50$  °C. The product literature gives additional details on the operation of the ion-selective electrodes [76].

Although the permeation setup of Figure 3.7.1 had been designed to allow the application of an electric field across the membrane, this option was not utilized in the present work.

At  $t=0$ , 10 000 ppm  $\text{Cl}^-$  were added to the feeder compartment. In the first several runs, chloride was added in the form of  $\text{NaCl}$ . Unfortunately, a substantial osmotic flow from the acceptor to the feeder compartment was observed, as indicated by the change in the electrolyte levels with time. According to Zaikov and others [24,77], the counterflow of water might interfere with the diffusion of chloride through the membrane and in extreme cases even prevent it entirely. In subsequent experiments, the problem was corrected by adding  $\text{Cl}^-$  to the feeder in the form of  $\text{MgCl}_2$  while in the same time adding  $\text{Mg}(\text{NO}_3)_2$  to the acceptor in order to maintain constant water molarity in both cell compartments. Alternatively,  $\text{NaCl}$  and  $\text{NaNO}_3$  were added to the feeder and acceptor, respectively.

A software program was developed to monitor and record the chloride concentration in the acceptor automatically. However, the drift of the ion-selective electrodes ( $\approx 2$  ppm/24 hours) prevented continuous measurements. Instead, the concentration was measured in time intervals of several hours and each measurement was preceded by a calibration of the electrode. Tests were performed in the 40-90 °C temperature range. During permeation tests at elevated temperatures, the permeation cell was cooled down to 40 °C before concentration measurement. A measurement, including the cool-down and the heat-up times usually lasted less 45-50 minutes.

Rigorous analysis of ion permeation measurements in the above multi-ion system is rather complicated, and experiments at different concentrations need to be performed in order to measure all the applicable parameters [24,27]. The simple analysis below ignores the charges on the ions and treats them as neutral molecules. Analyses of this type have been applied previously to electrolyte permeation [72].

The following initial and boundary conditions and assumptions applied to the permeation experiment in present setup:

- 1) Initial chloride and sodium concentrations in the membrane were assumed equal to zero as the membrane had not come in contact with neither  $\text{Na}^+$  nor  $\text{Cl}^-$  during processing.

Eventual surface contamination would have been removed during the storage of the processed wafers in 0.05 M La(NO<sub>3</sub>)<sub>3</sub>.

2) For small amounts of permeated ions, the concentrations in both the feeder and acceptor compartments could be assumed constant and equal to the initial values ( $C_A=0$  ppm,  $C_F=10000$  ppm). A more general treatment for the case of changing concentrations in the feeder and acceptor also exists in the literature [78,79].

3) The mass transport boundary layer on either side of the membrane could be ignored due to stirring, and due to the ionic diffusion coefficient in the electrolyte being much larger than the one in the membrane [72]. This assumption could also be verified by experiments with various stirring rates.

4)  $C(x=0)=C_F/K$  and  $C(x=d)=C_A \cdot K$ , where  $K$  was the distribution coefficient of chloride between the membrane and the electrolyte, involving the differences in the activity coefficients and in the standard states in the membrane and the electrolyte, an electrostatic factor, and the contribution of the swelling pressure [24,25].

5) The ionic diffusion coefficient in the membrane was assumed to be independent of the concentration.

Under the above conditions and assumptions, the non-steady state solution to the second Fick equation of diffusion for the total amount of diffusant which had passed through the membrane in time  $t$  was [80]:

$$\frac{Q_t}{K \cdot A \cdot d \cdot C_F} = \frac{D_m \cdot t}{d^2} - \frac{1}{6} - \frac{2}{\pi^2} \sum_{n=1}^{\infty} \frac{(-1)^n}{n^2} \exp\left(-\frac{D_m \cdot n^2 \cdot \pi^2 \cdot t}{d^2}\right) \quad (3.7.1)$$

where  $A$  was the membrane area,  $D_m$  the diffusion coefficient in the membrane,  $d$  the membrane thickness,  $K$  the distribution coefficient, and  $C_F$  was the diffusant's concentration in the feeder compartment. For  $t \rightarrow \infty$ , (3.7.1) approached (3.7.2):

$$\frac{Q_t}{K \cdot A \cdot d \cdot C_F} = \frac{D_m \cdot t}{d^2} - \frac{1}{6} \quad (3.7.2)$$

The plot of  $Q_t$  versus time had an intercept on the time-axis given by  $\vartheta = \frac{d^2}{6 \cdot D_m}$ , the "time-lag". Thus, the simple time-lag method could be used to determine  $D_m$ . In addition, the product  $D_m \cdot K$  could be calculated from the solution to the first Fickian equation for the steady state diffusional flux [80]:

$$J = D_m \cdot K \frac{C_F - C_A}{d} = \frac{\partial C}{\partial t} \frac{V_A}{A_m}, \quad (3.7.3)$$

where  $C_A$  was diffusant concentration in acceptor compartment. Consequently, the values of both  $K$  and  $D_m$  could be determined from (3.7.3) in combination with the time-lag.

Figure 3.7.2 a) shows the chloride concentration in the acceptor compartment as a function of time in a BPDA-PDA membrane-permeation experiment at 60 and 90 °C. As seen from the figure, the data conformed perfectly to the time-lag and steady-state analyses above. Figure 3.7.2 b) shows the activation energy plot of the chloride diffusion coefficients in spin-cast PMDA-ODA and BPDA-PDA membranes in the 50-90 °C temperature range.

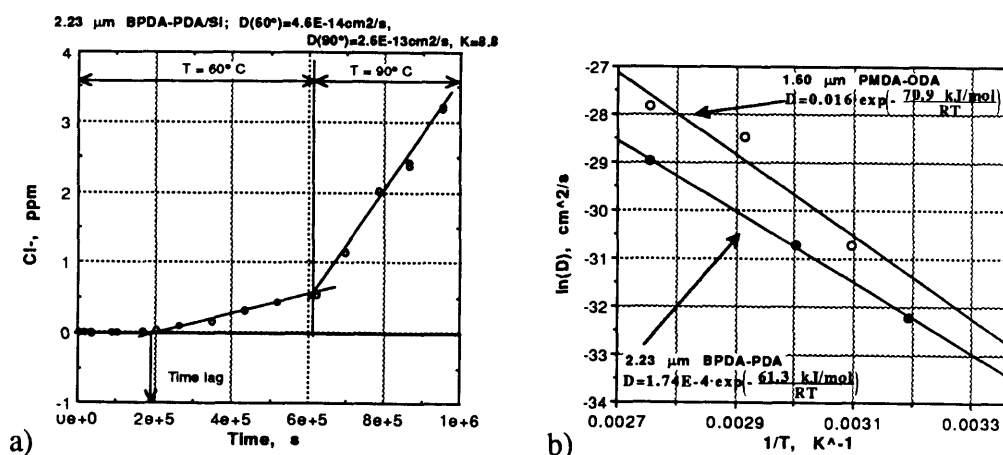


Figure 3.7.2. a) Chloride concentration in the acceptor compartment as a function of time during a BPDA-PDA membrane permeation experiment at 60 and 90 °C. All concentration measurements were performed at 40 °C. b) Activation energy plots for chloride diffusion through spin-cast PMDA-ODA and BPDA-PDA membranes.

It was mentioned previously that the spin-cast membranes did not behave completely like defect-free samples during IS tests of integrity. In order to verify the above diffusion results, permeation experiments were conducted on 7.5  $\mu\text{m}$  Kapton<sup>®</sup> 30 HN membranes which did not exhibit problems during the IS leak tests. Surprisingly, no chloride permeation could be detected through such membranes even after 8 days at 90 °C as shown in Figure 3.7.3.

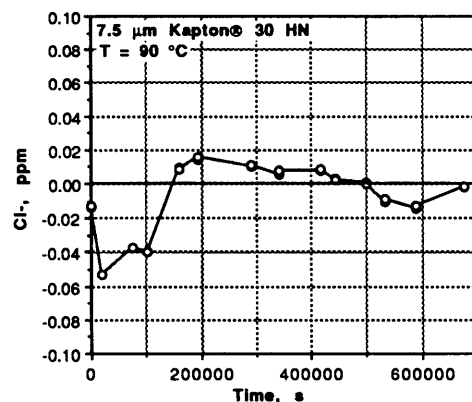


Figure 3.7.3. Permeation experiments with 7.5  $\mu\text{m}$  Kapton<sup>®</sup> HN 30 (PMDA-ODA) membranes revealed no chloride permeation even after 8 days at 90 °C.

The upper limit for the chloride diffusion coefficient in Kapton<sup>®</sup> at 90 °C was smaller than  $1 \times 10^{-13}$   $\text{cm}^2/\text{s}$ , approximately 7 times lower than the value obtained for the spin-cast PMDA-ODA sample at the same temperature. There are two possible explanations for this discrepancy:

- 1) The spin-cast membranes had defects as had been indicated by the IS measurements and the diffusion of  $\text{Cl}^-$  in defect-free coatings is actually slower than the value reported in Figure 3.7.2, or
- 2) The diffusion of  $\text{Cl}^-$  in Kapton<sup>®</sup> films was slower than in spin-cast PMDA-ODA films due to the differences in the films' morphology.

Considering that the reported water diffusion properties of Kapton® were very similar to those measured on spin-cast PMDA-ODA samples (Table 3.3.2), the second explanation is less likely. To resolve the issue conclusively, it was attempted to extend the permeation measurements over longer periods of time. Unfortunately, the PTFE fixture crept at the elevated temperature and attempts to prolong the exposure period inevitably resulted in leakage of electrolyte from the cell.

When evaluating the permeation results obtained through this simple analysis, the interdependence of the diffusion of cations and anions in the membrane arising from the charge neutrality condition has to be considered. The fact that experiments with  $Mg^{2+}$  and  $Na^+$  cations both yielded similar values for the chloride diffusion coefficient supported the assumption that the above values were indeed characteristic of the permeation of chlorides and not of the cationic species. Furthermore, from the above experiments it is safe to conclude that  $5E-15$  cm<sup>2</sup>/s is the approximate upper limit of the chloride diffusion coefficient in PI at room temperature. This contradicts the findings of Bellucci et al who have reported a much larger value, ca.  $10^{-13}$  cm<sup>2</sup>/s for the diffusion of chloride in PMDA-ODA at 30 °C [81]. The membranes' integrity had not been verified in that study. In addition, pure DI water without supporting electrolyte had been used in the acceptor compartment. This may have served to offset the ion-concentration measurements because the  $Cl^-$  and  $Na^+$ -activity coefficients may have changed as a function of ionic concentration in the acceptor.

Considering the large difference between the measured chloride and water diffusion coefficients, assumptions made by some [55] that water, sodium, and chloride diffused at the same rate in organic coatings appear completely incorrect.

Obviously, the issue of  $Cl^-$  diffusion through polyimide coatings merits further investigation since it is central to many theories regarding the role of the coating in preventing substrate corrosion.



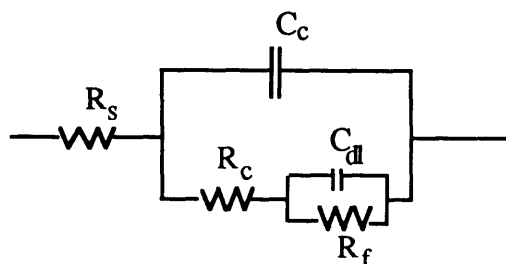


## 4. Degradation and Lifetime of Coated Substrates

This chapter presents the interpretation of the IS measurements and the results from the long-term exposure tests of the coated substrates. Section 4.1 describes the model that was used in conjunction with the CNLS numerical procedure for analysis of the IS data. The significance and applicability of the various model parameters for degradation and lifetime monitoring is discussed. In Section 4.2, the results from the long-term exposure to 0.5 M NaCl of the polyimide coatings of interest are presented. The ability of the short-term measurements to predict the coatings' long-term degradation and lifetime is discussed in Section 4.3.

### 4.1. Interpretation of Impedance Spectroscopy Data from Coated Substrates

In recent years, a large number of publications in the corrosion literature have dealt with the extraction of parameters characteristic of the degradation of coated substrates from impedance spectroscopy data [53,54,82-93]. Reviews of ca. 180 related publications before 1986 are given in [94] and [95]. Although all researchers have used essentially the same electric analog circuit model (Figure 4.1.1), they have differed considerably in their interpretations of the physical meaning of some of the circuit's parameters, as well as in their assessments of the utility of the individual parameters for monitoring the degradation of the coated samples.



$R_s$ =solution resistance;  $C_c$ =coating capacitance;  $R_c$ =coating resistance;  $C_{dl}$ =double-layer capacitance;  
 $R_f$ =charge-transfer resistance

Figure 4.1.1. The generally-accepted equivalent circuit for a polymer-coated metal [82].

The majority of the investigators have analyzed the data only graphically by quantifying certain features of the Bode plots, e.g. the "break-point frequencies",  $f_b$ , and the positions of the phase angle extrema (Figure 4.1.2).

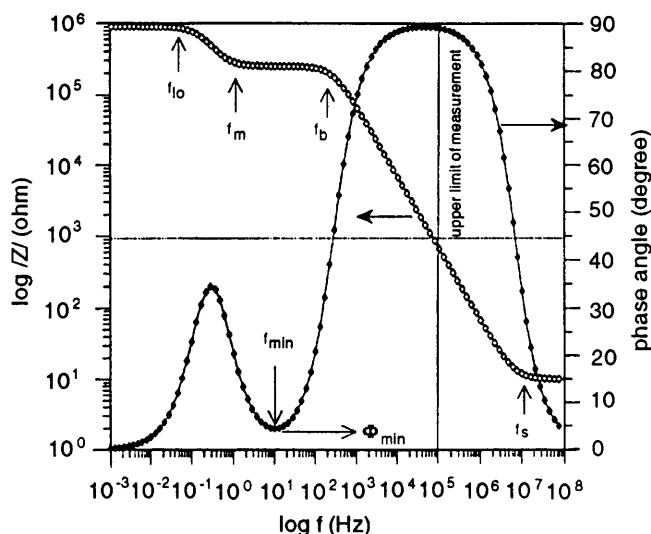


Figure 4.1.2. Characteristic features in the Bode plots of impedance data simulated by means of the coating equivalent circuit of Figure 4.1.1 [93].

Haruyama, Mansfeld and others have correlated some of the above characteristic points with the parameters of the equivalent circuit model by means of approximate relationships [53,82,86]. Among the assumptions used have been that the dielectric permittivity and resistivity of the coating remained unchanged during exposure [82,86], or that the entire change in the coatings' properties was due to the physical absorption of electrolyte and was thus reversible [89,93]. Several researchers have investigated qualitatively the evolution of the sample's impedance following the introduction of artificial defects [88,90,91]. Despite the great number of publications on the subject of coating evaluation via IS, it was impossible to find any comprehensive study of the relations between the various types of coating failure and the impedance response of the coated substrates. This could be attributed primarily to the difficulties involved in the physical characterization of the coatings in terms of manufacturing defects, as well as in terms of degradation during exposure. Furthermore, corrosion research has completely ignored the degradation of the polymer at or near the interface, even though chemical XPS and IR data have shown that it

might represent the limiting step in the failure of some polymer/metal combinations [12,96,97]. Other problems common to much of the published research include the qualitative nature of the data analysis. As demonstrated below, the graphical data analysis method promoted by many researchers [54,82,85-87,89,90,93] is not generally applicable and may be unreliable. Moreover, questionable data acquisition has been employed in some cases. For instance, rms voltage amplitudes as high as 100 mV, i.e. far above the thermal voltage at room temperature have been utilized by some, without testing for linearity of the response [93]. Finally, thermal activation has been neglected as failure-accelerating factor in long-term exposure studies resulting in extremely long experiments [54,98].

The degradation of polymer-coated metal substrates involves two distinct and parallel processes:

- 1) degradation of the bulk polymer, and
- 2) degradation of the polymer/metal interface.

The interpretation of the impedance data aimed at the quantification of the these processes will be discussed next.

A parallel -R=CPE- equivalent circuit combination in series with a resistor,  $R_s$  was found to represent the proper model for a free film or a coating during the initial stages of exposure (Section 2.2). Figure 4.1.3 a) shows the CNLS fit of the -R=CPE- model to impedance data from a 7.5  $\mu\text{m}$  Kapton<sup>®</sup> (PMDA-ODA) free film suspended in the permeation setup of Figure 3.7.1 in the initial hours after immersion. A similar fit to data from a 7.09  $\mu\text{m}$  PMDA-ODA (PI2545) coating on an Al-coated wafer is shown in Figure 4.1.3 b). Notably, the data in the two figures are very similar both qualitatively and quantitatively, despite the differences in the sample manufacturing methods, test setups, sample areas, and most importantly, despite the fact that Figure 4.1.3.a) represents a **free film**, while Figure 4.1.3.b) shows a **coating**. In both cases, the film resistances

determined from analysis of the IS data had been severely underestimated because of exceeding the validity limit of the IS setup (Section 2.2).

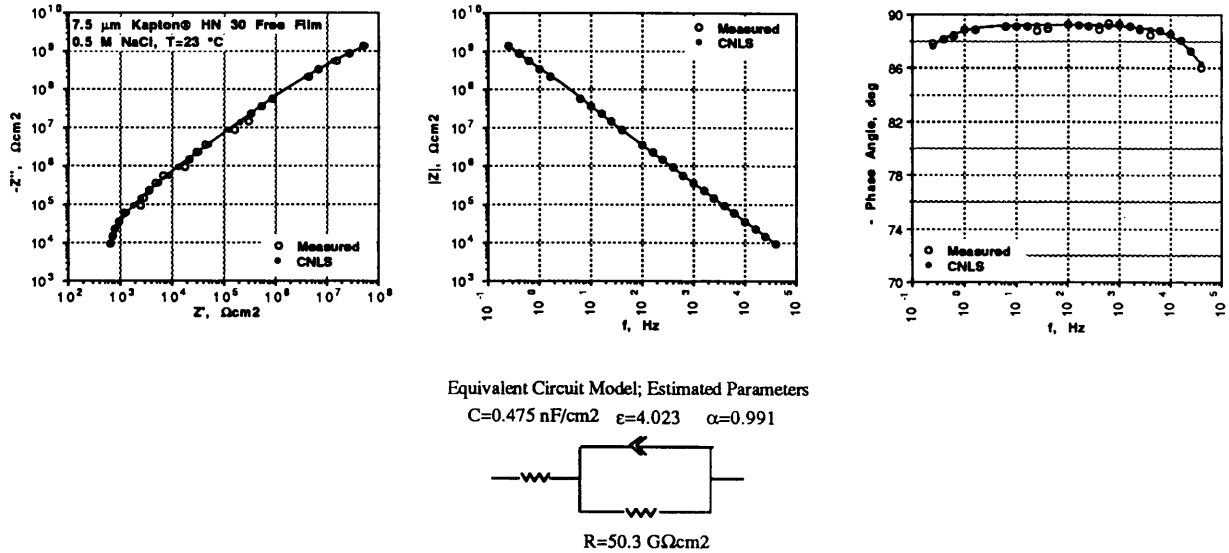
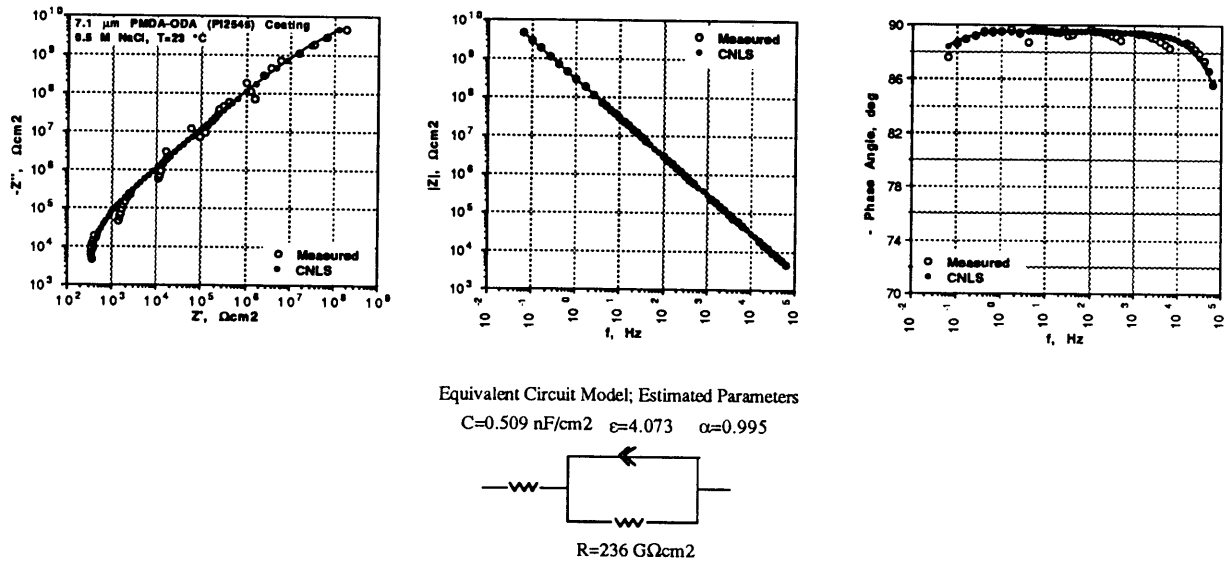


Figure 4.1.3. a) Impedance spectrum and CNLS parameter estimates for a 7.5  $\mu\text{m}$  PMDA-ODA free film suspended in 0.5 M NaCl at 23 °C.



Sample area=6.6 cm<sup>2</sup>. dc resistance (Keithley 617)  $\approx 1.15 \text{ T}\Omega\text{cm}^2$ ,  $1/\sigma \approx 1.6 \times 10^{15} \Omega\text{cm}$ . Note: the sawteeth pattern visible in the complex plane and Bode-angle plots was an artifact of the IS setup (PAR 273 current measurement) and did not represent actual physical effects. It was absent from Figure 4.1.3.a) due to the larger sample area (lower impedance) in that case.

Figure 4.1.3. b) Impedance spectrum and CNLS parameter estimates for a 7.09  $\mu\text{m}$  PMDA-ODA/Al (PI2545) coating in 0.5 M NaCl at 23 °C.

In the equivalent circuit of Figure 4.1.3 the solution resistance,  $R_s$  represented the combined resistances of the electrolyte, contacts and, in the case of thin film-coated samples, the metal film. The capacitance of the electrolyte,  $C_{el} = \tau_{el}/R_{el}$ , where  $\tau_{el}$  is the electrolyte's time constant was not included in the figure as it only appeared at frequencies above 100 kHz. The  $\llcorner$  - symbol in the equivalent circuit of Figure 4.1.3 represented a constant phase element which, as discussed in Section 2.2, was necessary to model the frequency dispersion in the electrical properties of the polyimide. The coating CPE in Figure 4.1.3, or the coating capacitance,  $C_C$  in the idealized circuit of Figure 4.1.1 were directly proportional to the relative permittivity,  $\epsilon'$  of the polymer (3.2.3).

The reversible increase in  $\epsilon'$  due to the uptake of water was the basis for Chapter 3. However, in contrast with the usual assumption in the corrosion literature, a significant part of the dielectric permittivity increase during environmental exposure was irreversible. This is illustrated in Figure 4.1.4 in which two permittivity transients obtained from the same 3.89  $\mu\text{m}$  PMDA-ODA/Cr coating and under same conditions are superimposed. After the initial permittivity transient measurement, the coating had been immersed for 16 days in 0.5 M NaCl at 60 °C. Although the exposure had been followed by drying in a dessicator for 10 days, the second permittivity transient registered a substantially higher coating permittivity.

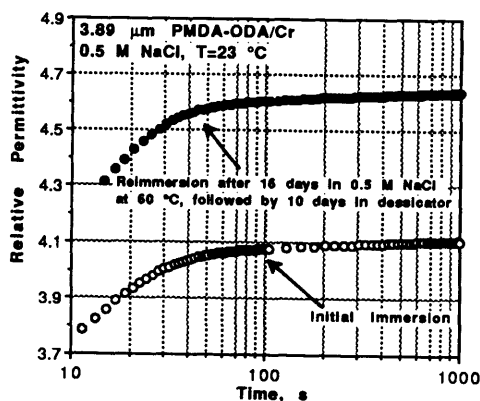


Figure 4.1.4. Comparison between a permittivity transient acquired upon initial immersion in 0.5 M NaCl and a second transient acquired on the same coating after 16 days of exposure to 0.5 M NaCl at 60 °C followed by 10 days drying in a dessicator.

Bellucci et al have suggested that the increase in the dielectric constant during long-term exposure to NaCl-electrolyte was the result of  $\text{Na}^+$  and  $\text{Cl}^-$ -absorption by the coating [51]. This hypothesis was tested by exposing a free film to 0.5 M NaCl for 75 hours, after which the electrolyte was replaced with deionized (DI) water. Contrary to Bellucci's predictions, the increasing trend in the evolution of the dielectric permittivity was preserved (Figure 4.1.5 a). Likewise, the exposure to DI water did not reverse the decreasing trend in the isochronal resistivity (Figure 4.1.5 b).

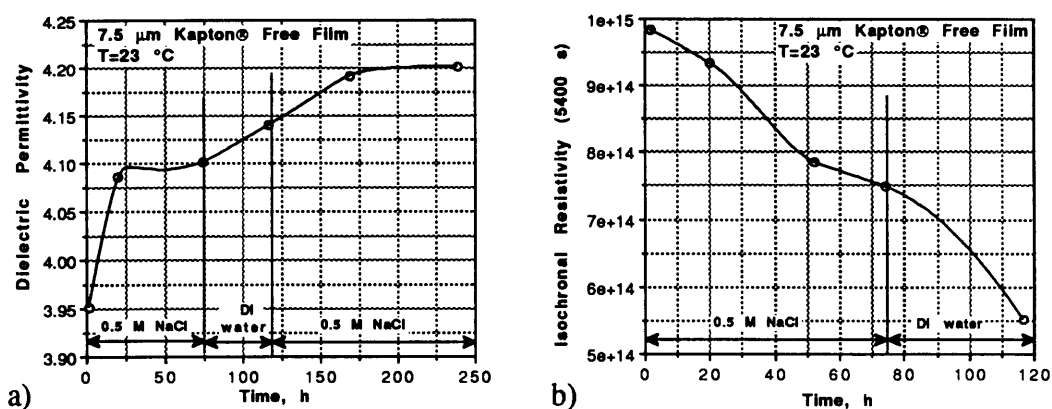


Figure 4.1.5. a) Increasing dielectric permittivity of free Kapton® film during exposure to 0.5 M NaCl or DI water at 23 °C. b) Isochronal resistivity (5400 s) of the same film as a function of exposure time. Specified film resistivity at 0% RH, 23 °C  $\approx 1.5 \times 10^{17} \Omega\text{cm}$ .

Instead of ionic uptake, the irreversible increase in permittivity during exposure was attributed to the generation of polar entities in the polymer, as a consequence of polyimide degradation processes such as imide breakdown. Hence, monitoring the evolution of the dielectric permittivity of the coating could be used to quantify the rate of degradation of the polymer during exposure. The rate of decrease of the CPE parameter  $\alpha$ , corresponding to a broadening in the distribution of relaxation times [13] and of the coating resistivity represented alternative measures of the rate of coating degradation.

The model of the bare metal/electrolyte interface was discussed in Section 2.2. In order to estimate the values of the model parameters (Figure 2.2.7), impedance spectra were acquired on metallized wafers without polymer coatings. Metal deposition was conducted

under normal conditions (Section 2.1), and the samples underwent the usual cure cycle together with regular polyimide-coated samples and were desiccated in air before testing. As determined via Auger spectroscopy, the resultant surface metal oxide layer was slightly thinner than that under polyimide coatings, due to interfacial reactions between the metal and the polyamic acid, and the evolution of water from the polymer in the latter case [12]. Figures 4.1.6 and 4.1.7 show the impedance spectra, CNLS fits, and estimated model parameters for bare Cr and Pt-coated wafers in 0.5 M NaCl at 23 °C.

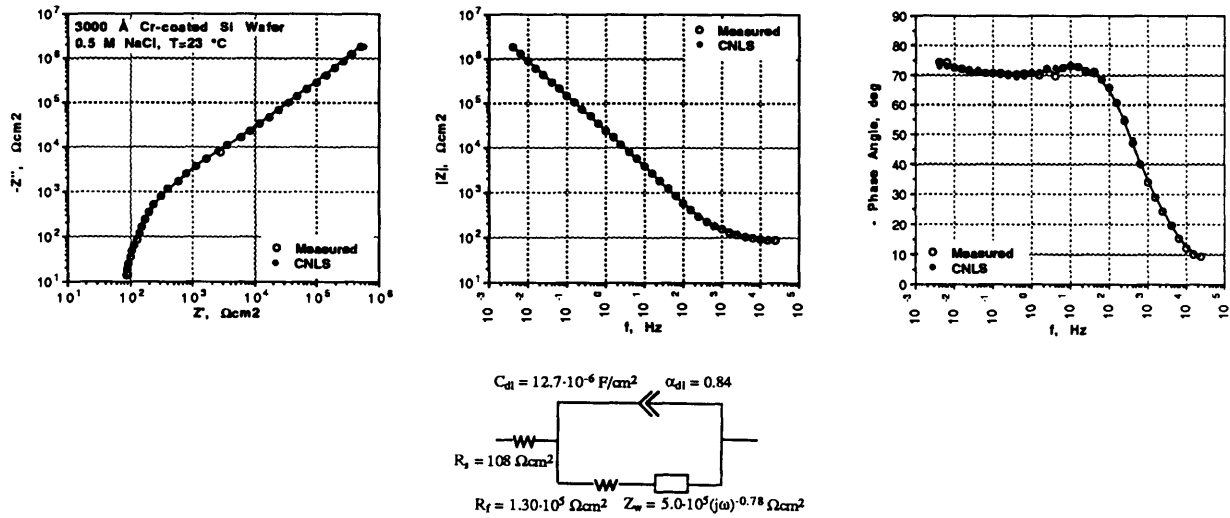


Figure 4.1.6. Impedance spectrum, CNLS fit, and estimated metal film/electrolyte interface parameters of a Cr-coated Si wafer without a polymer coating.

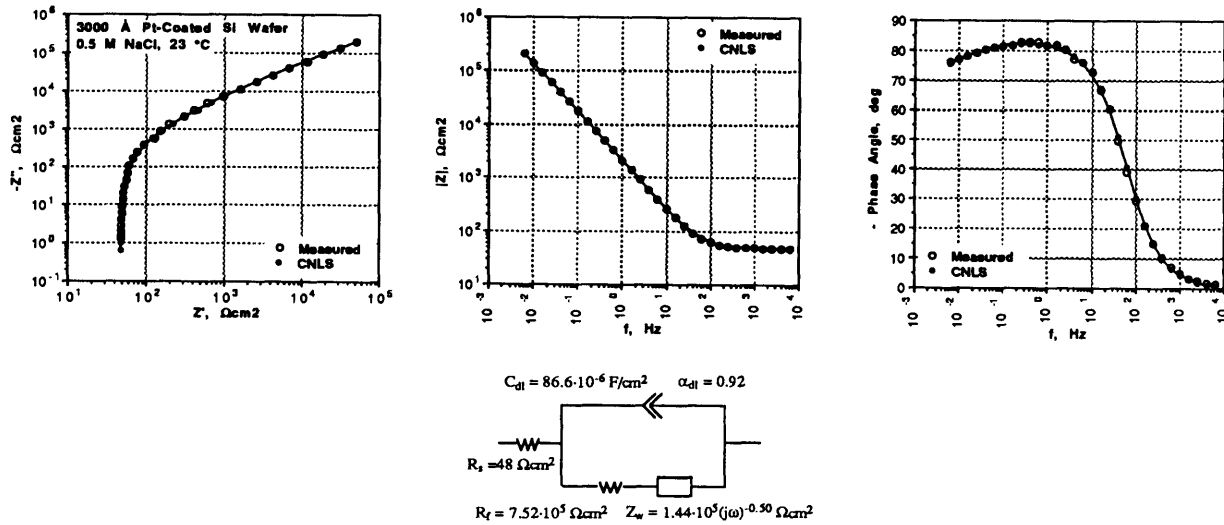


Figure 4.1.7. Impedance spectrum, CNLS fit, and estimated metal film/electrolyte interface parameters of a Pt-coated Si wafer without a polymer coating.

Analysis of IS data from several bare samples under the experimental conditions of Figures 4.1.6 and 4.1.7 revealed variations in the parameter estimates of ca. 25% around the mean with the double-layer capacitance exhibiting the narrowest range of estimates ( $\pm 10\%$ ). Because the conditions at the interface in areas of coating delamination and porosity are not generally known and vary during exposure, quantification of the degradation at the interface would require the use of interfacial parameters whose specific values are relatively insensitive to changes in local conditions. In order to evaluate the stability of the model parameters, several experiments with variations in the aeration, NaCl concentration, and surface oxidation conditions were conducted on a bare Cr-coated sample. Table 4.1.1 summarizes the response of the parameters of the equivalent circuit of the bare interface to the changes in test conditions.

Test Condition	CPE <sub>dl</sub>	R <sub>f</sub>	CPE <sub>w</sub>
<b>0.5 M NaCl, normal</b>	C <sub>dl</sub> =13.1 $\mu\text{F}/\text{cm}^2$ (0.84)	0.13 $\text{M}\Omega\text{cm}^2$	0.5 $\text{M}\Omega\text{cm}^2$ (0.78)
<b>0.5 M NaCl, deaerated</b>	C <sub>dl</sub> =8.8 $\mu\text{F}/\text{cm}^2$ (0.84)	0.11 $\text{M}\Omega\text{cm}^2$	0.4 $\text{M}\Omega\text{cm}^2$ (0.81)
<b>0.5 M NaCl, aerated</b>	C <sub>dl</sub> =8.1 $\mu\text{F}/\text{cm}^2$ (0.84)	0.15 $\text{M}\Omega\text{cm}^2$	0.4 $\text{M}\Omega\text{cm}^2$ (0.76)
<b>0.1 M NaCl, normal</b>	C <sub>dl</sub> =12.9 $\mu\text{F}/\text{cm}^2$ (0.84)	0.25 $\text{M}\Omega\text{cm}^2$	25.1 $\text{M}\Omega\text{cm}^2$ (0.76)
<b>0.5 M NaCl, normal, ox.</b>	C <sub>dl</sub> =12.4 $\mu\text{F}/\text{cm}^2$ (0.85)	0.93 $\text{M}\Omega\text{cm}^2$	1.9 $\text{M}\Omega\text{cm}^2$ (0.71)

Table 4.1.1. Estimated parameters of the equivalent circuit model of the bare Cr/ electrolyte interface as a function of test conditions (quiescent electrolyte).

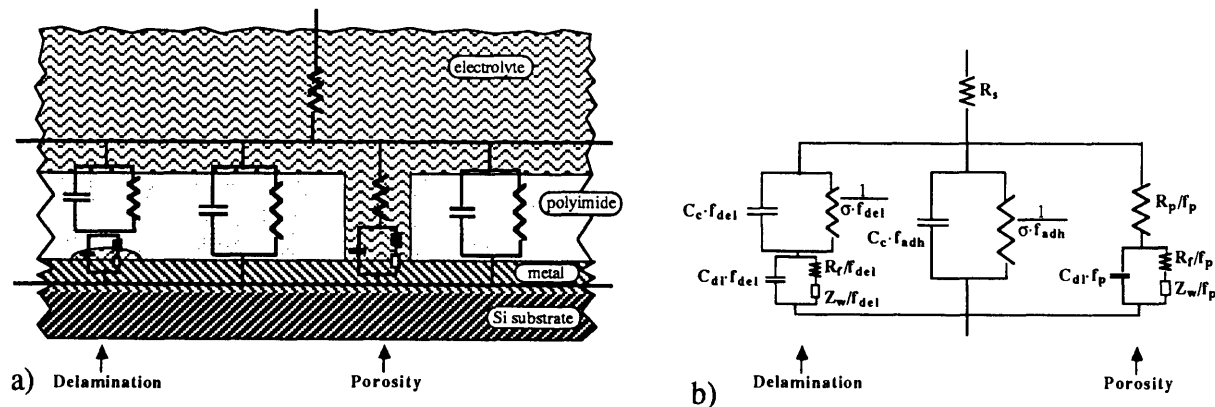
In the above table, the term "normal" referred to the electrolyte as it was employed in the long term exposure studies, i.e. without additional aeration or deaeration. The electrolyte in all samples was changed on weekly basis, providing fairly constant aeration conditions in the cells.

In general, the estimated values for  $C_{dl}$  were in good agreement with the nominal value of ca. 20  $\mu\text{F}/\text{cm}^2$  estimated by Bard and Faulkner for a typical metal/electrolyte interface [14]. Both aeration (using technical air), and deaeration (with nitrogen gas) lead to a significant decrease in the double-layer capacitance which might be attributed to physisorption of nitrogen gas molecules at the metal/electrolyte interface [14]. The charge-transfer resistance was affected strongest by the oxidation state of the metal surface, increasing sharply due to



oxidation of the metal film (the last row in Table 4.1.1 contained data acquired after the sample had been left for 48 hours in "normal" 0.5 M NaCl at 60 °C). In Table 4.1.1, the parameters of the generalized infinite length Warburg CPE corresponded to the modulus and exponent (in brackets) in equation (2.2.10). The NaCl- concentration and the metal oxidation significantly affected the Warburg impedance on bare samples. Moreover, during degradation of coated samples the change in the mass-transfer impedance might be highly nonlinear. Also, as discussed in Section 2.2, the charge-transfer resistance and Warburg impedance often exceeded the validity limit of the IS setup in moderately-degraded coated samples, therefore their CNLS estimates in general were less accurate than that of  $C_{dl}$ . The above, plus their dependence on the local NaCl-concentration, made  $R_f$  and  $Z_w$  unlikely candidates for indicators of the exposed interfacial area in coated samples. Of the three parameters characteristic of the bare interface, only the double-layer capacitance was likely to be of utility as a quantitative measure of the degradation of the interface.

In accordance with the preceding discussion of the polymer film and of the metal/electrolyte interface, the general equivalent circuit model of the (defective) coated sample was assembled in Figure 4.1.8.



$R_s$  = solution resistance,  $C_c$  = coating capacitance,  $\sigma$  = coating conductance,  $R_p$  = pore resistance,  $C_{dl}$  = double-layer capacitance,  $R_f$  = charge-transfer resistance,  $Z_w$  = generalized Warburg impedance,  $f_{adh}$  = fraction of defect-free, adhered, pore-free coated area,  $f_p$  = fraction of interfacial area exposed through pores in the coating,  $f_{del}$  = fraction of delaminated coated area (no direct connection to bulk electrolyte) ( $f_{adh} + f_p + f_{del} = 1$ ). All parameters per  $\text{cm}^2$  of specimen area.

Figure 4.1.8. Equivalent circuit model of a protective coating exhibiting delamination and porosity over a non-blocking electrode.

In recent years, many researchers have argued that delaminated regions (without a direct connection to the electrolyte) of organic coatings on steel and other metals could be detected by means of impedance spectroscopy [e.g. 82,86,93,98]. They have modeled such regions incorrectly by means of the equivalent circuit branch attributed in Figure 4.1.8 to pores, or have estimated the underfilm delaminated area from the "break-point frequency" and other characteristic features of the Bode-angle plot (Figure 4.1.2). It was shown already in Figure 4.1.3 that there were no qualitative differences between the impedance spectra of a coated sample ( $\approx 0\%$  delamination) and of a free film (100% delamination). Such results can be explained when the correct circuit branch (marked "Delamination") in Figure 4.1.8 is used to model delamination. Impedance spectra for a typical  $3\ \mu\text{m}$  pore-free coating with a dielectric permittivity  $\epsilon'=3$ , resistivity of  $10^{15}\ \Omega\text{cm}$ , and varying degrees of delamination were simulated by means of the corresponding equivalent circuit branch in Figure 4.1.8. The results for 0%, 50%, and 100% delamination are compared in Figure 4.1.9. The area-specific interfacial parameters were assumed equal to those of the bare Cr interface (Figure 4.1.6).

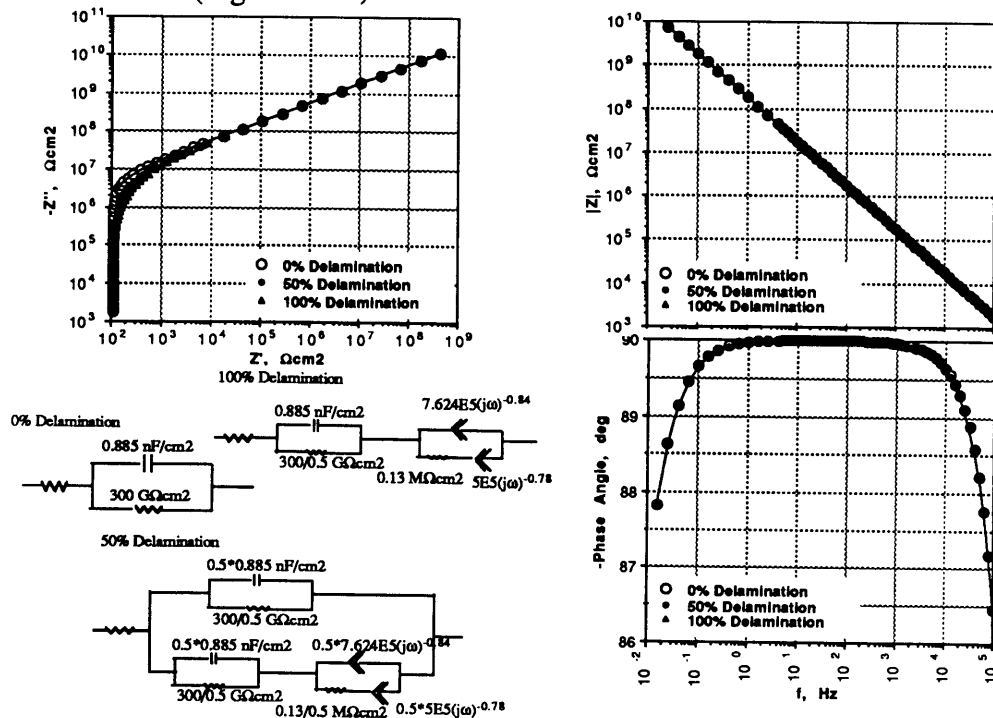


Figure 4.1.9. Simulated impedance spectra for a  $3\ \mu\text{m}$  pore-free coating with three different degrees of delamination.

The only difference between the three extremes of delamination was visible in the complex plane plot, in the high-frequency part of the real component of the impedance. However, the measured real impedance component carried an error well above the accuracy needed to detect such small differences. Absolutely no effects of delamination could be seen in the Bode plots. Therefore, even extreme degrees of delamination at the polymer/metal interface won't be detectable by impedance measurements as long as there is no direct connection between the electrolyte and the interface.

This was substantiated further by the results from the long-term exposure of polyimide/Al samples in which delamination was visible due to the black  $\text{Al}(\text{OH})_3$  formed at the interface (the composition of the black phase was verified by XPS). Impedance spectra from a  $1.35 \mu\text{m}$  HFDA-APBP/Al coating several hours after immersion and after 100 days in 0.5 M NaCl at 23 °C are superimposed in Figure 4.1.10. As illustrated by the photograph, after 100 days of exposure the coating had delaminated over a large area. Yet, the impedance spectra did not show any significant changes.

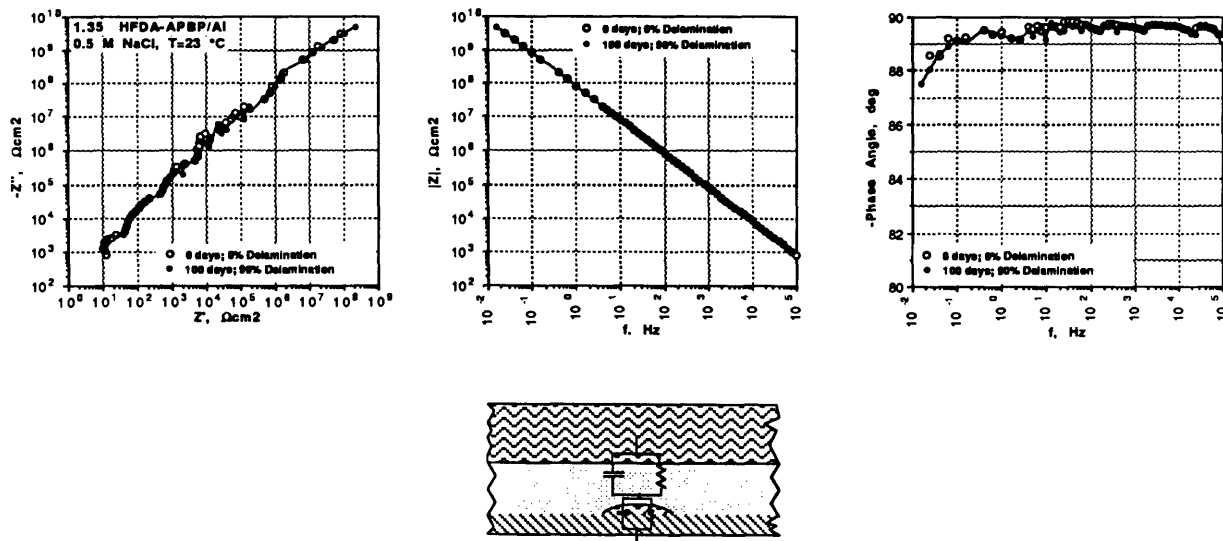


Figure 4.1.10. a) IS spectra of a  $1.35 \mu\text{m}$  HFDA-APBP/Al coating several hours and 100 days after immersion in 0.5 M NaCl at 23 °C.



Figure 4.1.10. b) Photograph (x100) of a region of the coating after the 100-day exposure. The light islands (Al) represent adhered areas. The surrounding black areas (Al(OH)<sub>3</sub>) represent delamination.

However, establishing a direct connection between the interface and the electrolyte by piercing a pore ( $\approx 0.01$  mm diameter) in the coating above a delaminated region caused the impedance data to show massive failure (Figure 4.1.11).

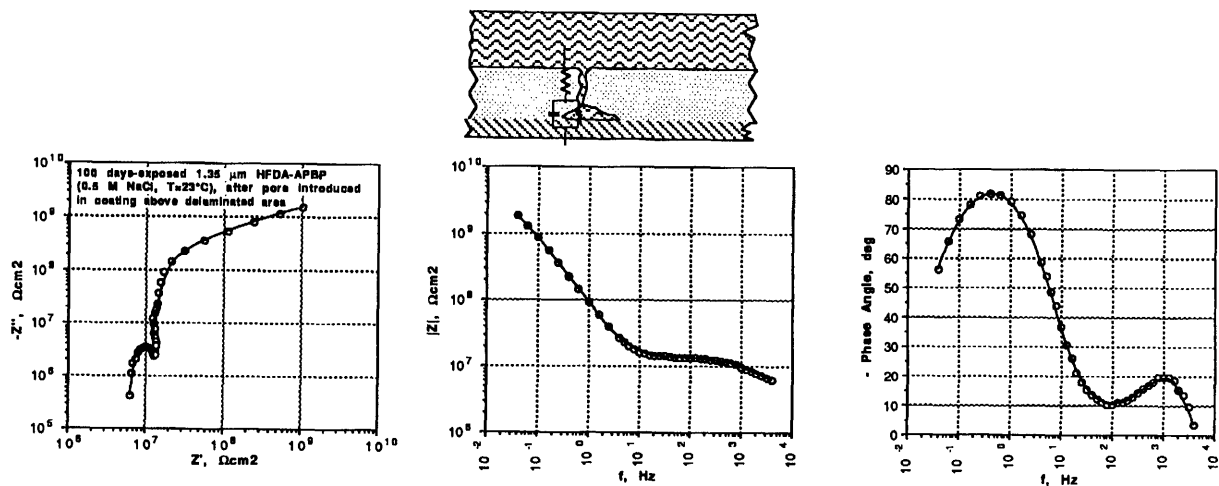


Figure 4.1.11. IS spectrum of the 100-days exposed 1.35  $\mu\text{m}$  HFDA-APBP/Al coating of Figure 4.1.10 1/2 hour after a small pore had been introduced in the coating above a delaminated region.

Acknowledging the inability of IS to detect delamination, the model of Figure 4.1.8 was simplified by ignoring delaminated areas. The resultant model (Figure 4.1.12) was very similar to the one in Figure 4.1.1 but more general, and with different interpretation of some of the parameters. The coating and double-layer capacitances had been replaced by constant phase elements as discussed previously.

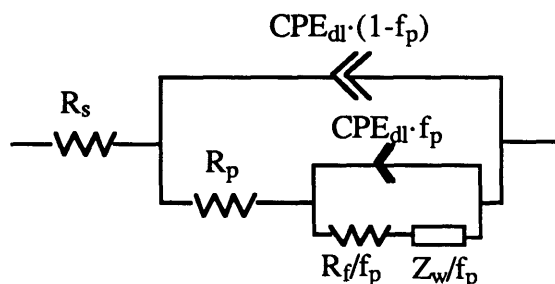


Figure 4.1.12. Simplified equivalent circuit model of the coated sample used for IS data analysis.

In Figure 4.1.12,  $f_p$  represented the fraction of exposed interfacial area which might be greater than the area directly under pores, due to the delamination of the coating at the pore edges. The above equivalent circuit was used as the model in the CNLS regression analysis of the long-term exposure data. Within the experimental frequency range (10 mHz - 100 kHz), the circuit modeled satisfactory all coatings, on all substrates, at all stages of degradation. Figure 4.1.13 illustrates the regression quality for a fit of the equivalent circuit to the impedance spectrum of a 4.76  $\mu\text{m}$  BTDA-ODA/MPDA coating on Cr after 7 days of exposure to 0.5 M NaCl at 60 °C.

CNLS analysis showed that the generalized Warburg impedance appeared only in coatings which had suffered major damage. For coatings with moderate damage, the Warburg appeared at very low frequencies, or not at all.

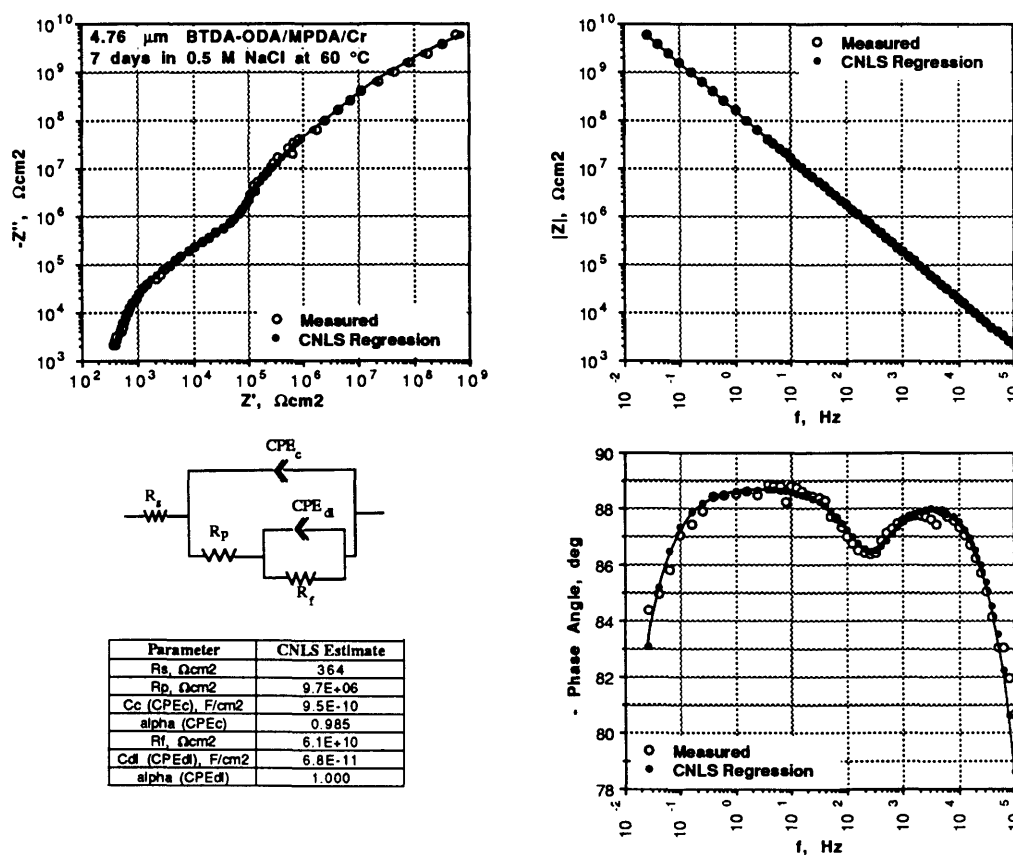


Figure 4.1.13. CNLS regression to impedance data from a 4.76  $\mu\text{m}$  BTDA-ODA/MPDA coating on Cr after 7 days of exposure to 0.5 M NaCl at 60  $^\circ\text{C}$ .

As discussed previously, experiments with bare metallized substrates had indicated that the double-layer capacitance would be the only interface-specific parameter which could be used to quantify the exposed interfacial area. To verify the applicability of  $C_{dl}$ , artificial defects (pinhole or scratch) were introduced in several coatings. In each case, the area of the defect was measured microscopically. Figure 4.1.14 a) shows Bode-angle plots of a 1.95  $\mu\text{m}$  BPDA-PDA/Cr coating before and after the introduction of a 0.0009  $\text{cm}^2$  pinhole. Also illustrated in the figure is the regression fit (using the model of Figure 4.1.12) to the impedance spectrum acquired 14 hours after defect introduction. The CNLS parameter estimates for IS data acquired 0.5 h and 14 h after defect introduction are compared in Figure 4.1.14 b). Both  $R_p$  and  $R_f$  changed substantially between the two scans while  $C_{dl}$

remained approximately constant. However, the absolute estimate for  $C_{dl}$  was  $\approx 1.77$  nF yielding a specific value of ca.  $2 \mu\text{F}$  per  $\text{cm}^2$  of exposed Cr/electrolyte interface, i.e. several times smaller than the value determined on bare, uncoated substrates with Cr metallization (Figure 4.1.6). The corresponding value for the Al-interface was determined from similar experiments to be ca.  $0.5 \mu\text{F}/\text{cm}^2$ .

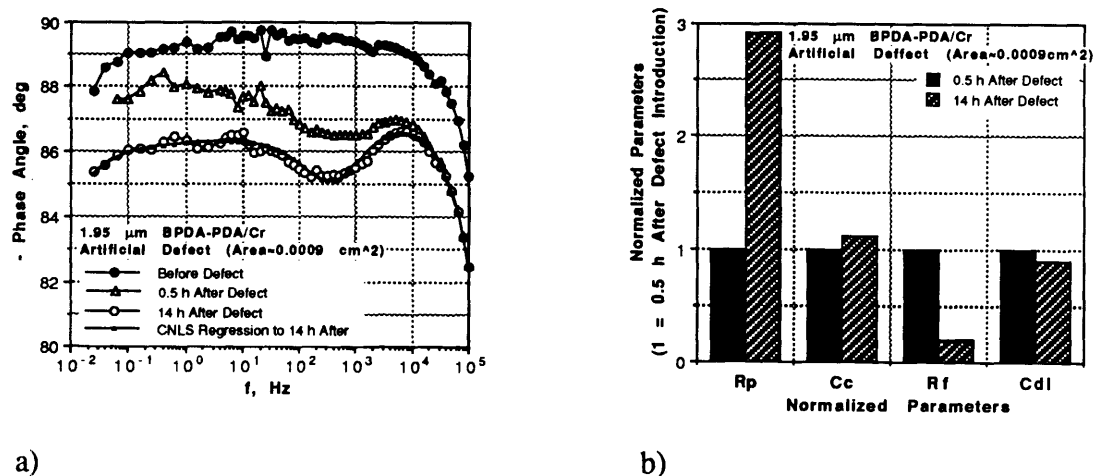


Figure 4.1.14. a) Bode-Angle plot of IS data from a  $1.95 \mu\text{m}$  BPDA-PDA/Cr coating exposed to  $0.5 \text{ M}$  NaCl at  $23 \text{ }^\circ\text{C}$ , before and after the introduction of an artificial defect. b) Evolution of the CNLS parameter estimates at  $0.5 \text{ h}$  and  $14 \text{ h}$  after defect introduction. The parameter estimates were normalized with respect to their values at  $0.5 \text{ h}$  after defect introduction.

The smaller than expected specific capacitance was attributed to modifications (oxide-growth) of the metal film surface as a result of chemical reactions with the polyimide during processing [12]. Subsequently, these values were confirmed for several samples, in which the scratched area was incrementally increased between impedance scans. The results are presented in Figure 4.1.15. The estimates of  $R_f$  shown in the figure did not correlate with the amount of exposed area due to exceeding the validity limit of the IS setup.

The linear relationship between  $C_{dl}$  and the defect area confirmed that  $C_{dl}$  was proportional to the amount of exposed interface, but showed that only semi-quantitative measurements of the exposed area would be possible, due to the variation in the specific  $C_{dl}$ -values among samples. In addition, like  $R_f$  the measurable  $C_{dl}$  was limited by the input capacitance of the

potentiostat to  $\geq 200$  pF. This, assuming  $C_{dl}=2 \mu\text{F}/\text{cm}^2$  translated into a minimum detectable exposed area of  $0.0001 \text{ cm}^2$ , an extremely large value by microelectronic standards.

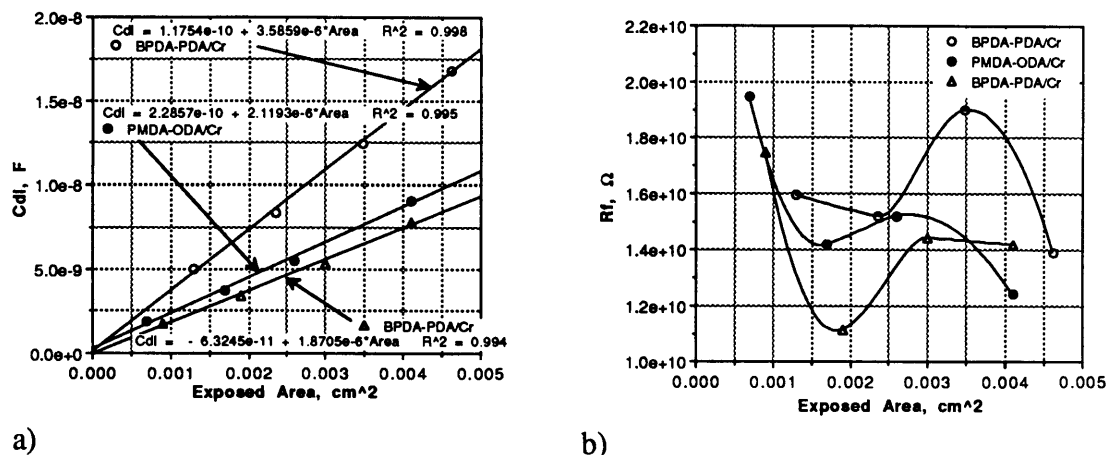


Figure 4.1.15. CNLS estimates of  $C_{dl}$  (a) and  $R_f$  (b) as a function of exposed (scratched) area. In each case, the IS scan was performed in  $0.5 \text{ M NaCl}$  at  $23^\circ\text{C}$ , ca. 3 h after introduction of the defect.

In order to determine the sensitivity of  $C_{dl}$  to the presence of oxides, the double-layer capacitances of a defective area were compared prior to, and following oxidation. Figure 4.1.16 shows an extreme case of oxidation in which the defective (scratched) sample (a) was subjected to a 100 s of anodic bias at  $+1.00 \text{ V}$  above the sample's open-circuit potential (OCP). Due to the formation of an oxide layer (b), the estimate of  $C_{dl}$  changed dramatically (c), incorrectly indicating a reduction in the exposed area.

All IS measurements in this study were conducted at the OCP of the sample and the above extreme situation did not apply. However, the above results show clearly that coating evaluation via IS measurements in the field may produce large errors. In general, except under strictly controlled conditions, the need to make assumptions about the specific values of the interfacial parameters would prevent accurate estimates of exposed area.



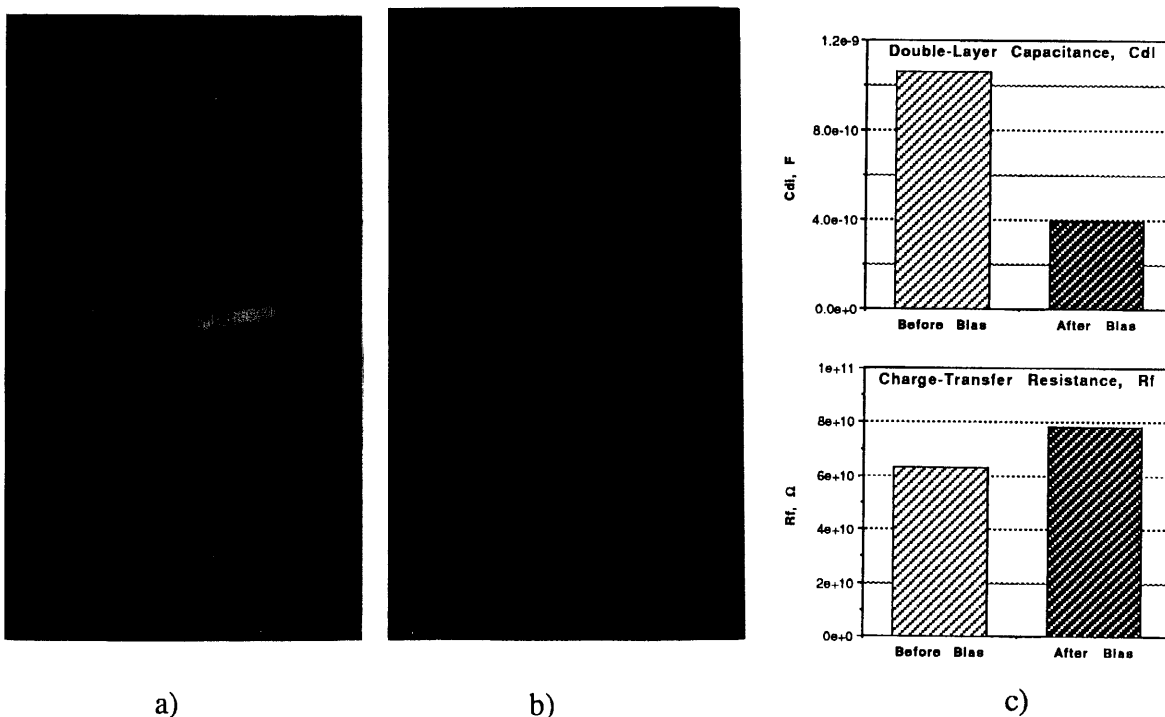


Figure 4.1.16. a) Exposed area in PMDA-ODA/Cr prior to anodic bias (x32).  
 b) Same area after 100 s of anodic bias at +1 V vs. OCP (x32).  
 c) Change in the CNLS estimates of  $C_{dl}$  and  $R_f$  as a result of anodic bias.

Finally, the preceding results exposed the limitations of the commonly used graphical analysis method. Almost none of the above impedance spectra exhibited a "break-point frequency" as defined in Figure 4.1.2, in spite of the presence of defects. Moreover, some spectra of clearly degraded samples did not show phase-angle minima or separation of the time constants (Figure 4.1.17), even though the data conformed perfectly to the model of Figure 4.1.12. Obviously, quantitative analysis of such data was only possible by numerical means. Thus, the graphical analysis method employed and promoted by many researchers in the field of corrosion is not generally applicable and should be regarded with skepticism.

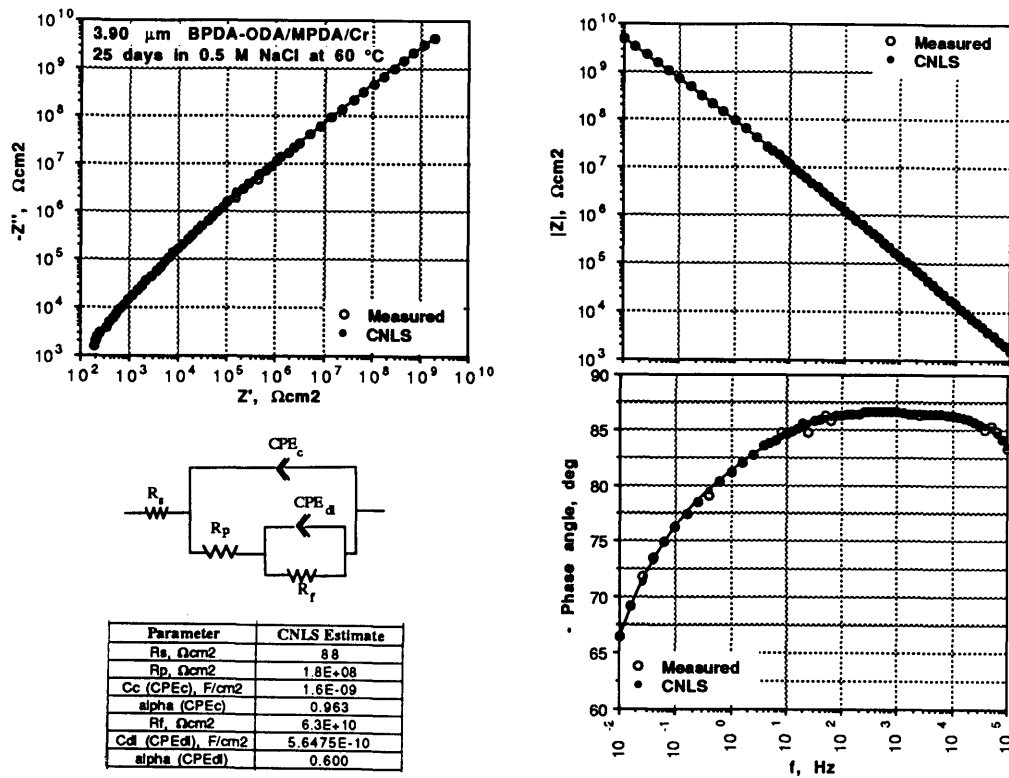


Figure 4.1.17. Impedance spectrum and CNLS parameter estimates of a BTDA-ODA/MPDA coating on Cr after 25 days in 0.5 M NaCl at 60 °C.

In addition, this section has highlighted the many problems that exist with any quantitative interpretation of impedance data from coated substrates. In general, the relatively poor sensitivity, as well as the lack of precise knowledge of the instantaneous values of the interfacial parameters may restrict the applicability of IS for detection and quantification of coating defects and degradation, and ultimately for lifetime prediction in the field.

However, IS may be used in laboratory conditions to quantify the rates of degradation of coated substrates and may thus represent a valuable tool in coatings research. The results from the evaluation, by means of IS, of the coating/metal systems of interest in this work are presented in the next section. IS was also used to evaluate the effect of processing on the coatings and the results of that study are presented in Chapter 5.

## 4.2. Results of Long-Term Exposure to 0.5 M NaCl

The typical evolution of the impedance spectra of the tested samples during exposure to 0.5 M NaCl at 23 °C is illustrated in Figure 4.2.1. The spectra were characterized by a very small, gradual decrease in the magnitude of the impedance over a long period of time, followed by an abrupt decline.

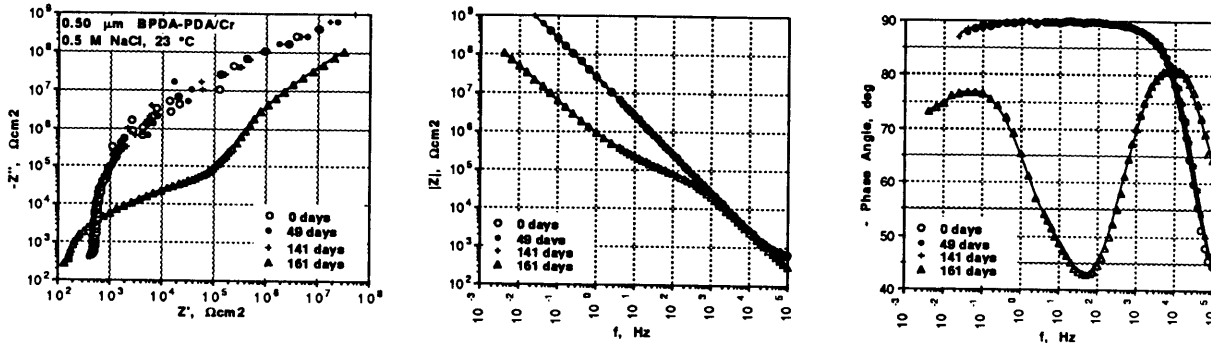


Figure 4.2.1. Long-term degradation of a 0.50  $\mu\text{m}$  BPDA-PDA/Cr sample during exposure to 0.5 M NaCl at 23 °C.

The sudden drop in impedance, accompanied by a shift of the open-circuit potential from positive to negative values was defined as coating failure, and the corresponding time since initial immersion as lifetime. CNLS analysis revealed an accompanying sharp decrease in  $R_f$ , the charge-transfer resistance, and an increase in  $C_{dl}$ , the double-layer interface capacitance, proportional to the amount of exposed interfacial area (Figure 4.2.2).

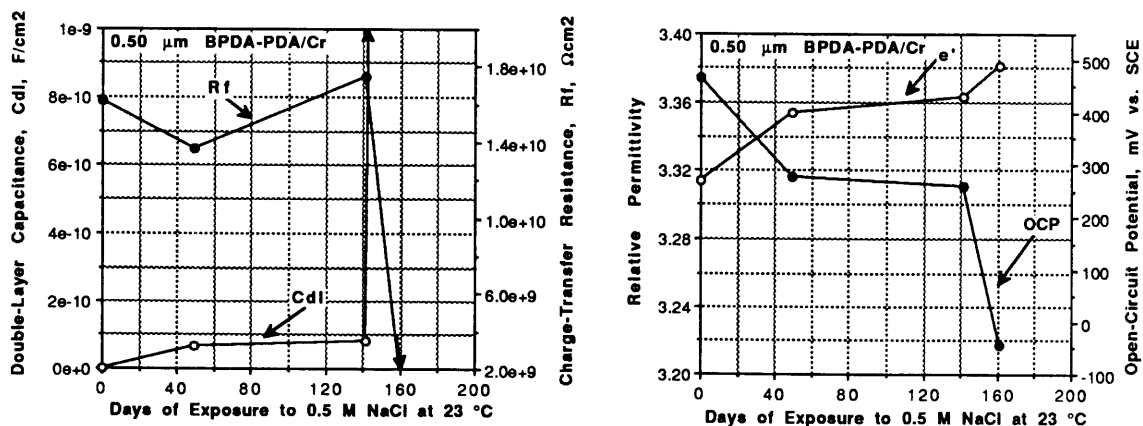


Figure 4.2.2. CNLS estimates of  $C_{dl}$ ,  $R_f$ , and  $\epsilon'$ , along with the open-circuit potentials for the BPDA-PDA coating of Figure 4.2.1. The sharp increase in exposed area indicated by  $C_{dl}$  and  $R_f$  was defined as coating failure.

As discussed in Section 4.1, the rate of increase of the coating's relative permittivity prior to failure was used as a measure of the degradation rate of the polyimide. Surprisingly, after the initial several hours of immersion and up to the time of failure a steady-state permittivity increase rate,  $d(\epsilon')/d(\sqrt{t})$  was established in all three tested coating types (Figure 4.2.3) enabling quantitative comparisons between the samples.

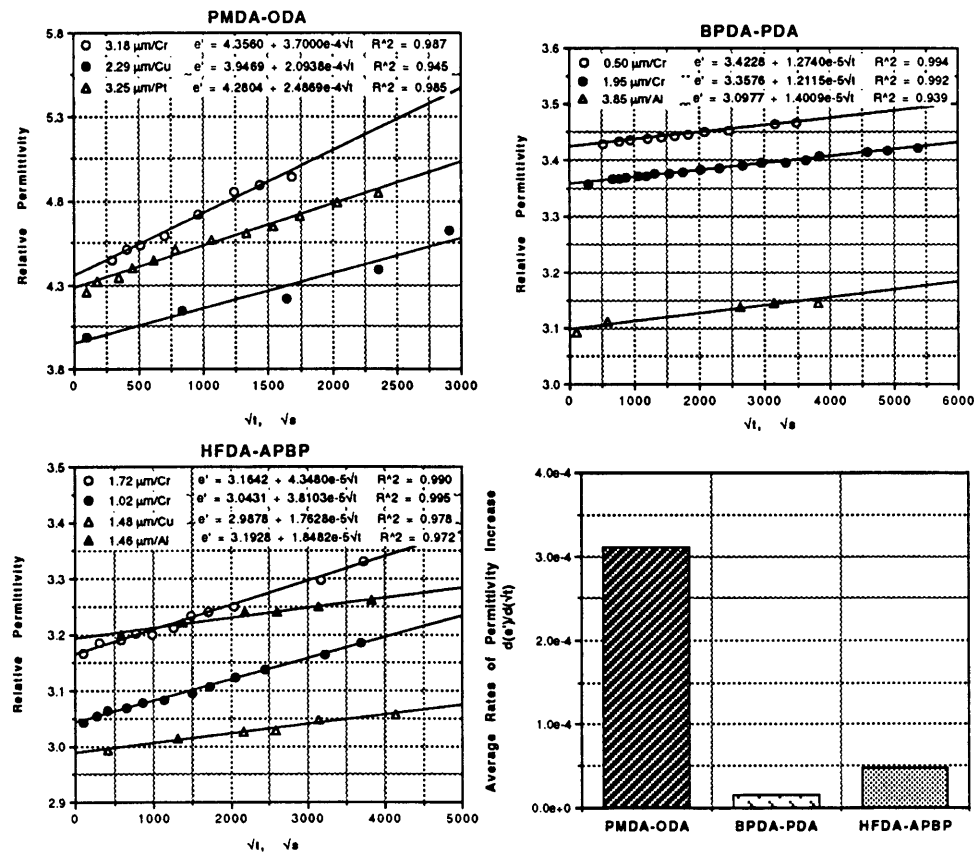


Figure 4.2.3. Illustration of the steady-state long-term rate of increase in dielectric permittivity,  $d(\epsilon')/d(\sqrt{t})$ , and its average values for PMDA-ODA, BPDA-PDA, and HFDA-APBP during exposure to 0.5 M NaCl at 23 °C.

Despite the square-root nature of the permittivity vs. exposure time relationship, the steady-state rate of permittivity increase was not a function of the coating thickness, indicating that the polymer degradation process was not diffusion-limited. In addition, the rate was independent of the type of the metal substrate.

The rates of permittivity increase were a function of the polyimide type. In the case of BPDA-PDA and PMDA-ODA which were chemically very similar, the much larger rate of the latter could be interpreted as faster polymer degradation, confirmed later by the lifetime results. However, different polymers in general might produce different degradation products, with differing contributions to the orientational polarization. Unless these are known, comparisons among the degradation rates of different polymer types based on the rates of relative permittivity increase would be invalid. By contrast, rate comparisons are valid among different samples within a given polyimide type. For instance, prior research had demonstrated significant positive effects of secondary cure on the lifetime of PMDA-ODA coatings [99]. This was confirmed by the present study in which coatings subjected to repeated cure - a second cure cycle identical to the standard cure cycle - exhibited much smaller rates of permittivity increase (Figure 4.2.4).

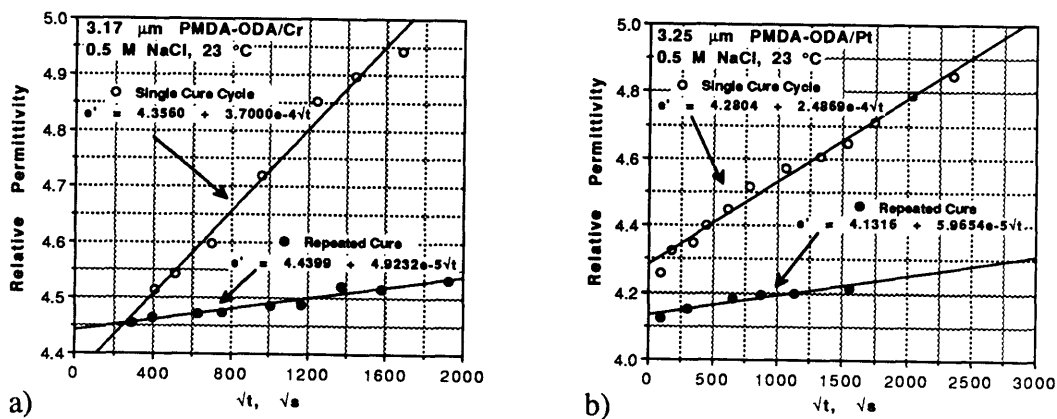


Figure 4.2.4. Comparison among standard-cure and secondary-cure PMDA-ODA degradation rates in 0.5 M NaCl at 23 °C.

Long-term evolution plots of the double-layer capacitance, representative of the three coating types are compared in Figure 4.2.5. PMDA-ODA-coated samples showed fastest degradation at the interface, followed by BPDA-PDA and HFDA-APBP. In addition, PMDA-ODA on Cu degraded significantly faster than the same polyimide on Cr. This had been expected from XPS and IR investigations of the chemical degradation of thin (<100 Å) polyimide coatings exposed to high-temperature/high-humidity environments, which had determined that copper catalyzed the degradation of the polyimide at the interface [12].

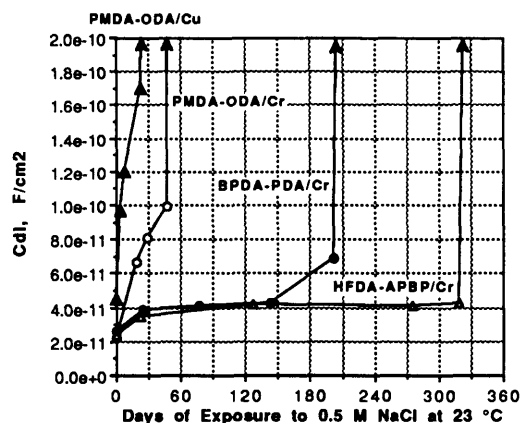


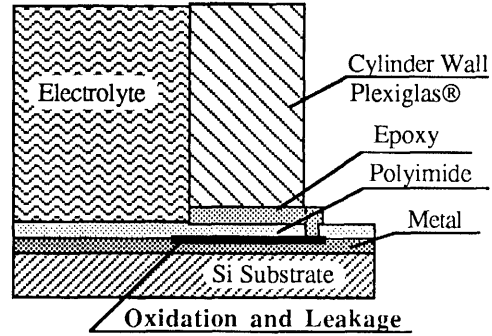
Figure 4.2.5. Increase in  $C_{dl}$  (proportional to the amount of exposed interfacial area) in PMDA-ODA, BPDA-PDA, and HFDA-APBP coatings ( $< 1 \mu\text{m}$ ) during exposure to 0.5 M NaCl at 23 °C.

In general, the rate of increase in exposed interfacial area in BPDA-PDA and HFDA-APBP was very small, near the limit of detection, and almost identical among samples. Unlike the permittivity, it did not exhibit any characteristic functionality.

Due to the uniform nature of samples, in the absence of major defects in the coating the circumference of the electrolyte container served as the natural locus of failure. Underfilm delamination could be observed on Al substrates. In each case, it began at the inner rim of the container where a differential aeration cell had been established with the neighboring exposed area, and spread both inward into the test area and outward beneath the Plexiglas<sup>®</sup> wall. Often, failure in IS terms was followed shortly by leakage of electrolyte from under the outer edge of the electrolyte container. As illustrated in Figure 4.2.6, this was a result of the delamination process encountering a free edge at the container outer rim. Both the delamination, as well as the flow of water along the delaminated areas were probably driven by the osmotic pressure gradient.



Photograph (x10) of area underneath the electrolyte container. Leakage occurred when delamination reached the outer edge (right) of the container.



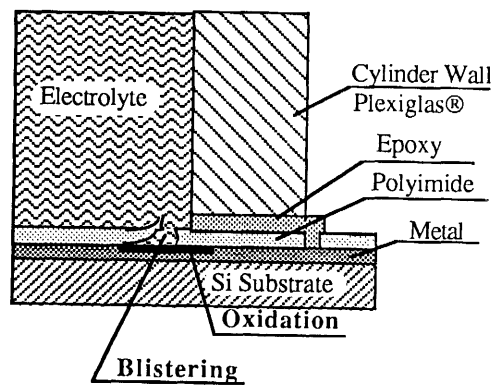
Sketch of delamination failure causing leakage of electrolyte.

Figure 4.2.6. Photograph and schematics of delamination-type failure (BPDA-PDA/Al).

Another type of failure, illustrated in Figure 4.2.7 was caused by blistering of the coating as a result of accumulation of water underneath or in it.



Photograph (x10) of area next to the electrolyte container. Blistering occurred above the delaminated area. Dark area to right is the container.



Sketch of the blistering failure.

Figure 4.2.7. Photograph and schematics of blistering-type failure (HFDA-APBP/Al).

XPS analyses of failed BPDA-PDA and HFDA-APBP polyimide films and substrates were conducted in the regions of failure. Delamination was cohesive in coatings on Cr, and adhesive in coatings on Al (Appendix C.1). The polyimide at both interfaces showed considerable degradation, as reported by others as well [97].

Table 4.2.1 summarizes the recorded times-to-failure of PMDA-ODA, BPDA-PDA, and HFDA-APBP coatings on Cr, Al, and Cu substrates.

Coating Type	PMDA-ODA (PI2545)	BPDA-PDA (PI2611)	HFDA-APBP (UD4212)
<b>Metal coating</b>			
<b>Cr</b> <i>#samples/#wafers/thickness range, um</i>	<b>62±11</b> <i>10/5/2.7-3.2</i>	<b>198±56</b> <i>15/5/0.5-2.2</i>	<b>332±56</b> <i>15/5/0.6-1.7</i>
<b>Al</b> <i>#samples/#wafers/thickness range, um</i>	<b>65±7</b> <i>4/2/2.4-2.5</i>	<b>109±24</b> <i>6/3/1.8-3.8</i>	<b>104±10</b> <i>(4/2/1.4-1.8)</i>
<b>Cu</b> <i>#samples/#wafers/thickness range, um</i>	<b>51±10</b> <i>3/1/2.3</i>	<b>68±5</b> <i>3/1/3.1</i>	<b>123±12</b> <i>3/1/1.5</i>

Table 4.2.1. Average days to failure  $\pm$  standard error of PMDA-ODA, BPDA-PDA, and HFDA-APBP coatings on Cr, Al, and Cu substrates in 0.5 M NaCl at 23 °C (64 samples from 24 wafers).

Clearly, HFDA-APBP coatings were most resistant to failure, followed by BPDA-PDA and PMDA-ODA. In addition, polyimide/Cr combinations were superior to polyimide/Al and polyimide/Cu.

Figure 4.2.8 illustrates the existing correlation between the polymer degradation rates and the times to failure of polyimide coatings on Cr. Although not perfect, this correlation indicates that polyimide degradation plays a substantial role in the failure process on Cr.



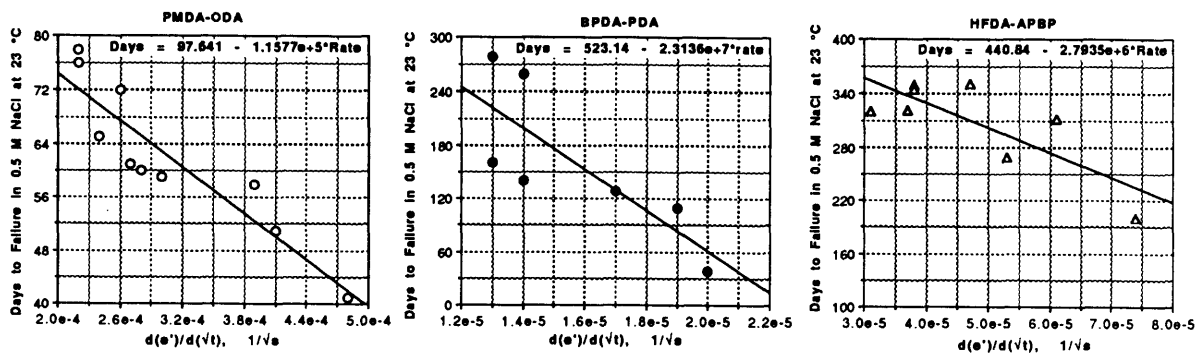


Figure 4.2.8. Times-to-failure of PMDA-ODA, BPDA-PDA, and HFDA-APBP coatings on Cr as a function of the steady-state rate of permittivity increase,  $d(\epsilon')/d(\sqrt{t})$ .

On the basis of the XPS results, the relative times-to-failure, and the correlation among the long-term polymer degradation rates and the times-to-failure it was concluded that failure in coatings on Cr was controlled by the degradation of the polyimide layer next to the interface, and that it occurred via cohesive delamination in the polyimide due to osmotic pressure. In general, polyimide coatings have been reported to react strongly with Cr substrates, providing strong adhesion [12]. However, the reaction leads to the formation of a modified polyimide layer at the interface [12], with a sharp transition between it and the bulk of the coating. This modified layer might serve as the locus of failure. The osmotic pressure gradient between the electrolyte and the polymer which ultimately causes failure may be maintained as a result of the inability of the large organic molecules created upon degradation of the polymer to diffuse out of the microblisters in the coating. In support of this hypothesis, osmotic delamination and blistering have been reported previously in organic composite materials [100]. Furthermore, cohesive osmotic delamination was observed and recorded directly during the long-term exposure of electron-beam treated coatings (Chapter 5).

Although failed Cu interfaces were not investigated via XPS, the trends in the lifetimes on Cu as a function of polyimide type were similar to those on Cr (Table 4.2.1). Therefore, a similar failure scenario may apply. Notably, the lifetime on Cu was generally shorter due to polyimide degradation catalysis as reported previously.

On Al, failure was limited by adhesive delamination at the interface and was less a function of the polyimide type. The osmotic pressure gradient causing delamination at the interface may result from the formation of soluble corrosion products or from an increase of the local pH. The lifetime of polyimide/Al samples was not a function of the coatings' degradation rates.

Finally, the lifetime of polyimide coatings on Cr was not limited by diffusion, as indicated by the lack of correlation between the coatings' thickness and the times-to-failure (Figure 4.2.9).

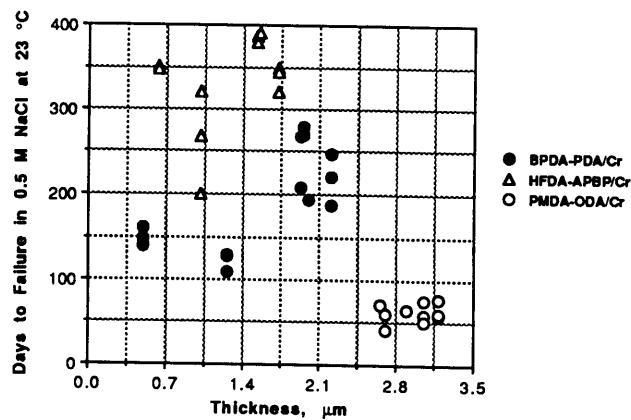


Figure 4.2.9. Times-to-failure of PMDA-ODA, BPDA-PDA, and HFDA-APBP coatings on Cr as a function of the coatings thickness.

### 4.3. Comparison among Short- and Long-Term Results. Feasibility of Lifetime Prediction

The parameters measurable by means of the short-term permittivity transients were the diffusion coefficient of water, the water uptake, and the magnitude,  $M$  of the logarithmic trend (3.2.26).

As illustrated in Figure 4.2.9, the lack of correlation between coating thickness and lifetime suggested that diffusion of any kind did not represent a rate-limiting step in the failure process. In addition, because the degradation of the polymer was a factor in failure on some of the substrates, the above also meant that polymer degradation itself was not limited by either water or chloride transport. Figure 4.3.1 illustrates the independence of the lifetimes of the three polyimide types of water transport through the coating. In the figure, the maximum steady state water flux through the coatings at 23 °C was calculated assuming  $C_w=0$  at the polyimide/metal interface of 2  $\mu\text{m}$  thick coatings, and the water diffusion coefficient and solubility values from Table 3.3.1. Notably, HFDA-APBP which exhibited the longest lifetime on Cr and Cu was also characterized by the largest water flux.

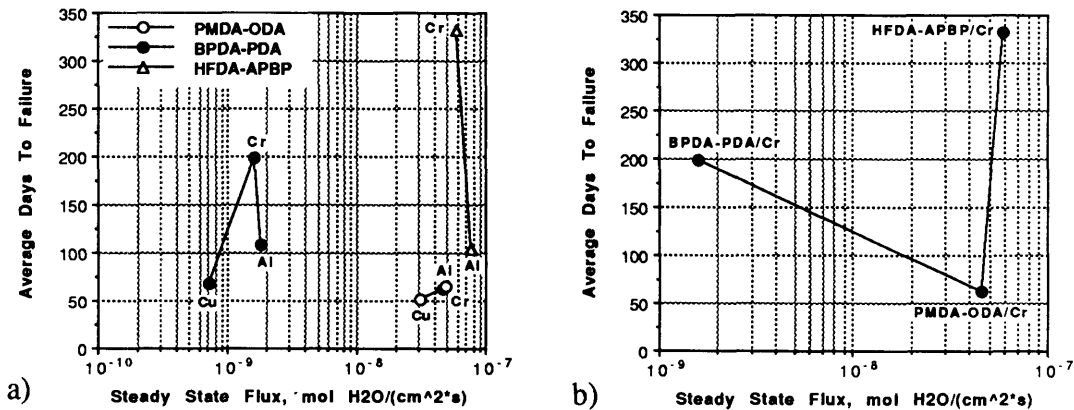


Figure 4.3.1. Comparisons between the steady-state water diffusion flux and the time-to-failure in PMDA-ODA, BPDA-PDA, and HFDA-APBP coatings exposed to 0.5 M NaCl at 23 °C. The water concentration at the polyimide/metal interface was assumed equal to zero. A coating thickness of 2  $\mu\text{m}$  was assumed. The water diffusion coefficient and solubility values were taken from Table 3.3.1.



## **5. Investigation of Effects of Processing on Polyimide Coatings**

This chapter presents the results of a study of the effects of several sets of processing conditions on the chemistry, the water uptake and diffusion, and the lifetime of the polyimide coatings. The test specimens for this study were supplied by Fujitsu Computer Packaging Technologies, Inc. (FCPT), a member of the EPP. To our knowledge, the motivation for the processing variations developed by FCPT had been the observed significantly lower residual stress in electron-beam cured polyimides, as well as their higher chemical resistance to acids and solvents [75]. In addition to investigating the effects of processing on water transport and lifetime, the study was used to verify the methods and analyses described in the previous chapters. This was possible and necessary because of the blind nature of the tests - disclosure of the samples materials and processing took place only after the results were reported back to FCPT. In addition, a second batch of samples included unidentified repeats. The results presented here illustrate the excellent reliability of the water uptake and transport measurements via the transient method (Chapter 3) and illustrate the utility of IS measurements for evaluation of the processing conditions. The chemical changes in the coating as a result of the processing were investigated thoroughly via XPS. Density measurements were performed by means of the density gradient column (Chapter 2.3). The long-term degradation of the coatings in 0.5 M NaCl at 60 °C was monitored by means of IS in accordance with the findings of Chapter 4. The established qualitative relationships between processing, chemistry, and properties are discussed at the end of this chapter.

### **5.1. Specimen Preparation and Processing**

Twenty-four polyimide-coated wafers were provided by Dr. Solomon Beilin of FCPT for investigation of the effects of non-standard processing, and particularly of electron-beam

treatment on the water uptake and lifetime-related properties of the coatings. The 6" Si wafers with thermally-grown SiO<sub>2</sub> (2 μm on each side) had Cr/Cu/Cr metallization on the front side. Subsequently, PI2611 (BPDA-PDA), PI2525 (BTDA-ODA/MPDA), or OCG627 (PMDA-ODA) polyimides had been spin-coated onto the substrate at 6000 rpm. The coatings had been selectively cured, e-beam exposed, and cured again. The following six different sets of processing conditions had been applied to the samples under investigation:

- STC - standard cure at 400 °C, in accordance with the polyimide suppliers' recommendations (see Table 2.1.1).
- LTC - low-temperature cure at 250 °C.
- ESTC - standard cure at 400 °C, followed by a 3000 μC/cm<sup>2</sup> total dosage e-beam treatment.
- ELTC - low-temperature cure at 250°C, followed by a 3000 μC/cm<sup>2</sup> total dosage e-beam treatment.
- CELTC - low-temperature cure at 250 °C, 3000 μC/cm<sup>2</sup> e-beam, and secondary cure at 400 °C.
- CEELTC - low-temperature cure at 250 °C, 5000 μC/cm<sup>2</sup> e-beam, and secondary cure at 400 °C.

E-beam treatment had been performed at 25 mTorr [75]. The intensity of the e-beam radiation was undisclosed but constant for all e-beam treated specimens.

## 5.2. Chemical Analyses via XPS

This section describes the changes in the materials' chemistry as a result of variations in processing. The analysis method and the spectrometer setup used for data acquisition were discussed in Chapter 2 and Appendix A, respectively. A constant 35° takeoff angle (TOA) was employed yielding data representative of the top 50 Å of the coating. It was likely that

a gradient of chemical structure existed through the coating. Such a gradient could have been investigated by means of angle-resolved XPS in which the takeoff angle was varied between 0 and 90 °, probing a depth of ca. 100 Å at the largest TOA. Due to time restrictions, angle-resolved XPS was not attempted for this study.

All changes described below are with regard to the standard cure samples (STC) of each material, however existing deviations from the stoichiometry in STC have also been noted. The raw XPS spectra, sample designations, and processed data from BPDA-PDA, BTDA-ODA/MPDA, and PMDA-ODA samples are contained in Appendix C.2.

Figures 5.2.1-3 show the XPS chemical structures of BPDA-PDA, BTDA-ODA/MPDA, and PMDA-ODA, respectively. In the figures, nonequivalent atoms were assigned numbers which were also used to identify resolvable peaks in the XPS spectra. Although some of the atoms marked with identical numbers are not strictly identical, the differences between their binding energies were too small to allow reliable individual peak deconvolution, and their contributions were lumped together into a common peak.

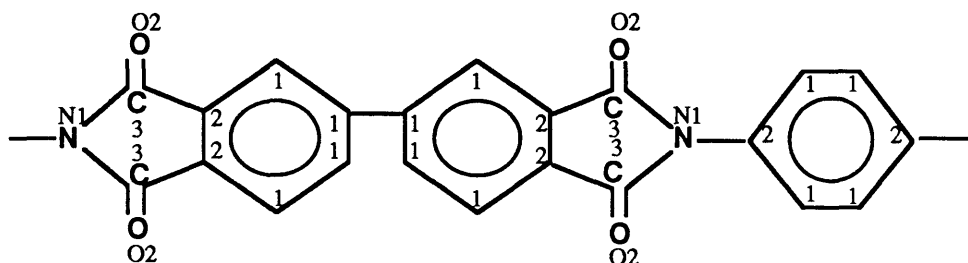


Figure 5.2.1. Chemical structure of BPDA-PDA (PI2611) with identified XPS contributions. Peak assignment was made in accordance with Bachman and Vasile [101].

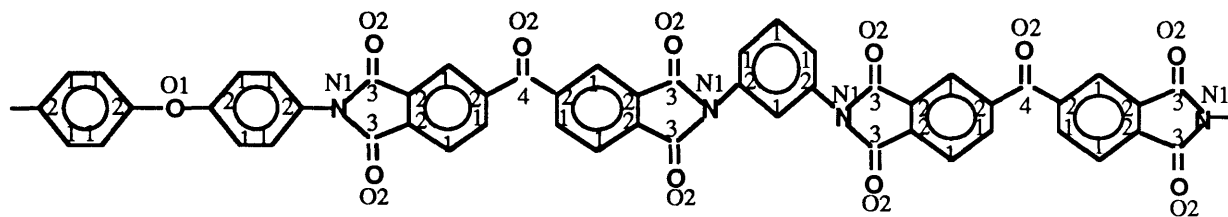


Figure 5.2.2. Chemical structure of BTDA-ODA/MPDA (PI2525) with identified XPS contributions. PI2525 was a blend of ca. 58% BTDA-ODA and 42% BTDA-MPDA [11].

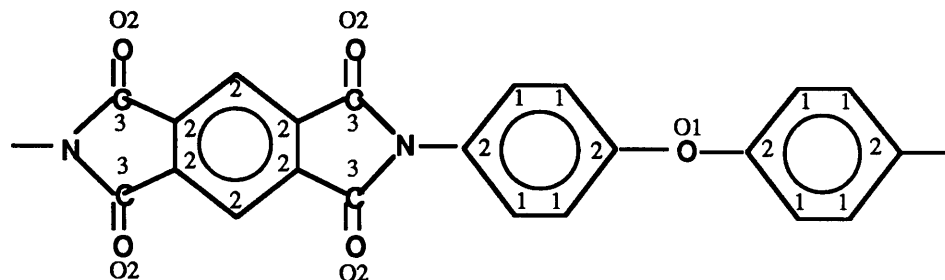


Figure 5.2.3. Chemical structure of PMDA-ODA (OCG627) with identified XPS contributions [102].

Table 5.2.1 gives the stoichiometric elemental composition and expected bond fractions in the carbon, oxygen and nitrogen spectra for the three materials.

Element or Spectrum →	C	O	N	C1s	C1s	C1s	C1s	O1s	O1s	N1s
Material	%	%	%	1	2	3	4	O1	O2	N1
BPDA-PDA	78.6	14.3	7.1	54.5	27.3	18.2	0	0	100	100
BTDA-ODA/MPDA	77.7	16.4	5.9	46.3	34.6	15.3	3.8	9.7	90.3	100
PMDA-ODA	75.9	17.2	6.9	36.4	45.5	18.2	0	20	80	100

Table 5.2.1. Stoichiometric composition and theoretical bond fractions in BPDA-PDA, BTDA-ODA/MPDA, and PMDA-ODA for XPS analysis. XPS peaks have been designated in accordance with Figures 5.2.1-3.

As shown in Appendix C.2, the chemical compositions of the standard samples (STC) were in good agreement with the stoichiometry of the materials, with only BPDA-PDA exhibiting a slight (1.8%) excess in oxygen. In the C1s spectra, the deficiencies in ether and imide carbon (C2) and carbonyl carbon (C3) have been routinely observed in standard cure BPDA-PDA samples [12]. All spectra of the STC sample of PMDA-ODA were remarkably similar to those reported by Nagarkar and Sichel for pristine Kapton-H film [102]. In that study, the researchers had attributed the difference between stoichiometric and actual peak fractions observed in Kapton (PMDA-ODA) to the film preparation method. In the O1s spectrum, all three materials exhibited excess in ether oxygen and deficiency in carbonyl oxygen, with BTDA-ODA/MPDA being closest to stoichiometry. Moreover, while BPDA-PDA and PMDA-ODA showed well-defined imide nitrogen (N1)



peaks, BTDA-ODA/MPDA displayed a nonstoichiometric second peak, characteristic of amide [102] or of imide degradation.

Lower temperature cure resulted in an excess of oxygen in samples of PMDA-ODA and BTDA-ODA/MPDA. In addition, a further increase was noted in the fraction of ether oxygen. No other significant differences with respect to STC were observed.

Electron beam treatment caused a dramatic increase in the atomic fraction of oxygen, especially in the ESTC samples. The increase was probably a consequence of oxygen and nitrogen implantation during e-beam irradiation in the 25 mTorr environment rather than to carbon depletion. The significant changes in the carbon and oxygen spectra indicated that the implanted oxygen formed predominantly ether type bonds in the polyimide. Another effect of the e-beam treatment was the large broadening of all XPS peaks, indicating a resultant wide distribution of energy states. There were signs of imide degradation in the N1s spectrum. In all three polyimides the binding energies of ether and imide carbon shifted to higher values (by  $\geq 0.5$  eV), while imide nitrogen binding energy shifted in the direction of amide nitrogen. Using Figure 2.2.8 as a reference, the shifts in the binding energy of the C2 peak in PMDA-ODA could be attributed to a decreasing imide ring fraction in combination with an increasing ether fraction, a further evidence of polyimide degradation. In addition, the binding energies of carbonyl carbon and carbonyl oxygen in PMDA-ODA and BTDA-ODA/MPDA shifted to significantly lower values.

While the STC and LTC samples of the three materials exhibited distinctive differences in their carbon, oxygen, and nitrogen spectra permitting easy identification of each material, all e-beam treated samples appeared remarkably similar and material identification was no longer possible. A further comparison with the XPS spectra from laser-ablated PMDA-ODA (Kapton-H) [102] revealed very close similarities (Appendix C.3).

A 400 °C cure following the e-beam treatment appeared to eliminate partially the effects of e-beam treatment on the chemical composition, however it did not change the bond structure substantially. Oxygen was lost from ether bonds generated by the e-beam treatment, but also from carbonyl bonds. The binding energy shifts remained largely unchanged, as did the broad distribution of energy states that had been caused by irradiation. In the nitrogen spectra, distinct amide peaks were displayed. Moreover, the second cure left the higher dosage radiation samples (CEELTC) of BPDA-PDA and PMDA-ODA nitrogen-deficient, a clear sign of degradation.

In summary, the surfaces of all three polyimides suffered severe degradation as a result of the electron beam treatment, very similar to that caused by laser ablation. In all cases, e-beam treatment produced practically the same material irrespective of the initial polyimide type. The damaging effects of the e-beam treatment on the polyimide, with the exception of oxygen implantation could not be reversed by the secondary cure at 400 °C.

### 5.3. Density, Water Uptake and Diffusion, and Long-Term Degradation

The results from the density, water uptake, and water diffusion measurements are summarized in Table 5.3.1.

<b>PI2611</b>								
Sample	T cure °C	e-beam μC/cm <sup>2</sup>	T 2nd cure °C	Thickness μm	Density g/cm <sup>3</sup>	Dw x 1E10 cm <sup>2</sup> /s (2.85=1)	Water Uptake, wt% (2.29=1)	Log Slope M
F5 (STC)	400	0	0	2.35	1.465	1.00	1.00	0.019
5/E (STC)	400	0	0	2.35	1.463	1.36	0.82	0.019
1/F (LTC)	250	0	0	2.63	1.447	1.62	1.18	0.020
F4 (ESTC)	400	3000	0	2.27	1.464	1.67	1.08	0.036
F1 (ELTC)	250	3000	0	2.34	1.450	2.21	1.67	0.038
3/G (ELTC)	250	3000	0	2.72	1.445	1.96	1.44	0.041
F2 (CELTC)	250	3000	400	2.46	1.458	3.58	1.41	0.020
F3 (CEELTC)	250	5000	400	2.33	1.458	4.18	2.00	0.021
<b>PI2525</b>								
Sample	T cure °C	e-beam μC/cm <sup>2</sup>	T 2nd cure °C	Thickness μm	Density g/cm <sup>3</sup>	Dw x 1E10 cm <sup>2</sup> /s (80.8=1)	Water Uptake, wt% (3.89=1)	Log Slope M
F10 (STC)	400	0	0	3.80	<1.400	1.00	1.00	0.040
9/E (STC)	400	0	0	4.26	<1.400	0.94	0.77	0.031
7/E (LTC)	250	0	0	4.76	<1.400	0.84	0.77	0.031
F9 (ESTC)	400	3000	0	3.85	<1.400	1.26	1.36	0.027
F6 (ELTC)	250	3000	0	4.00	<1.400	1.16	1.06	0.043
8/G (ELTC)	250	3000	0	4.50	<1.400	0.95	1.00	0.058
F7 (CELTC)	250	3000	400	3.88	<1.400	1.62	1.39	0.039
F8 (CEELTC)	250	5000	400	3.83	<1.400	1.89	1.37	0.041
<b>OCG627</b>								
Sample	T cure °C	e-beam μC/cm <sup>2</sup>	T 2nd cure °C	Thickness μm	Density g/cm <sup>3</sup>	Dw x 1E10 cm <sup>2</sup> /s (43.6=1)	Water Uptake, wt% (3.27=1)	Log Slope M
F15 (STC)	400	0	0	3.88	1.431	1.00	1.00	0.025
12/E (STC)	400	0	0	4.25	1.432	1.00	0.93	0.039
10/F (LTC)	250	0	0	4.91	<1.400	2.94	1.54	0.032
F14 (ESTC)	400	3000	0	3.89	1.431	1.14	1.19	0.028
F11 (ELTC)	250	3000	0	4.27	<1.400	3.39	2.38	0.037
11/G (ELTC)	250	3000	0	4.79	<1.400	3.35	2.19	0.078
F12 (CELTC)	250	3000	400	3.90	1.413	2.52	1.49	0.024
F13 (CEELTC)	250	5000	400	3.95	1.402	3.85	1.60	0.037

Table 5.3.1. Results from density, water uptake, and water diffusion measurements of 24 BPDA-PDA, BTDA-ODA/MPDA, and PMDA-ODA-coated wafers supplied by FCPT (0.5 M NaCl, 23 °C).

The sample-preparation and the experimental procedure for density measurements were described in Chapter 2.3. Unfortunately, as explained in Chapter 2.3, the density gradient column was not linear for  $\rho < 1.4000 \text{ g/cm}^3$ . Thus, some of the OCG627 and of all of the PI2525 samples ( $\rho \approx 1.39 \text{ g/cm}^3$ ) fell outside the valid column range.

Water uptake and diffusion were measured via the permittivity transient method. Even though the samples came from two different batches processed at FCPT at two different times (in Table 5.3.1, batch #1 was designated by an "F" before the sample number), the

results showed very consistent trends. In the few cases where some discrepancy was observed, the differences in processing were also evidenced by the deviations in the sample's density and thickness. As mentioned previously, the samples' identities were disclosed only after the results had been reported to FCPT, and density measurements and the XPS study were conducted following the disclosure. Therefore, these results represent an important indirect proof of the reliability of the permittivity transient method.

Figure 5.3.1 illustrates the dependence of the diffusion coefficients of water in the three polyimides on the processing. The data were normalized to the standard cure sample (STC) in the first batch ("F") of each material.

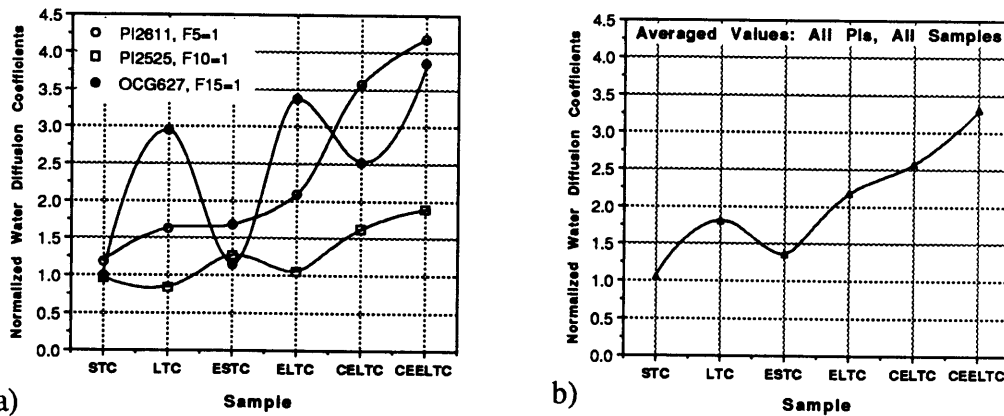


Figure 5.3.1. a) Normalized diffusion coefficients of water in BPDA-PDA, BTDA-ODA/MPDA, and PMDA-ODA/Cr coatings as a function of processing. The data were normalized to F5, F10, and F15, respectively (Table 5.3.1). Repeated samples were averaged. b) Normalized diffusion coefficients of water as a function of processing averaged over all 3 polyimide types (averages of data in a ).

The temperature of primary cure had a dramatic effect on the water diffusion coefficient in PMDA-ODA. Cure at 250 °C resulted in a  $\approx 300\%$  increase in  $D_w$  with respect to the standard cure sample. Its effect on the other two polyimides was far less pronounced:  $\approx 25\%$  increase in BPDA-ODA, and  $\approx 20\%$  decrease in BTDA-ODA/MPDA. In all three materials, the 3 mC/cm<sup>2</sup> e-beam treatment lead to a ca. 20% increase in  $D_w$ , except in the 400°-cured BPDA-PDA (PI2611 ESTC) where the increase was about 40%. The higher e-

beam dosage ( $5 \text{ mC/cm}^2$ ) lead to an additional increase in  $D_w$ . Secondary cure at  $400 \text{ }^\circ\text{C}$  following primary cure at  $250 \text{ }^\circ\text{C}$  and e-beam treatment caused a  $\approx 75\%$  increase in  $D_w$  in BPDA-PDA and BTDA-ODA/MPDA.

The effect of processing on the water uptake was qualitatively similar, as shown in Figure 5.3.2, with the low-temperature cure and e-beam-combination having the most significant impact.

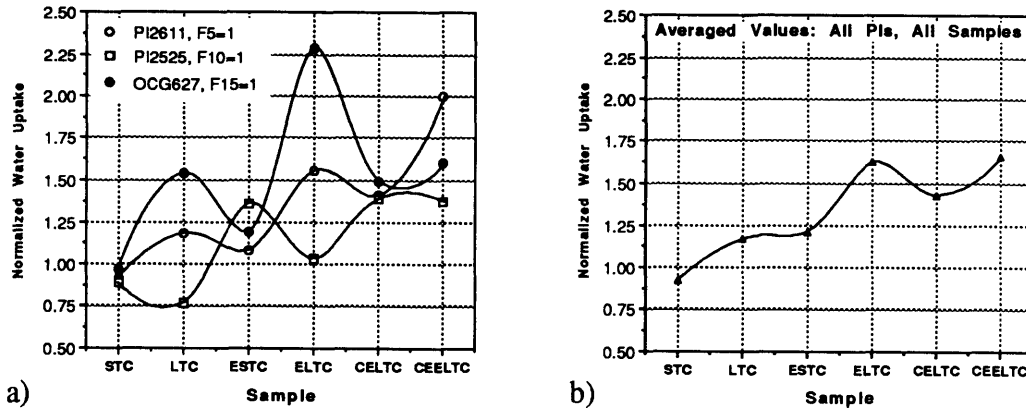


Figure 5.3.2. a) Normalized water uptake by BPDA-PDA, BTDA-ODA/MPDA, and PMDA-ODA/Cr coatings as a function of processing. The data were normalized to F5, F10, and F15, respectively (Table 5.3.1). Repeated samples were averaged. b) Normalized water uptake as a function of processing averaged over all 3 polyimide types (averages of data in a) ).

In general, deviations from the standard cure cycle lead to increased water uptake and water diffusion coefficients. Assuming that a smaller water diffusion coefficient and water uptake were among the processing objectives, of the 3 PIs only BTDA-ODA/MPDA (PI2525) would have benefited slightly from a primary cure at  $250 \text{ }^\circ\text{C}$ . Therefore, with regard to the proposed ELTC treatment which had been judged beneficial in terms of other properties [75], BTDA-ODA/MPDA (PI2525) would be the only material whose water-related properties would not be significantly affected ( $\text{ELTC} \approx \text{STC}$ ).

The qualitative similarity of the trends in water diffusion and water uptake as a function of processing indicated a correlation among them. This is shown in Figure 5.3.3 which combines the data from all samples.

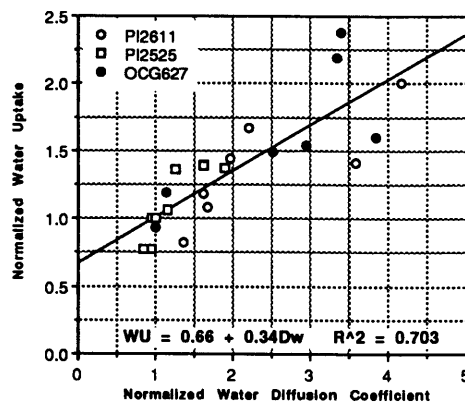


Figure 5.3.3. Positive correlation between the water diffusion coefficient and the water uptake in BPDA-PDA, BTDA-MPDA/ODA, and PMDA-ODA coatings on Cr.

The diffusion coefficients were approximately twice more sensitive to processing changes than the water uptake. The significant correlation suggested that the changes in  $D_w$  and water uptake were governed by common factors. The coating's morphology, characterized in terms of the free volume or density ( $V_f \propto 1/\rho$ , Table 3.3.1) was probably one of them. In both BPDA-PDA and PMDA-ODA, the density was exclusively determined by the cure temperature (Figure 5.3.4 a). In addition, the water-related properties of PMDA-ODA were dominated by the density (Figure 5.3.4 b).

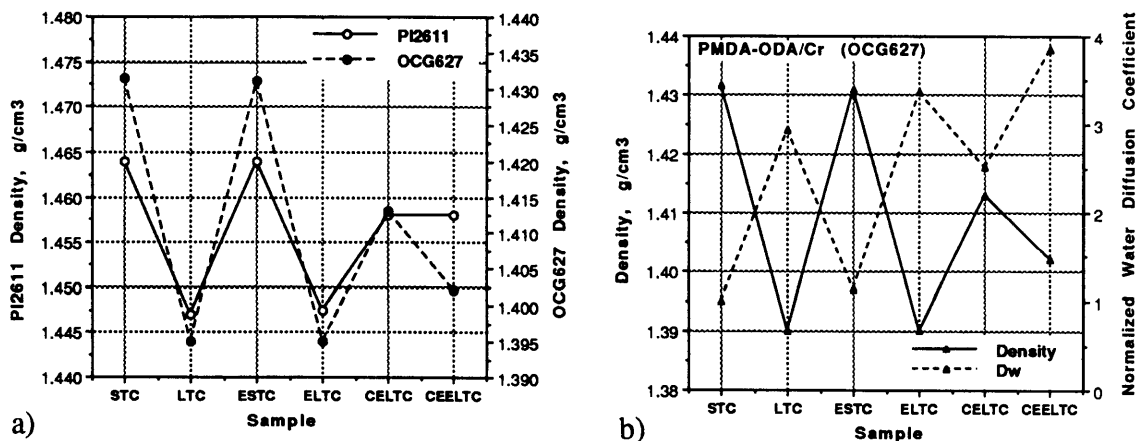


Figure 5.3.4. a) Density of BPDA-PDA (PI2611) and PMDA-ODA (OCG627) coatings on Cr as a function of processing. Note: the density of OCG627 LTC and ELTC samples were measured only approximately, as they fell outside the range of the density column ( $\rho \geq 1.4000 \text{ g/cm}^3$ ). b) Negative correlation between density and water diffusion coefficients in PMDA-ODA. A similar correlation was observed for water uptake.

Similarly, the water uptake and densities were negatively correlated in BPDA-PDA. However, there was not even a qualitative correlation between the water diffusion coefficients and densities in BPDA-PDA, indicating that the free volume was not the only factor affecting diffusion.

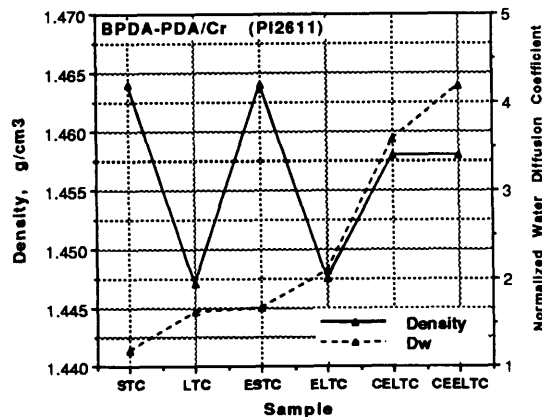


Figure 5.3.5. Densities and water diffusion coefficients in BPDA-PDA.

E-beam treated samples cured at 250 °C exhibited remarkably large post-Fickian logarithmic slopes (3.2.26) in the permittivity transients (Figure 5.3.6).

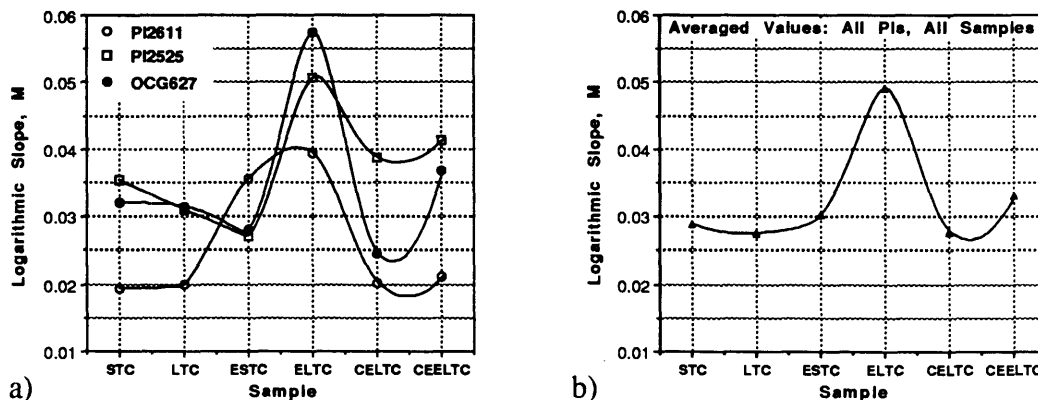


Figure 5.3.6. PI-type-specific (a), and average (b) magnitudes of the logarithmic trends in the permittivity transients upon initial immersion in 0.5 M NaCl at 23 °C, as a function of the processing conditions.

The results of the long-term degradation of PI2525/Cr samples in 0.5 M NaCl at 60 ° C are shown in Figure 5.3.7. Figure 5.3.8 illustrates the corresponding results for the OCG627/Cr samples. The difference ( $\epsilon' - \epsilon'_o$ ), where  $\epsilon'_o$  was the permittivity at the start of immersion was plotted on the y-axis, because it eliminated the effect of the variations in the

amount of absorbed water among the samples. As in Chapter 4,  $d(\epsilon')/d(\sqrt{t})$  was used as an indicator of the polymer degradation. The area-specific double-layer capacitance was assumed to be representative of the degradation at the interface. Both parameters were estimated by means of CNLS analysis using the equivalent circuit model of Figure 4.1.12.

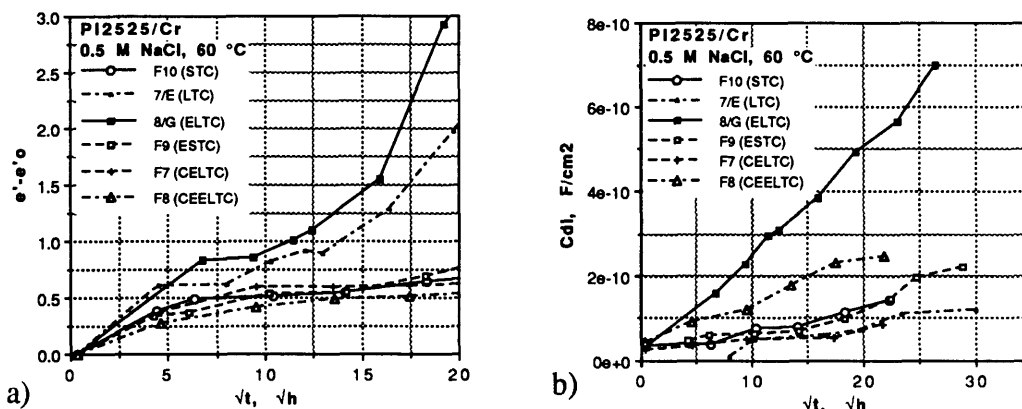


Figure 5.3.7. a) Long-term increase in the relative permittivity of processed BTDA-ODA/MPDA (PI2525) coatings on Cr in 0.5 M NaCl at 60 °C. b) Long-term degradation of the interface (increase in exposed area) in processed BTDA-ODA/MPDA coatings on Cr in 0.5 M NaCl at 60 °C.

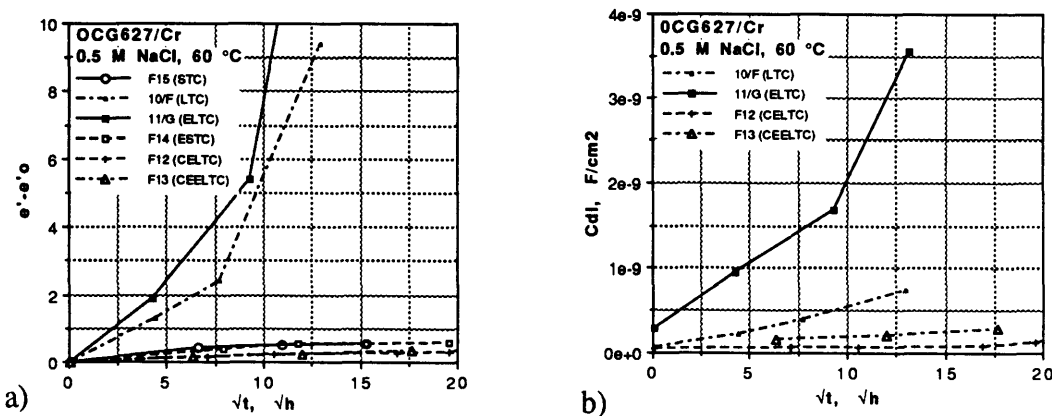


Figure 5.3.8. a) Long-term increase in the relative permittivity of processed PMDA-ODA (OCG627) coatings on Cr in 0.5 M NaCl at 60 °C. b) Long-term degradation of the interface (increase in exposed area) in processed PMDA-ODA coatings on Cr in 0.5 M NaCl at 60 °C.

The highest temperature at which the coatings had been held during cure, "soak temperature" (Table 2.1.1), was the only factor which affected the rate of degradation of the coated samples significantly, irrespective of whether the samples had been e-beam treated or not. In both PMDA-ODA and BTDA-ODA/MPDA, the ELTC and LTC samples exhibited rapid deterioration. In addition, PMDA-ODA coatings cured at 250 °C degraded



much faster than the corresponding BTDA-ODA/MPDA coatings. The e-beam treatment seemed to have had a significant degrading effect only in samples cured at 250 °C, and a secondary cure at 400 °C restored the degradation rate to that of the standard-cure samples.

Similarly to coatings at room temperature (Chapter 4), the nature of failure in the processed coatings was cohesive delamination near the edge of the cell cylinders. However, a new phenomenon which was not detectable via IS and did not lead to failure in IS terms was observed visually in the two ELTC samples of BTDA-ODA/MPDA. This phenomenon represented internal blistering of the coating, in which a thin surface layer cracked and lifted off the bulk of the coating after several days of exposure to 0.5 M NaCl at 60 °C. The thickness of the blistered layer, measured by profilometry was approximately 200-300 Å (Figure 5.3.9).



x50 x50 x200  
Figure 5.3.9. Internal blistering in BTDA-ODA/MPDA coatings cured at 250 °C and treated with 3000  $\mu\text{C}/\text{cm}^2$  e-beam radiation. At right (c), the remaining unblistered coating was scratched completely to expose the Cr film. The remaining coating thickness was 4.32  $\mu\text{m}$ . The thickness of the blistered layer was ca. 300 Å.

#### 5.4. Summary of Processing Effects

The following is a summary of the effects of the individual processing steps on the chemistry, density, water-related properties, and environmental degradation of the three polyimides.

##### 1) Cure temperature (250-400 °C):

- polyimide chemistry was affected insignificantly,
- low cure temperature resulted in a reduced density of the coating (more free volume),
- the water uptake and diffusion in PMDA-ODA and BPDA-PDA increased with decreasing cure temperature, however slightly lower uptake and diffusion were observed in BTDA-ODA/MPDA. PMDA-ODA was affected most significantly by the cure temperature;
- low cure temperature resulted in a significantly faster environmental degradation in both BTDA-ODA/MPDA and PMDA-ODA. Again, PMDA-ODA was much stronger affected than BTDA-ODA/MPDA.

##### 2) Electron-beam treatment:

- caused massive polyimide degradation comparable to laser ablation, plus excess in ether oxygen,
- did not affect the coating density significantly,
- water uptake and diffusion were affected negatively (increased), however the effect was smaller than that of the cure temperature,
- accelerated the environmental degradation in samples cured at the low temperature, however had no significant detrimental effect on samples cured at 400 °C.

##### 3) Post-e-beam cure at 400 °C:

- did not reverse the chemical degradation of the polyimide, however significantly reduced the excess in ether oxygen,
- caused an increase in the density of the coatings,

- except in PMDA-ODA, did not reverse the negative effects of the low temperature primary cure on the water uptake and diffusion,
- almost completely restored the environmental stability of the coating.

The overall conclusion of the study was that a 400 °C cure was absolutely necessary in order to guarantee the environmental stability of the coated sample. The reason for the environmental instability of samples cured at 250 °C is unclear. It has been suggested that residual polyamic acid might be present in such samples, however the XPS studies would have detected it. Other researchers also have reported completely cured polyimide at 250 °C [12]. Still, the density difference between coatings cured at 250 °C and standard-cure coatings, as well as the change of density upon secondary cure documented above indicate a significant change taking place in the coating. The increase in the diffusion coefficients and water uptake in secondary-cured coatings despite the accompanying increase in density represents a proof that the above was more than just a free-volume change.

The fact that the e-beam treatment caused severe degradation of the polyimide but did not significantly alter its environmental stability as long as high-temperature cure (400 °C) was employed, indicated that the massive degradation was only limited to the immediate surface of the coating. The observed internal osmotic blistering in ELTC-coatings, possible only in the presence of a very sharp transition between the damaged layer and the undamaged bulk offered a further argument in favor of this hypothesis. In addition, this hypothesis was supported by the fact that the Fickian diffusion model with constant  $D_w$  remained fully adequate for e-beam treated coatings. Hence, the treatment probably caused small and almost uniform damage beyond the first 300 Å.

Apart from illustrating the damage to the coating caused by the e-beam treatment, Figure 5.3.9 constitutes a proof of the osmotic blistering hypothesis used to explain the cohesive

coating failure in polyimide coatings on Cr and Cu substrates in Chapter 4. The presence of a similar sharp transition layer of modified polyimide at the interface has been confirmed by others [12]. Thus, the situation in all coatings immediately above the polymer/metal interface may be quite similar to the situation below the surface of e-beam treated coatings.

Finally, the results from this study confirmed once again the conclusions of Chapter 4, that there was absolutely no correlation between the amount of water uptake and the water diffusion rate and the environmental stability of the coated samples (PI2525 vs. OCG627, or CEELTC and CELTC samples vs. LTC and ELTC samples). There also was no significant correlation between the magnitude of the logarithmic slopes and degradation rate (e.g. LTC vs. ELTC, or CEELTC vs. LTC). Hence, as already concluded in Chapter 4, short-term permittivity transient measurements could not be used to predict the long-term performance and the lifetime of the processed samples.

## 6. Conclusions and Future Work

### 6.1. Conclusions

The main goal of this work was to investigate the feasibility of lifetime prediction for coated polyimide/metal structures exposed to 0.5 M NaCl by means of short-term, non-destructive, *in-situ* measurements. The success of a predictive procedure depended on what parameters were measurable non-destructively in the short-run, and on the existence of correlations between those parameters and the long-term performance of the coated substrates. The "short-run" was defined as the initial 5000-10000 s after exposure of a coating to the electrolyte. Parameters measurable within that time period via the permittivity transient method included the water diffusion coefficient and water solubility in the coating, and the magnitude of the post-saturation logarithmic trend in permittivity - a parameter representative of solute-polymer or solute-solute interactions. Long-term exposure studies by means of impedance spectroscopy and XPS showed that failure in polyimide/Cr structures occurred by cohesive blistering in the coating near the interface, while failure in polyimide/Al coatings consisted of mixed-mode delamination at the interface. For the purposes of this study, failure was defined as the sharp increase in exposed interfacial area measured by IS, and associated with the arrival of delamination at the polyimide-free edge along the outer rim of the electrolyte container.

It was established that failure was not limited by the mass transport of water through the coating, and thus was not predictable from the short-term experiments.

To our knowledge, this work was the first to employ the permittivity transient method routinely for investigation of a large number of samples. A model was developed and fitted to the data via the non-linear least squares procedure. Permittivity transient experiments were non-destructive, could be used *in-situ*, and involved very little sample preparation.

Measurements of water solubility in the polymer required calibration with gravimetric water uptake data. Measurements on both free films and on coated substrates were possible.

During the short-term exposure to aqueous electrolytes, the relative permittivity of the coatings increased reversibly, due to the added polarizability of the absorbed water. The coating permittivity at the moment of water saturation was linearly proportional to the solubility of water in the polymer. The relative permittivity of absorbed water, related to the size of the clusters of water molecules, was directly proportional to the free-volume fraction in the respective polyimide. In HFDA-APBP, the cluster size was similar to that in liquid water and much larger than that in the other three polyimides. Water diffusion in all studied polyimides was Fickian, with concentration-independent diffusion coefficients. The water diffusion coefficients were measured as a function of the polyimide type, coating thickness, metal substrate, and processing. In most coatings, the free-volume fraction was the dominant factor in determining the diffusion coefficient of water.

Permittivity transient measurements were also used to measure the diffusion in the coatings of some organic solutes: alcohol, acetone, and acetic acid. Moreover, the permittivity transient technique could be employed to detect processing defects, provided that the defective area in the coating was sufficiently large.

Complications in the interpretation of the permittivity transient data stemmed from the observed post-saturation logarithmic trend in permittivity. This trend was apparent for water and organic solutes alike, and was most likely due to solute-polymer or solute-solute interactions of hydrogen-bonding type. The process was reversible. Although its exact nature needs further investigation, the existence of a post-saturation trend adds a hysteresis to the relationship between water uptake and the relative permittivity of the polymer, and may therefore present problems for the potential application of polyimides in capacitive humidity sensors. The observed irreversible increase in the polymer permittivity due to degradation creates additional problems for such applications.

Impedance spectroscopy has been long used to monitor the degradation and lifetime of coated substrates, however there is considerable controversy regarding the data analysis and interpretation. This work demonstrated that the graphical analysis of the IS spectra was unreliable and could not be generalized. Furthermore, IS could not detect underfilm delamination in the absence of a low-resistance connection (pore or blister) between the delaminated interface and the electrolyte.

Under laboratory conditions IS could be used to quantify the degradation of coated substrates, both in terms of polymer degradation as well as the exposed interfacial area, and may serve as an useful tool in coatings research. In coatings on Cr which failed cohesively, the long-term degradation rate of the polymer, manifested in the irreversible increase in the coating permittivity was related to the time-to-failure.

With regard to its potential application in the field, the sensitivity of IS for detection of defective areas was found to be less than what is required in microelectronics. Furthermore, IS data were sensitive to oxidation at the interface, a potential problem when the prior history of the specimens and the instantaneous values of the area-specific interfacial parameters are unknown. The high resistivity of the polyimide coatings imposed further limitations on the technique.

In terms of their lifetime in 0.5 M NaCl, the various polyimide/Cr combinations were ranked as follows: HFDA-APBP > BPDA-PDA >> BTDA-ODA/MPDA > PMDA-ODA. Although the failure mode on Cr was cohesive, this ranking did not correspond to the ranking of the four polyimides in terms of their tensile stress or fracture toughness, which was: BPDA-PDA > PMDA-ODA > HFDA-APBP [12]. Instead, the rate of the chemical degradation of the polymer which influenced both the cohesive strength and the magnitude of the osmotic pressure gradient was probably the key factor in the failure of coatings on Cr.

The lifetime of the coatings on Al was much shorter than that on Cr, and a mixed-mode failure was observed. This was in agreement with mechanical testing data which had established the poor adhesion of all of the investigated polyimides to Al [12]. Although it appeared likely that the lifetime of the various polyimide/Al combinations would be a function of the strength of adhesion, insufficient data did not allow a positive statement. However, even though improving the adhesion might increase the lifetime of the polyimide/Al interfaces, their reliability is compromised additionally by the weakness of the Al/Al(OH)<sub>3</sub> interface. Therefore, polyimide/Al interfaces in MCMs may have to be avoided when possible.

Polyimide coatings performed worst on Cu, as expected from prior chemical investigations of polyimide/Cu interfaces [12]. The problem has been widely recognized, and such interfaces are usually avoided by deposition of intermediate metal layers.

With regard to processing, cure at 400 °C was absolutely necessary for BPDA-PDA, PMDA-ODA, and BTDA-ODA/MPDA (HFDA-APBP was not investigated). Low-temperature cure (250 °C) resulted in strongly accelerated degradation, especially in PMDA-ODA. Electron-beam treatment after cure at 250 °C could not replace cure at 400 °C, and in some cases even caused additional acceleration of the degradation process. By contrast, secondary or repeated cure at 400 °C had a beneficial effect on the lifetime of PMDA-ODA.

Chloride diffusion was not reflected in the permittivity transients and could not be measured non-destructively. Membrane permeation experiments established the upper limit of the chloride diffusion coefficient at ca.  $10^{-15}$  cm<sup>2</sup>/s at room temperature in BPDA-PDA and PMDA-ODA.



## 6.2. Future Work

The following important issues remain to be addressed by future work:

1. The physical nature of the logarithmic trend in permittivity should be investigated further, e.g. by means of deuterium nuclear magnetic resonance spectroscopy (NMR), or by IR. Furthermore, the magnitude of the logarithmic trend as a function of the activity of water in the coatings requires investigation. One method of achieving this without alterations to the current setup is by using a solvent which does not diffuse into the polymer, and which can dissolve water. Alternatively, a patterned metal electrode can be deposited onto the coating, and experiments conducted in controlled relative humidity environments.

2. The amount of water in the coating necessary to induce chemical degradation (hydrolysis) of the polyimide should be investigated by subjecting specimens to different RH environments and monitoring their degradation via XPS or IR. In addition, the effect of long-term exposure to RH on the mechanical properties of the polyimides needs further study.

3. The investigation and observation of failure in the present work was difficult because it occurred near or under the rim of the electrolyte container. Furthermore, failure times were subject to fluctuations depending upon the location of initial delamination and its direction. A solution would include control of the locus of initial delamination. This could be achieved by the incorporation of a "weak spot" on the substrate. In the case of substrates failing by adhesive delamination, such a region can be produced by controlled local contamination, or by a local deposition of another metal with lower adhesion strength. Several approaches are possible in the case of a cohesive failure mode: in specimens cured on hot-plates, the flow of heat to a defined area on the substrate can be reduced, producing a region which is less well cured than the rest of the coating and will therefore degrade

faster. Alternatively, a bimetallic galvanic couple can be patterned on the substrate to produce fixed cathodic regions, above which the coating is likely to degrade faster as a result of the high pH environment ("saponification"). In all cases, the distance to delamination failure has to be fixed. This could be accomplished by the use of concentric, ring-shaped electrodes, for instance a thin counter-electrode ring encircling the weak spot at a constant distance.

4. Investigations of the kinetics of failure require knowledge of the local conditions at the interface. Semi-quantitative, *in-situ* measurements of the underfilm pH could be accomplished by incorporating phenolphthalein indicating powder into the coatings, after mixing it with the polyamic acid precursor. Preliminary experiments conducted for this study showed that the pH-indicating capability of the powder was preserved after cure at 250 °C.

5. The fact that most reliability tests of organic coatings are conducted in NaCl-containing environments attests to the general assumption that chlorides play a significant role in the coating failure. Therefore, the diffusion of chlorides in the polyimide coatings merits further investigation. To accomplish this, membrane permeation appears to be a suitable method. However, verification of the specimen preparation is critical in such experiments.

6. Despite the great number of articles on the subject of measurement of water diffusion and uptake by polyimides, a clear picture of the physical mechanism of diffusion, the sites occupied by the absorbed water, as well as of the role of water in the degradation of the polyimides is still absent. Better understanding of these issues would allow the design of more reliable coatings.

## Appendix A

### Setup parameters for XPS Data Acquisition

Following are the pertinent XPS instrumentation settings and data analysis parameters for all of the XPS work in this thesis:

#### Spectrometer

- Spectrometer: Surface Science Instruments SSX-100 ESCA at Harvard-MIT Surface Analytical Facility (McKay Lab, Rm. 106, Harvard University, Cambridge); Operated by Pradnya Nagarkar, Research Associate at the H. H. Uhlig Corrosion Lab, MIT.
- X-ray source:  $Al_{K\alpha}$ ,  $E=1487$  eV, monochromatic.
- Pass energy:  $\approx 7$  eV.
- Flood gun: 5.0 eV
- Spot: 1000/600  $\mu\text{m}$ .
- UHV:  $<10^{-8}$  mbar.
- Data acquisition duration:  $\approx 20\text{-}30$  min/sample.
- Take-off angle: 35 deg, equivalent to a probing depth of  $\approx 5$  nm.

#### Data Analysis

- All peaks 100% Gaussian unless otherwise specified.
- Binding energy reference: aromatic carbon (C1s) at 284.70 eV [19].
- Photoemission cross-sections,  $\alpha_i$ : C1s=0.25, N1s=0.42, O1s=0.66, F1s=1.00.
- Formula for calculating the atomic fractions of elements,  $x_i$ :

$$x_i = \frac{CC_i}{\sum_{i=1}^3 CC_i} \quad i = \text{C, O, N} \quad (\text{A.1})$$

where  $CC_i$  represents the corrected counts of element  $i$ , calculated as follows:

$$CC_i = \frac{\sum_{j=1}^n \text{Area}_j}{(\text{number of scans}) \cdot \alpha_i} \quad (\text{A.2})$$

where  $j$  is a non-equivalent atom or bond type of element  $i$ ,  $\text{Area}_j$  is the area under the peak corresponding to  $j$ , and  $\alpha_i$  is the photoemission cross-section of element  $i$ .



## Appendix B

### Equilibrium vs. Transient Water Uptake

This appendix provides an illustration of the difference between the equilibrium and the transient water uptake in terms of the measured coating capacitance. From Section 3.2.2

$$C_{\text{equil}} = C_{\text{dry}} + a \cdot C_{\text{equil}}^{\text{w}} \quad \text{or} \quad \epsilon'_{\text{equil}} = \epsilon'_{\text{dry}} + b \cdot C_{\text{equil}}^{\text{w}} \quad (\text{B.1})$$

where  $C_{\text{equil}}^{\text{w}}$  is the equilibrium water uptake by the coating, and  $C_{\text{equil}}$  and  $\epsilon'_{\text{equil}}$  are the corresponding values of the coating capacitance and relative permittivity. From (B.1) it follows that

$$\epsilon'(x,t) = \epsilon'_{\text{dry}} + b \cdot C^{\text{w}}(x,t) \quad (\text{B.2})$$

where  $\epsilon'(x,t)$  is the local dielectric constant and  $C^{\text{w}}(x,t)$  is the local water concentration. However, from (B.1) does not follow that

$$C(t) = C_{\text{dry}} + a \cdot \overline{C^{\text{w}}}(t) \quad (\text{B.3})$$

where  $C(t)$  is the coating capacitance and  $\overline{C^{\text{w}}}(t)$  is the average water concentration in the coating.

The simple example below illustrates the above statement. Assume numerical values for the parameters in (B.1):  $a=0.3$ ,  $C_{\text{dry}}=3$ . Figure B.1 shows two coatings. The first one is in equilibrium (no concentration gradient) with water content  $C_{\text{equil}}^{\text{w}}=\overline{C^{\text{w}}}=3$ . The second one is in a transient state with the same average concentration  $\overline{C^{\text{w}}}=3$  but different water concentrations in the two halves of the coating. According to (B.3) both coatings should have the same capacitances. However, the capacitances of the two coatings are different.

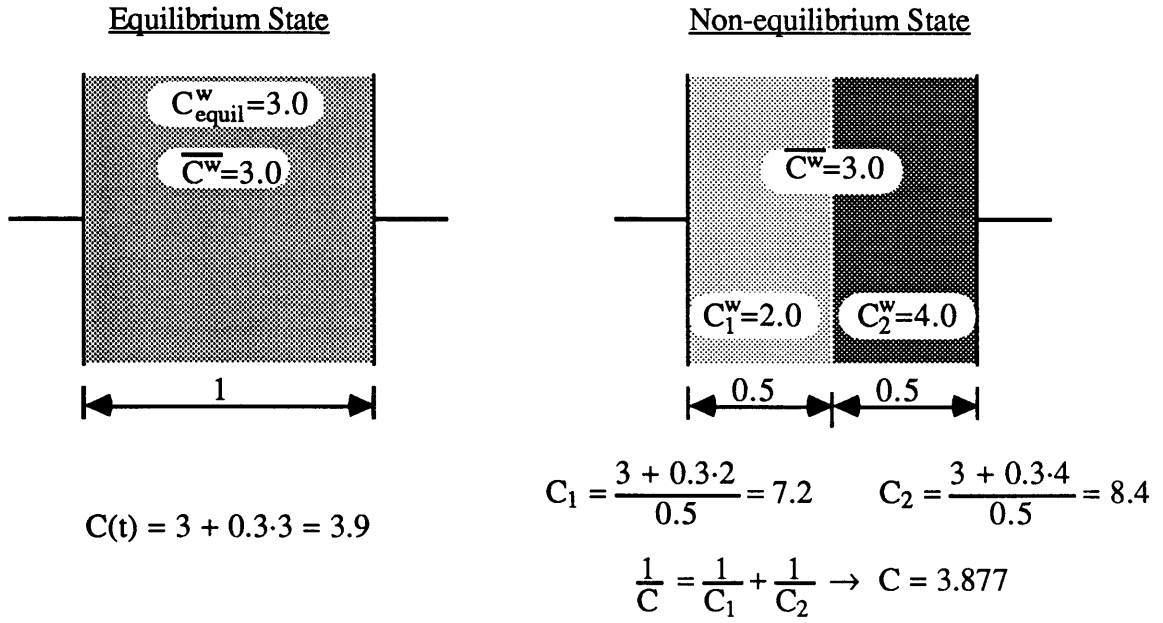


Figure B.1. A comparison between two coatings with the same average water concentration. The capacitance values of the coatings are different due to the presence of a water concentration gradient in one of them.

# Appendix C

## XPS Analyses of Failed and Processed Samples

### Appendix C.1. XPS Analyses of Failed Samples

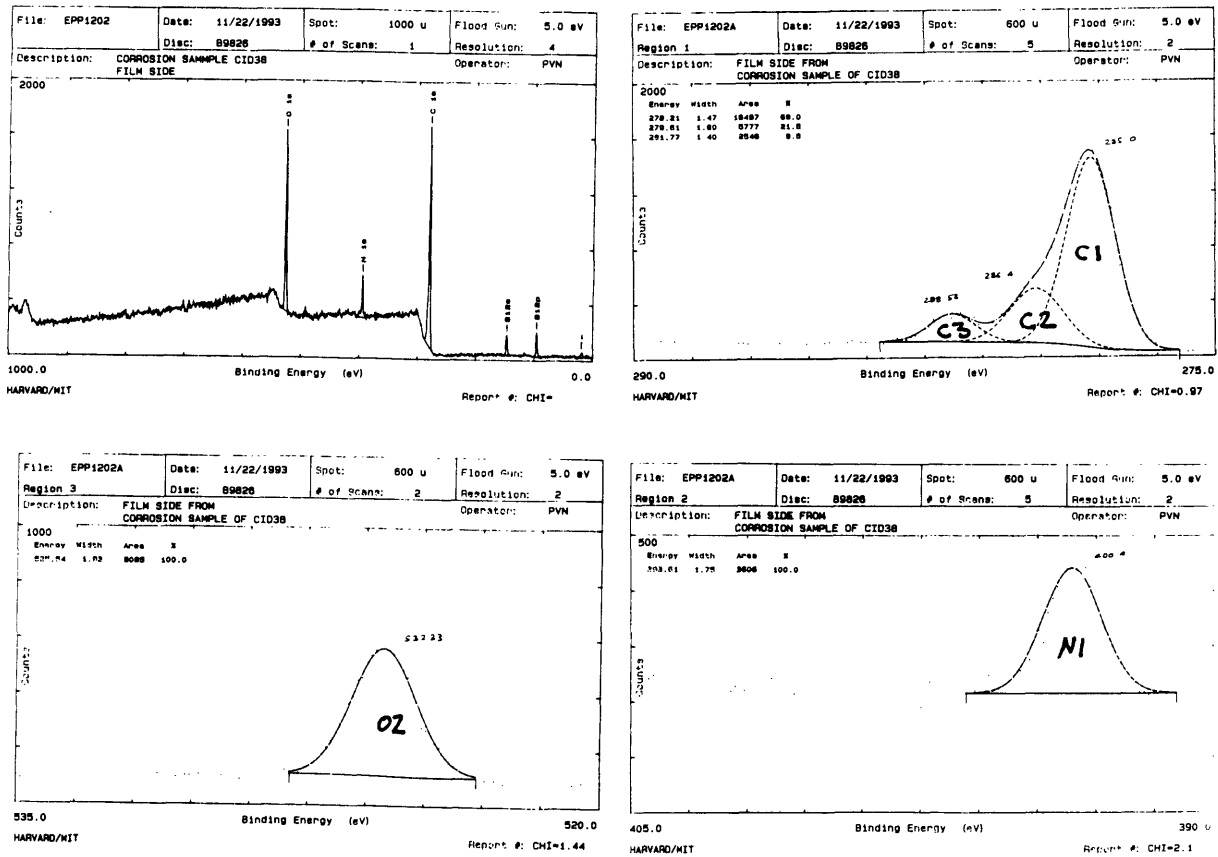


Figure C.1.1. Survey, C1s, O1s, and N1s spectra of film side of failed BPDA-PDA/Cr sample at location of failure. Survey scan shows absence of Cr, indicative of cohesive delamination. Peak assignments in accordance with Figure 5.2.1.

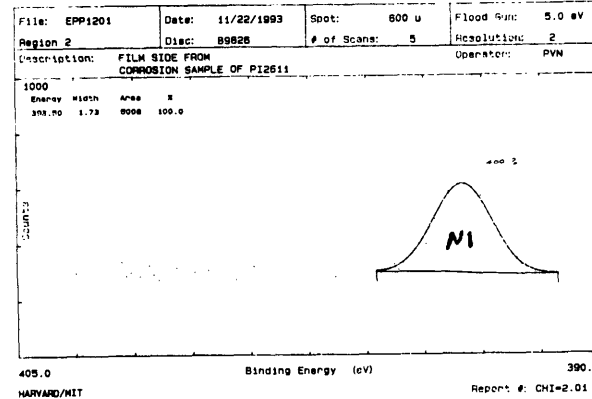
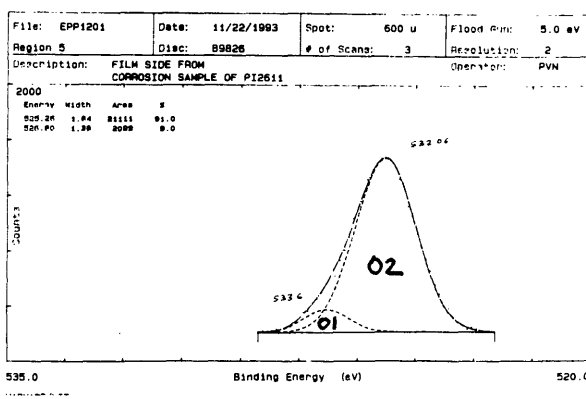
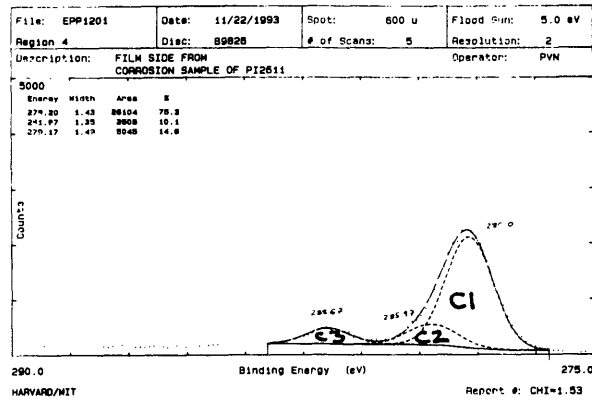
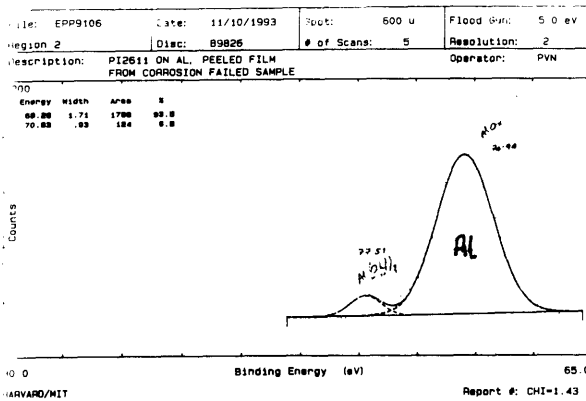
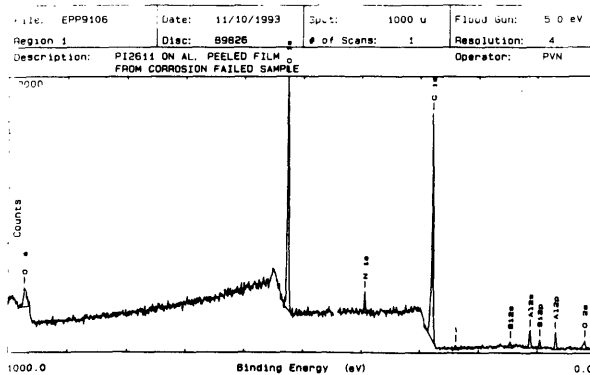


Figure C.1.2. Survey, Al1s, Cl1s, O1s, and N1s spectra of film side of failed BPDA-PDA/Al sample at location of failure. Survey scan shows presence of Al, indicative of adhesive delamination. Al1s spectrum shows presence of Al(OH<sub>3</sub>). Peak assignments in accordance with Figure 5.2.1.



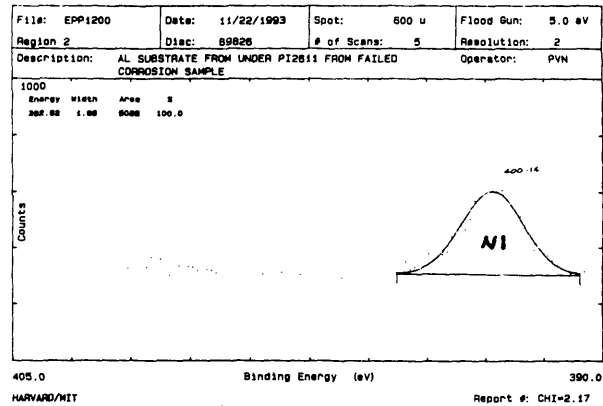
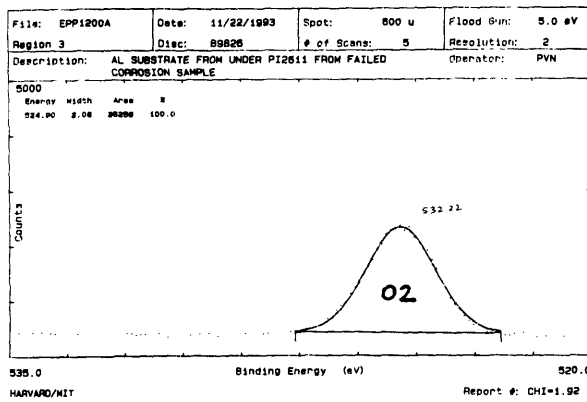
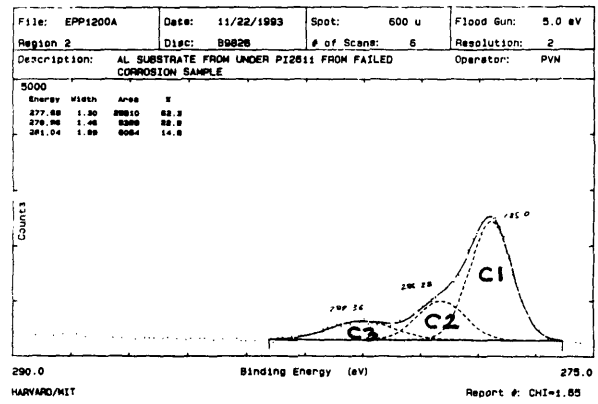
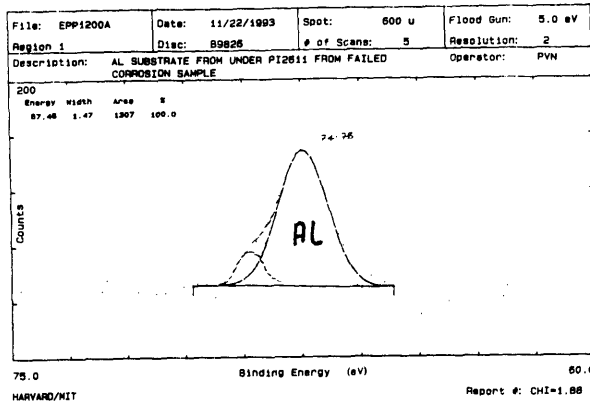
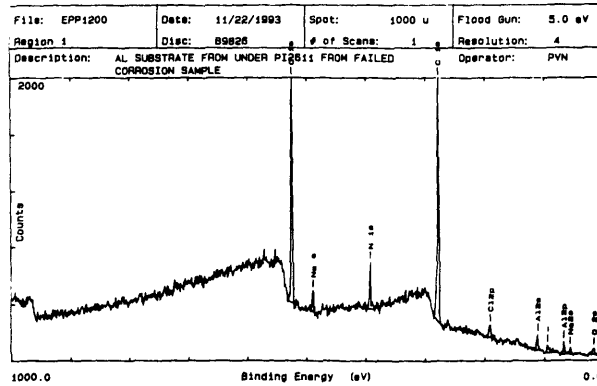


Figure C.1.3. Survey, Al1s, C1s, O1s, and N1s spectra of substrate side of failed BPDA-PDA/Al sample at location of failure. Survey scan shows presence of polyimide, indicative of adhesive delamination. Al1s spectrum shows presence of Al(OH<sub>3</sub>). Peak assignments in accordance with Figure 5.2.1.

## Appendix C.2. XPS Analysis of Processed Samples

### 1. XPS Data from Processed BPDA-PDA (PI2611)

Elem/Peak	C	O	N	C1	BE	FWHM	C2	BE	FWHM	C3	BE	FWHM
Sample	%	%	%	%	eV	eV	%	eV	eV	%	eV	eV
STC	77.8	16.1	6.1	82.5	284.70	1.34	4.3	285.75	0.84	13.1	288.10	1.04
LTC	78.5	15.6	5.9	75.3	284.70	1.34	11.6	285.59	1.10	13.1	288.23	1.29
ESTC	70.1	22.4	7.4	59.2	284.70	1.49	23.1	286.10	1.64	17.6	288.15	2.00
ELTC	73.5	19.9	6.5	68.1	284.70	1.54	18.2	286.23	1.60	13.7	288.13	1.75
CELTC	76.9	16.8	6.3	67.8	284.70	1.46	20.4	285.98	1.59	11.8	287.93	1.95
CEELTC	78.8	16.4	4.8	76.8	284.70	1.56	15.9	286.33	1.52	7.2	288.14	1.65
Elem/Peak		O1	BE	FWHM	O2	BE	FWHM	N1	BE	FWHM	amide	BE
Sample		%	eV	eV	%	eV	eV	%	eV	eV	%	eV
STC		12.5	533.13	1.62	87.5	531.56	1.40	100.0	400.11	1.31	0.0	
LTC		11.4	533.32	1.37	88.6	531.67	1.54	100.0	400.16	1.43	0.0	
ESTC		42.0	533.09	1.94	58.0	531.61	1.87	100.0	399.85	2.32	0.0	
ELTC		38.9	533.10	1.84	61.1	531.62	1.84	100.0	399.87	2.27	0.0	
CELTC		31.7	533.35	2.08	68.3	531.72	1.85	68.0	400.18	1.78	32.0	398.74
CEELTC		21.8	533.52	1.70	78.2	531.86	1.84	60.0	400.02	1.80	40.0	398.78

Table C.2.1. XPS data from analysis of six BPDA-PDA samples.

**Legend for Table C.2.1:**

- STC = standard temperature cure (400 °C); no other treatment,  
LTC = low temperature cure (250 °C); no other treatment,  
ESTC = standard temperature cure (400 °C) followed by 3000  $\mu\text{C}/\text{cm}^2$  e-beam treatment,  
ELTC = low temperature cure (250 °C) followed by 3000  $\mu\text{C}/\text{cm}^2$  e-beam treatment,  
CELTC = low temperature cure (250 °C) followed by 3000  $\mu\text{C}/\text{cm}^2$  e-beam treatment followed by second cure at 400 °C,  
CEELTC = low temperature cure (250 °C) followed by 5000  $\mu\text{C}/\text{cm}^2$  e-beam treatment followed by second cure at 400 °C,
- C, O, N = atomic fractions of carbon, oxygen, and nitrogen,  
C1, C2, C3 = peak assignments in the C1s spectrum in accordance with figure 5.2.1,  
O1, O2 = peak assignments in the O1s spectrum in accordance with figure 5.2.1. NOTE: O1 (ether oxygen) peak is absent from the theoretical structure of BPDA-PDA.  
N1, amide = peak assignments in the N1s spectrum in accordance with figure 5.2.1. NOTE: amide peak is absent from the theoretical structure of fully cured and undegraded BPDA-PDA.  
FWHM = full width at half maximum (see Section 2.3.2),  
BE = binding energy (see Section 2.3.2).

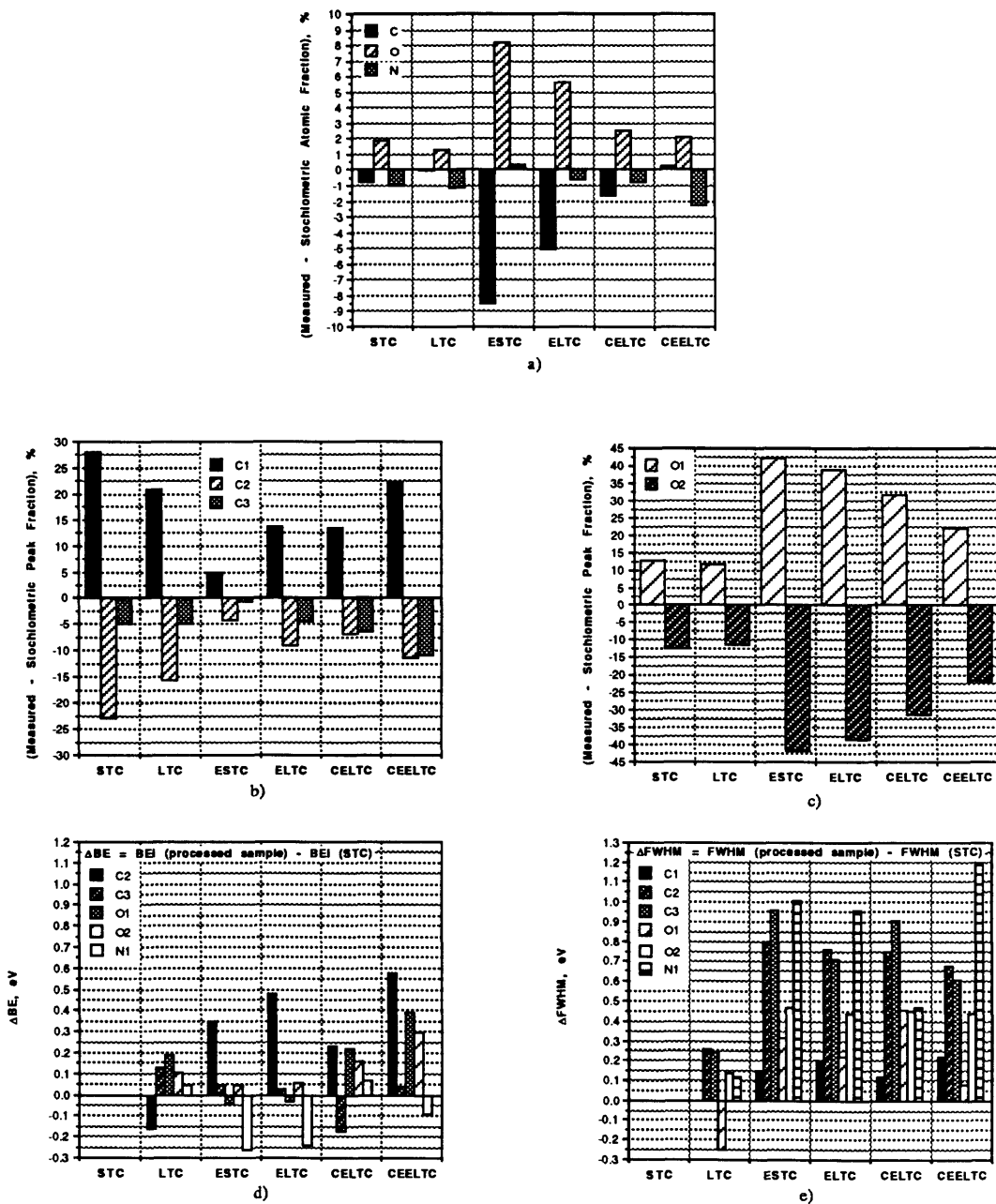


Figure C.2.1. Graphical representation of processed XPS data from six BPDA-PDA samples (peak assignments according to Figure 5.2.1):  
 a) Deviation from the stoichiometric chemical composition,  
 b) Deviation from the theoretical peak fractions in C1s,  
 c) Deviation from the theoretical peak fractions in O1s,  
 d) Relative shifts in peak BEs with respect to STC,  
 e) Relative peak broadening with respect to STC.

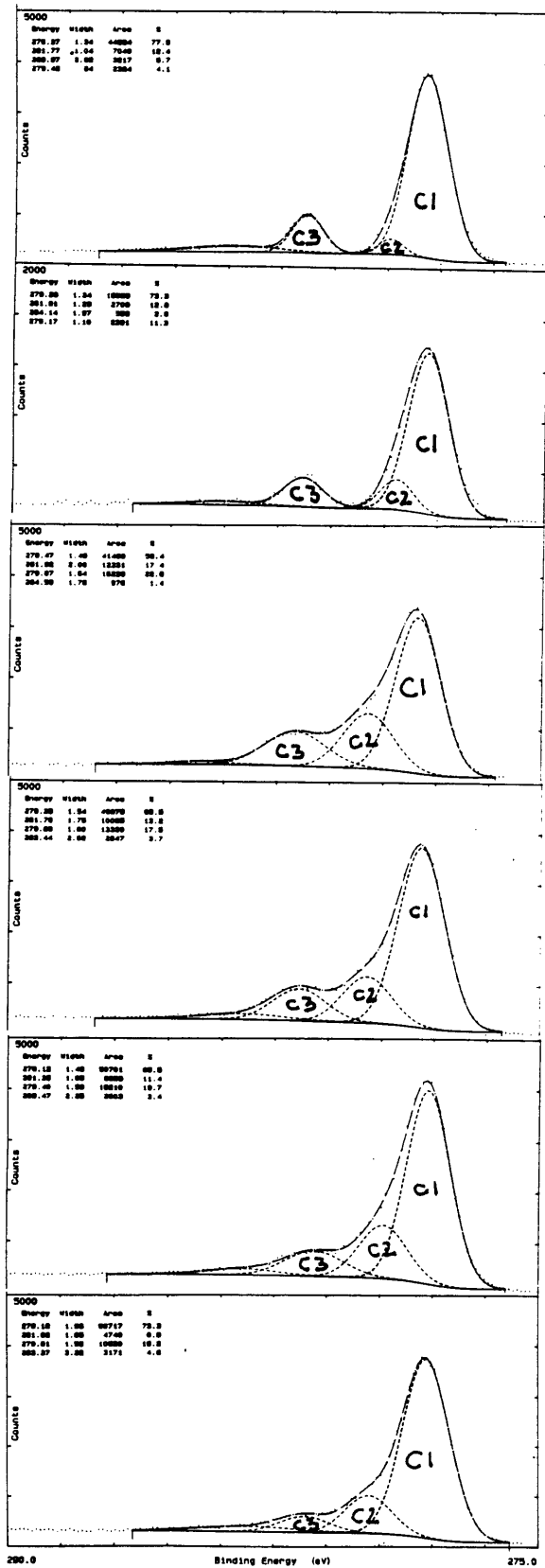


Figure C.2.2. C1s Spectral Evolution of 6 BPDA-PDA Samples.

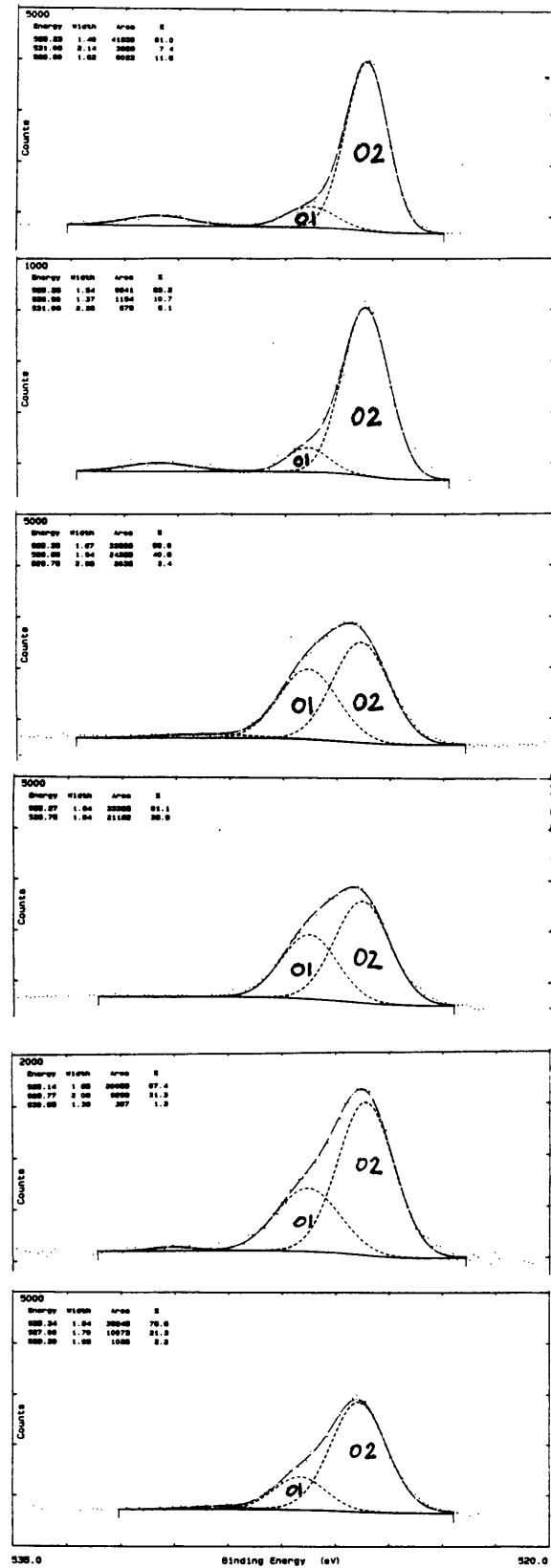


Figure C.2.3. O1s Spectral Evolution of 6 BPDA-PDA Samples.

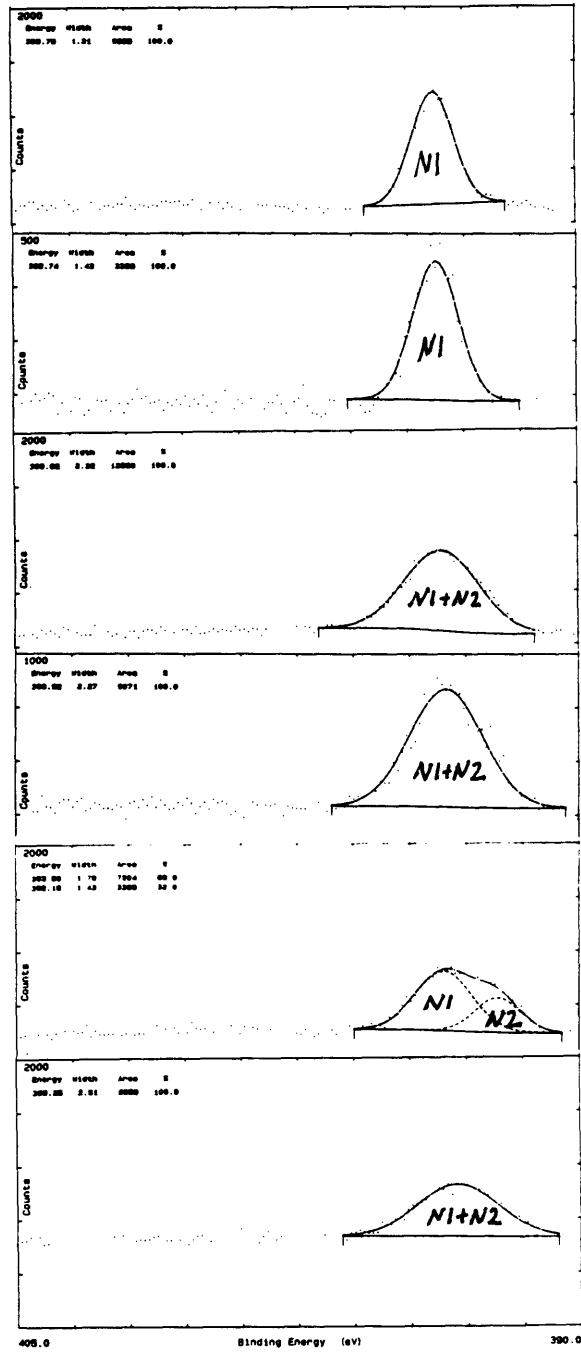


Figure C.2.4. N1s Spectral Evolution of 6 BPDA-PDA Samples.

## 2. XPS Data from Processed BTDA-ODA/MPDA (PI2525)

Elem/Peak	C	O	N	C1	BE	FWHM	C2	BE	FWHM	C3	BE	FWHM	C4
Sample	%	%	%	%	eV	eV	%	eV	eV	%	eV	eV	%
STC	78.4	16.5	5.1	47.0	284.70	1.28	37.3	285.41	1.17	11.1	288.46	1.18	4.6
LTC	76.3	18.2	5.5	53.5	284.70	1.36	32.5	285.51	1.17	10.8	288.46	1.20	3.3
ESTC	73.2	20.1	6.7	63.8	284.70	1.52	22.8	286.13	1.68	13.4	288.19	1.96	0.0
ELTC	74.7	19.0	6.3	65.9	284.70	1.47	18.8	286.10	1.46	15.4	288.01	2.01	0.0
CELTC	79.4	15.5	5.1	77.5	284.70	1.54	15.7	286.23	1.57	6.9	288.20	1.76	0.0
CEELTC	78.1	14.6	7.3	59.3	284.70	1.36	27.8	285.84	1.70	12.9	287.75	2.34	0.0
Elem/Peak			O1	BE	FWHM	O2	BE	FWHM	N1	BE	FWHM	amide	BE
Sample			%	eV	eV	%	eV	eV	%	eV	eV	%	eV
STC			15.3	533.30	1.42	84.7	531.88	1.44	86.5	400.51	1.29	13.5	399.15
LTC			14.6	533.25	1.30	85.4	531.89	1.37	95.6	400.41	1.46	4.4	398.73
ESTC			36.4	533.15	1.90	63.6	531.73	1.61	61.9	400.39	1.66	38.1	399.11
ELTC			40.8	533.12	2.01	59.2	531.67	1.95	100.0	399.78	2.16	0.0	
CELTC			25.8	533.38	1.83	74.2	531.79	1.71	61.6	400.23	1.76	38.4	399.78
CEELTC			22.8	533.57	1.86	77.2	531.98	1.68	62.7	400.31	1.92	37.3	398.72

Table C.2.2. XPS data from analysis of six BTDA-ODA/MPDA samples.

### Legend for Table C.2.2:

- STC = standard temperature cure (400 °C); no other treatment,  
LTC = low temperature cure (250 °C); no other treatment,  
ESTC = standard temperature cure (400 °C) followed by 3000  $\mu\text{C}/\text{cm}^2$  e-beam treatment,  
ELTC = low temperature cure (250 °C) followed by 3000  $\mu\text{C}/\text{cm}^2$  e-beam treatment,  
CELTC = low temperature cure (250 °C) followed by 3000  $\mu\text{C}/\text{cm}^2$  e-beam treatment followed by second cure at 400 °C,  
CEELTC = low temperature cure (250 °C) followed by 5000  $\mu\text{C}/\text{cm}^2$  e-beam treatment followed by second cure at 400 °C,
- C, O, N = atomic fractions of carbon, oxygen, and nitrogen,  
C1, C2, C3, C4 = peak assignments in the C1s spectrum in accordance with figure 5.2.2. NOTE: C4 was not always resolved. In such instances, it contributes mostly to the C2 peak.  
O1, O2 = peak assignments in the O1s spectrum in accordance with figure 5.2.2,  
N1, amide = peak assignments in the N1s spectrum in accordance with figure 5.2.2. NOTE: amide peak is absent from the theoretical structure of fully cured and undegraded BTDA-ODA/MPDA.  
FWHM = full width at half maximum (see Section 2.3.2),  
BE = binding energy (see Section 2.3.2).

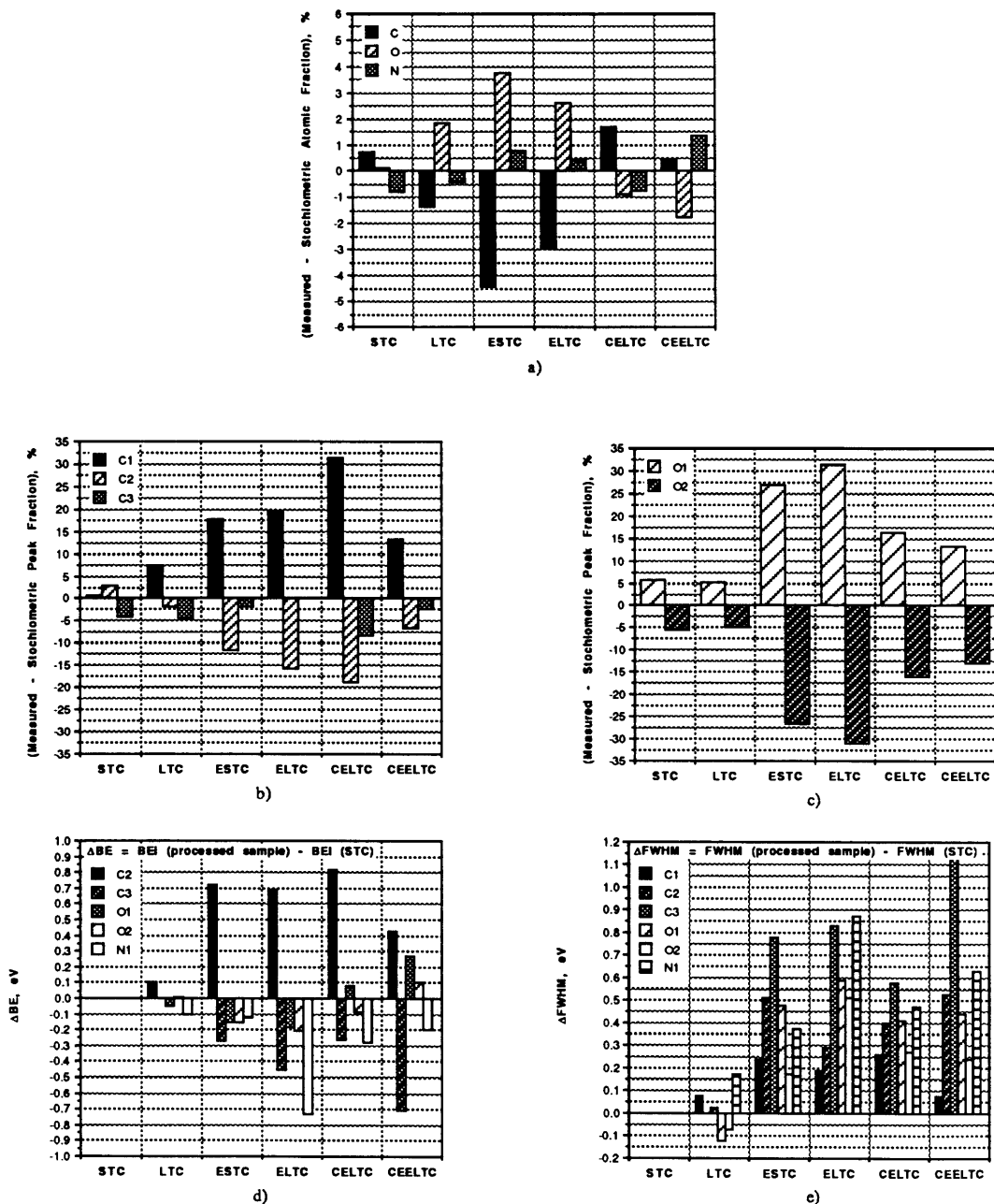


Figure C.2.5. Graphical representation of processed XPS data from six BTDA-ODA/MPDA samples (peak assignments according to Figure 5.2.2):  
a) Deviation from the stoichiometric chemical composition,  
b) Deviation from the theoretical peak fractions in C1s,  
c) Deviation from the theoretical peak fractions in O1s,  
d) Relative shifts in peak BEs with respect to STC,  
e) Relative peak broadening with respect to STC.

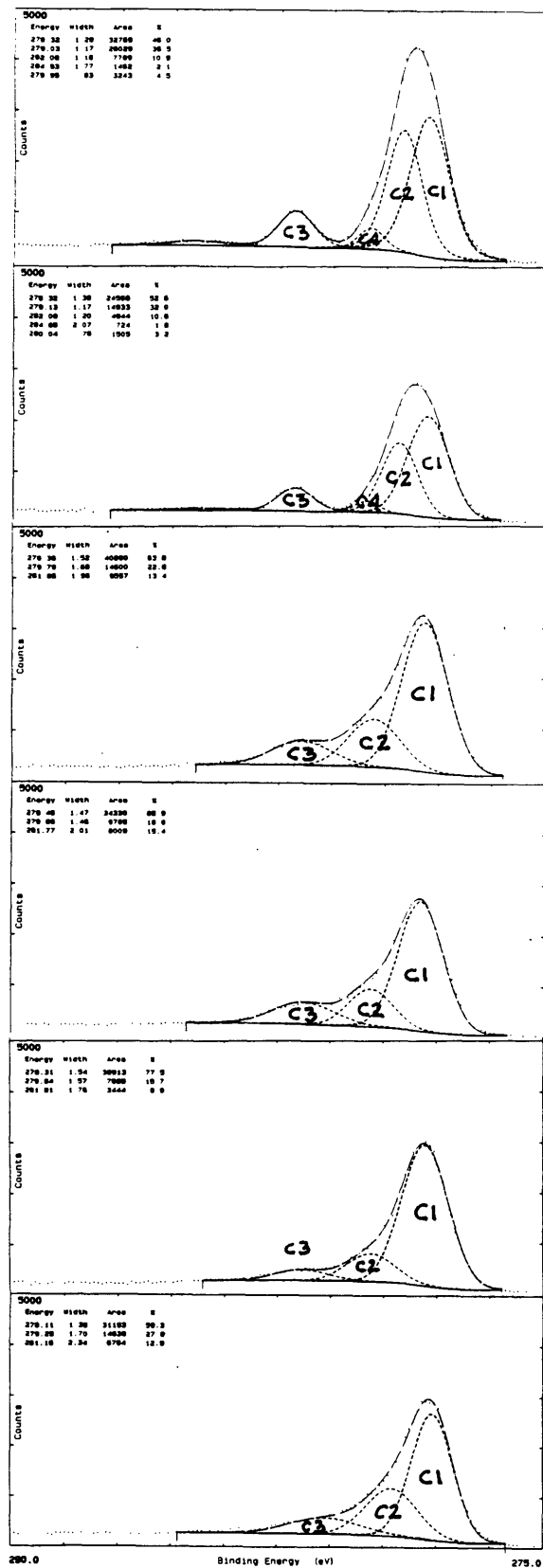


Figure C.2.6. C1s Spectral Evolution of 6 BTDA-ODA/MPDA Samples.

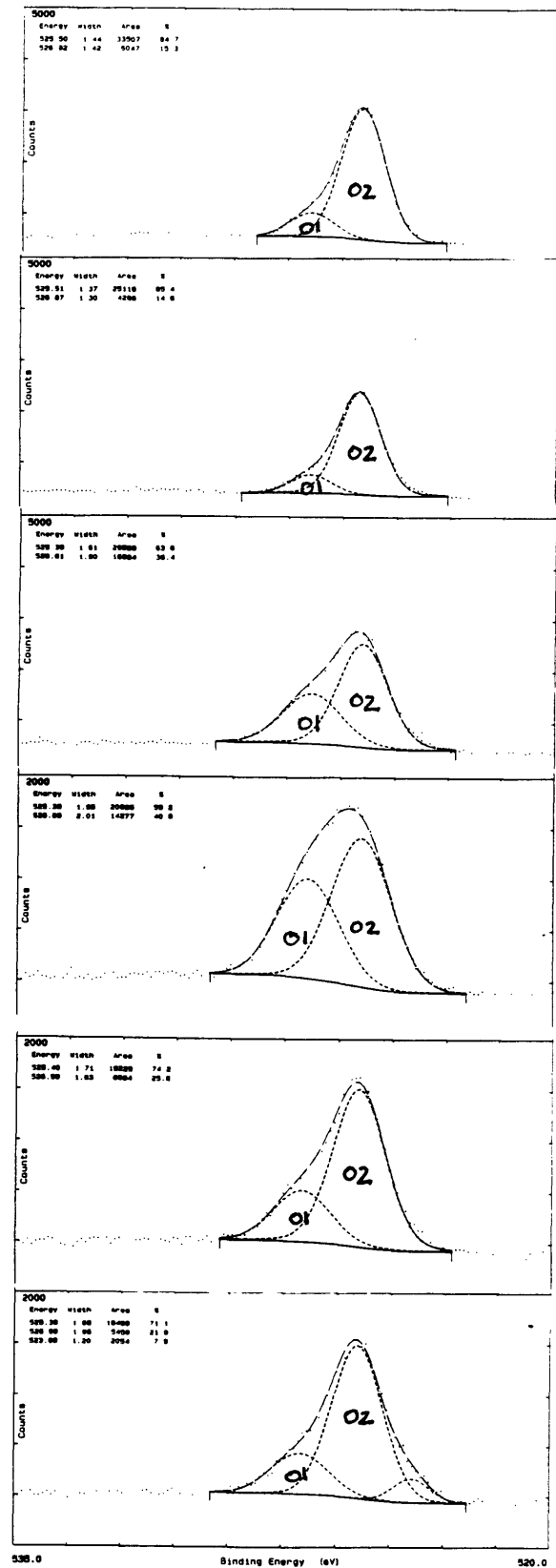


Figure C.2.7. O1s Spectral Evolution of 6 BTDA-ODA/MPDA Samples.



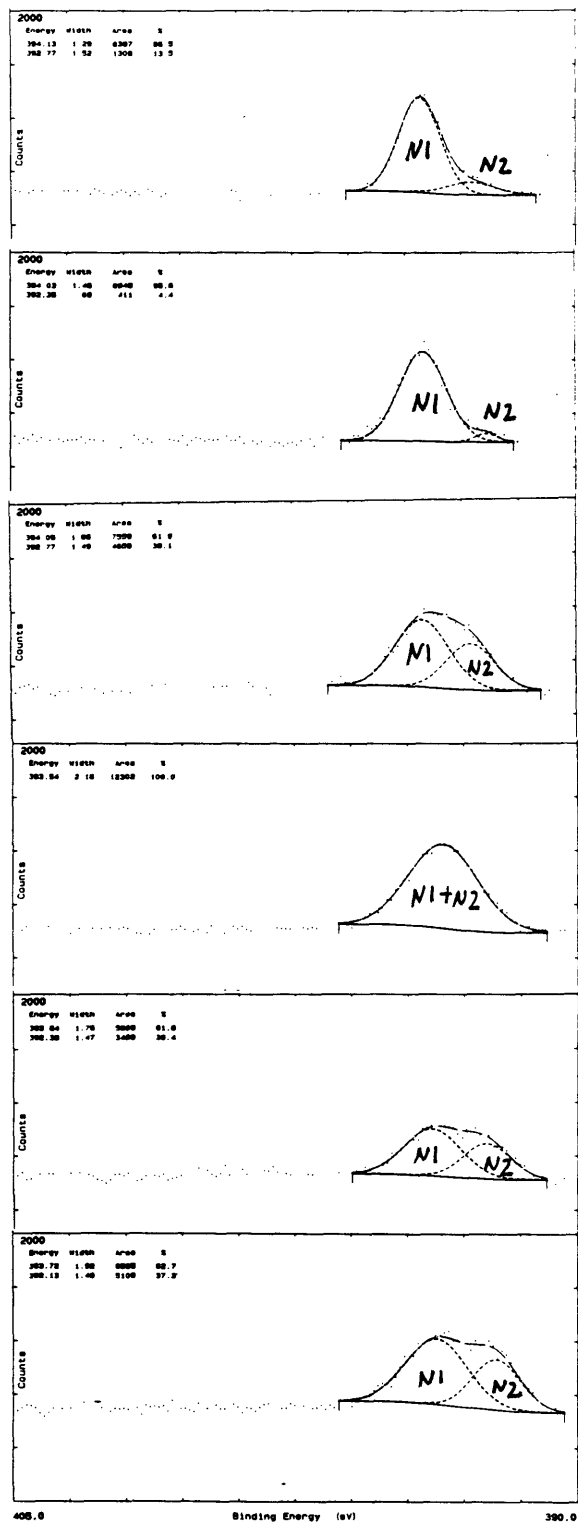


Figure C.2.8. N1s Spectral Evolution of 6 BTDA-ODA/MPDA Samples.

### 3. XPS Data from Processed PMDA-ODA (OCG627)

Elem/Peak	C	O	N	C1	BE	FWHM	C2	BE	FWHM	C3	BE	FWHM
Sample	%	%	%	%	eV	eV	%	eV	eV	%	eV	eV
STC	76.9	16.7	6.4	44.1	284.70	1.34	43.1	285.77	1.46	12.8	288.69	1.09
LTC	75.0	18.8	6.3	41.7	284.70	1.24	44.7	285.73	1.44	13.6	288.65	1.31
ESTC	73.0	20.1	6.9	63.8	284.70	1.53	23.0	286.15	1.68	13.2	288.19	1.76
ELTC	74.7	18.5	6.7	66.0	284.70	1.58	22.7	286.22	1.67	11.2	288.10	1.76
CELTC	78.5	15.5	5.9	71.5	284.70	1.47	20.4	286.02	1.60	8.2	288.34	1.79
CEELTC	76.5	19.3	4.2	70.3	284.70	1.38	18.3	285.93	1.49	11.4	287.85	2.15

Elem/Peak		O1	BE	FWHM	O2	BE	FWHM	N1	BE	FWHM	amide	BE
Sample		%	eV	eV	%	eV	eV	%	eV	eV	%	eV
STC		30.3	533.36	1.38	69.7	532.04	1.36	100.0	400.54	1.36	0.0	
LTC		36.1	533.20	1.53	63.9	531.78	1.51	100.0	400.13	1.48	0.0	
ESTC		45.4	533.09	1.92	54.6	531.60	1.79	100.0	399.90	2.40	0.0	
ELTC		45.3	533.05	1.95	54.7	531.56	1.88	100.0	399.62	2.36	0.0	
CELTC		38.3	533.30	1.87	61.7	531.71	1.79	74.1	400.08	1.74	25.9	398.48
CEELTC		34.0	533.36	1.93	66.0	531.78	1.96	61.3	400.25	1.64	38.7	398.63

Table C.2.3. XPS data from analysis of six PMDA-ODA samples.

**Legend for Table B.2.3:**

- STC = standard temperature cure (400 °C); no other treatment,  
LTC = low temperature cure (250 °C); no other treatment,  
ESTC = standard temperature cure (400 °C) followed by 3000  $\mu\text{C}/\text{cm}^2$  e-beam treatment,  
ELTC = low temperature cure (250 °C) followed by 3000  $\mu\text{C}/\text{cm}^2$  e-beam treatment,  
CELTC = low temperature cure (250 °C) followed by 3000  $\mu\text{C}/\text{cm}^2$  e-beam treatment followed by second cure at 400 °C,  
CEELTC = low temperature cure (250 °C) followed by 5000  $\mu\text{C}/\text{cm}^2$  e-beam treatment followed by second cure at 400 °C,
- C, O, N = atomic fractions of carbon, oxygen, and nitrogen,  
C1, C2, C3 = peak assignments in the C1s spectrum in accordance with figure 5.2.3. NOTE: C2 represents an unresolved combination from several shifted carbon peaks.  
O1, O2 = peak assignments in the O1s spectrum in accordance with figure 5.2.3,  
N1, amide = peak assignments in the N1s spectrum in accordance with figure 5.2.3. NOTE: amide peak is absent from the theoretical structure of fully cured and undegraded PMDA-ODA.  
FWHM = full width at half maximum (see Section 2.3.2),  
BE = binding energy (see Section 2.3.2).

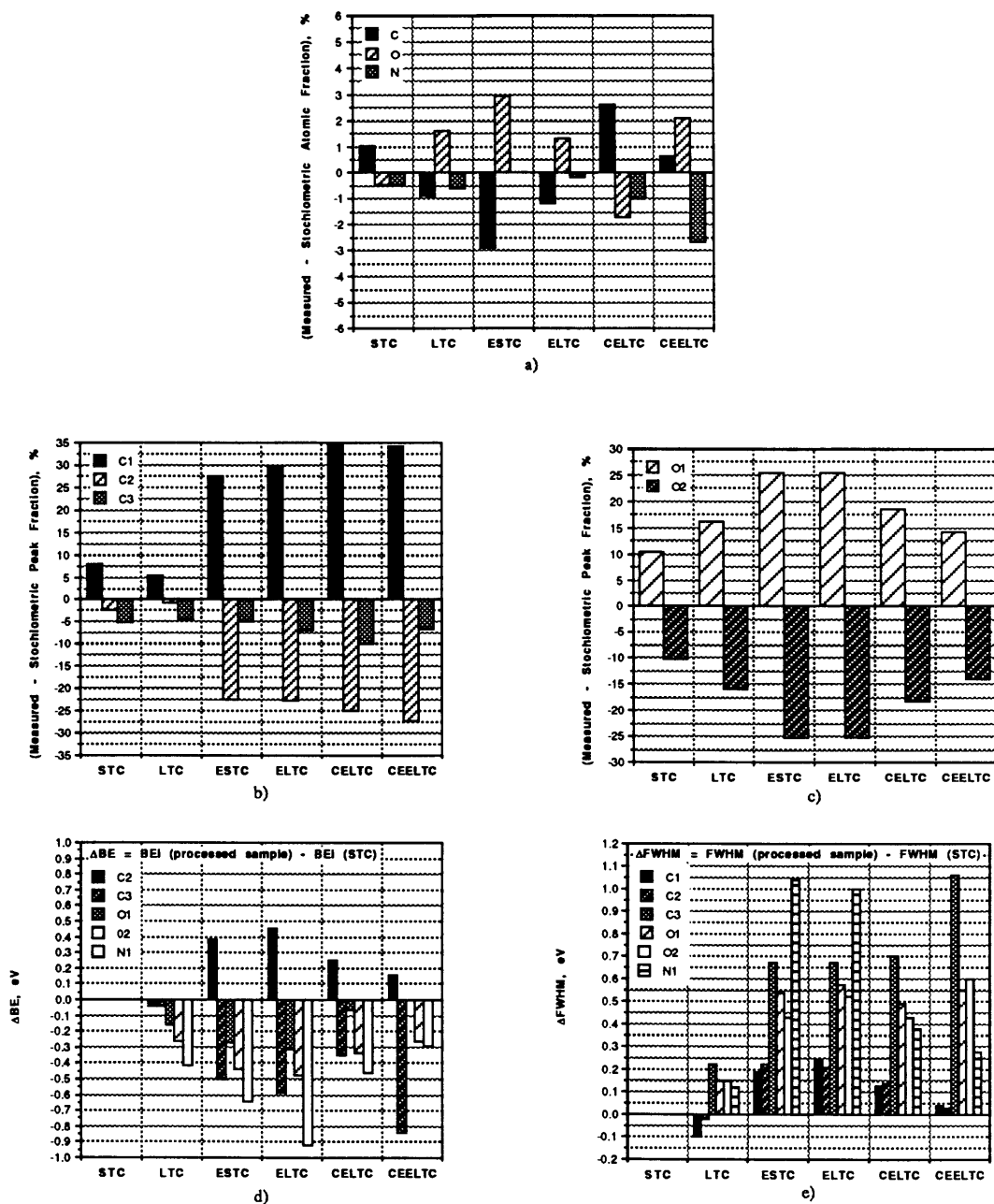


Figure C.2.9. Graphical representation of processed XPS data from six PMDA-ODA samples (peak assignments according to Figure 5.2.3):  
a) Deviation from the stoichiometric chemical composition,  
b) Deviation from the theoretical peak fractions in C1s,  
c) Deviation from the theoretical peak fractions in O1s,  
d) Relative shifts in peak BEs with respect to STC,  
e) Relative peak broadening with respect to STC.

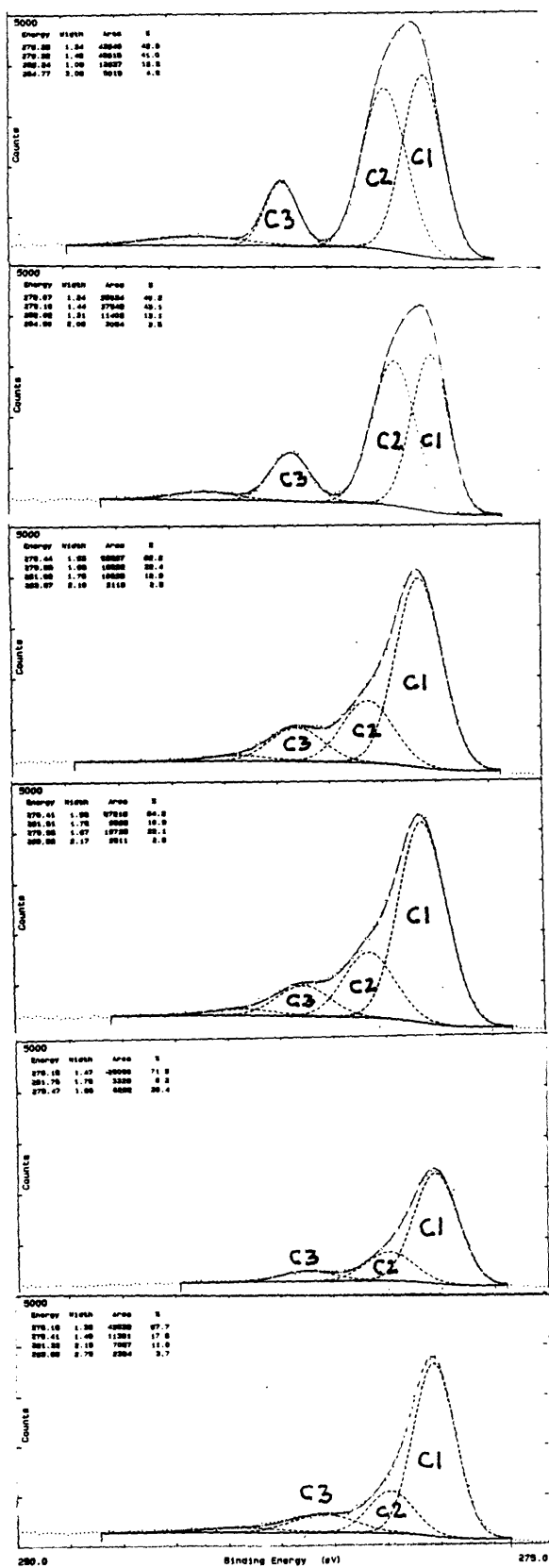


Figure C.2.10. C1s Spectral Evolution of 6 PMDA-ODA Samples.

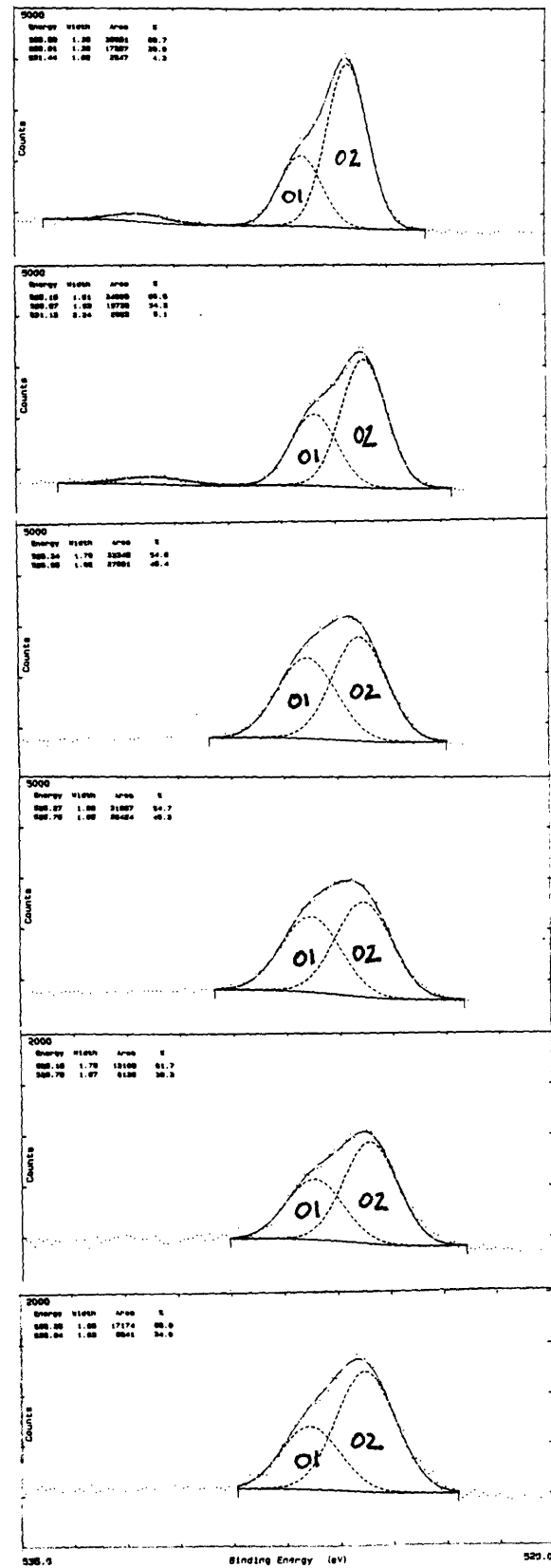


Figure C.2.11. O1s Spectral Evolution of 6 PMDA-ODA Samples.

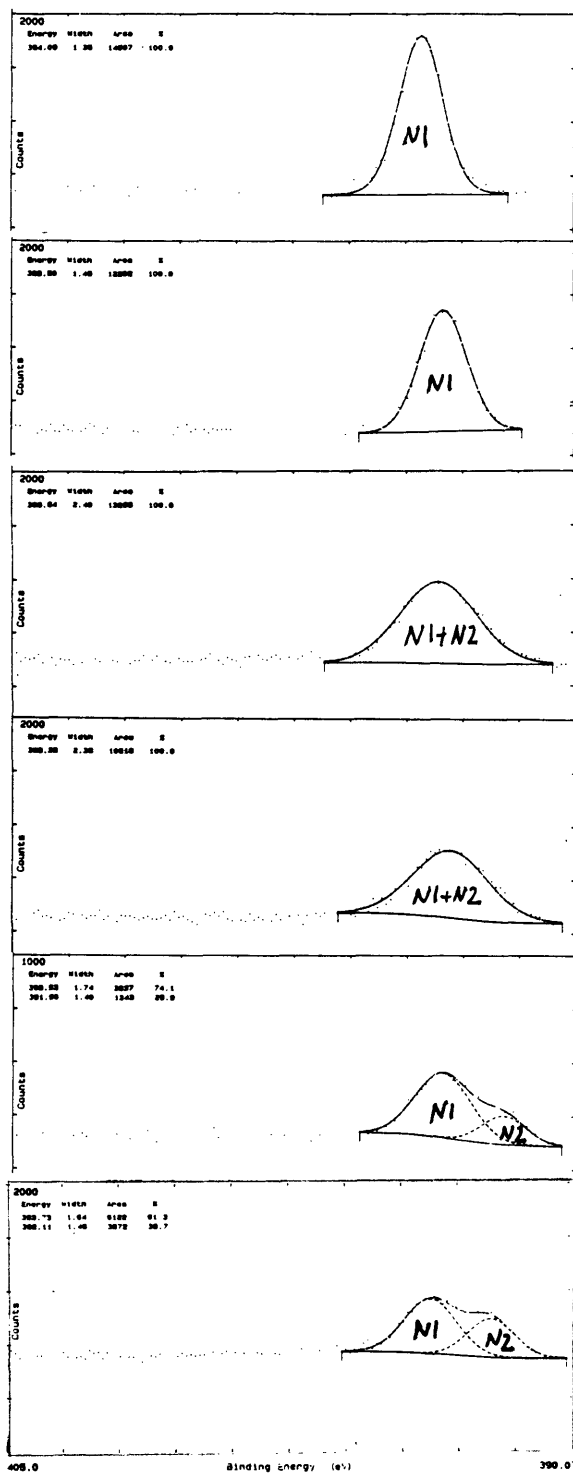


Figure C.2.12. N1s Spectral Evolution of 6 PMDA-ODA Samples.

Appendix C.3.XPS Data from Heat Treated and Laser-Ablated Kapton®

[102]



0.04 cm

Figure C.3.1. Micrograph of laser-ablated polyimide [102].

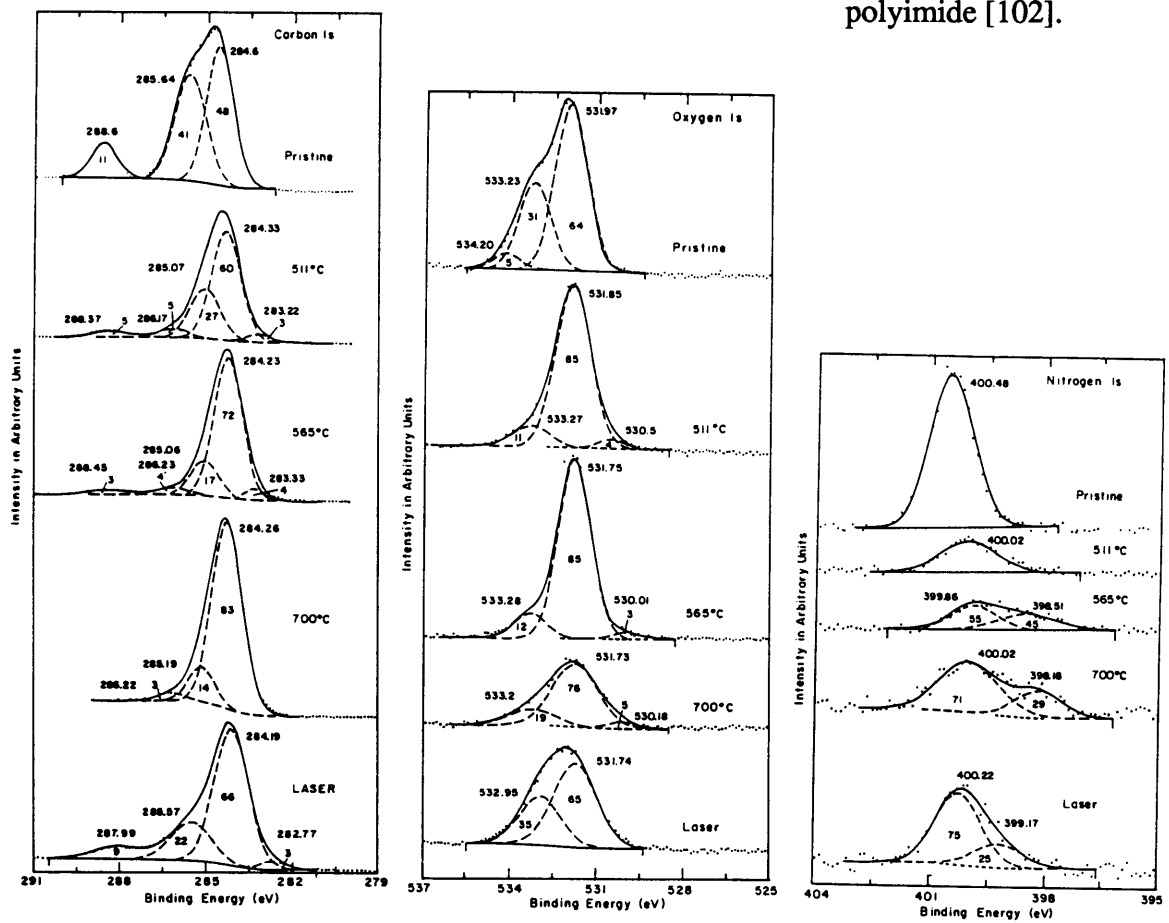


Figure C.3.2. XPS spectra of C1s, O1s, and N1s in pristine and treated Kapton® (heat treatment and laser ablation). The peak contributions (%) are indicated inside the peaks [102].

## Bibliography

1. D. A. Doane, P. D. Franzon, eds., "Multichip Module Technologies and Alternatives", Van Nostrand Reinhold (1993).
2. D. P. Seraphim, R. Lasky, C. Li, eds., "Principles of Electronic Packaging", McGraw-Hill (1989).
3. D. Wilson et al, eds., "Polyimides", Blackie, Glasgow (1990).
4. H. J. Neuhaus et al, J. Electronic Matls., **14**, pp. 379-404 (1985).
5. M. D. Adams et al, in "Electronic Packaging and Corrosion in Microelectronics", M. E. Nicholson, ed., pp. 15-23, ASM International (1987).
6. G. W. Warren, I. Chatterjee, in "Corrosion of Electronic Materials and Devices", J. D. Sinclair, ed., The Electrochem. Soc, Inc. 91-2, pp. 176-185 (1991).
7. R. T. Howard, in "Electronic Packaging and Corrosion in Microelectronics", M. E. Nicholson, ed., pp. 131-144, ASM International (1987).
8. G. Chandra, in "Electronic Packaging Materials Science V", E. D. Lillie et al, eds., MRS Symposium Proc. 203, pp. 97-108 (1991).
9. R. Frankovich et al, in "Electronic Packaging Materials Science V", E. D. Lillie et al, eds., MRS Symposium Proc. 203, pp. 189-202 (1991).
10. K. M. Takahashi, in "Corrosion of Electronic Materials and Devices", J. D. Sinclair, ed., The Electrochemical Society, Inc. 91-2, pp. 40-57 (1991).
11. P. V. Nagarkar et al, "XPS Studies of Polyimide-On-Chromium And Chromium-On-Polyimide Interfaces", in Abstracts of the Fourth Intl. Conference on Polyimides, pp. 149-152, Ellenville, NY (1991).
12. E. O. Shaffer, S. D. Senturia, eds., "The EPP Databook", MIT, Cambridge, MA (1993).
13. J. R. Macdonald, Ed., "Impedance Spectroscopy", John Wiley & Sons (1987).
14. A. J. Bard, L. R. Faulkner, "Electrochemical Methods", John Wiley & Sons (1980).
15. A. R. Blythe, "Electrical Properties of Polymers", Cambridge University Press, Cambridge (1979).
16. T. Miyamoto, K. Shibayama, J. Appl. Phys., **44**, p. 5372 (1973).
17. J. R. Macdonald, "CNLS: Complex Nonlinear Least Squares Immitance Fitting Program - LEVM Version 3.05", UNC, Chapel Hill, NC (1989).
18. D. Briggs, M. P. Seah, "Practical Surface Analysis", V.1, John Wiley & Sons (1990).
19. G. Beamson, D. Briggs, "High Resolution XPS of Organic Polymers", John Wiley & Sons (1992).
20. Ghosh, P. K., "Introduction to Photoelectron Spectroscopy", John Wiley & Sons (1983).
21. S. Noe, " A Prism Coupling Study of Optical Anisotropy in Polyimide Including Moisture, Stress, and Thickness Effects", PhD Dissertation, DMSE, MIT, Cambridge, MA (1992).
22. ASTM: D 1505 - 85, "Standard Test Method for Density of Plastics by the Density-Gradient Technique", ASTM, Philadelphia (1986).
23. R. E. Wiley, "Setting up a Density Gradient Laboratory", *Plastics Technology*, **8**, pp. 31-41 (1962).
24. G. E. Zaikov et al, "Diffusion of Electrolytes in Polymers", VSP BV, Utrecht (1988).
25. J. Comyn, Ed., "Polymer Permeability", Elsevier (1985).
26. J. Crank, G. S. Park, Eds., "Diffusion in Polymers", Academic Press (1968).
27. N. Lakshminarayanaiah, "Transport Phenomena in Membranes", Academic Press (1969).
28. D. D. Denton, "Moisture Transport in Polyimide Films in Integrated Circuits", PhD Dissertation, DEECS, MIT, Cambridge, MA (1987).

29. B. S. Lim, "Effect of Structure and Composition of Polyimide Films on Sorption and Dielectric Properties", PhD Dissertation, SEAS, Columbia University, NY (1991).
30. K. Okamoto et al, "Sorption and Diffusion of Water Vapor in Polyimide Films", *J. Polym. Sci., B: Polym. Phys.*, **30**, pp. 1233-1231 (1992).
31. H. Pranjoto, D. D. Denton, "Steady State Behavior and Kinetics Modeling of PMDA-ODA PI as a Function of Cure Schedule Using Gravimetric Method", 4th Intl. Conference on Polyimides, Abstracts, pp. 111-114, Ellenville, NY (1991).
32. E. Sacher, J. R. Susko, "Water Permeation of Polymer Films. I. Polyimide", *J. Appl. Polym. Sci.*, **23**, pp. 2355-2364 (1979).
33. B. S. Lim et al, "Sorption of Water and Organic Solutes in Polyimide Films and Its Effects on Dielectric Properties", *J. Polym. Sci., B: Polym. Phys.*, **31**, pp. 545-555 (1993).
34. S. Z. Li et al, "Diffusion and Deuteron Nuclear Magnetic Resonance Study of the Distribution of Water Molecules in Polyimide Films", *J. Electrochem. Soc.*, **139**, pp. 662-667 (1992).
35. R. M. Felder et al, "Dual-Mode Sorption and Transport of Sulfur Dioxide in Kapton Polyimide", *J. Polym. Sci.: Polym. Phys.*, **19**, pp. 1895-1909 (1981).
36. D. K. Yang et al, "Sorption and Transport Studies of Water in Kapton® Polyimide", *J. Appl. Polym. Sci.*, **30**, pp. 1035-1047 (1985).
37. G. Mensitieri et al, "Water Sorption Kinetics in PEEK", *J. Appl. Polym. Sci.*, **37**, pp. 381-392 (1989).
38. C. R. Moylan et al, "Solubility of Water in Polyimides: Quartz Crystal Microbalance Measurements", *J. Polym. Sci. B: Polym. Phys.*, **29**, pp. 87-92 (1991).
39. J. Y. Pan, "A Study of Suspended-Membrane and Acoustic Techniques for the Determination of the Mechanical Properties of Thin Polymer Films", PhD Dissertation, DEECS, MIT, Cambridge, MA (1991).
40. H. M. Tong, K. L. Saegner, "Bending-Beam Study of Water Sorption by Thin PMMA Films", *J. Appl. Polym. Sci.*, **38**, pp. 937-950 (1989).
41. J.-H. Jou et al, "Structure Effect on Water Diffusion and Hygroscopic Stress in Polyimide Films", *J. Appl. Polym. Sci.*, **43**, pp. 857-875 (1991).
42. J.-H. Jou et al, "Bending Beam Measurement of Moisture Diffusion in Polyimide Films on Silicon Substrate", *Polym. Journal*, **23**, pp. 1123-1133 (1991).
43. J.-H. Jou et al, "Effects of Imide Structure/Thickness/Curing on Solvent Diffusion in Polyimides", *Macromolecules*, **25**, pp. 5186-5191 (1992).
44. D. Denton et al, "Moisture Diffusion in Polyimide Films in Integrated Circuits", *J. Electronic Matls.*, **14**, pp. 119-136 (1985).
45. F. Bellucci, L. Nicodemo, "Water Transport in Organic Coatings", *Corrosion*, **49**, pp. 235-247 (1993).
46. D. K. Yang et al, "The Effects of Morphology and Hygrothermal Aging on Water Sorption and Transport in Kapton® Polyimide", *J. Appl. Polym. Sci.*, **31**, pp. 1619-1629 (1986).
47. P. J. Harrop, "Dielectrics", Butterworths, London (1972).
48. D. A. MacInnes, "The Principles of Electrochemistry", New York Dover (1961).
49. Akhadov, Y. Y., "Dielectric Properties of Binary Solutions", Pergamon Press (1981).
50. M. Matsuguchi et al, "Effect of Sorbed Water on the Dielectric Properties of Acetylene-Terminated Polyimide Resins and Their Application to a Humidity Sensor", *J. Electrochem. Soc.*, **140**, pp. 825-829 (1993).
51. F. Bellucci et al, "Protective Properties of Polyimide (PMDA-ODA) on Aluminum Metallic Substrate", *J. Electrochem. Soc.*, **138**, pp. 40-48 (1991).



52. M. J. Kloppers et al, "Transport and Dielectric Properties of PET as Determined via Electrochemical Techniques", *J. Appl. Polym. Sci.*, **48**, pp. 2197-2205 (1993).
53. F. Mansfeld, C. Tsai, "Determination of the Protective Properties of Polymer Coatings from High-Frequency Impedance Data", *Proc. 12th ICC*, **1**, pp. 128-150, NACE-Houston (1993).
54. J. R. Scully, "Electrochemical Impedance of Organic-Coated Steel: Correlation of Impedance Parameters with Long-Term Coating Deterioration", *J. Electrochem. Soc.*, **136**, pp. 979-990 (1989).
55. B. Popov et al, "Using EIS as a Tool for Organic Coating Solute Saturation Monitoring", *J. Electrochem. Soc.*, **140**, pp. 947-951 (1993).
56. H. Leidheiser, M. Kendig, "The Mechanism of Corrosion of Polybutadiene-Coated Steel in Aerated Sodium Chloride", *Corrosion*, **32**, pp. 69-75 (1976).
57. L. Hartshorn, N. Megson, E. Rushton, *J. Soc. Chem. Industry*, **56**, p. 266 (1937).
58. F. Bellucci et al, "A Study of Corrosion Initiation on Polyimide Coatings", *Corr.Sci.*, **33**, pp. 1203-1226 (1992).
59. R. B. Bird, W. E. Stewart, E. N. Lightfoot, "Transport phenomena", Wiley, New York (1960).
60. S. T. Sackinger, "The Determination of Swelling Stresses in Polyimide Films", PhD Dissertation, DCE, University of Massachusetts (1990).
61. CRC, "CRC Handbook of Chemistry and Physics", 56th Edition, CRC Press, Cleveland, OH (1976).
62. A. Bondi, "Van der Waals Volumes and Radii", *J. Phys. Chem.*, **64**, pp. 441-451 (1964).
63. D. W. van Krevelen, "Properties of Polymers", Elsevier (1976).
64. S. Sikorski, PhD Dissertation, DMSE, MIT, Cambridge, MA (1994).
65. Leu et al, "Thermomechanical Properties of Polyimides: The Effect of Curing Conditions on the Thickness-Dependent Properties", MRS Fall Meeting, Boston, November (1993).
66. E. Sacher, J. R. Susko, "Water Permeation of Polymer Films. III. High Temperature Polyimides", *J. Appl. Polym.Sci.*, **26**, pp. 679-686 (1981).
67. Amoco Chemical Product Literature, Bulletin UL-P3, "ULTRADEL™", Amoco Chemical Co., Chicago, IL (1991).
68. B. N. Khare et al, "Infrared and Dielectric Studies of Chloroform as Proton Donor in Hydrogen-Bond Formation", *J. Chem. Phys.*, **47**, pp. 5173-5179 (1967).
69. E. McCafferty et al, *Trans.Faraday Soc.*, **66**, p. 1720 (1970).
70. S. N. Vinogradov, R. H. Linnell, "Hydrogen Bonding", VNR Company (1971).
71. R. G. Green, "Hydrogen Bonding by C-H Groups", J. Wiley & Sons (1974).
72. L. M. Doane, J. A. Bruce, R. G. Narechania, "Hydrogen Fluoride Diffusion Through a Polyimide Membrane", *J. Electrochem. Soc.*, **135**, pp. 3155-3159 (1988).
73. Lobo, V. M. M., "Handbook of electrolyte solutions", Elsevier (1989).
74. Horvath, A. L., "Handbook of aqueous electrolyte solutions : physical properties, etc", Halsted Press (1985).
75. S. Beilin, Fujitsu Computer Packaging Technologies, Personal Communication.
76. Orion Research Inc., Models 84-11, 94-17, Product Information, Boston (1987).
77. O. Kedem, A. Katchalsky, "Thermodynamic Analysis of the Permeability of Biological Membranes to Non-Electrolytes", *Biochim.Et Biohys.Acta*, **27**, pp. 229-246 (1958).
78. C. W. Versluijs, J. A. Smit, "Nonstationary Diffusion through a Membrane Separating Two Finite Volumes of Stirred or Unstirred Solutions", *J. Membrane Sci.*, **4**, pp. 183-207 (1978).
79. C. J. P. Hoogervorst et al, "Nonstationary Diffusion through Membranes: Part 1." *J. Phys. Chem.*, **62**, pp.1311-1324 (1978).

80. J. Crank, "The Mathematics of Diffusion", Oxford University Press, London (1979).
81. A. Schussler et al, "Na+ and Cl- Transport Across PI Films", *J. Appl. Polym. Sci.*, **42**, pp. 1567-1577 (1991).
82. S. Haruyama, M. Asari, T. Tsuru, "Corrosion Protection by Organic Coatings", M. Kendig, H. Leidheiser, Eds., Proc. Vol. 672, p.197, Electrochem. Society, Pennington, NJ (1987).
83. J. Titz, "Characterization of Organic Coatings on Metal Substrates by EIS", *Corrosion*, **46**, p.221 (1990).
84. M. Kendig, J. Scully, "Basic Aspects of Electrochemical Impedance Applications for the Life Prediction of Organic Coatings on Metals", *Corrosion*, **46**, pp. 22-29 (1990).
85. R. Hirayama, S. Haruyama, "Electrochemical Impedance for Degraded Coated Steel Having Pores", *Corrosion*, **47**, pp. 952-958 (1991).
86. F. Mansfeld, C. H. Tsai, "Determination of Coating Deterioration with EIS. I. Basic Relationships", **47**, pp. 958-965 (1991).
87. S. A. McCluney et al, "Comparing EIS Methods for Estimating the Degree of Delamination of Organic Coatings on Steel", *J. Electrochem. Soc.*, **139**, pp. 1556-1560 (1992).
88. F. M. Geenen et al, "Study of the Degradation Mechanism of Epoxy Coatings on Steel Using EIS", Proc. 11th ICC, **2**, pp. 231-240, NACE (1992).
89. J. N. Murray, H.P. Hack, "Long-Term Electrochemical Characterization of Epoxy-Coated Steel Using EIS", Proc. 12th ICC, **1**, pp. 151-156, Houston, TX, NACE (1993).
90. A. Amirudin, P. Jernberg, D. Thierry, "Determination of Coating Delamination and Underfilm Corrosion during Atmospheric Exposure by means of EIS", Proc. 12th ICC, **1**, pp. 171-181, Houston, TX, NACE (1993).
91. M. Kendig et al, "Microscopic Monitoring of the Cathodic Degradation of Polyimide-Coated Al Metallization", *Electrochim. Acta*, **38**, pp.1877-1881 (1993).
92. M. W. Kendig, S. Jeanjaquet, J. Lumsden, "Electrochemical Impedance of Coated Metal Undergoing Loss of Adhesion", ASTM STP 1188, J. R. Scully, D. C. Silverman, M. W. Kendig, Eds., pp. 407-427, ASTM, Philadelphia (1993).
93. C. H. Tsai, F. Mansfeld, "Determination of Coating Deterioration with EIS. II. Development of a Method for Field Testing of Protective Coatings", *Corrosion*, **49**, pp.726-737 (1993).
94. EG&G Princeton Applied Research, Application Note AC-5, Princeton, NJ (1986).
95. H. Leidheiser, "Corrosion of Painted Metals - A Review", *Corrosion*, **38**, pp. 374-383 (1982).
96. P. V. Nagarkar et al, "Interfacial Interactions Affecting Polyimide Reliability", Proc. 39th Electronic Components Conference, Houston, TX, IEEE (1989).
97. R. M. Latanision et al, "Corrosion Engineering in Device Packaging", *Mat. Res. Soc. Symp. Proc.*, **203**, pp. 87-95, MRS (1991).
98. J. N. Murray, H.P. Hack, "Long-Term Testomg of Epoxy-Coated Steel in ASTM Seawater Using EIS", *Corrosion*, **47**, pp. 480-489 (1991).
99. E. K.-Y. Tan, "Corrosion initiation studies of polyimide-coated metallic substrates", MS Thesis, DMSE, MIT (1991).
100. A. J. Sedriks, "Advanced Materials in Marine Environments", *Materials Performance*, **33**, pp. 56-63 (1994).
101. B. J. Bachman, M. J. Vasile, *J. Vac. Sci. Tech. (A)*, **7**, p. 2709 (1989).
102. P. V. Nagarkar, E. K. Sichel, "XPS Study of Polyimide H-Film after Heat-Treatment and Laser Processing", *J. Electrochem. Soc.*, **136**, pp. 2979-2982 (1989).

## Biographical Note

The author was born in Rousse, Bulgaria, on the once blue Danube. After a very happy childhood and graduation from the local English Language Gymnasium (High School), where he learned to speak English and Russian with a proper Bulgarian accent, the author was accepted by the Technical University in Rousse to study Mechanical Engineering. However, first he was constricted into the Bulgarian Army and served for two years in the Rhodope Mountains near the border with Greece. There he studied German from a textbook hidden in the barrel of the howitzer, and listened to the VOA over a transistor radio sewn under the armpit in his uniform. After a honorable discharge, the author decided to spend some time as far away as possible, and applied to the Bergakademie-Freiberg (BAF) near Dresden in East Germany. Upon arrival, he discovered that he had been studying the wrong language. With time he learned, but to this day he cannot completely comprehend why a German "table" is a he instead of a she. The author thoroughly enjoyed his experience in East Germany, not least because of the liberal ways of the natives. To this day, he has many dear friends there who he misses. Despite all extraneous diversions, the author managed to graduate with honors. At that time, his pen-friend from Boca Raton mentioned to him about the famous Florida Atlantic University. The author vividly remembers the laughter of his best friends whom he secretly told of his plans. So began an year-long secret odyssey which, mostly thanks to his father and to the help of some other people, ended with success. When he got on the plane to Miami in September, 1989, he had no idea that the system would crumble only two months after his departure. In Boca, the author fell in love with the sea. Unfortunately, this intimate relationship was cut short by his coming to Boston, but it was here that he finally met his wife.

Now, the author is happily married and looking forward to life after school. His brother and sister-in-law are both in medical graduate school in New Orleans, and all of them are missing and are being missed by their parents and grandparents back home.

The interference of so many happy memories may explain some of the shortcomings of this thesis.

5090-19

---